Relativistic corrections to weak lensing convergence

by

Sambatra Hagatiana Andrianomena

The thesis is submitted to
the Department of Mathematics and Applied Mathematics
University of Cape Town, South Africa
in partial fulfillment of the requirements for the award of
the degree of Doctor of Philosophy

Supervisor: **Assoc. Prof. Chris Clarkson**

May 18, 2016

Acknowledgements

I would like to thank all the staffs and students at the Institute of Cosmology and Gravitation at the University of Portsmouth for their hospitality during my visits there, especially David Bacon who, apart from being a great collaborator, devoted so much of his time explaining me the concepts on Doppler magnification, key ideas on observations and forecasts, and giving me advice about life in general. I am really thankful to Camille Bonvin, whom I really enjoy collaborating with, for helping me understand important key aspects of the project on Dipole modulation. I also thank all the great people I met with at CERN. I am thankful to Jean-Philippe Uzan, our collaborator on the paper about non-linear contribution to weak lensing and Krzysztof Bolejko for his collaboration on the Doppler lensing paper.

I would like to thank Roy Maartens for all those discussions we had about a great part of this work. He has always been helpful, especially over the last few months before the submission of this thesis where, apart from dealing with work, I was wrapped up with various other things. Without his help, advice and guidance I wouldn't have made it through.

I would like to thank all the staff members of the Mathemathics and Applied Mathematics Department, Nicky and Rushana for their assistance on different administrative related issues. A special thanks to all my officemates and collegues, Pierre, Daan, Emma, Teboho, Thomas, Sulona, Timothy, Maripa, Muzi, Tony and especially Manana who always helped me with some technicalities related to software and gave me great insights into math problems. I also thank the postdocs, Vinicius, Bob, David with whom I had great discussions and especially Vincent who helped me with the ray-tracing project. I would like to thank Obinna for helping me with so many things like technical stuff about perturbation theory and teaching me about xPand package. I owe a big thanks to Bishop who helped me with things related to coding.
I am grateful to Andreas Faltenbacher who provided me strong background on coding with Fortran and inspired me the beauty of coding. He has been very helpful about coding related issues.

Chris Clarkson, my great supervisor ... hmm where do I start? Wait ... right, with Prina, sometimes Julien and other postdocs, we hang out, discuss, joke and laugh about things around some pints that he most of the time if not everytime, offers me. This, I believe, contributes a lot to my productivity, not the pints of course but the relaxed and enjoyable moments that I had with those great people. Chris has always been very supportive in

various aspects of my life as a PhD student and in general, calms me down and encourages me when I am really worried about stuffs. At the early stage of my PhD, he really spent lots of time to take me through things, from which I learnt a lot, not to mention the numerous times I popped into his office to ask him some questions (sometimes even stupid ones) or to just bug him. He tolerates my being clumsy regarding other stuffs. For all that and his help and guidance through all the stages of this work, I am very grateful to him.
I would like to thank Prina who was also one of our collaborators and a very good friend. She was always there to help me and answer my questions.

I would like to thank my aunt, sister and my mom who has always advised me ever since I was a kid that knowledge is the key to everything in life.

Last but not least, my wife, Valérie, who throughout this work always tries hard to know, understand about every single thing I am dealing with. She has always offered me her unconditional support. Her caring and encouraging words really pushed me to carry on through those moments of struggle. I am forever thankful to her. Our baby girl, Acacia, whose smile and laughter are just priceless, is the most beautiful thing that has ever happened to us.

To my loving wife Valérie and our daughter Acacia

Declaration

The results presented in this work are achieved by the author under the supervision of Chris Clarkson (University of Cape Town) and in collaboration with David Bacon (University of Portsmouth), Roy Maartens (University of Western Cape), Camille Bonvin (European Organization For Nuclear Research (CERN)), Krzysztof Bolejko (University of Sydney), Obinna Umeh (University of Western Cape), Prina Patel (University of Western Cape), Jean-Philippe Uzan (Institut d'Astrophysique de Paris, Université Pierre et Marie Curie, Sorbonne Universités, Institut Lagrange de Paris), Philip Bull (University of Oslo) and Teboho Moloi (University of Cape Town). The following peer-reviewed papers resulted from my collaboration with these people

- **S. Andrianomena**, C. Clarkson, P. Patel, O. Umeh and J. P. Uzan, "Non-linear relativistic contributions to the cosmological weak-lensing convergence." *JCAP* **06** 023, 2014
- David Bacon, **S. Andrianomena**, C. Clarkson, K. Bolejko and R. Maartens, "Cosmology with Doppler Lensing." *Mon. Not. Roy. Astron. Soc.* **443**, 1900-1915, 2014.

Chapter 3 is entirely based on the first paper above, with more detailed derivations. Chapter 4 is a re-formatted reprints of the second paper above with much more focus on the section I contributed the most. Chapter 5, Section 5.1 is based on "Dipolar modulation in the size of galaxies: the effect of Doppler magnification" C. Bonvin, **S. Andrianomena**, D. Bacon, C. Clarkson, P. Bull, R. Maartens and T. Moloi, in preparation. Section 5.2 in Chapter 5 are also entirely new results based on "Constraints on modified gravity using Doppler magnification" **S. Andrianomena**, C. Clarkson, C. Bonvin, D. Bacon, P. Bull, R. Maartens and T. Moloi, in preparation.

I hereby declare that this thesis has not been submitted, either in the same or different form, to this or any other university for a degree and it represents my own work.

Abstract

A fundamental issue in modern science is the dark energy problem - the apparent accelerating expansion of the universe. Many cosmological observations of the Cosmic Microwave Background (CMB), Baryon Acoustic Oscillation (BAO) and weak lensing have been carried out to try to understand the nature of this repulsive dark force. With the advent of advanced experiments like the Square Kilometer Array we enter the era of precision cosmology where measurements of effects such as weak lensing will be achieved at a sub-percent level, implying strong constraints on dark energy. The full picture of weak lensing includes linear and non-linear correction terms to its standard formula. In this thesis we address the questions: Are some of these effects detectable? Under which conditions can we safely neglect them such that the analysis of future weak lensing observations is not biased? Induced by gravity, peculiar velocity of galaxies can potentially be used to probe the growth of structure in our universe. Peculiar velocities induce a lensing-like effect, which we consider as Doppler magnification. By developing new statistical tools which are based on Doppler magnification, we investigate the dark energy problem. These new statistical probes also enable us to explore the viability of other theories that attempt to account for the apparent acceleration of the cosmic expansion by modifying Einstein's General Relativity.

Table of Contents

List of Figures

List of Tables

Chapter 1
Introduction

Over the last few decades, many experiments have been conducted with the aim of testing different proposed models that could best describe the universe. Each model has its own caveats but so far, the concordance model, also known as *Lamba Cold Dark Matter* (ΛCDM) is the most preferred by observations. The ΛCDM paradigm consists of Einstein's General relativity plus Λ which is known as dark energy – a yet unknown form of energy with negative pressure – to account for the recent apparent acceleration of the cosmic expansion. Cold dark matter, which is a non-baryonic matter, hasn't been detected yet but its existence is supported by various astrophysical observations like the bullet cluster [4] and the flat rotation curve of spiral galaxies [5, 6]. It also plays an important role in the hierarchical clustering of matter in which structure is thought to start small but grows by attracting more matter via gravity - the bottom-up picture. In ΛCDM model, dark energy ($\sim 74\%$) and cold dark matter ($\sim 22\%$) make up the dominant part of the cosmic budget of the universe whereas the visible matter (stars and galaxies etc ...) constitutes only a few percents ($\sim 4\%$). Different experiments have been conducted in order to constrain this most favored model of the universe.

Cosmic Microwave Background experiments

Well after the end of inflation, as the universe was expanding, the rate of scattering of the baryonic contents by photons was roughly equal to the cosmic expansion rate, such that the primordial plasma was no longer in thermodynamic equilibrium. At $T_{\rm dec} \sim 3000\,\mathrm{K}$ [8], the photons decoupled from matter and were able to free stream so the universe became transparent. A Cosmic Microwave Background (CMB) experiment is designed to observe this relic radiation from the epoch of recombination that occurred at $z \sim 1100$. The CMB is full of information and can give many insights into the geometry of the universe, the matter content of the universe and the physics that took place during inflation. The latest results from *Planck* [9] showed that the universe is flat with a spatial curvature very close to zero $|\Omega_K| < 0.005$, favored the existence of Dark energy with equation of state parameter

$w = -1.006 \pm 0.045$ and are consistent with a simplest model of inflation. It is worth noting that this constraint on the equation of state parameter w was obtained from combining *Planck* lensing, Baryon Acoustic Oscillations (BAO), Joint Light-curve Analysis (supernovae data) and H_0 data.

Type IA supernovae

Supernovae type Ia also constitute powerful probes in modern cosmology. Due to the fact that their physics is thought to be well studied and they roughly have the same absolute magnitude make them good candidate for standard candles, objects known to have the same intrinsic brigthness [10]. Once the apparent magnitude is obtained through observations, its luminosity distance can be inferred through the distance-modulus relation [11]

$$m - M = 5\log\left(\frac{d_L}{10\text{pc}}\right) + K, \tag{1.1}$$

where m and M are the apparent magnitude and absolute magnitude respectively, d_L is the luminosity distance and K is a correction term. Its redshift can be measured using spectroscopy. On the background, the distance-redshift relation depends on the geometry and the matter content of the universe such that for a cosmological model, one can infer the cosmological parameters from measuring the distance. Supernova type Ia was indeed used to show that expansion of our universe is accelerating due to a vacuum energy with negative pressure (Λ) [12–14].

Baryon Acoustic Oscillation (BAO)

During the radiation era, perturbations in the primordial plasma generated sound waves leading to acoustic oscillations which are imprinted in the cosmic microwave background anisotropy and matter power spectrum. At decoupling, when the photons free-streamed, the sound wave no longer propagated, leaving the baryons within a spherical shell around the initial overdensity from which the sound wave originated. This is imprinted in the clustering of galaxies at typical scale, known as sound horizon scale. In [15], the acoustic peak was first detected in the galaxy correlation function using catalogue of luminous red galaxies in the Sloan Digital Sky Survey (SDSS) at a scale of 150 Mpc. The feature is characterized by a little bump at that scale in the real space correlation function. The BAO experiment consists of measuring the location of the bump from which the ratio between the effective distance D_V, combination of the comoving angular diameter distance and the Hubble rate, and the

comoving sound horizon scale r_s are derived. This can be used to probe the acceleration of the cosmic expansion and the structure growth [16, 17].

Alcock-Paczynski test (AP)

One of the cosmological tests that is known to be assumption-free is the Alcock-Paczynski test. The key idea is to measure how the ratio between the angular size and the radial size of a spherically symmetric distribution of objects varies as a function of redshift. In [18], by using AP test, it was concluded that the standard concordance model (ΛCDM) is the model which is favored.

Weak lensing

Light emitted by a distant source gets deflected by the intervening matter along its way to the observer. This deflection induces some distortion in the observed image of the object, characterised by an elongation in one direction (shear) and magnification/demagnification of the image of the object (convergence). The shear and convergence are now observables [19, 20]. Weak lensing turns out to be a very powerful probe in modern cosmology as outlined in [21] where it was used to constrain cosmological models [22–24]. In chapter II, weak lensing will be discussed more in detail.

In an era of precision cosmology, different independent experiments can be combined to get more accurate constraints. Most of the methods listed above have also been used to probe different alternative theory to General Relativity (GR) with a vacuum energy. In the next section we will look at how peculiar velocities of objects can be used as a cosmological probe.

1.1 Why peculiar velocities?

1.1.1 Introduction

In linear theory, overdense regions grow denser by gravitational collapse – more matter falls onto it due to gravity. The infall of objects gives rise to what is known as peculiar motion, a small deviation relative to the Hubble flow. As will be discussed, peculiar velocity is a very

good cosmological probe to study the structure growth.
Over-densities induce peculiar velocity as described by the continuity equation on sub-horizon scales [11]

$$\delta' + ikv = 0, \tag{1.2}$$

where δ is the matter density perturbation, v the velocity, k the wavenumber and prime is the derivative with respect to conformal time. Using the fact that the time dependence of the density fluctuations of matter is encoded in the growth factor D, solution to the evolution equation of density perturbations describing how matter grows at late time, in linear perturbation theory, we thus have [11]

$$v(k,a) = \frac{i\delta(k,a)}{k}\frac{D'(a)}{D(a)}. \tag{1.3}$$

We can now introduce the dimensionless growth rate f defined as the logarithmic derivative of the growth factor with respect to the scale factor a

$$f = \frac{d\ln D}{d\ln a}. \tag{1.4}$$

A very good appromixation of the growth rate which is often used is a power law of the form [25]

$$f \equiv \Omega_m^{\gamma} \tag{1.5}$$

where Ω_m is the matter density parameter and γ the growth index whose best fit in ΛCDM is $\gamma \approx 0.55$ but takes different values in different theories of gravity. Changing the time derivative to a derivative with respect to the scale factor in Eq. (1.3) while exploiting Eq. (1.4) amounts to

$$v(k,a) = if(a)H(a)a\frac{\delta(k,a)}{k}, \tag{1.6}$$

where $H(a)$ is the Hubble rate. In real observations, what is measured is the real space counterpart of the peculiar velocity [26]

$$\boldsymbol{v}(\boldsymbol{r}) = \frac{H_0}{4\pi}\frac{f}{b}\int d^3\boldsymbol{r'}\delta_g(\boldsymbol{r'})\frac{\boldsymbol{r'}-\boldsymbol{r}}{|\boldsymbol{r'}-\boldsymbol{r}|^3}, \tag{1.7}$$

where $\delta_g(\boldsymbol{r})$ denotes galaxy overdensity which is related to the matter fluctuations via a linear bias factor b

$$\delta_g \equiv b\delta. \tag{1.8}$$

In reality this expression contains more relativistic correction terms like redshift space distortions, lensing etc ... but to a leading order we can adopt this linear relationship [27, 28]. The galaxy overdensity is an observable and can be used as a biased tracer of the underlying matter distribution (Eq. (1.8)).

Peculiar motions induce some distortions in the apparent clustering of matter in redshift space. A circular overdense region in real space would appear smeared along the line of sight on non-linear scales, whereas on linear scales it would appear flattened. It would look like an ellipse whose major axis is perpendicular to the line of sight as shown in Fig. 1.1 (from [11]). This would then distort the measured power spectrum P_s in redshift space according to [29]

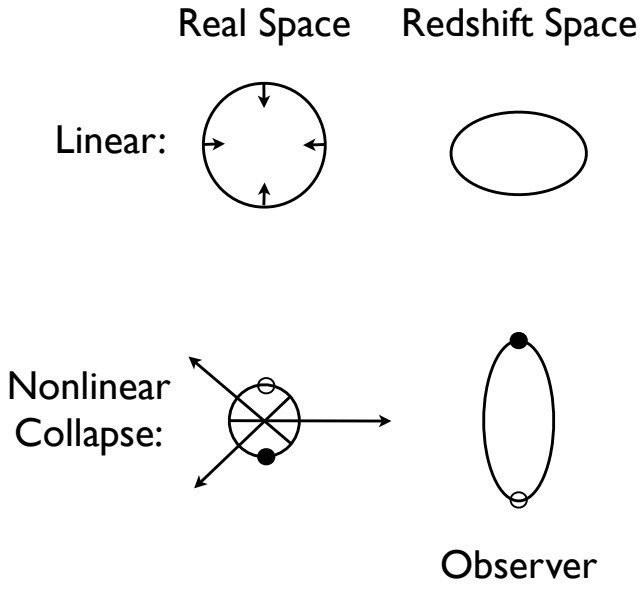

Figure 1.1: Shows how a circular contour in real space is distorted in redshift space for both linear and nonlinear cases.

$$P_s(k) = [1 + \beta\mu_{\boldsymbol{k}}^2]^2 P(k), \tag{1.9}$$

with $\mu_{\boldsymbol{k}}$ being the cosine between the wavevector $\hat{\boldsymbol{k}}$ and the direction of observation. β, known as redshift space distortion parameter, is the ratio between the growth rate and the linear bias $\beta = f/b$ and quantifies the deviation of P_s with respect to the true power spectrum. A positive value of the second term within the square brackets will enhance the

correlation function in redshift space. There exists a variety of techniques to measure the distortion parameter but as can be seen from Eq. (1.7), one way could be the use of peculiar velocity surveys or taking the ratio between the monopole and quadrupole of Eq. (1.9) as in redshift space distortion analysis

1.1.2 Peculiar velocity measurements

Assuming a model of the universe, redshift can be used to estimate distance of galaxies. However, the potential of a redshift survey is limited by the fact it can not disentangle the peculiar component from the galaxy's measured redshift. The total velocity of a galaxy is composed of the Hubble velocity due to cosmic expansion and the peculiar velocity which is induced by gravity due to inhomogeneities

$$v = cz - H_0 r, \tag{1.10}$$

where r is the galaxy comoving distance and z the redshift. Therefore measuring peculiar velocities requires the estimation of redshift together with redshift independent distance measurements.

Distance indicator

There are many redshift independent techniques to estimate distances but we only look at some of the widely used methods. The Tully-Fisher (TF) relation [30] makes use of the correlation between the rotational velocity of a late type galaxy (spirals) and its luminosity

$$L(v_{\rm rot}) \propto v_{\rm rot}^{\alpha}, \tag{1.11}$$

which can be also written as[1] [31, 32]

$$M(\varsigma) = A - B\varsigma, \tag{1.12}$$

where A and B, which are empirically determined, are the zeropoint and slope of the relation

[1] by convention this relation is written as

$$M(\eta) = A - b\eta,$$

but to avoid confusion in terms of notation we will adopt the one in the text.

respectively. The absolute magnitude M can also be expressed as [31, 32]

$$M = \text{const} - 2.5 \log(L). \tag{1.13}$$

The quantity ς is related to the rotational velocity according to

$$\varsigma = \log(2v_{\text{rot}}) - 2.5. \tag{1.14}$$

The observables are the rotational velocity and the apparent magnitude of the galaxy, then one can use the distance modulus formula to estimate its distance. In the seminal work [30], the TF relation was calibrated using the Local group, namely the M81 and M101, in which the galaxies are all with well known properties (distance, global hydrogen profile width etc ...). The TF relation is extensively used in today's largest peculiar velocity survey SFI++ [33].

Originally, for early type galaxies (elliptical), the Faber-Jackson relation which expresses the luminosity as a function L of velocity dispersion σ_e according to [34–36]

$$L \propto \sigma_e^{\alpha}, \tag{1.15}$$

was used to estimate distances. However, the large uncertainty in the estimation arises from the scatter of the relation which is worse than that of the TF relation. In [37], they found that introducing another parameter, the mean surface brigthness $\langle \mu_e \rangle$ (or $\langle I_e \rangle$ in linear flux units), greatly improves the accuracy. They then deduced the relation between the effective radius R_e of an early type galaxy (ellipticals) with its central velocity dispersion and its effective surface brightness

$$R_e \propto \sigma_e^{1.39} \langle I_e \rangle^{-0.90}, \tag{1.16}$$

known as the Fundamental Plane (FP) [37, 38]. Further, the effective radius and the surface brightness can be combined into one parameter D_n, a photometric diameter enclosing I_e, to yield [39]

$$D_n \propto \sigma_e^{1.20 \pm 0.1}, \tag{1.17}$$

also known as the $D_n - \sigma$ relation. The FP relation (or $D_n - \sigma$ relation) is then used as distance indicator for elliptical galaxies.

Due to small variations in their absolute magnitudes, corrections are required such that type Ia supernova can be used as standard candles. The idea of standardising the absolute magnitudes of type IA supernovae was pioneered in [40] where they found correlations between the light curve and absolute magnitude and between color curve and absolute magnitude.

Different techniques of standardisation which are methods for light curve fitting have then emerged. Among them are the multicolor light curve shape (MLCS) [41] and the second Spectrally Adaptive Lightcurve Template (SALT-II) [42]. As concluded in [41], after applying the MLCS method, type Ia supernova turns out to be a distance indicator with high precision. In [43] for example, they built a peculiar velocity catalogue with much better precision in estimate of distances of objects using type Ia supernovae.

It was shown that the magnitude in the I-band of the tip of the first-ascent red giant branch (TRGB) can be used to derive the distance modulus of the host galaxy whose resolution is required to be good enough [44]. The distance precision derived from this technique is comparable to those obtained from variable star based method such as Cepheid and RR Lyraes.

It is worth mentioning that variable stars, such as Cepheids [45–48] and RR Lyraes [49, 50] among others, are also used as distance indicators. The technique uses the correlation between the period in their light curves and their luminosity, known as PL relation. Unlike, other distance indicators, variable stars can only be used to estimate distances to globular cluster or nearby galaxies. However, Cepheids for example were used to calibrate other distance indicators like type Ia supernova or TF relation [51].

Biases

What most of all those techniques have in common is that they suffer from systematics which can severely bias the derived quatities, such as the radial peculiar velocity. In a magnitude limited sample, brighter objects are more favored than dimmer ones and as a result, the mean magnitude of the sample is less than it should be – whereas if there was no selection effect where all objects were equally selected, the mean magnitude would be larger – this is known as Malmquist bias (see [38] and reference therein). For example, in [52], a fitting method, based on a combination of linear inverse TF and the distance modulus expression, was proposed to deal with the Malmquist bias. The technique was tested on a mock galaxy catalog from N-body simulation and was able to provide a very good estimate of peculiar velocities. Another issue when estimating peculiar velocity from distance modulus measurements is the assumption that the derived peculiar velocity error distribution is Gaussian. The problem arises from the fact that the exponentiation of the Gaussian errors of the distance modulus skews the corresponding error distribution of the peculiar velocity [53], leading to misinterpretation of the results in the worst case. In [38] for example, they dealt with this non-Gaussianity of the peculiar velocity error distribution by

using a Bayesian technique when they derived peculiar velocities from 6dFGS catalog [54]. Around the same time [55] also prescribed an unbiased estimator of peculiar velocity, for low and high redshift. Applied to *Cosmicflows-2* [56], they effectively obtained a Gaussian distribution of peculiar velocities, therefore no further corrections were needed. Instead of devising new estimator of v, in [55], they rather built a technique that minimizes the biases in peculiar velocity measurements. The approach is to iteratively loop through all the peculiar velocities in a catalog, *Cosmicflows-2* in their case, and correct for them if necessary, such that the resulting distribution is a Gaussian. Then for consistency, once corrected, the velocities were, in turn, used to rederive distances - free of Malmquist biases.

The different techniques that have been developed to get a better estimate of peculiar velocity are all motivated by the fact that the biases inherent to the derived quantity, if severe, might lead us to misinterpret the results or simply prevent us from better understanding the bigger picture.

1.1.3 Peculiar velocity as a cosmological probe

Redshift space distortion and Growth rate

In observations, redshift space distortion measurements allow the estimation of the growth rate by deriving $\beta\sigma_{8,g}$, the combination of the distortion parameter with *rms* of galaxy density fluctuations within a sphere of $8h^{-1}$Mpc in radius. By assuming a linear bias $\sigma_{8,g} = b\sigma_8$, the measured quantity $\beta\sigma_{8,g}$ which is independent of bias is thus the normalized growth rate $f\sigma_8$.

Several attempts to measure the Kaiser effect – encoded in the β parameter – have been made using redshift surveys. It was shown that β can be estimated from measuring ratio of angular moments of correlation function then applied his estimator to IRAS 1.936 Jy sample to get $\beta = 0.69^{+0.28}_{-0.24}$ [57]. The following year, in [58], they were able to provide a constraint on β. Following [59], in [60], they used the measurement of the mean pairwise streaming of galaxies v_{12} to obtain $\beta = 0.45^{+0.27}_{-0.18}$. Other independent measurements of β – somewhat more accurate as shown in [61] – come from peculiar velocity surveys.

In [62], like others [63–65], they adopted the "*method of velocity-velocity comparison*" to constrain redshift distortion. They modeled the peculiar velocities from 2M++ [66], a redshift survey, then compared them with measured peculiar velocities from SFI++ [33] and The First Amendment Supernovae [43]. They obtained $\beta = 0.431 \pm 0.021$ implying $f\sigma_8 = 0.401 \pm 0.024$,

consistent with other probes. A new approach to estimate the growth rate without resorting to distance measurement like TF was developed by [67]. They made use of the fact that through the expression of the distance modulus, the predicted peculiar velocity field from galaxy survey allows one to infer the absolute magnitude which in turn affects galaxy luminosity via the Luminosity Function (LF) $\Phi(M)$ [1, 67]. Applying this technique to Sloan Digital Sky Survey Data Release 7 (SDSS DR7) [68], they found $f\sigma_8 = 0.37 \pm 0.13$ at $z \sim 0.1$ [1]. In [61], they also showed how well peculiar velocities can improve constraints on growth rate ($f\sigma_8$) and redshift-space distortion (β). Fig. 1.2 (from [1]) shows recent measurements of the growth rate as a function of redshift from different surveys. In [69], they derived the quantity v_{12} from a peculiar velocity survey using the estimator

$$\tilde{v}_{12} = \frac{2\sum(s_A - s_B)p_{AB}}{\sum p_{AB}^2}, \tag{1.18}$$

where $s_A = \boldsymbol{r}_A \cdot \boldsymbol{v}_A/r$ is the radial component of the peculiar velocity, an observable, and $p_{AB} = \hat{\boldsymbol{r}} \cdot (\hat{\boldsymbol{r}}_A + \hat{\boldsymbol{r}}_B)$. When applied to mock data, they concluded that the method was quite robust and gave a powerful measure of $f\sigma_8^2$.

Dark energy

In their approach which also exploits the mean pairwise peculiar velocities, [70] introduced a projected version of the estimator in [69]. They further improved their statistic by taking into account the uncertainty in photometric redshift. Via a Fisher forecast analysis, they assessed the constraining power of the projected mean pairwise peculiar velocity by considering Large-Scale Supernova Surveys and obtained very good constraints on the dark energy parameters comparable to those of *Planck* - improving the Dark Energy Task Force figure of merit (FoM) by factor of 1.8 when combined with *Planck* prior. Nevertheless their results are still dependent on how well we understand supernovae in order to reduce its intrinsic absolute magnitude dispersion and also on the redshift information.

As highlighted by [71] (and references therein), the impact of not taking into account local Supernovae type Ia peculiar velocities on the derived cosmological parameters is not negligible. Using data from IRAS PSCz galaxies they showed that if ignored, the peculiar motions can induce a systematic error of $\Delta w = +0.04$ on the estimation of dark energy equation of state parameter w.

Alternative theories of gravity

It is argued that the mean pairwise streaming velocity could also provide a better understanding of the nature of gravity [72–74]. In [72] (and reference therein), they claimed to have detected a strong departure from General Relativity in the line of sight projected pairwise velocity dispersion estimated from high-resolution N-body simulations. Interestingly in [73], they were investigating departure from GR by introducing one modification that accounts for the light propagation $G_{\rm light}(k,a)$ via the lensing potential and another for non-relativistic matter $G_{\rm matter}(k,a)$ via Poisson's equation

$$\nabla^2\psi = 4\pi G_N a^2 \bar{\rho}_m \Delta_m \times G_{\rm matter}(k,a), \tag{1.19}$$

$$\nabla^2(\psi+\phi) = 8\pi G_N a^2 \bar{\rho}_m \Delta_m \times G_{\rm light}(k,a), \tag{1.20}$$

with G_N being Newton's gravitational constant, $\bar{\rho}_m$ the background matter density and Δ_m the comoving density perturbation. To constrain those parameters, they used galaxy power spectrum multipoles measured from WiggleZ and BOSS Data Release 11 CMASS galaxy redshift surveys and velocity power spectrum measured from 6dFGS [54] (and references therein). They derived the best-fit values of $G_{\rm light}(k,a)$ and $G_{\rm matter}(k,a)$ by adopting a MCMC likelihood analysis and found no departure from GR at 2σ confidence level.
In a different approach which attempts to constrain a scale dependent normalized growth rate $f\sigma_8(k,a=1)$ [75] found no evidence of scale dependence of the parameter $f\sigma_8$ using 6dFGSv catalog.

To date, the variety of techniques that use peculiar motion of galaxies as a cosmological probe have been developed to shed new light on the nature of dark energy and how gravity behaves on cosmological scales. As outlined throughout this subsection, the constraining power of peculiar velocity can help us drastically improve constraints on cosmological parameters.

1.2 Aims of this project

Weak lensing convergence comes as correction term to the angular diameter distance

$$D_A = \overline{D}_A(1-\kappa), \tag{1.21}$$

where $\overline{D}_A$ is the background quantity and κ the convergence. For many years, when doing predictions using weak lensing convergence, a good approximation which is to only consider

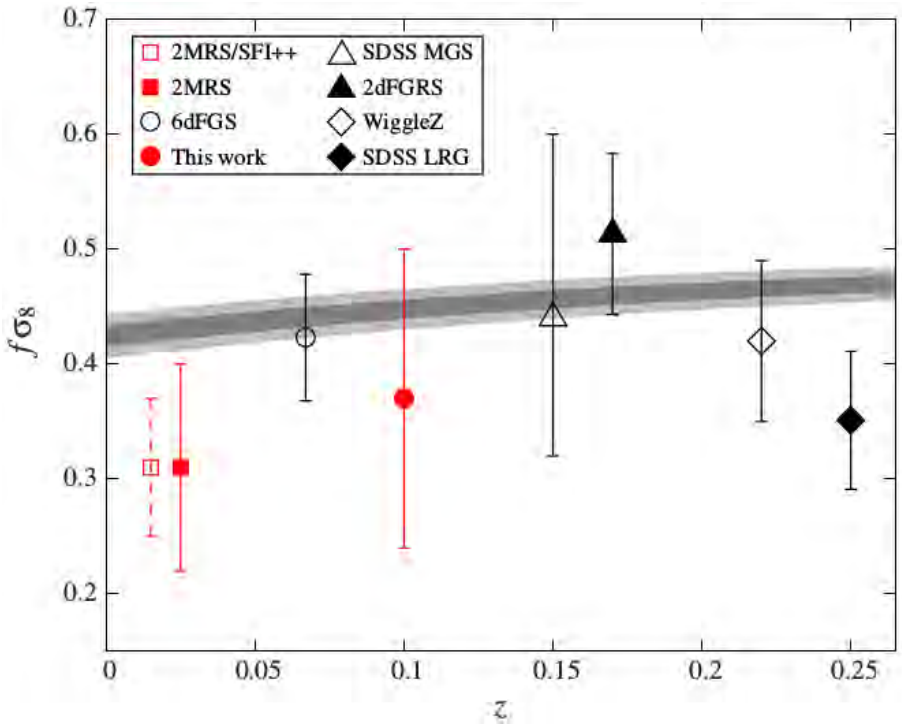

Figure 1.2: Recent $f\sigma_8$ measurements from differents surveys as a function of redshift z. Shaded grey and light grey areas show the constraints, 1σ and 2σ respectively, from *Planck* [1].

the line of sight (L.O.S) integration of the density fluctuations has been used

$$\kappa = \frac{3}{2}\frac{H_0^2\Omega_{m0}}{c^2}\int dr \frac{r'(r-r')}{r}\frac{\delta}{a}, \tag{1.22}$$

where c is the speed of light and Ω_{m0} today's matter density parameter. However, full relativistic treatment shows that cosmic convergence contains many terms at first and second order in perturbation theory [76–78]. The advent of future experiments like SKA with a larger survey volume and great resolution will enable us to measure the relativistic effects with an unprecedented precision, therefore analysing data in that era requires a special care. What we propose to investigate here is a step towards this era of precision cosmology.

1.2.1 Second order effects

At first order in perturbation theory, scalar, vector and tensor modes evolve independently, therefore can be studied separately. Large Scale Structure that we see today is attributed to scalar modes which are well understood. Gravitational waves which are related to tensor

perturbations and whose detections will support the theory of the inflationary phase of the universe are still being hunted using experiments like BBO [79,80]. The effect of gravitational waves on the B-modes of the CMB polarization offers the main possibility for their detections. The secondary contribution of both vector and tensor modes to the B-mode polarization of the CMB was investigated [81, 82]. It was found that their effect is dominated by that of lensing by Large Scale Structure which transforms E-mode into B-mode polarization of the CMB [81]. Second order contributions of vector and tensor modes to the CMB temperature anisotropies were discussed [83, 84]. Vector perturbations were also proven to give rise to a deflection angle, therefore contribute to weak lensing [85]. As discussed in [86], vector modes are generated by the interaction of first order scalar modes of different wavelengths. Secondary tensor modes are produced at second order by mode mixing of primordial density fluctuations but unlike the vector modes, they can be sourced by scalar modes at a single wavelength [87]. We propose to quantify the effects of these vector and tensor modes in weak lensing and investigate whether they need to be taken into account in future weak lensing measurements.

1.2.2 Doppler magnification

At low and intermediate redshift ($z \lesssim 1.7$), a galaxy with a peculiar velocity pointing away from an observer is observed at redshift z_s and looks brighter than a typical galaxy with null peculiar velocity at the same redshift z_s. Whereas a galaxy with a peculiar velocity pointing towards us, observed at a redshift z_s' looks dimmer than a typical galaxy with null peculiar velocity at that redshift z_s'. This lensing like effect is what we call *Doppler lensing* or *Doppler magnification* interchangeably, since it precisely affects the cosmic convergence κ and therefore the magnification. The contribution of the Doppler term at first order and up to second order to the area distance was derived in [76–78]. In [88], they showed that this local term only affects the cosmic convergence κ at first order but can contribute to the shear at second order. Since this velocity term peaks on large scales $\ell \sim 10$, future surveys will be required to probe large volume of the sky in order to detect its effect.

By considering an observer looking through a void along the line of sight at low redshift, the standard cosmic convergence fails to account for the change in magnitude of local objects in and near the void [89](see Fig. 1.3 from [89]). It was shown that the Doppler effect completely prevails over the usual cosmic convergence. This suggests that depending on the scales of interest, one needs to be careful as to which term(s) dominate when interpreting data from observations.

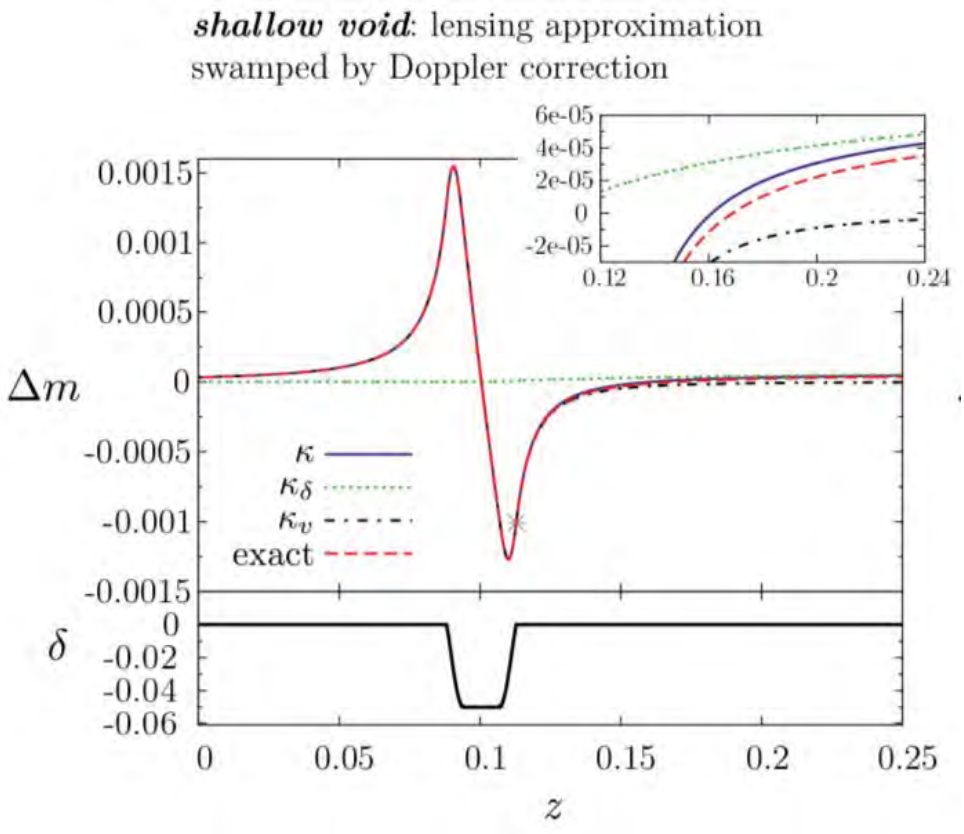

Figure 1.3: Change in magnitude Δm, which is due to different contributions to the cosmic convergence, as a function of z. The observer at $z = 0$ is looking through the void along the line of sight.

In an early work [90], they computed the anisotropies in luminosity distance and already showed that at low redshifts the contribution of the peculiar motion to the fluctuations $\delta D_L/\bar{D}_L$ prevails over other contributions like those of gravitational lensing and Sachs-Wolfe effect. The impacts of those anisotropies, more precisely the peculiar velocity, on cosmological parameter inference have been analysed [91–93]. In [92] for example, they examined the uncertainties induced by peculiar velocities of type Ia supernovae on estimating dark energy equation of state parameter. In [93], treating peculiar velocities as systematics in supernova surveys, they devised an approach to account for peculiar motions rather than adopting a cut for supernovae at low redshifts. In [91], they presented a more rigorous treatment of the covariance matrix which is composed of a Poisson noise and the cosmic variance – or coherent/correlated component as they call it. They showed that peculiar velocity contributes to the Poisson noise but in general this contribution is small. However, the peculiar motion induced cosmic variance C_ℓ^{vel} can be significant, dominating its lensing counterpart, especially at low redshifts (see also [88]). They then addressed the question of whether the peculiar

velocity can be treated as the signal rather than systematics (also pointed out in [93]). Precisely, the originality in this work lies in treating the peculiar motion of objects as a signal that allows us to constrain cosmological parameters.

As discussed earlier, peculiar motion of object can be used as a cosmological probe to study growth of structure and address the issue about the apparent acceleration of the expansion of the universe - shedding new light on the dark energy problem. In this thesis, we want to probe growth of structure and dark energy using Doppler magnification. By building a new statistical tool, we aim at putting new constraints on dark energy and other cosmological parameters. Alternative theories of gravity seek to explain the recent acceleration of the cosmic expansion by modifying Einstein's General Relativity, avoiding the need of a vacuum energy with repulsive force. We then address the question : Can we gain more insights into modified gravity theories by using our new statistics?

The plan of the thesis is as follows. Chapter 2 deals with cosmological perturbation theory and its application where we look at the basic tools that will be used throughout this thesis and give a quick review on weak gravitational lensing which is relevant for later chapters. We present our results on the contribution of non-linear vector modes to the cosmic convergence in Chapter 3. The results on the cosmological parameters constraints obtained from using our new statistical tool are presented in Chapter 4. Another statistical tool, still based on the Doppler magnification, which exploits the dipole arising from peculiar motion of objects falling onto an overdensity is presented in Chapter 5. There, we also show our forecasts for cosmological parameters in the concordance model and investigate the possible constraints we can put on some parametrised models of modified gravity. Finally we give our general conclusion.

Chapter 2
Cosmological perturbation theory and weak lensing

In this chapter we review the basics of perturbation theory. It is not meant to be exhaustive but provide useful tools and results for later chapters. We first look at the background universe then review the concept of perturbing space-time and show its perturbed metric. The approach of perturbing a quantity, be it scalar, vector or tensor is presented. At first order, scalar, vector and tensor perturbations can be dealt with separately by using Scalar Vector Tensor decomposition (SVT). After addressing the gauge problem in perturbation theory, we show how to construct gauge invariant quantities that are the observables. We present the Einstein Field Equations (EFEs) in a perturbed universe in a Newtonian gauge which is the gauge we mainly use throughout this work. As part of this work addresses the non-linear contribution of the vector and tensor modes to weak lensing convergence, we thus give a small overview on how those secondary modes arise and highlight the relevant equations which are used in Chapter 3. There are many applications of cosmological perturbation theory but what interests us in this thesis is specifically weak gravitational lensing. Therefore, in the last section, we give some basics on gravitational lensing then conclude this chapter by deriving the standard expression of weak lensing convergence.

2.1 Homogeneous Universe

The notion of spatially homogeneous and isotropic universe constitutes the foundation of modern cosmology. The Copernican Principle states that we do not live in a special place in the universe [94]. This homogeneity only holds on scales larger than 100 Mpc but as we go below, on scales of clusters of galaxies, it is highly inhomogeneous. This spatial homogeneity of the universe has been subject to several tests using different methods [95–97]. According to observations, the background universe is described by a flat Friedmann-Lemaitre-Robertson-Walker (FLRW) model with the line element

$$ds^2 = -dt^2 + a(t)^2 \delta_{ij} dx^i dx^j, \tag{2.1}$$

with $a(t)$ the scale factor and δ_{ij} Kronecker delta symbol. In perturbation theory, it is more preferable to work with conformal time η rather than cosmic time. They are related by

$$d\eta = dt/a, \tag{2.2}$$

so that

$$ds^2 = a(\eta)^2(-d\eta^2 + \delta_{ij} dx^i dx^j). \tag{2.3}$$

We can introduce the background metric $\bar{g}_{\mu\nu}$ as

$$ds^2 = \bar{g}_{\mu\nu} dx^\mu dx^\nu. \tag{2.4}$$

It is noted that the greek letters μ, ν = 0,1,2,3 whereas i = 1,2,3. On the background, the metric is related to the Minkowski metric $\eta_{\mu\nu}$ by

$$\bar{g}_{\mu\nu} = a(\eta)^2 \eta_{\mu\nu}. \tag{2.5}$$

We will now look at the EFEs in a smooth universe.

2.1.1 Equation of motion

Like in classical mechanics, to work out the equation of motion of a particle one can apply the Hamilton's principle by maximising the action which is an integral of the Lagragian. In the case of General Relativity we consider the Einstein-Hilbert action [98]

$$\begin{aligned} S &= S_R + S_\Lambda + S_\mathcal{L}, & (2.6)\\ &= \frac{1}{2\kappa}\int_\mathcal{V} d^4x\sqrt{-g}R - \frac{1}{\kappa}\int_\mathcal{V} d^4x\sqrt{-g}\Lambda + \int_\mathcal{V} d^4x\sqrt{-g}\mathcal{L}, & (2.7) \end{aligned}$$

where $\kappa = 8\pi G$, g the determinant of the metric $g_{\mu\nu}$, R the Ricci scalar, $\mathcal{L}$ the lagrangian of matter and finally Λ the cosmological constant. To get the equation of motion, one needs to extremize Eq. (2.6) by varying it with respect to the metric. Varying the first term in

Eq. (2.6)

$$\delta S_R = \int_{\mathcal{V}} d^4x \delta(\sqrt{-g} R_{\mu\nu} g^{\mu\nu}), \tag{2.8}$$

$$= \int_{\mathcal{V}} d^4x \left[\delta\sqrt{-g} R + \sqrt{-g}\delta R_{\mu\nu} g^{\mu\nu} + \sqrt{-g} R_{\mu\nu}\delta g^{\mu\nu}\right] \tag{2.9}$$

To treat the first term of Eq. (2.9), we resort to the expression of the determinant of the metric [99]

$$\delta \ln |g| = -g_{\mu\nu}\delta g^{\mu\nu}. \tag{2.10}$$

Thus

$$\delta\sqrt{-g} = -\frac{1}{2}\sqrt{-g} g_{\mu\nu}\delta g^{\mu\nu} \tag{2.11}$$

As for the second term of Eq. (2.9), the variation of the Ricci tensor can be computed on a Lorentz local frame such that the first derivatives of $g_{\mu\nu}$ vanishes but not its second derivative, leading to

$$\delta R_{\mu\nu} = \partial_\lambda(\delta\Gamma^\lambda_{\mu\nu}) - \partial_\mu(\delta\Gamma^\lambda_{\lambda\nu}). \tag{2.12}$$

Since Eq. (2.12) is a tensor equation, it is valid in all frames such that the partial derivatives can be turned into covariant derivatives. The second term of Eq. (2.9) can be now cast into a form of an integral of divergence of a quantity over a volume $\mathcal{V}$ which, by Stokes Theorem, is equivalent to an integral of the quantity over the boundary surface enclosing $\mathcal{V}$. Therefore, it vanishes. Since varying S_Λ is rather straightforward, let us turn to the variation of $S_\mathcal{L}$

$$\delta S_\mathcal{L} = \int_{\mathcal{V}} d^4x \left(\frac{\partial\mathcal{L}}{\partial g_{\mu\nu}}\delta g^{\mu\nu}\sqrt{-g} + \mathcal{L}\delta\sqrt{-g}\right). \tag{2.13}$$

Using Eq. (2.11) yields

$$\delta S_\mathcal{L} = \int_{\mathcal{V}} \mathrm{dx}^4 \left(\frac{\partial\mathcal{L}}{\partial g_{\mu\nu}} - \frac{1}{2}\mathcal{L} g_{\mu\nu}\right)\delta g^{\mu\nu}\sqrt{-g}. \tag{2.14}$$

The term in brackets is defined to be the stress-energy tensor

$$T_{\mu\nu} = \frac{\partial\mathcal{L}}{\partial g_{\mu\nu}} - \frac{1}{2}\mathcal{L} g_{\mu\nu}. \tag{2.15}$$

The Einstein Field Equation finally reads

$$G_{\mu\nu} + \Lambda g_{\mu\nu} = 8\pi G T_{\mu\nu}, \tag{2.16}$$

where the Einstein tensor is

$$G_{\mu\nu} = R_{\mu\nu} - \frac{1}{2}Rg_{\mu\nu}.$$

The Bianchi identity implies $\nabla_\mu G^{\mu\nu} = 0$, which together with $\nabla_\mu g^{\mu\nu} = 0$ also means that the matter is covariantly conserved, i.e

$$\nabla_\mu T^{\mu\nu} = 0. \tag{2.17}$$

Eq. (2.17) is the conservation equation.

2.1.2 Friedmann equations

The energy momentum is given by

$$\overline{T}^{\mu\nu} = \overline{\rho}\,\overline{u}^\mu\overline{u}^\nu + \overline{p}(\overline{u}^\mu\overline{u}^\nu + \overline{g}^{\mu\nu}) \tag{2.18}$$

with $\overline{u}^\mu = (1/a)(1, \mathbf{0})$ is the background 4-velocity of a comoving observer and $\bar{\rho}$ and $\bar{p}$ are the energy density and pressure respectively on the background. The background quantities are only time dependent. The 4-velocity $\overline{u}^\mu$ is time-like future directed with $\overline{u}^\mu\overline{u}_\mu = -1$ giving $\overline{u}_\mu = a(-1, \mathbf{0})$. From the continuity equation in Eq. (2.17) we have that

$$\bar{\rho}' = -3\mathcal{H}(\bar{\rho} + 3\bar{p}). \tag{2.19}$$

At zeroth order in perturbation theory the EFEs in Eq. (2.16) gives the Friedmann equations

$$\mathcal{H}^2 = \frac{8\pi G}{3}\bar{\rho}a^2 + \frac{\Lambda a^2}{3}, \tag{2.20}$$

$$\mathcal{H}' = -\frac{8\pi G}{6}(\bar{\rho} + 3\bar{p})a^2 + \frac{\Lambda a^2}{3},. \tag{2.21}$$

The prime $'$ denotes derivative with respect to the conformal time η and $\mathcal{H} = a'/a = aH$ is the conformal Hubble parameter. The version of Eq. (2.20) as a function of cosmic time reads

$$H^2 = \frac{8\pi G}{3}\bar{\rho}_{eff} \tag{2.22}$$

where $\bar{\rho}_{eff} = \bar{\rho} + \Lambda/(8\pi G)$ in general combines energy density of radiation, matter (baryonic and non-baryonic), curvature and dark energy, but since in most of our calculations we consider an era well after radiation-matter equality in a flat universe, the effective energy

density is just a combination of matter and vacuum energy. Another form of Eq. (2.22)

$$H(a) = \frac{H_0}{a^{3/2}}\sqrt{\Omega_m + \Omega_\Lambda a^3}, \tag{2.23}$$

where Ω_m and Ω_Λ are the matter density parameter and dark energy density parameter respectively and H_0 the Hubble rate at present $H_0 = 100\,h$ km.s^{-1}.Mpc^{-1} [9]. It is noted that Eq. (2.20) and Eq. (2.21) are not independent and one can get Eq. (2.21) from Eq. (2.20) by exploiting Eq. (2.19). Therefore we only have two equations for three unknowns. To close the system, one resorts to the definition of the equation of state of matter which is the ratio between the energy density with the pressure

$$w = \frac{\bar{p}}{\bar{\rho}}. \tag{2.24}$$

By taking the derivative of w with respect to the conformal time while using Eq. (2.19) one easily gets

$$\frac{w'}{1+w} = -3\mathcal{H}(c_S^2 - w), \tag{2.25}$$

where c_S is the sound speed defined as

$$c_S^2 = \frac{\bar{p}'}{\bar{\rho}'}. \tag{2.26}$$

For a constant equation of state parameter w (e.g $w = 0, -1/3, -1$ for dust, radiation and dark energy respectively) we thus have $c_S^2 = w$.

2.1.3 Distance in cosmology

A photon emitted by a distant source has an energy E_S. Due to cosmic expansion, it loses energy as it travels to the observer, its wavelength gets stretched. The redshift z is the ratio between the energy of a photon at emission and its energy (E_O) as it arrives at the observer

$$\frac{E_S}{E_O} = 1 + z = \frac{1}{a}. \tag{2.27}$$

Determining the redshift of a spectroscopically resolved source requires measuring the shift of the frequencies of its line emissions towards the low energy of the energy spectrum. In an

expanding universe, the physical radial distance of a source from us is

$$r = a\chi, \tag{2.28}$$

where χ is the comoving distance which is also a function of the scale factor as

$$\chi = \int_{a_S}^{1} \frac{da}{a^2 H(a)}. \tag{2.29}$$

Using $dz = -da/a^2$, it yields

$$\chi = \frac{1}{H_0} \int_0^z \frac{dz}{E(z)}, \tag{2.30}$$

where

$$E(z) = \frac{H(z)}{H_0}. \tag{2.31}$$

The conformal time is the comoving distance that light has traveled since the beginning of time

$$\eta = \int_0^{t_O} \frac{dt}{a(t)}. \tag{2.32}$$

On the past light cone, the comoving distance and the conformal time are related by $d\eta = -d\chi$. One way to estimate the distance of an object is by measuring the flux $\mathcal{S}$ which is the sum of the energy of all the photons emitted per unit time per unit area

$$\mathcal{S} = \frac{L}{4\pi D_L^2}, \tag{2.33}$$

therefore

$$D_L = \sqrt{\frac{L}{4\pi \mathcal{S}}}. \tag{2.34}$$

By knowing the absolute magnitude of an object M(say supernova), its distance can be estimated by measuring its apparent magnitude m via the distance-modulus formula

$$\mu = 5 \log_{10} \left(\frac{D_L}{10\text{pc}} \right), \tag{2.35}$$

where $\mu = m - M$. In an expanding universe, the angular diameter distance is defined as the ratio between the physical size d of an object located at a given redshift z and its angular diameter (or angle subtended by the object) θ_{obj}

$$D_A = \frac{d}{\theta_{\text{obj}}}. \tag{2.36}$$

It is written as a function of the comoving distance

$$D_A = \frac{\chi}{1+z}, \tag{2.37}$$

and also depends on the cosmological model which is considered. Via the distance duality equation, we have the relationship between the luminosity distance and the angular diameter distance.

$$D_L = (1+z)^2 D_A. \tag{2.38}$$

In the next section, we will look at a perturbed universe.

2.2 Perturbation of the cosmological model

In perturbation theory, a quantity is composed of a homogeneous background part and an inhomogeneous perturbed part which is considered as small. In other words, all the quantities are perturbed according to

$$s(\eta, \boldsymbol{x}) = \overline{s}(\eta) + \delta s(\eta, \boldsymbol{x}), \tag{2.39}$$

where $\delta s(\eta, \boldsymbol{x})$ can be in fact expanded order by order in a power series [100–102]

$$\delta s(\eta, \boldsymbol{x}) = \sum_{n=1}^{\infty} \frac{\epsilon^n}{n!} \delta s^{(n)}(\eta, \boldsymbol{x}), \tag{2.40}$$

where the smallness parameter ϵ denotes the order in perturbation. In what follows we will denote the order of a perturbation of a quantity by a superscript in brackets. Let us now look at the perturbed metric.

2.2.1 Scalar Vector Tensor (SVT) decomposition

In a perturbed flat FLRW universe we have that

$$ds^2 = a^2 \left[-(1+2A)d\eta^2 + V_i d\eta dx^i + (\delta_{ij} + 2h_{ij}) dx^i dx^j \right], \tag{2.41}$$

where A is a scalar perturbation, V_i a vector perturbation also known as shift and h_{ij} a tensor perturbation. According to Helmholtz theorem, a vector field can be decomposed

into divergence-free part and a curl-free part. Therefore

$$V_i = \partial_i V + \tilde{V}_i, \tag{2.42}$$

with $\partial_i V$ is the covariant derivative of a scalar V on the 3 hypersurface and we have the constraint $\partial^j \tilde{V}_j = 0$. Like the vector, we can further extract two scalar parts, one vector part and a pure tensor part from the tensor perturbation h_{ij} as

$$h_{ij} = C\delta_{ij} + \partial_{ij}E + \partial_{(i}F_{j)} + \tilde{h}_{ij}, \tag{2.43}$$

where C and E are scalar perturbations, F_i is a vector perturbation subject to $\partial^i F_i = 0$, $\partial_{(i}F_{j)} = \frac{1}{2}(\partial_j F_i + \partial_i F_j)$ is symmetric and $\tilde{h}_{ij}$ is the pure transverse traceless tensor part ($\partial_{ij}\tilde{h}^{|i} = 0$, $\tilde{h}^i_i = 0$). From the expression of the perturbed metric $g_{\mu\nu} = \bar{g}_{\mu\nu} + \delta g_{\mu\nu}$, it yields

$$\delta g_{00} = -2a^2 A, \tag{2.44}$$

$$\delta g_{0i} = a^2 V_i, \tag{2.45}$$

$$\delta g_{ij} = 2a^2 h_{ij}. \tag{2.46}$$

With 2 constraints imposed on each of the pure vector perturbations, 4 constraints on the pure tensor perturbations, it amounts to 10 degrees of freedom (d.o.f) in total. By imposing the constraint $g_{\mu\nu}g^{\mu\lambda} = \delta^\lambda_\nu$ we arrive at

$$\delta g^{00} = \frac{2}{a^2}A, \tag{2.47}$$

$$\delta g^{0i} = \frac{1}{a^2}(\partial^i V + \tilde{V}^i), \tag{2.48}$$

$$\delta g^{ij} = -\frac{2}{a^2}(C\delta^{ij} + \partial^{ij}E + \partial^{(i}F^{j)} + \tilde{h}^{ij}). \tag{2.49}$$

2.2.2 Energy momentum stress-tensor

The perturbed 4-velocity reads

$$u^\mu = \frac{1}{a}(1 - A, v^i), \quad \frac{dx^\mu}{d\tau} = u^\mu, \tag{2.50}$$

using $g_{\mu\nu}u^\mu u^\nu = -1$ gives

$$u_\mu = a(-1 - A, V_i + v_i). \tag{2.51}$$

It is worth noting that the quantity v_i can be decomposed in a curl-free part and a divergence-free part as $v_i = \partial_i v + \tilde{v}_i$. The energy momentum stress $T^{\mu\nu}$ in a perturbed universe

$$T^{\mu\nu} = u^\mu u^\nu(\rho + p) + pg^{\mu\nu}, \tag{2.52}$$

which is also split into a background and perturbed parts

$$T^{\mu\nu} = \overline{T}^{\mu\nu} + \delta T^{\mu\nu}. \tag{2.53}$$

Taking into account

$$p = \overline{p} + \delta p, \tag{2.54}$$
$$\rho = \overline{\rho} + \delta\rho, \tag{2.55}$$

we obtain

$$\delta T^{00} = \frac{\overline{\rho}}{a^2}(\delta - 2A), \tag{2.56}$$
$$\delta T^{0i} = \frac{1}{a^2}[(\overline{\rho} + \overline{p})(v^i - A) + \delta p + \overline{p}V^i], \tag{2.57}$$
$$\delta T^{ij} = \frac{1}{a^2}[\delta p\delta^{ij} - 2h^{ij}\overline{p}]. \tag{2.58}$$

where the matter density fluctuation $\delta = \delta\rho/\overline{\rho}$.

2.3 Gauge problem

In perturbation theory, it is assumed that the perturbed manifold with its perturbed metric $(\mathcal{M}^1, g_{\mu\nu})$ is close to the background manifold $(\mathcal{M}^0, \overline{g}_{\mu\nu})$. The theory of General relativity is covariant under any choice of coordinate system but the problem arises from perturbing quantities. There are many ways to perturb a background space-time [8] such that some quantities that are not physical may arise from this freedom of choice. These unphysical quantities are called gauge artifacts. In this section, we will focus on how one can construct gauge invariant quantities which are the observables.

2.3.1 Gauge transformation

For each quantity in the background manifold, one wishes to find its correspondence in the perturbed manifold. Therefore, a linear map $\psi : \mathcal{M}^0 \to \mathcal{M}^1$ can be introduced such that, points in one manifold can be mapped onto the other. Since this mapping is not unique, by an infinitesimal coordinate transformation in the perturbed manifold one can get new perturbed quantities. This infinitesimal diffeomorphism is then completely defined by specifying a vector field $\xi^\mu = (\xi^0, \partial^i\xi + \tilde{\xi}^i)$ that generates the transformations such that the perturbation of any scalar quantities transforms at first order as [101]

$$\widehat{\delta s} = \delta s + \mathfrak{L}_\xi \overline{s}, \tag{2.59}$$

where $\mathfrak{L}_\xi = \xi^\mu(\partial/\partial x^\mu)$ is the Lie derivative with respect to the vector field ξ^μ and $\widehat{\delta s}$ is the new perturbed quantity. Depending on the quantity (scalar, vector or tensor) it is acting on, at first order we have [100] (and reference therein)

$$\begin{aligned} \mathfrak{L}_\xi S &= \xi^\mu S_{,\mu}, \\ \mathfrak{L}_\xi U_\mu &= U_{\mu,\lambda}\xi^\lambda + U_\lambda \xi^\lambda_{,\mu}, \\ \mathfrak{L}_\xi V_{\mu\alpha} &= V_{\mu\alpha,\nu}\xi^\nu + V_{\mu\nu}\xi^\nu_{,\alpha} + V_{\nu\alpha}\xi^\nu_{,\mu}. \end{aligned} \tag{2.60}$$

Now, to see how the quantities in the metric perturbation transforms at first order, we look at the overall transformation

$$\widehat{\delta g}_{\mu\nu} = \delta g_{\mu\nu} + \overline{g}_{\mu\nu,\alpha}\xi^\alpha + \overline{g}_{\mu\alpha}\xi^\alpha_{,\nu} + \overline{g}_{\alpha\nu}\xi^\alpha_{,\mu} \tag{2.61}$$

yielding

$$\begin{aligned} \widehat{A} &= A + \mathcal{H}\xi^0 + \xi^{0\prime}, \\ \widehat{C} &= C + \mathcal{H}\xi^0, \\ \widehat{E} &= E + \xi, \\ \widehat{V} &= V - \xi^0 + \xi', \\ \widehat{F}_i &= F_i - \tilde{\xi}_i, \\ \widehat{\tilde{V}}_i &= \tilde{V}_i + \tilde{\xi}_i', \\ \widehat{\tilde{h}}_{ij} &= \tilde{h}_{ij}. \end{aligned} \tag{2.62}$$

It is worth noting that from Eq. (2.62), we can deduce that the pure tensor perturbation $\tilde{h}_{ij}$ is gauge invariant at first order [1]. For the energy-stress momentum sector, by exploiting Eqs. (2.60) and (2.62), the transformations of the density perturbation $\delta\rho$, pressure perturbation δp and the velocity perturbation v_i read

$$\begin{aligned} \widehat{\delta\rho} &= \delta\rho + \overline{\rho}'\xi^0, \\ \widehat{\delta p} &= \delta p + \overline{p}'\xi^0, \\ \widehat{v} &= v - \xi', \\ \widehat{\tilde{v}}_i &= \tilde{v}_i - \tilde{\xi}_i'. \end{aligned} \tag{2.63}$$

The method described by Eq. (2.59) is called the active approach but there is also another method called passive approach which consists of considering two mappings of a same point on the background onto two points q and p of two different coordinate systems on the perturbed space-time. The relationship between the two coordinate systems at the same point on the perturbed manifold can be defined as

$$\widehat{x}^\mu = x^\mu - \xi^\mu. \tag{2.64}$$

As an example by imposing the condition that the total density is invariant under infinitesimal coordinate transformation $\widehat{\rho}(\widehat{x}^\mu) = \rho(x^\mu)$, the relation between density perturbations in different gauges can be established [100]

$$\widehat{\rho}(\widehat{x}^\mu) = \overline{\rho}(\eta) - \overline{\rho}'(\eta)\xi^0 + \widehat{\delta\rho}(x^\mu). \tag{2.65}$$

Exploiting Eq. (2.55) thus yields

$$\widehat{\delta\rho} = \delta\rho + \overline{\rho}'(\eta)\xi^0, \tag{2.66}$$

which is the same as the transformation given in Eq. (2.63). The passive approach was extensively used in the seminal papers [103–105] at first order in perturbation theory but the active one is both more intuitive and easier to handle especially when dealing with perturbed quatities at second order and higher. We now look at the construction of gauge invariant variables.

[1] This is no longer true at second order in perturbation theory.

2.3.2 Gauge-invariant quantities and gauge choice

Gauge-invariant variables are those that remain unchanged under the coordinate transformation described in Eq. (2.59). This is in fact the Stewart-Walker lemma that states that the gauge independent variables are those such that $\mathfrak{L}_\xi \overline{s} = 0$ for any vector field ξ^μ that is used to generate the transformation. Constructing gauge-invariant quantities is very important in perturbation theory as it allows one to eliminate in the calculations the gauge modes which are non-physical. Rearranging the transformations given in Eq. (2.62), two scalar quantities that are gauge independent can be constructed [103]

$$\Phi \equiv A + \mathcal{H}(V - E') + (V - E')', \tag{2.67}$$

$$\Psi \equiv C - \mathcal{H}(V - E'). \tag{2.68}$$

Φ and Ψ are named the Bardeen potentials. For the gauge invariant density perturbations, there are possible choices that are defined in different gauges [98, 100]

$$\delta^N = \delta + \frac{\overline{\rho}'}{\overline{\rho}}(V - E'), \tag{2.69}$$

$$\delta^C = \delta + \frac{\overline{\rho}'}{\overline{\rho}}(v + V), \tag{2.70}$$

where the superscripts N and C denote Newtonian gauge and comoving gauge respectively. A gauge invariant velocity reads

$$v^N = v + E', \tag{2.71}$$

and finally a gauge-invariant vector quantity is of the form [100]

$$\widehat{V}_i = \widehat{F}_i = V_i + F_i' \tag{2.72}$$

By choosing a time slicing, the gauge generator ξ^μ is completely defined so that calculations can be carried out within that particular gauge. We now review some of the gauges that are widely used.

Longitudinal gauge

Also known as conformal Newtonian gauge or zero shear gauge, the generator is completely fixed by imposing the condition that off-diagonal scalar perturbations in the metric are set

equal to zero

$$\widehat{V} = \widehat{E} = 0. \tag{2.73}$$

By using Eq. (2.62), we thus have $\xi = -E$ and the time part of the generator is $\xi^0 = V - E'$. This implies the gauge invariant density perturbation in conformal Newtonian gauge given in Eq. (2.69). From Eq. (2.67), we find that the scalar perturbations A and C coincide with the Bardeen potentials

$$\Phi = A, \quad \Psi = C. \tag{2.74}$$

In the absence of anisotropic stress in this gauge we also have $\Psi = \Phi$. This gauge is also named the Poisson gauge when including vector pertubations and the generator is completely fixed by choosing $\widehat{\tilde{V}}_i = 0$, yielding

$$\tilde{\xi}_i = \int \tilde{V}_i \mathrm{d}\eta + \mathcal{C}_i(x^j), \tag{2.75}$$

$\mathcal{C}_i$ being an arbitrary integration function. Therefore

$$\widehat{F}_i = F_i - \int \tilde{V}_i \mathrm{d}\eta + \mathcal{C}_i(x^j). \tag{2.76}$$

Synchronous gauge

It is a gauge where, the time-slicing is chosen such the perturbations are only in the spatial part. This can be achieved by requiring $\widehat{A} = 0$ and $\widehat{V}_i = 0$ giving

$$\xi^{0\prime} a + a' \xi^0 + aA = 0, \tag{2.77}$$

solving the time part of the generating vector

$$\xi^0 = -\frac{1}{a}\left(\int aA \mathrm{d}\eta + \mathfrak{C}_1(x^i)\right). \tag{2.78}$$

Exploiting Eqs. (2.78) and (2.62) gives

$$\xi = \int (\xi^0 - V)\mathrm{d}\eta + \mathfrak{C}_2(x^i). \tag{2.79}$$

Finally we have that

$$\xi_i = -\int \tilde{V}_i \mathrm{d}\eta + \mathfrak{C}_3(x^k). \tag{2.80}$$

It is noted that $\mathfrak{C}_1, \mathfrak{C}_2$ and $\mathfrak{C}_3$ are all integration functions. In synchronous gauge, the world-lines are orthogonal to the spatial hyperface. In his early work on cosmological perturba-

tion [106], Lifshitz used this gauge which is still very popular and widely used in Boltzmann code like CMBFAST or CAMB [107, 108].

Comoving gauge

In this gauge, a vanishing three-velocicty of the fluid is imposed $\widehat{v} = 0$. The condition $\widehat{v} + \widehat{V} = 0$ is also required so that the fluid 4-velocity is orthogonal to the time slices. Therefore

$$\xi = \int v \mathrm{d}\eta + \mathfrak{T}(x^i), \tag{2.81}$$

$$\xi^0 = V + v, \tag{2.82}$$

where $\mathfrak{T}$ is an integration function. Using Eq. (2.63) and the background relations, we arrive at the expression given in Eq. (2.70). Taking into account Eq. (2.69) gives the relationship between the density fluctuations in the two gauges

$$\delta^C = \delta^N + \frac{\overline{\rho}'}{\overline{\rho}}(v + E'). \tag{2.83}$$

Uniform density gauge

One can also impose a spacetime foliation such that the density perturbation vanishes $\overline{\delta\rho} = 0$. Using Eq. (2.63), this fixes the time part of the generating vector field

$$\xi^0 = -\frac{\delta\rho}{\overline{\rho}'}. \tag{2.84}$$

A gauge independent curvature perturbation can be defined in this gauge [109, 110]

$$-\zeta = C + \mathcal{H}\frac{\delta\rho}{\overline{\rho}'}. \tag{2.85}$$

2.4 Perturbed Einstein Field Equations

2.4.1 Bardeen equation

The EFEs read

$$\nabla^2\Psi - 3\mathcal{H}(\mathcal{H}\Phi + \Psi') = \frac{1}{2}\kappa a^2\overline{\rho}\delta^N, \tag{2.86}$$

$$(\mathcal{H}\Phi + \Psi')_{|i} = \frac{1}{2}\kappa a^2 v^N_{|i}(\overline{\rho} + \overline{p}), \tag{2.87}$$

$$\Psi'' + 2\mathcal{H}\Psi' + \mathcal{H}\Phi' + (\mathcal{H}^2 + 2\mathcal{H}')\Phi + \frac{1}{3}\nabla^2(\Psi - \Phi) = \frac{1}{2}\kappa a^2\delta p^N, \tag{2.88}$$

$$\Phi - \Psi = 0. \tag{2.89}$$

Here δp^N denotes pressure perturbation and we assume a pressureless fluid, such as matter on cosmological scales, so that $c_s^2 = 0$. The trace-free part of the EFEs (Eq. (2.89)) in general involves an anisotropic tensor Π_{ij} but for our purposes we assume $\Pi_{ij} = 0$. This implies that the two Bardeen potentials are the same ($\Psi = \Phi$), which is what we adopt in what follows, unless otherwise stated. The time-time component of EFEs Eq. (2.86) is known as the relativistic Poisson equation. On small scales, the second term of the left handside of the equation is negligible so that Ψ coincides with the gravitational potential in Newtonian theory. By exploiting Eq. (2.87) which allows us to compute the peculiar velocity - a key variable in this thesis - the relativistic Poisson equation and some background relations, we arrive at the expression of the matter density contrast δ^N

$$\delta^N = \frac{2a}{3\Omega_{\rm m}H_0^2}\nabla^2\Psi + 3\mathcal{H}v^N. \tag{2.90}$$

The trace part of EFEs (Eq. (2.88)) which gives the evolution of the gravitational potential is known as the Bardeen equation

$$\Psi'' + 3\mathcal{H}\Psi' + (\mathcal{H}^2 + 2\mathcal{H}')\Psi = 0. \tag{2.91}$$

The continuity equations from $\nabla_\mu T^{\mu\nu} = 0$ read

$$(\delta^N)' = (1+w)(\nabla^2 v^N - 3\Psi') + 3\mathcal{H}\left(w\delta^N - \frac{\delta p^N}{\overline{\rho}}\right), \tag{2.92}$$

$$(v^N)' = -\left(\mathcal{H}(1-3w) + \frac{w'}{1+w}\right)v^N - \Psi - \frac{\delta p^N}{\overline{\rho}(1+w)}. \tag{2.93}$$

Together with the conservation equations, one can use the Poisson equation to re-derive the Bardeen equation.

In ΛCDM, the solution of Eq. (2.91) can be factorized as $\Psi(\eta, \boldsymbol{x}) = g(\eta)\Psi(\boldsymbol{x})$ where $\Psi(\boldsymbol{x})$ (or equivalently $\Psi(\boldsymbol{k})$ in Fourier space) denotes the potential well after both horizon crossing and radiation-matter equality, and the growth suppression factor $g(\eta)$ which describes the growth of the gravitational potential after decoupling is determined from [77]

$$g''(\eta) + 3\mathcal{H}g'(\eta) + a^2\Lambda g(\eta) = 0. \tag{2.94}$$

The solution of Eq. 2.94 is well approximated by a fitting formula [111, 112]

$$g(z) = \frac{5}{2}g_\infty\Omega_m(z)\Big[\Omega_m(z)^{4/7} - \Omega_\Lambda(z) + \Big(1 + \frac{1}{2}\Omega_m(z)\Big)\Big(1 + \frac{1}{70}\Omega_\Lambda(z)\Big)\Big]^{-1}, \tag{2.95}$$

where g_∞ is the normalization factor such that the growth suppression factor at $z = 0$ is $g(z = 0) = 1$ and

$$\Omega_m(z) = \frac{\Omega_{m0}(1+z)^3}{E(z)^2}, \tag{2.96}$$

$$\Omega_\Lambda(z) = \frac{\Omega_{\Lambda 0}}{E(z)^2}. \tag{2.97}$$

We recall the function $E(z)$ is given by Eq. (2.31).

2.4.2 Power spectrum

In general, one uses the linearity of the perturbation equations to decompose the gravitational potential in terms of a transfer function T which accounts for the evolution of the potential through the horizon crossing and the radiation-matter transition. It is well approximated by [112], as $\Psi(\boldsymbol{k}, \eta) = T(k, \eta)\Psi_i(\boldsymbol{k})$ in Fourier space, defining the Fourier modes by

$$\Psi(\boldsymbol{x}, \eta) = \int \frac{d^3\boldsymbol{k}}{(2\pi)^{3/2}}\Psi(\boldsymbol{k}, \eta)\mathrm{e}^{\mathrm{i}\boldsymbol{k}\cdot\boldsymbol{x}}. \tag{2.98}$$

It is noted that in general the transfer function $T(k)$ is only scale dependent but its scale and time dependent form $T(k, \eta)$ includes the growth suppression factor $g(\eta)$, i.e $T(k, \eta) =$

$T(k)g(\eta)$. The scalar power spectrum is defined as

$$\langle \Psi(\boldsymbol{k},\eta)\Psi^*(\boldsymbol{k}',\eta')\rangle = \frac{2\pi^2}{k^3}\mathcal{P}_\Psi(k,\eta,\eta')\delta^{(3)}(\boldsymbol{k}-\boldsymbol{k}')\,, \tag{2.99}$$

where $\delta^{(3)}$ stands for the Dirac distribution. The power spectrum today can be related to the initial power spectrum predicted from inflation. Assuming scale invariance (which is a good approximation for our analysis since secondary modes are quite insensitive to the spectral index), the inflationary power spectrum is characterized by its primordial power $\Delta^2_{\mathcal{R}}$, typically of order $\Delta^2_{\mathcal{R}} \approx 2.41 \times 10^{-9}$ at a scale $k_{\rm CMB} = 0.002$ Mpc^{-1} [113]. It follows that

$$\mathcal{P}_\Psi(k,\eta) = \left(\frac{3\Delta_{\mathcal{R}}}{5g_\infty}\right)^2 g^2(\eta)T^2(k), \tag{2.100}$$

The non-linear evolution of structure growth on small scales results in an enhancement of the power spectrum on small scales with respect to its linear counterpart (see for example Fig. 3.1). To account for these non-linearities, one uses in general Halofit formula which is a fitting formula obtained from N-body simulation [173]. The accuracy of the Halofit formula is limited by the resolution of the simulation from which it is derived and it can not be used to account for the non-linear evolution of the velocity perturbations.

In the next section, we will have a look at second order perturbations, more precisely the vector modes and tensor modes. We will discuss how they are generated and evolve then will present their today's power spectrum which is relevant for the next Chapter on the contribution of these modes to cosmic convergence.

2.5 Second order induced vector modes

Vector metric perturbations, at linear order, are often neglected in the standard picture in cosmology as they were not produced during inflation. From EFEs, we get both the constraint and evolution equations of these modes

$$(\mathcal{H}^2 - \mathcal{H}')\tilde{V}_i - \frac{1}{4}\nabla^2\tilde{V}_i = 4\pi G a^2 \tilde{v}_i \overline{\rho}(1+w), \tag{2.101}$$

$$2\mathcal{H}\tilde{V}_i + \tilde{V}_i' = 0. \tag{2.102}$$

Eq. (2.102) clearly shows that since at linear order where each mode – scalar, vector and tensor – evolves independently, there is no source for the vector modes. Therefore, as the universe expands they decay rapidly. However, previous works [83, 86, 111, 114] showed that at second order, the vector modes are induced by first order density perturbations. During radiation dominated era, all the modes are well outside the Hubble radius. The mode $\boldsymbol{k}_1$ with shorter wavelength enters first the Hubble radius whereas the other $\boldsymbol{k}_2$, with longer wavelength, enters the Hubble radius at later time. Upon entering the Hubble sphere, $\boldsymbol{k}_2$ interacts with $\boldsymbol{k}_1$, which is already well within, and this interaction between modes produces vector modes [86]. The overall power of the induced vector mode depends on how much the wavenumbers of the two generators differ from each other, the smaller the difference, the larger the overall power. What is of interest to us is to see how these vector perturbations are generated during matter dominated era and how large is the amplitude of their today's power spectrum. In what follows we will simply present the relevant equations and highlight the final expression of their power spectrum.

2.5.1 Vorticity

As one needs to go up to second order in perturbation theory to compute the vector metric perturbations generated by first order density perturbation, we work in Poisson gauge with the perturbed line element [114]

$$ds^2 = -a^2\Big[(1+2\Psi)d\eta^2 - V_i dx^i d\eta + (1-2\Psi)\gamma_{ij}dx^i dx^j\Big]. \tag{2.103}$$

It is worth noting that since we are only interested in second order vector perturbations sourced by first order scalar modes, we only have V_i denoting the second order gauge invariant vector modes ($\partial_i V^i = 0$) and Ψ the first order Bardeen potential in the metric. The perturbed matter four velocity reads

$$u_\mu = -a\Big[1+\Psi+\frac{1}{2}v^j v_j, -v_i - \frac{1}{2}(v_i^{(2)} - V_i) + 2\Psi v_i\Big], \tag{2.104}$$

where $v_i = \partial_i v$ is the scalar part of the first order potential v obtained from the $0j$ component of the EFEs Eq. (2.86)

$$v = -\frac{\mathcal{H}\Psi + \Psi'}{4\pi G a^2 \bar{\rho}(1+w)}, \tag{2.105}$$

and $v_i^{(2)}$ is the divergence free second order peculiar velocity. To get the contravariant four velocity, we use the constraint $u^\mu u_\mu = -1$. Thus

$$u^\mu = \frac{1}{a}\left[1 - \Psi + \frac{3}{2}\Psi^2 + \frac{1}{2}v_j v^j, v^i + \frac{1}{2}v^i_{(2)}\right]. \tag{2.106}$$

The vorticity, $\omega_{\mu\nu}$, in the matter four velocity is due to the vector modes and defined as [105, 111]

$$\omega_{\mu\nu} = h^\alpha_{[\mu} h^\beta_{\nu]} \nabla_\beta u_\alpha, \tag{2.107}$$

where the square brackets denote antisymmetrization with respect to μ, ν indices and $h_{\mu\nu} = g_{\mu\nu} + u_\mu u_\nu$ is a projector tensor into the instantaneous fluid rest space. We recall that the variable $\omega_{\mu\nu}$ is a sum of a first and second order quantities, $\omega_{\mu\nu} = \delta^{(1)}\omega_{\mu\nu} + \delta^{(2)}\omega_{\mu\nu}$, and is subject to $\omega_{\mu\nu}u^\nu = 0$. At first order we have that $\delta^{(1)}\omega_{\mu\nu} = 0$. As proved by [111], first order scalar modes can not source vorticity at non-linear order, so that

$$\delta^{(2)}\omega_{\mu\nu} = 0. \tag{2.108}$$

We are now in position to compute the gauge invariant second order vector mode V_i.

2.5.2 Vector modes

By taking into account the metric in Eq. (2.103) and exploiting the expression of the perturbed four velocity Eq. (2.104) to compute the second order vorticity $\delta^{(2)}\omega_{ij}$ Eq. (2.107), one gets [111, 115]

$$\delta^{(2)}\omega_{ij} = \frac{a}{2}\left[\partial_{[i}v^{(2)}_{j]} - \partial_{[i}V_{j]} + 6\partial_{[i}\Psi\partial_{j]}v + 2\partial_{[i}v'\partial_{j]}v\right]. \tag{2.109}$$

From the second order $0i$ component of EFEs, we get another constraint equation

$$6\mathcal{H}^2\Omega_m(1+w)(v_i^{(2)} - V_i) = -\nabla^2 V_i + 8\left[2\Psi'\partial_i\Psi + \frac{2}{3\mathcal{H}^2\Omega_m}\nabla^2\Psi\partial_i(\Psi' + \mathcal{H}\Psi)\right]. \tag{2.110}$$

By solving for $v_i^{(2)} - V_i$ in Eq. (2.110) and substituting it along with the expression of v in Eq. (2.105) into Eq. (2.109), we get

$$\delta^{(2)}\omega_{ij} = \frac{a}{12(1+w)\mathcal{H}^2\Omega_m}\left[\nabla^2\partial_{[i}V_{j]} - \frac{16}{3(1+w)\mathcal{H}^2\Omega_m}(\nabla^2\partial_{[i}\Psi)\partial_{j]}(\Psi' + \mathcal{H}\Psi)\right]. \tag{2.111}$$

By using the constraint Eq. (2.108), we finally get

$$V_i = \frac{16}{3\mathcal{H}^2\Omega_m(1+w)}\nabla^{-2}\Big[\nabla^2\Psi\partial_i(\Psi' + \mathcal{H}\Psi)\Big]. \tag{2.112}$$

2.5.3 Power spectrum

The Fourier transform of vector perturbation contains two polarisations and the real space solution of Eq. (2.112) reads [111]

$$V_i(\boldsymbol{x},\eta) = \int \frac{\mathrm{d}^3\boldsymbol{k}}{(2\pi)^{3/2}}\Big[V_+(\boldsymbol{k},\eta)e_i^+(\boldsymbol{k}) + V_-(\boldsymbol{k},\eta)e_i^-(\boldsymbol{k})\Big]\mathrm{e}^{\mathrm{i}\boldsymbol{k}\cdot\boldsymbol{x}}, \tag{2.113}$$

where the vectors $e_i^{\pm}$ form an orthonormal basis of a plane perpendicular to the wavevector $\boldsymbol{k}$. The definition of the power spectrum of each polarisation is given by

$$\langle V_\lambda^*(\boldsymbol{k},\eta)V_{\lambda'}(\boldsymbol{k}',\eta')\rangle = \frac{2\pi^2}{k^3}\delta^3(\boldsymbol{k}-\boldsymbol{k}')\mathcal{P}_V(k,\eta,\eta')\delta_{\lambda\lambda'}, \;\; \lambda = \pm. \tag{2.114}$$

From now on, we shall drop the subscript λ denoting each polarisation as the power spectrum $\mathcal{P}_V$ is the same in each case. The solution in Fourier space of the Eq. (2.112) is [111]

$$V(\boldsymbol{k},\eta) = \frac{16ie^j(\boldsymbol{k})}{3\Omega_m(2\pi)^{3/2}k^2}\int \mathrm{d}^3k'|\boldsymbol{k}-\boldsymbol{k}'|^2k'_j\mathcal{B}(\boldsymbol{k}-\boldsymbol{k}',\boldsymbol{k}',\eta), \tag{2.115}$$

in which $\mathcal{B}$ is defined as

$$\mathcal{B}(\boldsymbol{k}_1,\boldsymbol{k}_2,\eta) = \frac{1}{\mathcal{H}^2}\Psi(\boldsymbol{k}_1,\eta)\Big(\Psi'(\boldsymbol{k}_2,\eta) + \mathcal{H}\Psi(\boldsymbol{k}_2,\eta)\Big). \tag{2.116}$$

Exploiting Eq. (2.115), we can compute the correlator Eq. (2.114) and identify the expression of the power spectrum. The computations are a bit more involved so we will just give the final expression

$$\mathcal{P}_V(k,\eta,\eta') = \left(\frac{2\Delta_{\mathcal{R}}}{5g_\infty\sqrt{\Omega_{\mathrm{m}}}H_0}\right)^4\mathcal{V}(\eta)\mathcal{V}(\eta')k^2\Pi(k)\,, \tag{2.117}$$

with

$$\mathcal{V}(\eta) = 3a(\eta)g(\eta)[g'(\eta) + \mathcal{H}(\eta)g(\eta)], \tag{2.118}$$

governs the growth of the vector power spectrum, and $\Pi(k)$ is a convolution integral of order unity (see Eq. (C7) of Ref. [111] for its explicit expression). $\Delta^2_{\mathcal{R}}$ denotes the initial power spectrum of the curvature perturbation. We refer the interested readers to [111] for

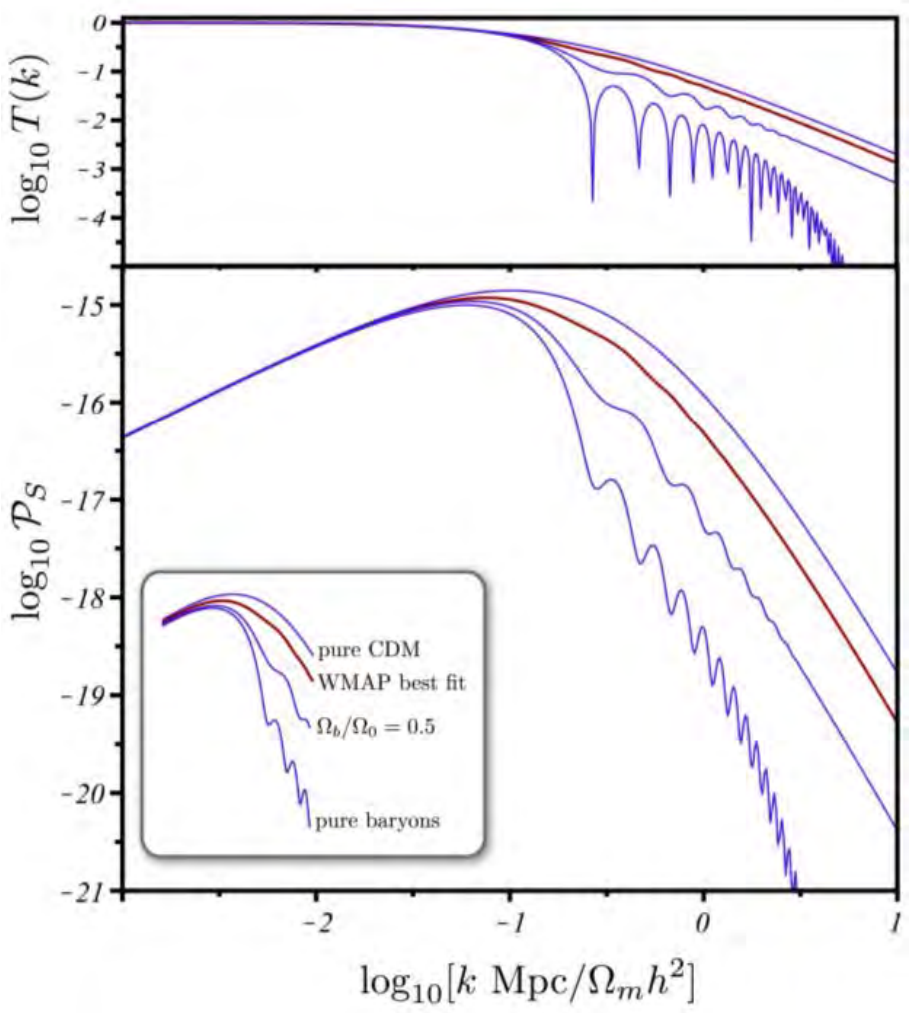

Figure 2.1: *Top panel*: the transfer functions as a function of the wavenumber, for different amount of baryons. *Bottom panel*: the power spectra of vector perturbations $\mathcal{P}_V$ ($\mathcal{P}_S$ in the plot).

more detailed derivations. In the power spectrum $\mathcal{P}_V$ plotted in Fig. 2.1 (from [111]), we also notice the imprint of the acoustic oscillations as in the case of the scalar modes. This can be explained by the fact that the vector perturbations are sourced by first order scalar modes. As the amount of baryons is increased, the amplitude of the power spectrum after the turnover, around 0.1 $\mathrm{Mpc}/\Omega_m h^2$, decreases.

The power in each polarisation is, thanks to spatial isotropy, the same and is defined in the same way as for the scalars for each polarisation. During the matter dominated era the vector contribution grows as $a^{1/2}$ which is the reason why it is not completely negligible today [86, 111]. Their contribution peaks in power at the equality scale, and has the same spectrum as

Ψ below this scale, but with $\lesssim$1% of the amplitude [111]. The vector mode power spectrum we shall use in our analysis can be parameterised [111] as Eq. (2.117) . The amplitude of the vectors decays on scales smaller than the equality scale, $k > k_{\rm eq} \approx 0.073\,\Omega_{\rm m}h^2{\rm Mpc}^{-1}$, with the same scaling as Ψ. Assuming cosmological parameters as determined by Ref. [113], the power in the vector modes is well approximated by [111]

$$\mathcal{P}_V \approx 6.5\times10^{-5}\mathcal{P}_\Psi \quad \text{for} \quad k \gtrsim k_{\rm silk} \approx 0.09\,{\rm Mpc}^{-1}\,, \tag{2.119}$$

so that the amplitude of the metric vector perturbations is nearly 1% that of the metric scalar modes on small scales. In general, for a model without baryons, $\mathcal{P}_V \approx z_{\rm eq}^{-1}(5.49\,\Omega_{\rm m}h^2 - 0.13)^{2.33}\mathcal{P}_\Psi \sim (\ln k)^2/k^4$ for $k \gtrsim k_{\rm silk} \approx 0.09\,{\rm Mpc}^{-1}$. On large scales, $\mathcal{P}_V$ scales like k, with a peak in the spectrum around the equality scale (see Fig. 2.2 from [111]). In [116], the power spectrum of this frame-dragging effect was computed using high resolution N-body simulation. The results shown in Fig. 2.2 are consistent with those found in [116].

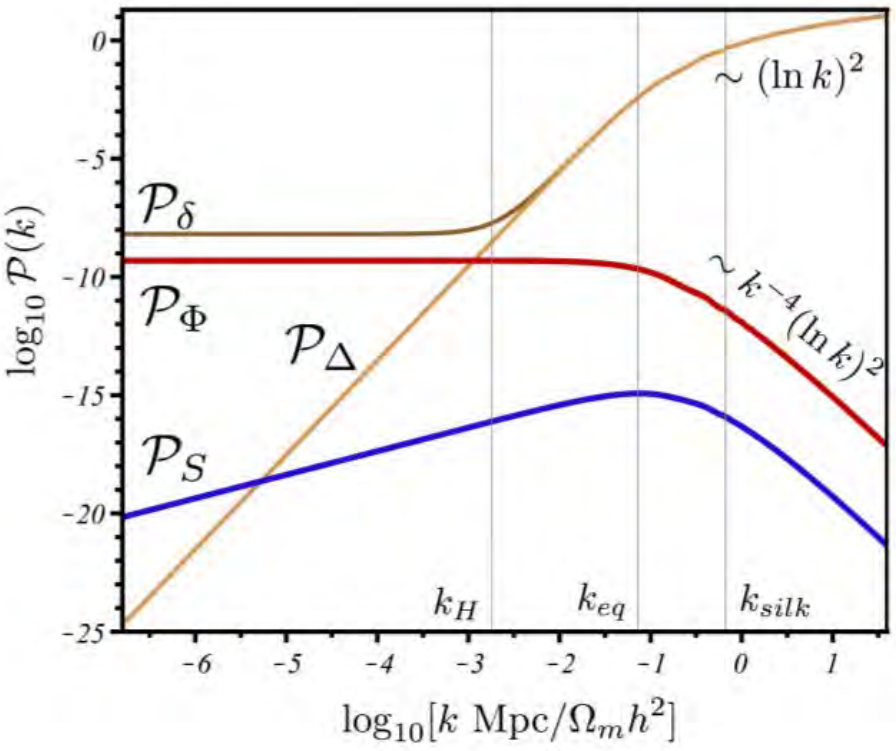

Figure 2.2: Today's power spectrum of the vector modes $\mathcal{P}_V$ (in the plot it is $\mathcal{P}_S$) as a function of wavenumber k. It is compared to other first order variable power spectrum, namely that of the density contrast $\mathcal{P}_\delta$, Bardeen potential $\mathcal{P}_\Psi$ ($\mathcal{P}_\Phi$ in the plot) and the comoving density perturbation, $\Delta = \delta - 3\mathcal{H}v$, $\mathcal{P}_\Delta$.

2.6 Second order induced tensor modes

Primordial gravitational waves are generated by initial quantum fluctuations during the inflationary phase of the Universe. Their detection which depends on their amplitude, fixed by the energy scale of inflation, will be a smoking gun of the exponential rapid expansion scenario in the early universe. At linear order in perturbation theory, the evolution equation of tensor perturbation, which we recall is gauge invariant, is given by the trace-free part of the $i-j$ components of EFEs

$$h''_{ij} + 2\mathcal{H}h_{ij} - \nabla^2 h_{ij} = 0, \tag{2.120}$$

where we have neglected the anisotropic stress and assumed flat universe. In either radiation or matter dominated era, the amplitude of the mode is constant and is damped while exhibiting oscillations as it enters the Hubble radius [98].

Previous works [81, 87] showed that gravity waves are also sourced at second order by primordial density fluctuations. These secondary modes, together with the vector modes and gravitational lensing, can induce B-modes type of the CMB polarization [87]. Another indirect probe of gravitational radiation, either primordial or secondary, is their effects on weak lensing which are responsible of the image rotation [117]. In [117] they showed that contribution of the secondary modes to the shear curl mode is larger than that of the primordial ones.

2.6.1 Tensor modes

For our purposes, we will mainly focus on the secondary modes generated by first order scalar modes. The second order tensor modes evolve according to

$$h''_{ij} + 2\mathcal{H}h'_{ij} - \nabla^2 h_{ij} = \Pi_{ij} \tag{2.121}$$

where the effective anisotropic stress arises from the contribution of non-linear scalar modes and is explicitely given by

$$\begin{aligned} \Pi_{ij} \equiv & \Big\{ -16\Psi\partial_i\partial_j\Psi - 8\partial_i\Psi\partial_j\Psi \\ & + \frac{4}{\mathcal{H}^2\Omega_{\rm m}}\left[\mathcal{H}^2\partial_i\Psi\partial_j\Psi + 2\mathcal{H}\partial_i\Psi\partial_j\Psi' + \partial_i\Psi'\partial_j\Psi'\right]\Big\}^{TT} \end{aligned} \tag{2.122}$$

where TT denotes a tensor projection [87]. In a similar way but without resorting to a tensor projector, the evolution equation of the second order tensor modes was obtained [81]

$$\nabla^2\nabla^2(h_{ij}''+2\mathcal{H}h_{ij}'-\nabla^2 h_{ij}) = \nabla^2\partial^k\partial_m R_k^m\delta_{ij}+2\nabla^2(\nabla^2 R_{ij}-\nabla_i\partial_k R_j^k-\partial^k\partial_j R_{ik})+\partial_i\partial_j\partial^k\partial_m R_k^m. \tag{2.123}$$

The trace-free tensor[2]

$$R_k^m = g^2\left(1+\frac{2E^2(z)f^2}{3\Omega_m(1+z)^3}\right)(\partial^m\Psi_0\partial_k\Psi_0-\frac{1}{3}(\nabla\Psi_0)^2\delta_k^m). \tag{2.124}$$

The solution of Eq. (2.123) is of the form [81]

$$h_{ij}(\boldsymbol{x},\eta) = \frac{40}{(2\pi)^3}\int\frac{d^3\boldsymbol{k}}{k^4}e^{i\boldsymbol{k}\cdot\boldsymbol{x}}\mathcal{S}_{ij}(\boldsymbol{k})\left(\frac{1}{3}-\frac{j_1(k\eta)}{k\eta}\right), \tag{2.125}$$

where j_1 stands for the $\ell=1$ spherical Bessel function and

$$\mathcal{S}_{ij} = \nabla^2\Theta_0\delta_{ij}+\partial_i\partial_j\Theta_0+2(\partial_i\partial_j\Psi_0\nabla^2\Psi_0-\partial_i\partial_k\Psi_0\partial^k\partial_j\Psi_0). \tag{2.126}$$

The quantity Θ_0 is given by

$$\Theta_0 = \frac{1}{2}\nabla^{-2}\Big[(\nabla^2\Psi_0)^2-\partial_i\partial_k\Psi_0\partial^i\partial^k\Psi_0\Big]. \tag{2.127}$$

2.6.2 Power spectrum

In Fourier space, the tensor perturbation h_{ij} has 2 independent degrees of freedom that can be decomposed as $+,\times$ polarisations as

$$h_{ij}(\boldsymbol{x},\eta) = \int\frac{\mathrm{d}^3\boldsymbol{k}}{(2\pi)^{3/2}}\sum_{\lambda=+,\times}h_\lambda(\boldsymbol{k},\eta)\varepsilon_{ij}^\lambda(\boldsymbol{k})\,\mathrm{e}^{\mathrm{i}\boldsymbol{k}\cdot\boldsymbol{x}}\,, \tag{2.128}$$

where ε_{ij}^λ is the polarisation tensor, satisfying $\varepsilon_{ij}^\lambda\delta^{ij}=\varepsilon_{ij}^\lambda k^i=0$ and $\varepsilon_{ij}^\lambda\varepsilon_{\lambda'}^{ij}=\delta_{\lambda'}^\lambda$. Again, power in each polarization states are identical, thanks to spatial isotropy, and are defined by

$$\langle h_\lambda^*(\boldsymbol{k},\eta)h_{\lambda'}(\boldsymbol{k}',\eta')\rangle = \frac{2\pi^2}{k^3}\delta^3(\boldsymbol{k}-\boldsymbol{k}')\mathcal{P}_h(k,\eta,\eta')\delta_{\lambda\lambda'},\ \ \lambda=+,\times, \tag{2.129}$$

[2]Again the relation $\Psi(\boldsymbol{x},\eta)=\Psi_0(\boldsymbol{x})g(\eta)$ has been used.

where $\mathcal{P}_h(k,\eta)$ is well approximated by [81, 117, 118]

$$\mathcal{P}_h(k,\eta) = \frac{6C\Delta^4_{\mathcal{R}} g_\infty}{25} \frac{k_* \left[1 - 3\frac{j_1(k\eta)}{k\eta}\right]}{k\left[1 + 7\frac{k_*}{k} + 5\left(\frac{k_*}{k}\right)^2\right]^3}, \tag{2.130}$$

where $C \sim 0.06$ for a scale-invariant spectrum and $k_* = \Omega_{\rm m} h^2 {\rm Mpc}^{-1}$. The second order gravitational wave background also peaks in power around the equality scale, and is surprisingly larger than its primordial background on these scales, as shown in Fig. 2.3(from [118]). The formula presented in Eq. (2.130), from Ref. [81], predicts an excess in power on small scales compared to the more accurate formula of Ref. [118], but is sufficiently accurate for our purposes (see Ref. [117] for a direct comparison).

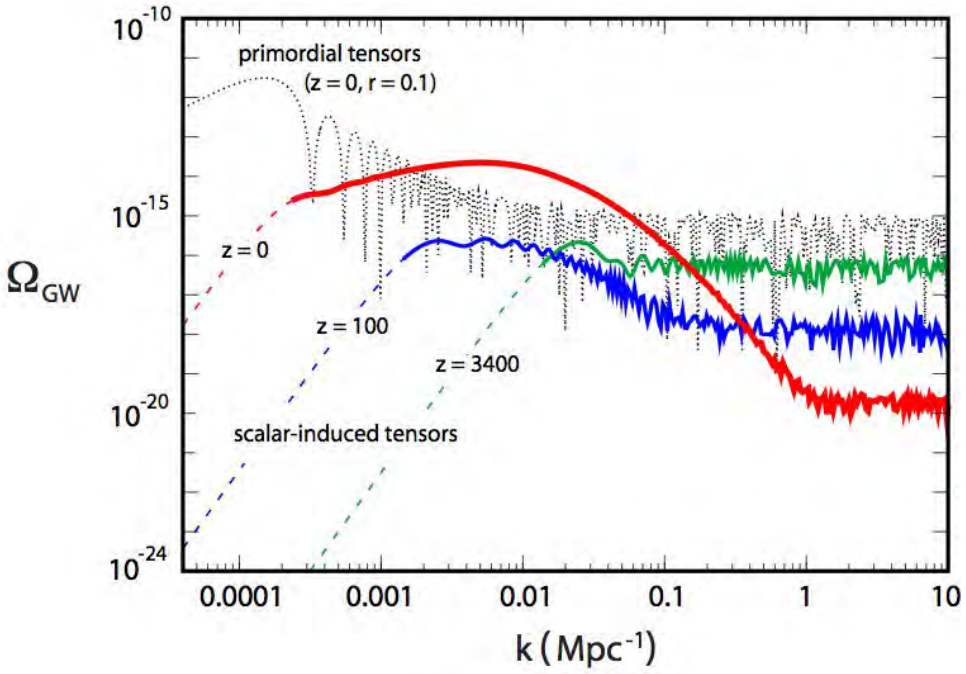

Figure 2.3: Comparing the power spectra of the primordial gravitational waves (grey dotted line) with those of the scalar-induced ones (solid lines).

In the following section, we will look at how perturbation theory is applied to understand cosmological phenomena, more precisely in our case it is weak gravitational lensing. We will first give a brief overview of gravitational lensing then derive the standard expression of the weak lensing convergence whose relativistic corrections and their applications, in later chapters, constitute the key results in this thesis.

2.7 Gravitational lensing

2.7.1 Introduction

One of the most astonishing predictions of Einstein's General Relativity is the bending of lights in the vicinity of a spherical massive body. Among the first tests of General relativity in solar system was the deflection of lights by the sun during solar eclipse. It was predicted that the deflection angle, also dubbed Einstein angle, is [119]

$$\hat{\alpha} = \frac{4GM}{c^2\xi}, \tag{2.131}$$

where M is the mass of the body and ξ is the impact parameter, assumed to be much larger than the Schwarzschild radius

$$R_S = \frac{2GM}{c^2}.$$

Gravitational lensing has many applications in astronomy and cosmology such as a powerful tool to infer the distribution of the lens object [120–122]. We will now see in the following section the basic equation of lensing.

2.7.2 Basics of lensing

Deflection angle

In optics, when a beam of relativistic particles propagates from one medium with a refractive index n_1 to another with a refractive index n_2, its speed decreases or increases depending on whether $n_1 < n_2$ or $n_1 > n_2$ respectively. The gravitational field induced by a massive body is related to refractive index [119]

$$n = 1 - \frac{2}{c^2}\Phi, \tag{2.132}$$

where Φ is the gravitational potential and c the speed of light. It is worth noting that for a potential well, $\Phi < 0$. This means that the effective refractive index is greater than 1, which thus implies that the speed of a beam of relativistic particles $v = c/n$ in the medium, to first order, is reduced compared to its speed in a free vacuum

$$v = c\left(1 + 2\frac{\Phi}{c^2}\right). \tag{2.133}$$

Due to its reduced speed when propagating through the gravitational field, the time at which the light arrives at the observer is delayed, as opposed to a light travelling through a vacuum. This delay is called Shapiro delay. As it passes through the gravitational field, the photon trajectory gets deflected by an amount [98, 123]

$$\boldsymbol{\alpha} = \frac{2}{c^2} \int \nabla_\perp \Phi \, dz, \tag{2.134}$$

which is a line of sight integral of the two dimensional gradient (in the plane perpendicular to the line of sight) of the gravitational potential. We note here that z denotes spatial coordinate alone the line of sight. Given the fact that in general the deflection is small, a Born approximation where the integral in Eq. (2.134) is evaluated along unperturbed trajectory, can be applied. For the case of a deflection induced by a point-like of mass M , the potential reads

$$\Phi = -\frac{GM}{\sqrt{b^2 + z^2}}, \tag{2.135}$$

where G is the gravitational constant and b the impact parameter. Thus

$$\nabla_\perp \Phi = \frac{GM\boldsymbol{b}}{(b^2 + z^2)^{3/2}}, \tag{2.136}$$

so that the deflection reads

$$\boldsymbol{\alpha} = \frac{4GM\boldsymbol{b}}{c^2 b^2}. \tag{2.137}$$

The interval $\Delta z \sim \pm b$ within which the deflection is the most important is very small with respect to the distance scale in the geometrical configuration. Therefore, one can consider the lens as thin such that a two dimensional mass distribution $\Sigma(\boldsymbol{\xi})$ which is a projection of the three dimensional mass distribution $\rho(\boldsymbol{\xi}, z)$ can be used. Thus [98, 119, 123]

$$\Sigma(\boldsymbol{\xi}) \equiv \int \rho(\boldsymbol{\xi}, z) \, \mathrm{d}z. \tag{2.138}$$

The total deflection at a position $\boldsymbol{\xi}$ induced by a mass distribution reads [119]

$$\vec{\alpha}(\boldsymbol{\xi}) = \frac{4G}{c^2} \int d^2\xi' \Sigma(\boldsymbol{\xi'}) \frac{\boldsymbol{\xi} - \boldsymbol{\xi'}}{|\boldsymbol{\xi} - \boldsymbol{\xi'}|^2} \tag{2.139}$$

Ray-tracing equation

A light ray is emitted by a source located at a distance D_S. As it feels the gravitational

field induced by a lens at a distance D_{OL}, its trajectory gets deflected by an amount α and finally arrives at the observer at an angle β. The observer sees the image of the source S at I as shown in Fig. 2.4 (from [98, 124]). In the small angle approximation we thus have that

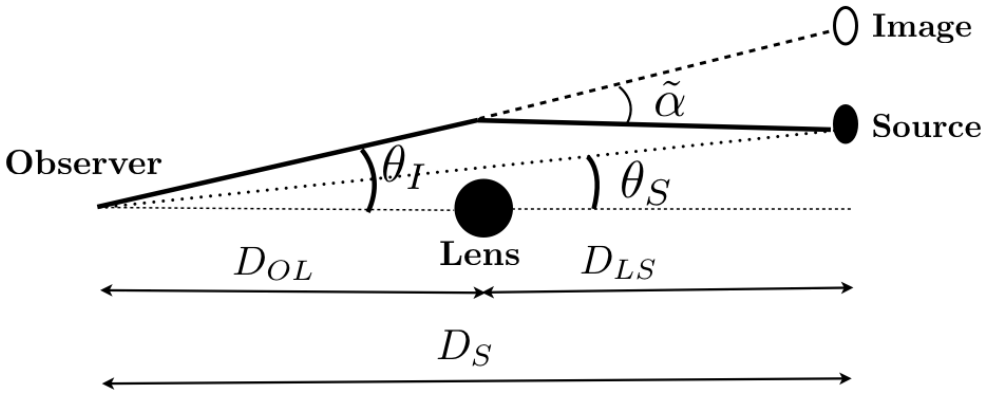

Figure 2.4: Geometrical configuration of gravitational lensing.

$$\boldsymbol{\theta}_I = \boldsymbol{\theta}_S + \tilde{\boldsymbol{\alpha}}\frac{D_{LS}}{D_S}. \tag{2.140}$$

The true position S of the source at the source plane is therefore given

$$\boldsymbol{\theta}_S = \boldsymbol{\theta}_I - \boldsymbol{\alpha}, \tag{2.141}$$

where we have used the reduced angle $\boldsymbol{\alpha} = \tilde{\boldsymbol{\alpha}}(D_{LS}/D_S)$. Eq .(2.141) is known as the *Lens equation*. The expression of the reduced angle $\tilde{\boldsymbol{\alpha}}$ can be expressed in terms of dimensionless surface mass density by introducing the critical mass density

$$\Sigma_c = \frac{c^2}{4\pi G}\frac{D_S}{D_{OL}D_{LS}}, \tag{2.142}$$

which yields

$$\vec{\alpha}(\boldsymbol{\theta}_I) = \frac{1}{\pi}\int d^2\boldsymbol{\theta}'_I \frac{\Sigma(\boldsymbol{\theta}'_I)}{\Sigma_c}\frac{\boldsymbol{\theta}_I - \boldsymbol{\theta}'_I}{|\boldsymbol{\theta}_I - \boldsymbol{\theta}'_I|^2}, \tag{2.143}$$

where we have used $\boldsymbol{\xi} = D_{OL}\boldsymbol{\theta}_I$. Exploiting the fact that [98, 125]

$$\nabla_{(2)}\ln \boldsymbol{\theta}_I = \frac{\boldsymbol{\theta}_I}{|\boldsymbol{\theta}_I|^2}, \tag{2.144}$$

where $\nabla_{(2)}$ is a two dimensional gradient, we can describe the reduced deflection angle as a

gradient of a potential $\boldsymbol{\alpha} = \nabla_{(2)}\psi$, such that

$$\psi = \frac{1}{\pi}\int d^2\boldsymbol{\xi}' \frac{\Sigma(\boldsymbol{\theta}'_I)}{\Sigma_c}\ln(|\boldsymbol{\theta}_I - \boldsymbol{\theta}'_I|) \tag{2.145}$$

Magnification and Distortion

The bending of light rays as they travel to the observer induces some distortion in the observed image of the source such that it is magnified or sheared. In lensing, there is no absorption or emission along the light paths so that the surface brightness of the source $I(\boldsymbol{\theta}_S)$ is conserved, therefore we have that

$$I(\boldsymbol{\theta}_I) = I[\boldsymbol{\theta}_S(\boldsymbol{\theta}_I)]. \tag{2.146}$$

By assuming a position $\boldsymbol{\theta}_I^0$ in the lens plane with its correspondence $\boldsymbol{\theta}_S(\boldsymbol{\theta}_I^0)$ in the source plane, the expansion at first order around $\boldsymbol{\theta}_I^0$ yields

$$I(\boldsymbol{\theta}_I) = I[\boldsymbol{\theta}_S^0 + \boldsymbol{\mathcal{A}}(\boldsymbol{\theta}_I^0)(\boldsymbol{\theta}_I - \boldsymbol{\theta}_S^0)], \tag{2.147}$$

in which $\boldsymbol{\theta}_S^0 = \boldsymbol{\theta}_S(\boldsymbol{\theta}_I^0)$ and the distortion matrix $\boldsymbol{\mathcal{A}}$

$$\boldsymbol{\mathcal{A}}(\boldsymbol{\theta}_I) \equiv \frac{\partial \boldsymbol{\theta}_S}{\partial \boldsymbol{\theta}_I}. \tag{2.148}$$

Introducing the delfecting potential ψ we have

$$\mathcal{A}_{ij} = \delta_{ij} - \frac{\partial^2\psi}{\partial\theta_i\partial\theta_j}. \tag{2.149}$$

This Jacobian matrix is symmetric and can be expressed as a function of the convergence κ and the two components of the shear $\gamma = \gamma_1 + \mathrm{i}\gamma_2$ [8, 98]

$$\mathcal{A}_{ij} = \begin{pmatrix} 1-\kappa-\gamma_1 & -\gamma_2 \\ -\gamma_2 & 1-\kappa+\gamma_1 \end{pmatrix}. \tag{2.150}$$

We therefore have that $\gamma_1 = (\partial_1\partial_1\psi - \partial_2\partial_2\psi)/2$ and $\gamma_2 = \partial_1\partial_2\psi$. It is noted that the order of magnitude of the distortion is a function of the dimensionless surface mass density Σ/Σ_c. In the case $\Sigma/\Sigma_c > 1$, we deal with strong lensing where the background sources appear as

giant luminous arcs or have multiple images whereas if $\Sigma/\Sigma_c < 1$ we deal with weak lensing in which the distortion is not prominent. The magnification μ which is the ratio between the flux of the source image and that of the unlensed source is expressed as the inverse of the determinant of the distortion matrix $\boldsymbol{\mathcal{A}}$

$$\mu = \frac{1}{\det \boldsymbol{\mathcal{A}}}, \tag{2.151}$$

giving

$$\mu = \frac{1}{(1-\kappa)^2 - |\gamma|^2}. \tag{2.152}$$

In the case of weak lensing regime where the convergence and shear are small, we have the approximation $\mu \simeq 1 + 2\kappa$. In this thesis, we are mainly interested in weak lensing regime, the interested readers may refer to [119,125] for a rigorous treatment of gravitational lensing.

2.7.3 Weak lensing

Geometry of a ray bundle

In order to analyse infinitesimal deformation in a light bundle, one has to derive the evolution equation of the geodesic deviation $\mathcal{E}^\mu$ between two neighbouring geodesics in the congruence. Any geodesic in a light bundle can be written as a function of a geodesic chosen as a reference and a connecting vector $\mathcal{E}^\mu$ describing how far from the reference geodesic the arbitrary one is [98]

$$x^\mu(\lambda) = \bar{x}^\mu(\lambda) + \mathcal{E}^\mu(\lambda), \tag{2.153}$$

where λ is an affine parameter assumed to be zero at the observer where the light bundle from the source focuses. We can now define a coordinate system at the observer such that we have the null vector $k^\mu \equiv d\bar{x}^\mu/d\lambda$, which is tangent to the null geodesic and subject to $k^\mu k_\mu = 0$, $k^\nu \nabla_\nu k^\mu = 0$, the observer four-velocity u^μ with $u^\mu u_\mu = -1$ and finally a two dimensional plane perpendicular to the line of sight characterized by the basis vectors n_1^μ, n_2^μ with the constraints $n_\mu^1 n_2^\mu = \delta_2^1$, $n_a^\mu k_\mu = n_a^\mu u_\mu = 0$. The deviation is now decomposed as [98, 125]

$$\mathcal{E}^\mu = \mathcal{E}_0 k^\mu + \mathcal{E}_1 n_1^\mu + \mathcal{E}_2 n_2^\mu, \tag{2.154}$$

where $\mathcal{E}_0$ can be set to zero. The evolution equation of the connecting vector $\mathcal{E}^\mu$ is given by

the geodesic deviation equation

$$\frac{d^2\mathcal{E}^\mu}{d\lambda^2} = R^\mu_{\nu\alpha\beta}k^\nu k^\alpha \mathcal{E}^\beta. \tag{2.155}$$

Introducing the optical tidal matrix $\mathcal{R}$ while exploiting Eq. (2.154)

$$\frac{d^2\boldsymbol{\mathcal{E}}}{d\lambda^2} = \boldsymbol{\mathcal{R}}\cdot\boldsymbol{\mathcal{E}}, \tag{2.156}$$

where $\boldsymbol{\mathcal{E}}$ represents the component of $\mathcal{E}^\mu$ in the basis vectors $n^u_a (a = 1, 2)$ and $\boldsymbol{\mathcal{R}} = \mathcal{R}^b_a = R^\mu_{\nu\alpha\beta}k^\nu k^\alpha n_{a\mu}n^{b\beta}$. The linear property of the geodesic equation assures [98, 125]

$$\boldsymbol{\mathcal{E}}(\lambda) = \boldsymbol{\mathcal{D}}\cdot\boldsymbol{\theta},\ \frac{d\boldsymbol{\mathcal{E}}}{d\lambda} = \boldsymbol{\theta}, \tag{2.157}$$

$\boldsymbol{\mathcal{D}}$ being a 2×2 matrix whose propagation equation is obtained from the condition $\mathcal{E}(\lambda = 0) = 0$ and Eq. (2.156)

$$\frac{d^2\boldsymbol{\mathcal{D}}}{d\lambda^2} = \boldsymbol{\mathcal{R}}\cdot\boldsymbol{\mathcal{D}}, \tag{2.158}$$

with the initial conditions $\boldsymbol{\mathcal{D}}(0) = 0$ and $d\boldsymbol{\mathcal{D}}/d\lambda(0) = \boldsymbol{I}$, $\boldsymbol{I}$ being the 2×2 identity matrix. The mapping between the angular position of the image $\boldsymbol{\theta}$ and that of the source $\boldsymbol{\theta}_S$, $\boldsymbol{\theta}_S = \boldsymbol{\mathcal{A}}\cdot\boldsymbol{\theta}$ and the definition of the angular diameter distance $\boldsymbol{\theta}_S = \boldsymbol{\mathcal{E}}(\lambda_S)/D_A(\lambda_S)$, which relates the displacement vector $\boldsymbol{\mathcal{E}}(\lambda_S)$ at the source plane to the angular position of the source $\boldsymbol{\theta}_S$, yield

$$\boldsymbol{\mathcal{A}} = \frac{\boldsymbol{\mathcal{D}}(\lambda_S)}{D_A(\lambda_S)}. \tag{2.159}$$

We are now in position to derive the expression of the distortion matrix, depending on the cosmological model we choose.

Light propagation in a lumpy universe

In this section, we will derive the expression of the cosmic convergence in a Friedmann-Robertson-Walker universe based on the evolution equation of $\mathcal{D}$ (Eq. (2.158)) we obtained in the previous section. Given that the optical tidal matrix $\boldsymbol{\mathcal{R}}^{(0)}$ is related to the curvature K of the three space at zeroth order, Eq. (2.158) takes a more convenient form [98, 125]

$$\frac{d^2\boldsymbol{\mathcal{D}}^{(0)}}{d\lambda^2} = -K\boldsymbol{\mathcal{D}}^{(0)}, \tag{2.160}$$

whose zeroth order solution reads [98]

$$\boldsymbol{\mathcal{D}}^{(0)}(\lambda) = f_K(\lambda)\boldsymbol{I}, \tag{2.161}$$

leading to $\boldsymbol{\mathcal{A}}^{(0)} = \boldsymbol{I}$. $f_K(\lambda) = \lambda$ for a flat universe. At first order we get [98]

$$\frac{d^2\boldsymbol{\mathcal{D}}(\lambda)}{d\lambda^2} = -K\boldsymbol{\mathcal{D}}(\lambda) + \lambda\boldsymbol{\mathcal{R}}(\lambda), \tag{2.162}$$

with the solution

$$\boldsymbol{\mathcal{D}}(\lambda) = \int_0^\lambda \lambda'(\lambda - \lambda')\boldsymbol{\mathcal{R}}(\lambda')d\lambda'. \tag{2.163}$$

Therefore the distortion matrix reads

$$\boldsymbol{\mathcal{A}}(\lambda) = \int_0^\lambda \frac{\lambda'(\lambda - \lambda')}{\lambda}\boldsymbol{\mathcal{R}}(\lambda')d\lambda'. \tag{2.164}$$

At first order in perturbation in Longitudinal gauge where the two Bardeen potential are equal, the optical matrix is

$$\mathcal{R}_{ab} = -2\nabla_a\nabla_b\Phi, \tag{2.165}$$

leading to [98, 119, 125, 126]

$$\mathcal{A}_{ab} = \delta_{ab} - \nabla_a\nabla_b\psi, \tag{2.166}$$

where ψ denotes the deflecting potential

$$\psi(\boldsymbol{n}, \chi) = \frac{2}{c^2}\int_0^\chi \frac{\chi'(\chi - \chi')}{\chi}\Phi(\boldsymbol{n}, \chi')d\chi', \tag{2.167}$$

in which we have made the substitution $\lambda = -\chi$ on the past light-cone. On the scale of interest, it is usual to approximate the transverse Laplacian Δ_2 by the three dimensional counterpart ∇^2, enabling us to substitute the density contrast into Eq. (2.167) via the Poisson's equation. Thus, we finally obtain the expression of the cosmic convergence κ

$$\kappa(\boldsymbol{n}, \chi) = \frac{3H_0^2\Omega_{m0}}{2c^2}\int_0^\chi \frac{\chi'(\chi - \chi')}{\chi}\frac{\delta(\boldsymbol{n}, \chi')}{a(\chi')}d\chi', \tag{2.168}$$

Ω_{m0} is the matter density parameter today. It is noted that in what follows, unless otherwise stated, we will use $c = 1$.

2.7.4 Power spectra

When computing the power spectrum of the effective convergence, one usually starts with the expression of the deflecting potential integrated along the line of sight, also known as the lensing potential averaged over sources

$$\psi(n^i) = 2\int_0^\infty \hat{g}(\chi)\Phi[\chi' n^i, \chi']d\chi, \tag{2.169}$$

where $\boldsymbol{n}$ is the direction of observation, $\hat{g}(\chi)$ is the lensing geometry which is a weighting function that accounts for the distribution of the sources for a given survey. One carries out the computations by expanding the quantity either in spherical harmonics, full-sky case or in Fourier modes, the flat-sky approximation.

Full-sky expression

While the detailed derivation of the full-sky case will be presented in Chapter 3 we will just outline here the main steps. Expanding ψ in spherical harmonic yields

$$\psi(\boldsymbol{n}) = \sum_{\ell m} \psi_{\ell m} Y_{\ell m}(\boldsymbol{n}). \tag{2.170}$$

The angular power spectrum $C_\ell^{\psi\psi}$ of the variable ψ is defined

$$\langle \psi_{\ell m} \psi^*_{\ell' m'} \rangle = C_\ell^{\psi\psi} \delta_{\ell\ell'} \delta_{mm'}. \tag{2.171}$$

The angular power spectrum of the effective convergence is computed exploiting the relationship

$$\kappa(\boldsymbol{n}) = \frac{1}{2}\Delta_2 \psi(\boldsymbol{n}) \tag{2.172}$$

where Δ_2 denotes the two dimensional Laplacian. Thus

$$\kappa_{\ell m} = -\frac{\ell(\ell+1)}{2}\psi_{\ell m}. \tag{2.173}$$

And we finally have that

$$C_\ell^{\kappa\kappa} = \frac{\ell^2(\ell+1)^2}{4} C_\ell^{\psi\psi} \tag{2.174}$$

We will now look at the same derivation in the flat-sky case.

Flat-sky approximation

For the case of the standard lensing convergence, the flat-sky approximation is reasonably good as the background sources are far from the observer. In this case the quantity ψ is then expanded in Fourier modes

$$\psi(\boldsymbol{n}) = \int \frac{d^2\ell}{2\pi}\psi(\boldsymbol{\ell})\mathrm{e}^{i\boldsymbol{\ell}\cdot\boldsymbol{n}}, \tag{2.175}$$

and the power spectrum P_ψ is defined

$$\langle\psi(\boldsymbol{\ell})\psi^*(\boldsymbol{\ell}')\rangle = P_\psi(\ell)\delta^{(2)}(\boldsymbol{\ell}-\boldsymbol{\ell}'). \tag{2.176}$$

Introducing the deflecting potential Φ in Eq. (2.175) gives

$$\psi(\boldsymbol{n}) = \int_0^\chi 2\hat{g}(\chi)\int \frac{d^3\boldsymbol{k}}{(2\pi)^{3/2}}\Phi(\boldsymbol{k},\eta)\mathrm{e}^{i\chi\boldsymbol{k}_\perp\cdot\boldsymbol{n}}\mathrm{e}^{ik_\parallel\chi}\mathrm{d}\chi\ , \tag{2.177}$$

where we have used $(\boldsymbol{x}_\parallel,\boldsymbol{x}_\perp) = (\chi,\chi n^i)$ and split the wavenumber into its two components $\boldsymbol{k} = (k_\parallel,\boldsymbol{k}_\perp)$. By setting $\boldsymbol{\ell} = \chi\boldsymbol{k}_\perp$ we get

$$\psi(\boldsymbol{n}) = \int_0^\chi 2\hat{g}(\chi)d\chi\int(2\pi)\frac{d^2\boldsymbol{k}_\perp}{(2\pi)}\frac{dk_\parallel}{(2\pi)^{3/2}}\Phi(\boldsymbol{k},\eta)\mathrm{e}^{i\boldsymbol{\ell}\cdot\boldsymbol{n}}\mathrm{e}^{ik_\parallel\chi}. \tag{2.178}$$

We now eliminate $\boldsymbol{k}_\perp$ in favour of $\boldsymbol{\ell}$ such that

$$\psi(\boldsymbol{n}) = \int\frac{d^2\boldsymbol{\ell}}{2\pi}\left[2\pi\int_0^\chi 2\frac{\hat{g}(\chi)}{f_K^2(\chi)}d\chi\frac{dk_\parallel}{(2\pi)^{3/2}}\Phi(\boldsymbol{k},\eta)\mathrm{e}^{ik_\parallel\chi}\right]\mathrm{e}^{i\boldsymbol{\ell}\cdot\boldsymbol{n}}\ . \tag{2.179}$$

Therefore we have

$$\psi(\boldsymbol{\ell}) = 4\pi\int_0^\chi\frac{\hat{g}(\chi)}{f_K^2(\chi)}d\chi\frac{dk_\parallel}{(2\pi)^{3/2}}\Phi(\boldsymbol{k},\eta)\mathrm{e}^{ik_\parallel\chi}. \tag{2.180}$$

The power spectrum reads [98]

$$\langle\psi(\boldsymbol{\ell})\psi^*(\boldsymbol{\ell}')\rangle \;=\; \frac{8\pi^2}{\ell^3}\int_0^\chi\hat{g}^2(\chi)\chi\mathcal{P}_\Phi\left(\frac{\ell}{\chi},\chi\right)d\chi\delta^{(2)}\left(\boldsymbol{\ell}-\boldsymbol{\ell}'\right)\ , \tag{2.181}$$

where

$$\langle\Phi(\boldsymbol{k},\eta)\Phi^*(\boldsymbol{k}',\eta')\rangle = \frac{2\pi^2}{k^3}\mathcal{P}_\Phi(k,\eta,\eta')\delta^{(3)}(\boldsymbol{k}-\boldsymbol{k}')\ .$$

To arrive at Eq. (2.181) we have used a Limber approximation such that on small scales it is the component of the wavenumber that is perpendicular to the line of sight that mainly

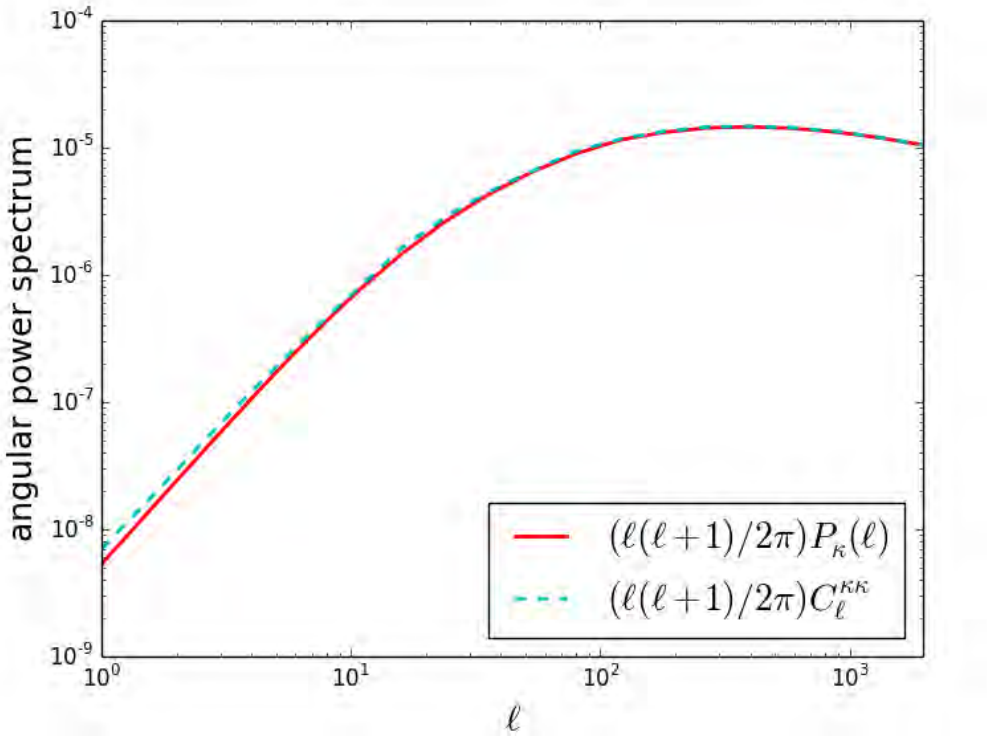

Figure 2.5: Angular power spectra as a function of multipole ℓ. The cyan dashed represents the full-sky expression $C_\ell^{\kappa\kappa}$ and the red solid is the flat-sky approximation $P_\kappa(\ell)$.

carries the power, therefore $k \sim k_\perp = \ell/\chi$. Using $\kappa(\boldsymbol{\ell}) = (1/2)\ell^2\psi(\boldsymbol{\ell})$, we finally have the expression of the power spectrum of the effective convergence

$$P_\kappa(\ell) = 2\pi^2\ell \int_0^\chi \hat{g}^2(\chi)\chi\mathcal{P}_\Phi\left(\frac{\ell}{\chi}, \chi\right) d\chi. \tag{2.182}$$

It is noted that on small scales (large ℓ) $C_\ell^{\kappa\kappa} = P_\kappa(\ell)$ (see Fig. 2.5).

Chapter 3
Non-linear relativistic contributions to the cosmological weak-lensing convergence

---

This chapter is based on the paper published in a peer-reviewed journal *JCAP*.

3.1 Introduction

Relativistic corrections to the standard model of cosmology come in a variety of forms, from the altering the dynamics of structure formation to the various effects associated to the interpretation of observations, in particular modifying the propagation of light. There has been considerable debate as to the importance and amplitude of these effects on the dynamics of the expansion of the universe and the growth of large scale structure (see, e.g., ref. [127] for an overview), and the amplitude and importance of these dynamical effects are still actively debated [128–145]. Though subdominant for linear structure formation, relativistic corrections are a generic prediction of General Relativity and are inevitable at a non-linear level through mode-mode coupling. The scalar gravitational potential induces rotational frame-dragging modes in spacetime (so-called vector modes) as well as gravitational waves (tensor modes). Neither of these have counterparts in Newtonian gravity as they both induce a non-zero magnetic Weyl curvature which is absent in Newtonian gravity and difficult to take into account in N-body numerical simulations [116, 146]. They therefore serve as an important tool in understanding purely relativistic aspects of structure formation and its observational consequences, as they set a lower limit on the amplitude of relativistic corrections. On top of dynamical corrections, relativistic effects also induce corrections to the propagation of light since it probes the complete spacetime geometry. This can alter the interpretation of cosmological observations at a level that cannot be neglected in an era of "precision cosmology". Provided one works within perturbation theory, the amplitude of these effects is computable

and completely fixed once the normalisation of the scalar power spectrum, at the linear level, is determined. For instance, some relativistic effects have been taken into account on the cosmic microwave background [147–150] and shown to be below the constraints on non-Gaussianity derived by Planck [151], but nevertheless in principle detectable on small angular scales, in particular through spectral distortions [152, 153]. This Chapter focuses on the effect of relativistic corrections on weak lensing observations, focusing mainly on the induced vector mode background. Weak gravitational lensing by the large-scale structure of the Uni- verse has now become a major tool of cosmology [125,154], used to study questions ranging from the distribution of dark matter to tests of general relativity [155,156]. The propagation of light in an inhomogeneous universe gives rise to both distortion and magnification induced by gravitational lensing. The effect of non-linear corrections on the Hubble diagram have been considered [77, 78, 157, 158] and shown to be non-negligible given the accuracy of contemporary observations [89,159–162]. Previous works considered the contributions of the vector metric perturbations to the shear and magnification using standard rulers [163, 164]. In this Chapter we consider the effect on the weak lensing convergence of non-linear effects that induce the existence of a vector and tensor modes background. We compare this to the various contributions to the convergence at first-order — the usual integral of the density contrast along the line of sight [125, 154], the contribution from the Doppler effect which is dominant at low redshifts and large scales [88, 89, 165], the Integrated Sachs-Wolfe (ISW) and Sachs-Wolfe (SW) terms which are relatively small and mainly neglected when computing cosmic convergence. The induced background of gravitational waves from scalar-scalar coupling was presented in ref. [87] during the radiation era, and its present-day spectrum calculated in ref. [118], with shear lensing effects studied in ref. [117], all following the pioneering analysis of ref. [81]. Surprisingly it was found that the induced gravitational wave background is significantly larger than any primordial background (even for a tensor-scalar ratio r $\sim$ 0.1) on intermediate scales of $\sim$ 100 Mpc, which is around the equality scale, though of course it is much smaller on small scales. Similarly, the induced vector mode background was presented in refs. [86, 111], and again a spectrum was found that peaks on 100 Mpc scales. Remarkably, however, it was found that the amplitude of the background of vector modes for the metric potential behaves on small scales with the same scaling as the gravitational potential, with nearly 1% of its amplitude. While both of these induced degrees of freedom have little effect on the dynamics of structure formation (they cannot directly source the density fluctuation as it is a scalar degree of freedom) they can influence the gravitational lensing produced by large-scale structure. Is it significant, and could it be a new way to detect relativistic aspects of structure formation? The effects of these contributions on weak lensing convergence predictions are computed in order to understand if

they can either be detected or, in the worst case, bias the analysis of future weak lensing experiments, such as Euclid or SKA; i.e., if the interpretation of the observation by assuming that the observed convergence corresponds to the convergence sourced by scalar modes only is an accurate enough assumption or whether some of these effects have to be included in the analysis. This part of the thesis addresses this question and computes the effect of these two non-linear effects on weak lensing observations by considering second order vector and tensor background. We restrict our analysis to the direct contribution from the dynamically induced vector modes and the hypothesis that the Born approximation still holds. In principle, one needs also to take into account second order effects on the geodesic deviation equation [166–170], as fully described in refs. [171, 172]. The calculations by relaxing the Born approximation will induce small changes to the signal. However, there are of course a variety of other geometrical effects which may dominate the signal [77, 78, 158] but our goal in this study is to investigate the convergence from dynamical effects only. In section 3.2 we describe how we account for non-linearities in the power spectra of both the scalar and vector modes and then, in section 3.3, the computation of the weak lensing power spectra, splitting the effects of the scalar, vector, tensor, Doppler, ISW and SW contributions in order to compare their magnitude. Since the contribution of the tensor modes remains negligible and both ISW and SW being relatively small, we focus in section 3.4 on the vector and Doppler contribution, estimating their magnitude in surveys such as Euclid and SKA. Some technical details about the velocity term, ISW and SW are gathered in appendices B.1,B.2, B.3.

3.2 Preliminaries

In the standard cosmological framework, the initial conditions set by inflation impose that at the linear order only scalar perturbations are significantly sourced. At late times, we can neglect the anisotropic stress of matter (mostly described by a pressure-free fluid on cosmological scales) and the spatial curvature (so that we assume that the spatial sections are Euclidean). We use the transfer function derived in Ref. [112] to model the linear transfer function, and make use of Halofit [173] to estimate nonlinear small scale effects. Due to non-linear evolution, the growth suppression factor becomes scale dependent as

$$g_{\rm nl}(\chi, k) = (z+1)\sqrt{\frac{P_{\rm nl}(\chi, k)}{P(k)}}. \tag{3.1}$$

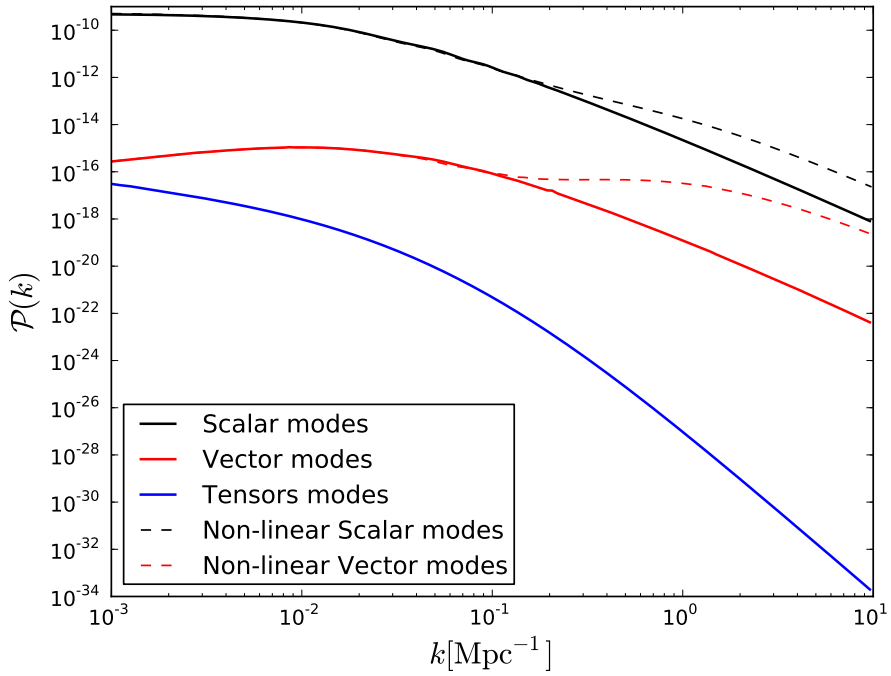

Figure 3.1: The power spectra of scalar (black line), vector (red line) and tensor (blue line) as a function of the comoving wavenumber k. Solid curves correspond to spectra computed assuming linear scalar modes at first-order, and the dotted curves include power from small-scale clustering estimated from Halofit.

We then use this growth suppression factor to account for the non-linearities. Since non-linear evolution occurs at small scales (large k), $g_{\rm nl}(\chi, k)$ behaves as the linear $g(\chi)$ which is k independent on large scales (k small). $P_{\rm nl}(\chi, k)$ and $P(k)$ are the non-linear matter power spectrum and today's linear matter power spectrum respectively. The small-scale behaviour of the second order vector modes can be estimated by replacing the linear transfer function with that given by Halofit in Eq (3.1), which is depicted on Fig. 3.1. This gives a more realistic estimation of the relativistic vector modes on small scales. We show in Fig. 3.1 the power spectra of the scalar (Eq. (2.100)), vector (Eq. (2.117)) and tensor modes (Eq. (2.130)) assuming a flat ΛCDM background universe with $\Omega_{\rm m}h^2 = 0.1326$, $\Omega_{\rm b}h^2 = 2.263 \times 10^{-2}$ and $h = 0.719$ as derived from the WMAP5 best fit model [113].

3.3 Weak lensing convergence and power spectra

3.3.1 Generalities

In the standard lore, the dominant contribution to weak lensing comes from the deflecting potential ϕ along a line of sight in the direction n^i (see *e.g.*, Refs. [85, 119, 125, 174]),

$$\phi = \Phi + \Psi + V_i n^i + h_{ij} n^i n^j \ , \tag{3.2}$$

which can be decomposed in contributions arising from the scalar-vector-tensor perturbations of the metric as

$$\phi = \phi_{_S} + \phi_{_V} + \phi_{_T}, \tag{3.3}$$

with $\phi_{_S} = \Phi + \Psi$, $\phi_{_V} = V_i n^i$ and $\phi_{_T} = h_{ij} n^i n^j$.

The distortion of the shape of background galaxies is described by the Sachs equation [98, 119, 125] in terms of a Jacobi matrix that can be rescaled, as long as the background spacetime is spatially homogeneous and isotropic [126], to define the amplification matrix $\mathcal{A}_{ab}$ (Eq. (2.166)), where the indices refer to the angle coordinates of a unit 2-sphere. From the decomposition of the amplification matrix in term of a convergence κ and a shear (γ_1, γ_2) in Eq. (2.150) we deduce that

$$\kappa(n^i, \chi) = \frac{1}{2} \nabla_\perp^2 \psi(n^i, \chi) \, , \tag{3.4}$$

where $\nabla_\perp^2$ is the 2-dimensional Laplacian on the unit 2-sphere. The previous expression (Eq. (3.4)) gives the convergence for a single source located at a radial distance χ, or similarly at a redshift z. However, observations usually deal with the convergence averaged over a source distribution n_s,

$$\kappa(n^i) = \int_0^\infty n_s(\chi) \kappa(n^i, \chi) d\chi \, , \tag{3.5}$$

where the upper limit of infinity is taken to mean well beyond the source distribution, or the horizon scale. Note that such an averaging over the source distribution is not mandatory if one has distance information about each bin of sources. Using the fact that $\int_0^\infty d\chi \int_0^\chi d\chi'$ is equivalent to integrate as $\int_0^\infty d\chi' \int_{\chi'}^\infty d\chi$ we obtain, after exchanging χ and χ', the expression

$$\kappa(n^i) = \frac{1}{2} \nabla_\perp^2 \int_0^\infty \hat{g}(\chi) \phi[f_K(\chi') n^i, \chi'] d\chi \tag{3.6}$$

with

$$\hat{g}(\chi) = \frac{1}{f_K(\chi)} \int_\chi^\infty n_s(\chi') \frac{f_K(\chi' - \chi)}{f_K(\chi')} d\chi' \ . \tag{3.7}$$

We recall from Eq. (2.169) that

$$\psi(n^i) = 2\int_0^\infty \hat{g}(\chi)\phi[f_K(\chi')n^i, \chi']d\chi, \tag{3.8}$$

and by substituting it into Eq. (3.6), we have

$$\kappa(n^i) = \frac{1}{2}\nabla_\perp^2\psi(n^i)\,. \tag{3.9}$$

The geodesic bundle propagates in the perturbed spacetime, which induces a correction of the redshift of the source, compared to the background redshift. Correcting the redshift in turn corrects the distance to the source, and so adds to the convergence. This affects only the convergence but not the shear (at linear order). Taking into account this effect induces three extra terms at first-order for the convergence: the Sachs-Wolfe and Integrated Sachs-Wolfe terms and a Doppler lensing term (Refs. [76, 88, 165]). The SW and ISW contributions are

$$\kappa_{\rm sw}(n^i,\chi) = \left(2 - \frac{1}{\mathcal{H}\chi}\right)\Phi(n^i,\chi), \tag{3.10}$$

$$\kappa_{\rm isw}(n^i,\chi) = 2\left(1 - \frac{1}{\mathcal{H}\chi}\right)\int_0^\chi d\chi'\,\Phi'(n^i,\chi') - \frac{2}{\chi}\int_0^\chi d\chi'\,\Phi(n^i,\chi'). \tag{3.11}$$

The Doppler contribution, in a spatially Euclidean background, is

$$\kappa_v(n^i,\chi) = -\left[1 - \frac{1}{\chi\mathcal{H}(\chi)}\right]n^i v_i\,, \tag{3.12}$$

for $\boldsymbol{n}$ pointing in the direction of observation, and with v_i given by

$$v_i(\eta,\boldsymbol{x}) = -\frac{2a}{3\Omega_m H_0^2}\partial_i(\Phi' + \mathcal{H}\Phi). \tag{3.13}$$

This contribution to the convergence was first identified in [76, 88], and investigated in more detail in [89, 165]. Note that when using these formula, the comoving distance to a source χ should be calculated from the background distance-redshift relation using the observed redshift (and not the unphysical background redshift).

3.3.2 Different contributions to the convergence

As discussed in § 5.2.1, we have 3 contributions to the convergence that arise from the scalar, vector and tensor contributions to Eqs. (3.2-3.3), to which we need to add the two Sachs-Wolfe terms and an important first-order contribution induced by the Doppler effect [88].

It follows that the observed weak lensing convergence has 4 contributions given by:

at first-order

$$\kappa_{_S}(n^i) = \frac{1}{2}\nabla_\perp^2 \int_0^\infty d\chi\, \hat{g}(\chi) \left[\Phi(n^i,\chi) + \Psi(n^i,\chi)\right] \quad , \tag{3.14}$$

$$\kappa_v(n^i) = \int_0^\infty d\chi\, n_s(\chi) \left[\frac{1}{\chi\mathcal{H}(\chi)} - 1\right] n_i v^i(n^i,\chi) \tag{3.15}$$

$$\kappa_{\rm sw}(n^i) = \int_0^\infty d\chi n_s(\chi) \left(2 - \frac{1}{\mathcal{H}\chi}\right) \Phi(n^i,\chi) \tag{3.16}$$

$$\kappa_{\rm isw}(n^i) = 2\int_0^\infty d\chi\ \hat{g}_{\rm isw1}(\chi)\Phi'(n^i,\chi) - 2\int_0^\infty d\chi \hat{g}_{\rm isw2}(\chi)\Phi(n^i,\chi), \tag{3.17}$$

where

$$\hat{g}_{\rm isw1} = \left(1 - \frac{1}{\mathcal{H}\chi}\right) \int_\chi^\infty d\chi' n_s(\chi')$$

$$\hat{g}_{\rm isw2} = \frac{1}{\chi} \int_\chi^\infty d\chi' n_s(\chi')$$

and *at second-order*

$$\kappa_{_V}(n^i) = \frac{1}{2}\nabla_\perp^2 \int_0^\infty d\chi\, \hat{g}(\chi) n_i V^i(n^i,\chi)\,, \tag{3.18}$$

$$\kappa_{_T}(n^i) = \frac{1}{2}\nabla_\perp^2 \int_0^\infty d\chi\, \hat{g}(\chi) n_i n_j h^{ij}(n^i,\chi)\,. \tag{3.19}$$

At second-order in vector and tensor modes, there are also the counterparts of the correction terms given in Eqs. (3.15),(3.16),(3.17) (see Refs. [77, 78]) but we are not considering them in this analysis. As already mentioned, we are only taking into account the dynamically induced vector modes. Note also that in these expressions, the variables are evaluated along the light cone and considered as function of the radial distance χ and the angular position n^i only. Given a source distribution, the left-hand side are purely function of position on the sky.

3.3.3 Expression of the power spectra

Given the previous expressions, one can deduce the angular power spectra of these different contributions to the convergence. To that purpose, we decompose each variable in spherical harmonics. For each contribution, the deflecting potential can be expanded as

$$\psi(\boldsymbol{n};\chi) = \sum_{\ell m} \psi_{\ell m}(\chi) Y_{\ell m}(\boldsymbol{n})\,, \tag{3.20}$$

where $\boldsymbol{n}$ is the position on the celestial 2-sphere, for a source located at χ. Taking into account spatial isotropy, its angular power spectrum is defined as

$$\langle \psi_{\ell m}(\chi)\psi^*_{\ell' m'}(\chi')\rangle = C_\ell^{\psi\psi}(\chi,\chi')\delta_{\ell\ell'}\delta_{mm'}\,. \tag{3.21}$$

Given Eq. (3.9), the coefficients of the expansion of the convergence are related to the $\psi_{\ell m}$ by

$$\kappa_{\ell m} = -\tfrac{1}{2}\ell(\ell+1)\psi_{\ell m}\,, \tag{3.22}$$

which implies that the angular power spectra of the cosmic convergence and deflecting potential are related by

$$C_\ell^{\kappa\kappa} = \tfrac{1}{4}\ell^2(\ell+1)^2 C_\ell^{\psi\psi}\,. \tag{3.23}$$

The power spectra are related to the real space angular correlation function,

$$C^{\psi\psi}(\boldsymbol{n}\cdot\boldsymbol{n}';\chi,\chi') = \langle \psi(\boldsymbol{n},\chi)\psi(\boldsymbol{n}',\chi')\rangle \tag{3.24}$$

by

$$C^{\psi\psi}(\boldsymbol{n}\cdot\boldsymbol{n}';\chi,\chi') = \sum_{\ell=0}^{\infty}\frac{2\ell+1}{4\pi}C_\ell^{\psi\psi}(\chi,\chi')P_\ell(\boldsymbol{n}\cdot\boldsymbol{n}')\,, \tag{3.25}$$

where P_ℓ stands for the Legendre polynomials.

When the integration over the source distribution is included (*i.e.* using Eqs. (3.6),(3.9)), one obtains similar expressions for the angular power spectra but with an extra integration over the sources distribution so that the dependence in χ disappears. We shall now work out the derivations of angular power spectrum of each term that contributes to the cosmic convergence. Then in order to alleviate the notations, we will present a generic representation of all the angular power spectra.

Scalar modes

We follow the standard description of weak lensing in a full sky analysis, following e.g, Refs. [98,119,125] and refer to Refs. [126,175] for more recent developments of the formalism. We recall that in the absence of the anisotropic stress, in Newtonian gauge $\Phi = \Psi$, the deflecting potential integrated over the line of sight (Eq. (3.6)) reduces to

$$\psi(\boldsymbol{n}) = 2\int_0^\infty d\chi\ \hat{g}(\chi)\Phi[\boldsymbol{x}(\boldsymbol{n}),\eta]\,, \tag{3.26}$$

where $\hat{g}$ is defined in Eq. (3.7). By using the Fourier decomposition Eq. (2.98) and the spherical harmonics expansion of the exponential (see B.1), it follows that

$$\psi(\boldsymbol{n}) = 2\int \frac{d^3\boldsymbol{k}}{(2\pi)^{3/2}}\int_0^\chi d\chi\hat{g}(\chi)4\pi\sum_{\ell m} i^\ell j_\ell(k\chi)\Phi(\boldsymbol{k},\eta)Y_{\ell m}(\boldsymbol{n})Y_{\ell m}(\hat{\boldsymbol{k}}). \tag{3.27}$$

Now using the definition in Eq. (3.20), it is easy to get the coefficient $\psi_{\ell m}$

$$\psi_{\ell m} \;=\; 2\int \frac{d^3\boldsymbol{k}}{(2\pi)^{3/2}}\int_0^\chi d\chi\hat{g}(\chi)4\pi i^\ell j_\ell(k\chi)\Phi(\boldsymbol{k},\chi)Y_{\ell m}(\hat{\boldsymbol{k}})\ , \tag{3.28}$$

where we have replaced $\eta = \eta_0 - \chi$ by χ since the integral is evaluated on the past lightcone. We can now compute the correlator

$$\begin{aligned}\langle\psi_{\ell m}\psi^*_{\ell' m'}\rangle \;=\; &\int_0^\chi d\chi d\chi' 2\hat{g}(\chi)2\hat{g}(\chi')(4\pi)^2 i^{\ell-\ell'} j_\ell(k\chi)j_{\ell'}(k'\chi')\langle\Phi(\boldsymbol{k},\chi)\Phi^*(\boldsymbol{k}',\chi')\rangle\\ &\int\frac{d^3\boldsymbol{k}}{(2\pi)^{3/2}}Y_{\ell m}(\hat{\boldsymbol{k}})\int\frac{d^3\boldsymbol{k}'}{(2\pi)^{3/2}}Y^*_{\ell' m'}(\hat{\boldsymbol{k}}')\ .\end{aligned} \tag{3.29}$$

Using Eq. (2.99), integrating over $\boldsymbol{k}'$, then decomposing $d^3\boldsymbol{k} = k^2 dk d^2\hat{\boldsymbol{k}}$ and integrating the product of spherical harmonics over $\hat{\boldsymbol{k}}$ to get the term $\delta_{\ell\ell'}\delta_{mm'}$.

$$\langle\psi_{\ell m}\psi^*_{\ell' m'}\rangle = 16\pi\int_0^\infty d\chi\int_0^\infty d\chi'\int_0^\infty\frac{dk}{k}\ \hat{g}(\chi)\hat{g}(\chi')j_\ell(k\chi)j_\ell(k\chi')\mathcal{P}_\Phi(k,\chi,\chi')\delta_{\ell\ell'}\delta_{mm'}\,, \tag{3.30}$$

By comparing Eq. (3.30) with the definition of the power spectrum in Eq. (3.21), it is straightforward to finally get the contribution of the scalar modes

$$C^{\psi_S\psi_S} = 16\pi\int_0^\infty d\chi\int_0^\infty d\chi'\int_0^\infty\frac{dk}{k}\ \hat{g}(\chi)\hat{g}(\chi')j_\ell(k\chi)j_\ell(k\chi')\mathcal{P}_\Phi(k,\chi,\chi') \tag{3.31}$$

Vector modes

The lensing potential integrated along the line of sight associated with the vector modes is

given by

$$\psi(\boldsymbol{n}) = \int_0^\infty d\chi \hat{g}(\chi) n^i V_i[\boldsymbol{x}(\boldsymbol{n}), \chi].$$

We decompose the vector perturbations in Fourier modes as in Eq. (2.113). The polarisation vectors can be expressed as

$$\boldsymbol{e}^\pm = \frac{1}{\sqrt{2}}(\boldsymbol{e}_1 \pm \mathrm{i}\boldsymbol{e}_2) \ ,$$

so that

$$n^i e_i^\pm = \frac{1}{\sqrt{2}} \sin\theta \mathrm{e}^{\pm \mathrm{i}\varphi} \ . \tag{3.32}$$

The power spectrum of each polarisation is then defined in Eq. (2.114), where we assume that the two polarisations are independent and using local isotropy to deduce that they enjoy the same spectrum. It follows that

$$\psi(\boldsymbol{n}) = \int_0^\infty d\chi \hat{g}(\chi) \sum_{\lambda=\pm 1} \int \frac{d^3\boldsymbol{k}}{(2\pi)^{3/2}} V_\lambda(\boldsymbol{k}, \eta) \frac{1}{\sqrt{2}} \sin\theta \mathrm{e}^{\lambda \mathrm{i}\varphi} \mathrm{e}^{\mathrm{i}\boldsymbol{k}\cdot\boldsymbol{x}} \ . \tag{3.33}$$

Contrary to the scalar case, we cannot simply decompose the exponential to read $\psi_{\ell m}$ because of the extra geometric factor. The simplest is to extract it as

$$\psi_{\ell m} = \int d^2\boldsymbol{n} \ \psi(\boldsymbol{n}) Y^*_{\ell m}(\boldsymbol{n}) \ , \tag{3.34}$$

so that is given by

$$\psi_{\ell m} = \frac{1}{\sqrt{2}} \int_0^\infty d\chi \hat{g}(\chi) \sum_{\lambda=\pm 1} \int \frac{d^3\boldsymbol{k}}{(2\pi)^{3/2}} V_\lambda(\boldsymbol{k}, \eta) \int d^2\boldsymbol{n} \sin\theta \mathrm{e}^{\lambda \mathrm{i}\varphi} Y^*_{\ell m}(\boldsymbol{n}) \mathrm{e}^{\mathrm{i}\boldsymbol{k}\cdot\boldsymbol{x}} \ . \tag{3.35}$$

Now, using that

$$\sin\theta \mathrm{e}^{\lambda \mathrm{i}\varphi} = -2\lambda \sqrt{\frac{2\pi}{3}} Y_{1\lambda}(\boldsymbol{n})$$

and decomposing the exponential in spherical harmonics, one gets

$$\psi_{\ell m} = 4\pi\sqrt{2} \int_0^\infty d\chi \hat{g}(\chi) \sum_{\lambda=\pm 1} (-\lambda) \sqrt{\frac{2\pi}{3}} \int \frac{d^3\boldsymbol{k}}{(2\pi)^{3/2}} V_\lambda(\boldsymbol{k}, \eta) \sum_{LM} \mathrm{i}^L j_L(k\chi) Y_{LM}(\hat{\boldsymbol{k}}) \mathcal{A}^\lambda_{LM,\ell m} \ . \tag{3.36}$$

The integral over the 3 spherical harmonics (see Eq. A. 6 for the computation of this integral)

$$\mathcal{A}^\lambda_{LM,\ell m} \ = \ \int d^2\boldsymbol{n} Y_{1\lambda}(\boldsymbol{n}) Y_{LM}(\boldsymbol{n}) Y^*_{\ell m}(\boldsymbol{n}) \ , \tag{3.37}$$

is conveniently computed by first assuming that $\hat{\boldsymbol{k}}$ is along the z-axis so that $Y_{LM}(\hat{\boldsymbol{k}}) =$

$\sqrt{(2L+1)/4\pi}\delta_{M0}$. We thus need to evaluate $\mathcal{A}^{\lambda}_{L0,\ell m}$, which is only non-vanishing when $m=\lambda \quad L=\ell\pm 1$ so that the only non-vanishing coefficients are

$$\mathcal{A}^{1\pm1}_{(\ell+1)0,\ell\pm1}=-\frac{1}{2}\sqrt{\frac{3}{2\pi}}\sqrt{\frac{\ell(\ell+1)}{(2\ell+1)(2\ell+3)}},\qquad \mathcal{A}^{1\pm1}_{(\ell-1)0,\ell\pm1}=\frac{1}{2}\sqrt{\frac{3}{2\pi}}\sqrt{\frac{\ell(\ell+1)}{(2\ell+1)(2\ell-1)}}. \tag{3.38}$$

If we let the sum

$$\alpha^{\lambda}_{\ell m}(\boldsymbol{k}=k\boldsymbol{e}_z)\equiv\sum_{LM}\mathrm{i}^L j_L(k\chi)Y_{LM}(\hat{\boldsymbol{k}})\mathcal{A}^{\lambda}_{LM,\ell m}. \tag{3.39}$$

Expanding it gives

$$\alpha^{\lambda}_{\ell m}(\boldsymbol{k}=k\boldsymbol{e}_z)=\mathrm{i}^{\ell-1}j_{\ell-1}\sqrt{\frac{2\ell-1}{4\pi}}\mathcal{A}^{1\lambda}_{\ell-10,\ell\pm1}-\mathrm{i}^{\ell+1}j_{\ell+1}\sqrt{\frac{2\ell+3}{4\pi}}\mathcal{A}^{1\lambda}_{\ell+10,\ell\pm1}, \tag{3.40}$$

and, after gathering the Bessel functions,

$$\alpha^{\lambda}_{\ell m}(\boldsymbol{k}=k\boldsymbol{e}_z)=-\mathrm{i}^{\ell+1}\frac{1}{\sqrt{2}}\sqrt{\frac{3}{2\pi}}\sqrt{\frac{2\ell+1}{4\pi}}j^{(11)}_{\ell}(k\chi)\delta_{m\lambda} \tag{3.41}$$

with

$$j^{(11)}_{\ell}(x)\equiv\sqrt{\frac{\ell(\ell+1)}{2}}\frac{j_\ell(x)}{x}\,.$$

Now, to evaluate the same quantity for any $\hat{\boldsymbol{k}}$, we need to perform a rotation $R(\hat{\boldsymbol{k}})$ that brings the $\boldsymbol{e}_z$ along $\hat{\boldsymbol{k}}$. Under such a rotation,

$$\alpha^{\lambda}_{\ell m}(\boldsymbol{k})=\sum_{m'=\pm1}D^{\ell}_{m,m'}[R(\hat{\boldsymbol{k}})]\alpha^{\lambda}_{\ell m'}(k\boldsymbol{e}_z)\ , \tag{3.42}$$

where

$$\int d\hat{\boldsymbol{k}}D^{\ell}_{m,\pm1}[R(\hat{\boldsymbol{k}})]\left(D^{\ell'}_{m',\pm1}[R(\hat{\boldsymbol{k}})]\right)^*=\frac{4\pi}{2\ell+1}\delta_{\ell\ell'}\delta_{mm'}\ . \tag{3.43}$$

So, finally, we have

$$\psi_{\ell m}=4\pi\int_0^\infty d\chi\hat{g}(\chi)\mathrm{i}^{\ell+1}\sqrt{\frac{2\ell+1}{4\pi}}j^{(11)}_{\ell}(k\chi)\sum_{\lambda=\pm}\lambda\int\frac{d^3\boldsymbol{k}}{(2\pi)^{3/2}}V_\lambda(\boldsymbol{k},\eta)\sum_{a=\pm1}D^{\ell}_{m,a}[R(\hat{\boldsymbol{k}})]\ . \tag{3.44}$$

Using Eq. (2.114) and integrating over $\hat{\boldsymbol{k}}$ while exploiting Eq. (3.43), it follows that

$$\langle\psi_{\ell m}\psi^*_{\ell'm'}\rangle=4\pi\int_0^\infty d\chi\int_0^\infty d\chi'\int\frac{dk}{k}\mathcal{P}_V(k,\eta,\eta')\hat{g}(\chi)\hat{g}(\chi')j^{(11)}_{\ell}(k\chi)j^{(11)}_{\ell}(k\chi')\delta_{\ell\ell'}\delta_{mm'}\ . \tag{3.45}$$

Again, working out $C^{\psi_V\psi_V}$ is easy by using the definition Eq. (3.21).

Tensor modes

An approach similar to that of the vectors can be used for tensor modes. The potential integrated along the line of sight is now given by

$$\psi(\boldsymbol{n}) = \int_0^\infty d\chi \hat{g}(\chi) n^i n^j h_{ij}[\boldsymbol{x}(\boldsymbol{n}), \chi] \ . \tag{3.46}$$

We decompose the tensor perturbations in Fourier modes as in Eq. (2.128) in which the polarization tensor is explicitely given by

$$\varepsilon_{ij}^{\lambda} = \frac{e_i^1 e_j^1 \delta_+^\lambda + e_i^2 e_j^2 \delta_-^\lambda}{\sqrt{2}}$$

so that

$$n^i n^j \varepsilon_{ij}^{\pm} = \frac{1}{2\sqrt{2}} (\sin\theta)^2 \mathrm{e}^{\pm 2\mathrm{i}\varphi}.$$

The power spectrum of the two polarisations is defined as

$$\langle h_a(\boldsymbol{k}, \eta) h_b^*(\boldsymbol{k}', \eta') \rangle = \frac{2\pi^2}{k^3} \mathcal{P}_h(k, \eta, \eta') \delta^{(3)}(\boldsymbol{k} - \boldsymbol{k}') \delta_{ab} \ . \tag{3.47}$$

It follows that

$$\psi(\boldsymbol{n}) = \int_0^\infty d\chi \hat{g}(\chi) \sum_{\lambda=\pm 1} \int \frac{d^3\boldsymbol{k}}{(2\pi)^{3/2}} h_\lambda(\boldsymbol{k}, \eta) \frac{1}{2\sqrt{2}} (\sin\theta)^2 \mathrm{e}^{\lambda 2\mathrm{i}\varphi} \mathrm{e}^{\mathrm{i}\boldsymbol{k}\cdot\boldsymbol{x}} \ . \tag{3.48}$$

Setting $2\lambda = \gamma$ and using

$$(\sin\theta)^2 \mathrm{e}^{\gamma \mathrm{i}\varphi} = 4\sqrt{\frac{2\pi}{15}} Y_{2\gamma}(\boldsymbol{n}),$$

the expression of the coefficients $\psi_{\ell m}$ are obtained from Eq. (3.34) as

$$\psi_{\ell m} = 4\pi\sqrt{2} \int_0^\infty d\chi \hat{g}(\chi) \sum_{\gamma=\pm 2} \sqrt{\frac{2\pi}{15}} \int \frac{d^3\boldsymbol{k}}{(2\pi)^{3/2}} h_\gamma(\boldsymbol{k}, \eta) \sum_{LM} \mathrm{i}^L j_L(k\chi) Y_{LM}(\hat{\boldsymbol{k}}) \mathcal{A}_{LM,\ell m}^{\gamma} \tag{3.49}$$

with

$$\mathcal{A}_{LM,\ell m}^{\gamma} \ = \ \int d^2\boldsymbol{n} Y_{2\gamma}(\boldsymbol{n}) Y_{LM}(\boldsymbol{n}) Y_{\ell m}^*(\boldsymbol{n}) \ . \tag{3.50}$$

By pure analogy with the previous case, it is convenient to first calculate this assuming that $\hat{\boldsymbol{k}}$ is along the z-axis so that $Y_{LM}(\hat{\boldsymbol{k}}) = \sqrt{(2L+1)/4\pi}\delta_{M0}$. We then need to evaluate $\mathcal{A}_{LM,\ell m}^{\gamma}$

which is only non-vanishing when $m = \gamma \quad L = \ell \pm 2, \ell$ so that the non-zero coefficients are

$$\mathcal{A}^{2\pm2}_{(\ell)0,\ell\pm2} = -\frac{1}{2}\sqrt{\frac{15}{2\pi}}\sqrt{\frac{(\ell+2)!}{(\ell-2)!}}\frac{1}{(2\ell+3)(2\ell-1)} , \tag{3.51}$$

$$\mathcal{A}^{2\pm2}_{(\ell+2)0,\ell\pm2} = \frac{1}{4}\sqrt{\frac{15}{2\pi}}\sqrt{\frac{(\ell+2)!}{(\ell-2)!}}\frac{1}{\sqrt{(2\ell+1)(2\ell+5)}(2\ell+3)} , \tag{3.52}$$

$$\mathcal{A}^{2\pm2}_{(\ell-2)0,\ell\pm2} = \frac{1}{4}\sqrt{\frac{15}{2\pi}}\sqrt{\frac{(\ell+2)!}{(\ell-2)!}}\frac{1}{\sqrt{(2\ell-3)(2\ell+1)}(2\ell-1)} . \tag{3.53}$$

The sum

$$\tilde{\alpha}^{\gamma}_{\ell m}(\boldsymbol{k} = k\boldsymbol{e}_z) \equiv \sum_{LM} \mathrm{i}^L j_L(k\chi) Y_{LM}(\hat{\boldsymbol{k}}) \mathcal{A}^{\gamma}_{LM,\ell m} \tag{3.54}$$

then reduces to 3 terms as

$$\begin{aligned}\tilde{\alpha}^{\gamma}_{\ell m}(\boldsymbol{k} = k\boldsymbol{e}_z) &= \mathrm{i}^{\ell} j_{\ell}(k\chi) Y_{\ell 0}(\hat{\boldsymbol{k}}) \mathcal{A}^{2\pm2}_{(\ell)0,\ell\pm2} + \mathrm{i}^{\ell+2} j_{\ell+2}(k\chi) Y_{\ell+20}(\hat{\boldsymbol{k}}) \mathcal{A}^{2\pm2}_{(\ell+2)0,\ell\pm2} + \mathrm{i}^{\ell-2} j_{\ell-2}(k\chi) \\ &\quad \times Y_{(\ell-2)0}(\hat{\boldsymbol{k}}) \mathcal{A}^{2\pm2}_{(\ell-2)0,\ell\pm2}.\end{aligned} \tag{3.55}$$

After simplifying and gathering the Bessel functions, it gives

$$\tilde{\alpha}^{\gamma}_{\ell m}(\boldsymbol{k} = k\boldsymbol{e}_z) = \frac{1}{\sqrt{2}} \mathrm{i}^{\ell+2} \sqrt{\frac{15}{2\pi}} \sqrt{\frac{2\ell+1}{4\pi}} j^{(22)}_{\ell}(k\chi) \delta_{\gamma m} \tag{3.56}$$

with

$$j^{(22)}_{\ell}(x) \equiv \sqrt{\frac{1}{8}\frac{(\ell+2)!}{(\ell-2)!}} \frac{j_{\ell}(x)}{x^2}.$$

To finish, we need to evaluate the same quantity for any $\hat{\boldsymbol{k}}$ by performing a rotation $R(\hat{\boldsymbol{k}})$ that brings the $\boldsymbol{e}_z$ along $\hat{\boldsymbol{k}}$. Under such a rotation,

$$\tilde{\alpha}^{\lambda}_{\ell m}(\boldsymbol{k}) = \sum_{m'=\pm2} D^{\ell}_{m,m'}[R(\hat{\boldsymbol{k}})] \tilde{\alpha}^{\lambda}_{\ell m'}(k\boldsymbol{e}_z) , \tag{3.57}$$

where the orthogonality relation of the Wigner D-functions,

$$\int d\hat{\boldsymbol{k}} D^{\ell}_{m,\pm2}[R(\hat{\boldsymbol{k}})] \left(D^{\ell'}_{m',\pm2}[R(\hat{\boldsymbol{k}})]\right)^* = \frac{4\pi}{2\ell+1} \delta_{\ell\ell'} \delta_{mm'} , \tag{3.58}$$

is used to get the coefficients of the expansion as

$$\psi_{\ell m} = 4\pi \sqrt{\frac{2\ell+1}{4\pi}} \int_0^{\infty} d\chi \hat{g}(\chi) \sum_{\gamma=\pm2} \int \frac{d^3\boldsymbol{k}}{(2\pi)^{3/2}} h_{\gamma}(\boldsymbol{k}, \eta) \mathrm{i}^{\ell+2} j^{(22)}_{\ell}(k\chi) \sum_{a=\pm2} D^{\ell}_{m,a}[R(\hat{\boldsymbol{k}})] . \tag{3.59}$$

Using Eq. (3.47) and integrating over $\hat{\boldsymbol{k}}$ while exploiting Eq. (3.58) leads to

$$\langle \psi_{\ell m} \psi^*_{\ell' m'} \rangle = 4\pi \int_0^\infty d\chi \int_0^\infty d\chi' \int \frac{dk}{k} \mathcal{P}_T(k,\eta,\eta') \hat{g}(\chi) \hat{g}(\chi') j_\ell^{(22)}(k\chi) j_\ell^{(22)}(k\chi') \delta_{\ell\ell'} \delta_{mm'} \,. \quad (3.60)$$

The expression of $C^{\psi_T \psi_T}$ follows easily from Eq. (3.21). It is worth noting that we have also computed three other first order contributions which are the velocity term, ISW term and SW term. In order to alleviate the main text we refer the readers to the more detailed derivations of the angular power spectra in Appendices B.1, B.2, B.3 respectively for the velocity term, ISW term, SW term. After integrating over the sources distribution, all power spectra (see Eqs. (3.30), (B. 6), (3.45), (3.60), (B. 22), (B. 15), (B. 16) and (B. 17)) can all be written as

$$C_\ell^{\psi_X \psi_X} = \left[A_\ell^{(s)}\right]^2 \int_0^\infty d\chi \hat{g}(\chi) \int_0^\infty d\chi' \hat{g}(\chi') \int \frac{dk}{k} \frac{j_\ell(k\chi)}{(k\chi)^s} \frac{j_\ell(k\chi')}{(k\chi')^s} \mathcal{P}_X(k,\chi,\chi') \,, \quad (3.61)$$

with

$$A_\ell^{(s)} = \sqrt{\frac{16\pi}{N_s^2 F_s} \frac{(\ell+s)!}{(\ell-s)!}} \quad (3.62)$$

where $X = \{S, V, T\}$, corresponding to $s = 0, 1, 2$. The power spectra of each mode, $\mathcal{P}_S = \mathcal{P}_\Phi$ etc., are respectively given by Eqs. (2.99), (2.117) and (2.130) and we have replaced $\eta = \eta_0 - \chi$ by χ since this the integral is evaluated on the past lightcone. The numbers $F_s = (1, 2, 8)$ for $s = (0, 1, 2)$ and $N_s = (1, 2, 2)$ is the number of polarisations of each mode. The Doppler contribution ($X = v$) takes a similar form (see Appendix B.1) with $A_\ell^{(s)} \to \sqrt{4\pi} A$, $\hat{g}(\chi) \to F(\chi)$, $j_\ell(k\chi)/(k\chi)^s \to j'_\ell(k\chi)$ and $\mathcal{P}_v \to k^2 \mathcal{P}_\Phi$. The two contributions from ISW and SW terms are both similar to the scalars modes with $s = 0$, $F_s = 1$ and $N_s = 1$ except that for SW $A^{(s)} = \sqrt{4\pi}$ whereas that of ISW is the same as the scalar modes (see Appendices B.2 to B.3). Each spectrum can be written in terms of a transfer function $T_X(k,\eta)$ which is normalized to unity at early times as

$$\mathcal{P}_X(k,\eta,\eta') = \mathcal{P}_{X,i}(k) T_X(k,\eta) T_X(k,\eta') \,. \quad (3.63)$$

This implies that Eq. (3.61) factors as

$$C_\ell^{\psi_X \psi_X} = \left[A_\ell^{(s)}\right]^2 \int_0^\infty \frac{dk}{k} \mathcal{P}_{X,i}(k) \left[\int_0^\infty d\chi \, \hat{g}(\chi) \frac{j_\ell(k\chi)}{(k\chi)^s} T_X(k,\chi)\right]^2 \,. \quad (3.64)$$

Similarly, the convergence angular power spectra, not integrated over the sources distribu-

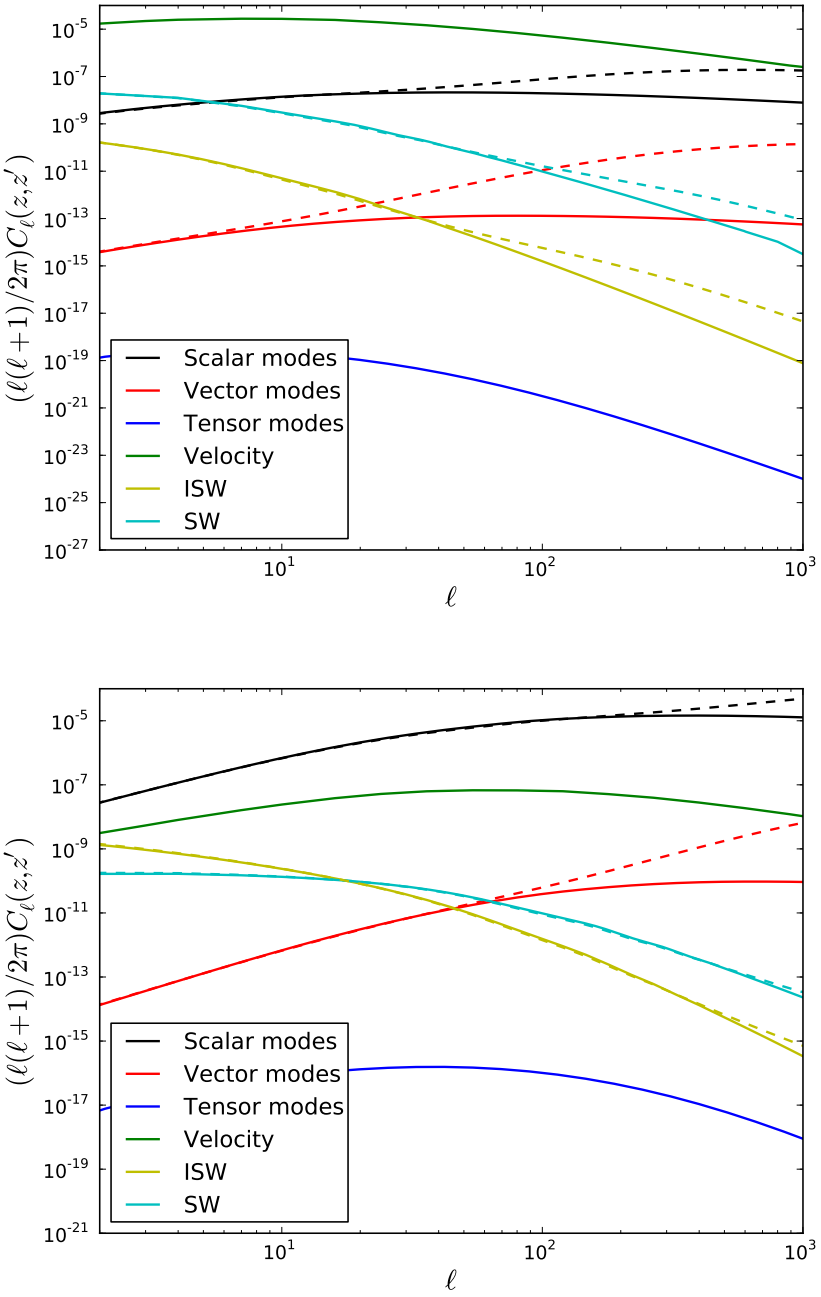

Figure 3.2: Lensing angular power spectra of the density contrast (scalars - black line), the Doppler contribution (green), vectors (red line), tensors (blue line), ISW term (yellow line) and SW term (cyan line), $C_\ell^{\kappa\kappa}(z, z')$, at $z = z' = 0.1$ (top) and $z = z' = 1.0$ (bottom). The dashed lines represent the non-linear evolution estimated using Halofit. z and z' are the redshifts of the sources on the two lines of sight.

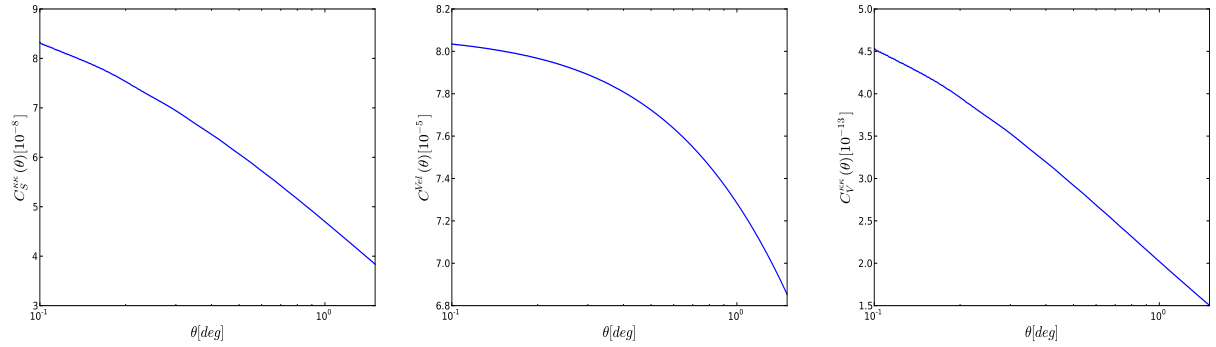

Figure 3.3: Real space angular correlation function, $C^{\kappa\kappa}(\theta)$, at $z = z' = 0.1$ for the scalars, Doppler, vectors from left to right. Note that in this regime the Doppler lensing is dominant.

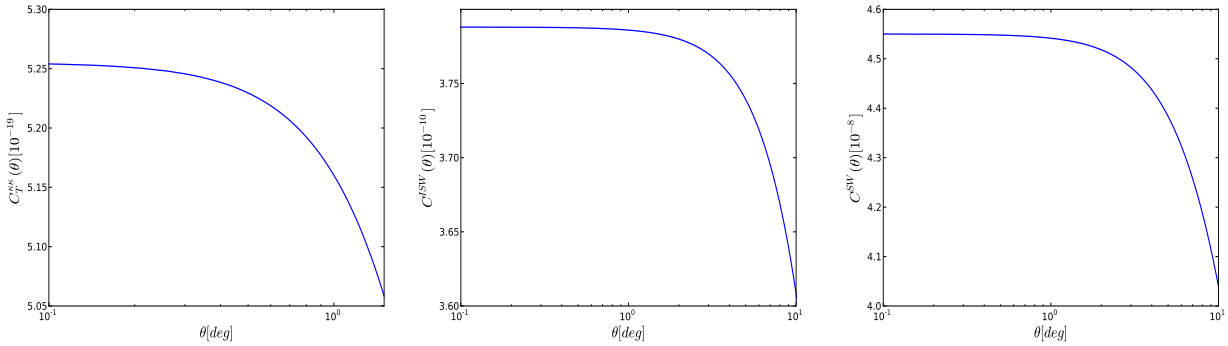

Figure 3.4: Real space angular correlation function, $C^{\kappa\kappa}(\theta)$, at $z = z' = 0.1$ for the tensors, ISW and SW from left to right.

tion, takes the form

$$C_\ell^{\psi_X\psi_X}(\chi_S,\chi'_S) = \left[A_\ell^{(s)}\right]^2 \int_0^{\chi_S} d\chi \frac{f_K(\chi_S-\chi)}{f_K(\chi_S)f_K(\chi)} \int_0^{\chi'_S} d\chi' \frac{f_K(\chi'_S-\chi')}{f_K(\chi'_S)f_K(\chi')} \times \int_0^\infty \frac{dk}{k} \frac{j_\ell(k\chi)}{(k\chi)^s} \frac{j_\ell(k\chi')}{(k\chi')^s} \mathcal{P}_X(k,\chi,\chi'). \tag{3.65}$$

Since integrating the Bessel function in Eq. (3.64) is computationally expensive and since the sources distribution is slowly varying over long distances, we shall resort to a Limber approximation which is a good approximation at large ℓ [172]. In such an approximation, $k\chi \simeq (\ell + 1/2)$ so that [176, 177] we have the property

$$\frac{2}{\pi} \int_0^\infty dk\, k^2 f(k) j_\ell(k\chi) j_\ell(k\chi') = \frac{\delta(\chi-\chi')}{\chi^2} f[(\ell+1/2)/\chi] \tag{3.66}$$

which is accurate to $\mathcal{O}[(\ell+1/2)^2]$ and is sufficient for our purposes. We then find

$$C_\ell^{\psi_X\psi_X} = \frac{64\pi^2}{N_s(2\ell+1)^{3+2s}}\frac{(\ell+s)!}{(\ell-s)!}\int_0^\infty d\chi\,\chi\mathcal{P}_{X,i}\left[\frac{2\ell+1}{2\chi}\right]\,\hat{g}(\chi)^2T^2\left[\frac{2\ell+1}{2\chi},\chi\right]. \qquad (3.67)$$

3.4 Weak lensing from second-order modes

The previous expressions allow us to compute numerically the angular power spectra of the 6 contributions to the cosmic convergence in particular to estimate the typical magnitude of the non-linear terms which we compare to the standard term κ_S, the Doppler term κ_v, ISW term $\kappa_{\rm isw}$ and SW term $\kappa_{\rm sw}$, which allows us to discuss whether assuming $\kappa_{\rm observation} = \kappa_S + \kappa_v$ is a good approximation to interpret the weak lensing observations. Since the two point function can be computed in real space (*i.e.*, the correlation function $C(\theta, z, z')$) or in harmonic space (*i.e.*, the angular power spectrum $C_\ell(z, z')$), we shall use the two representations.

3.4.1 Behaviour of the different contributions

We start by comparing in Fig. 3.2 the different contributions to the lensing angular power spectra without integrating over the sources distribution and assuming that the sources on the sky are located at the same redshift in $z = z' = 0.1$ or $z = z' = 1.0$. We recover that the velocity contribution dominates at low redshift [88] and that the gravity waves contribution is always negligible [117]. The results shown in Fig. 3.2 also suggest that there is a range in multipoles ℓ ($\ell \geq 50$) where the second order vector modes become more significant than both of the Sachs-Wolfe terms. A similar computation in real space, assuming $z = z' = 0.1$ is depicted in Fig. 3.3 and Fig. 3.4.

Focusing on the contribution of the vector modes, Fig. 3.5 shows how the amplitude of the angular power spectrum $C_{V,\ell}^{\kappa\kappa}(z, z')$ depends on the redshifts of the background galaxies and on the scale, while Fig. 3.6 shows the similar information in real space, *i.e.*, $C_V^{\kappa\kappa}(\theta, z, z')$. Fig. 3.7 shows the ratio of the vectors to the Doppler term, which shows that at intermediate redshifts the second-order frame dragging effects dominate the linear Doppler lensing. It is noted that although, we think that higher order contributions from the vector modes will be subdominant, this issue still needs to be addressed. We have included the non-linear power spectrum using Halofit to compute the vector modes shown in Fig. 3.2, but for the rest of the calculations for consistency, we only use the linear power spectrum to compute the contribution of the vector modes to the cosmic convergence.

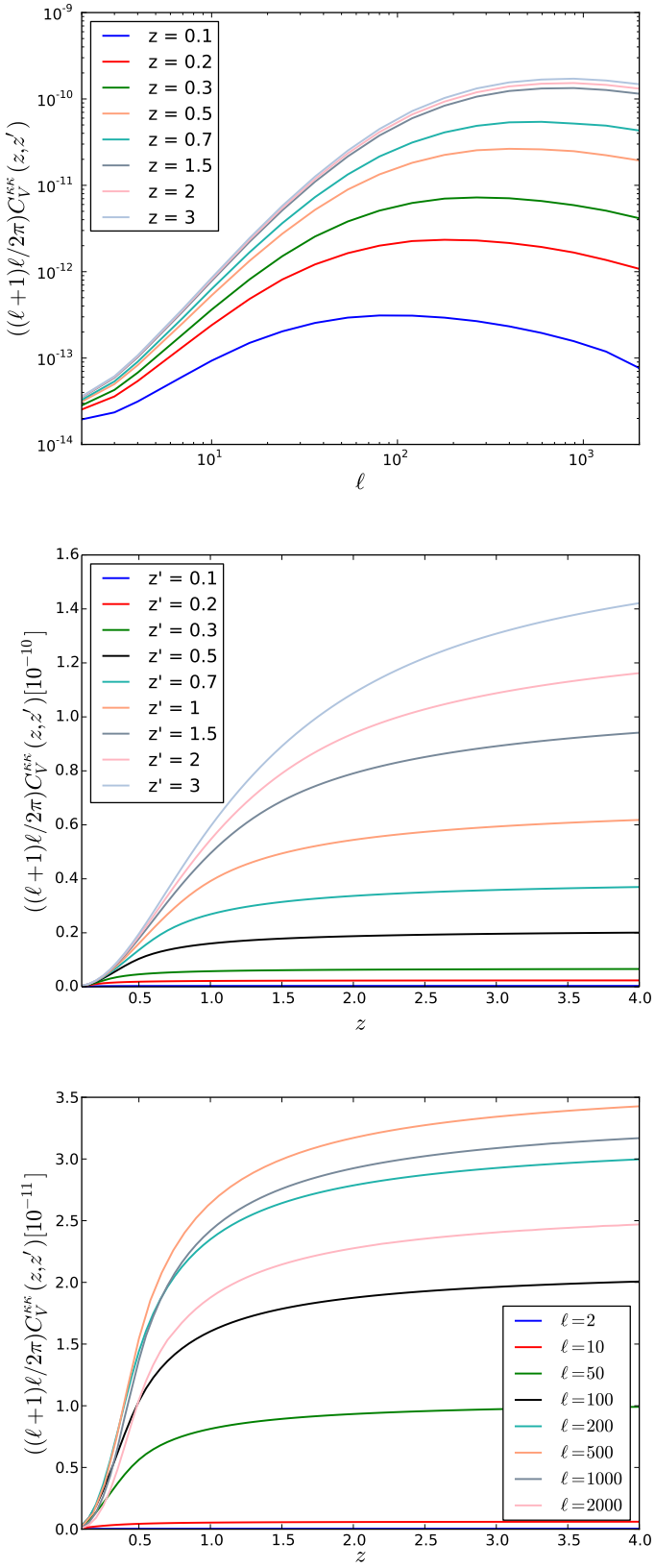

Figure 3.5: Angular power spectra of the vectors at different redshifts. (top) as a function of ℓ for $z' = 1$; (middle) as a function of z for different z' for $\ell = 100$ and (bottom) as a function of z for different multipole ℓ with $z' = 0.5$.

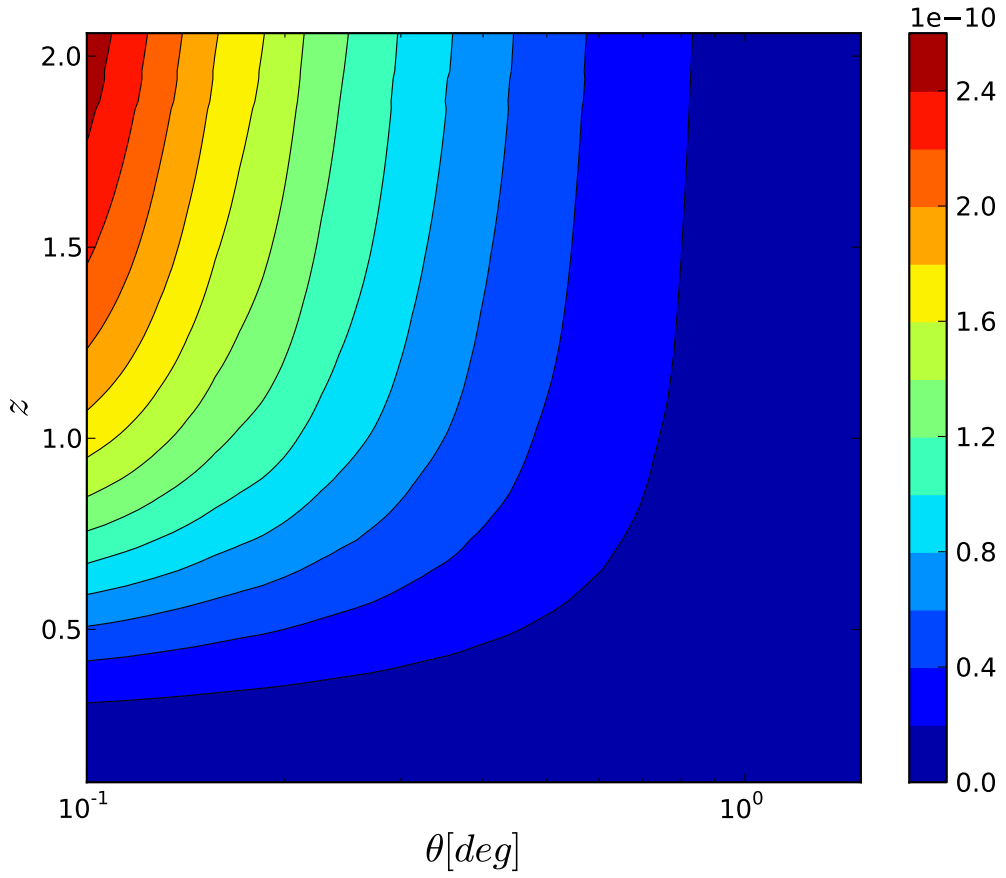

Figure 3.6: Amplitude of the angular power spectra of the vectors in real space with $z' = 1$.

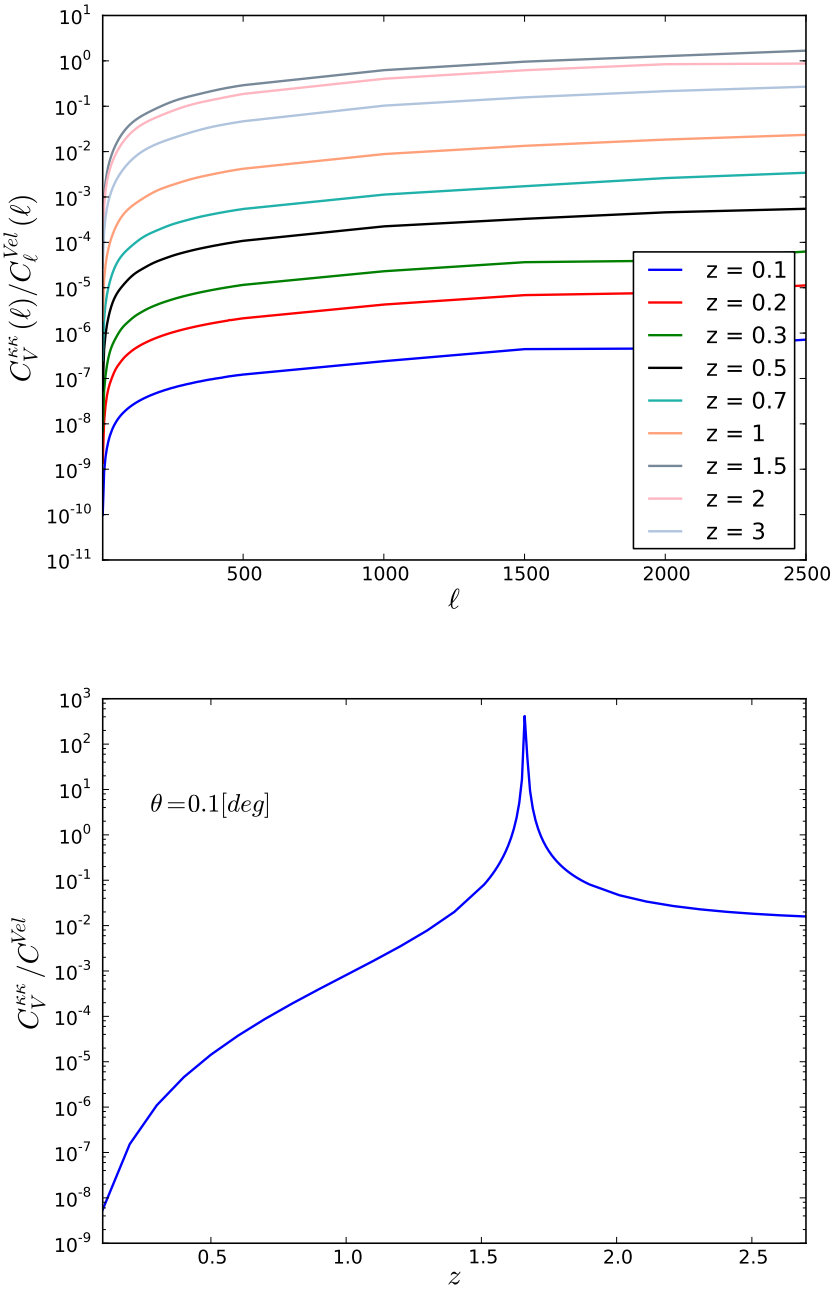

Figure 3.7: (top) : Ratio between the convergence from the vector mode background to the Doppler convergence C_ℓ^{Vel}. At moderate redshifts the second-order vectors are larger than the first-order contribution from the Doppler convergence. (bottom) : Ratio of the two correlation functions (vector modes and the velocity) $C_V^{\kappa\kappa}/C^{Vel}$ as a function of z ($z = z'$) where $\theta = 0.1$ degree.

3.4.2 Source distributions

The source distribution depends on the survey and is described through the function $n_{s,\chi}(\chi)$ or an equivalent function $n_{s,z}(z)$ in redshift space, where $n_{s,\chi}(\chi)d\chi = n_{s,z}(z)dz$. These distributions are normalised to unity. This then defines the lensing weight function $\hat{g}$, as shown in Eq. (3.7).

To start, let us assume that the sources are distributed at a single redshift so that

$$n_s(\chi) = \delta(\chi - \chi_s) \tag{3.68}$$

which implies

$$\hat{g}(\chi) = \frac{\chi_s - \chi}{\chi\chi_s}\Theta(\chi_s - \chi), \tag{3.69}$$

where Θ is the Heaviside distribution. This unrealistic but simple assumption provides a good way to understand the lensing effects as a function of redshift. Fig. 3.8 depicts the contribution to the lensing spectra for shells with sources located at different redshifts normalised to the scalar contribution. As we can see, the relative contribution from the vector modes is largest at low redshift, reflecting the fact that vector modes continue to grow at late times. It can also be noticed that second order vector modes completely dominates the Sachs-Wolfe term at small scales (large ℓ). The fact that SW term tends to zero at $z \simeq 0.7$ accounts for the large amplitude of the ratio $C_V^{\kappa\kappa}(\ell)/C_\ell^{SW}(\ell)$ at $z = 0.7$. Note that the difference in the pre-factors of both SW and Doppler terms explains the difference in redshifts at which each of them crosses zero.

In order to obtain more realistic orders of magnitude, we consider source distributions similar to the one of the future Euclid and SKA experiments. The normalised Euclid redshift distribution has the form given in Refs. [178–180]:

$$n(z) = Az^2 \exp\left[-\left(\frac{z}{z_0}\right)^\beta\right] \tag{3.70}$$

with $A = 5.792$, $\beta = 1.5$ and $z_0 = 0.64$, which gives a median redshift $z_m \sim 0.9$.

For SKA we make use of the SKA Simulated Skies simulations [181]. These are simulations of the submillimeter radio source population. We use all the extragalactic radio continuum sources in the central 10×10 sq. degrees out to a redshift of $z = 20$. In these simulations, the sources are drawn from either observed or extrapolated luminosity functions and grafted onto an underlying dark matter distribution with biases which reflect their measured large-scale

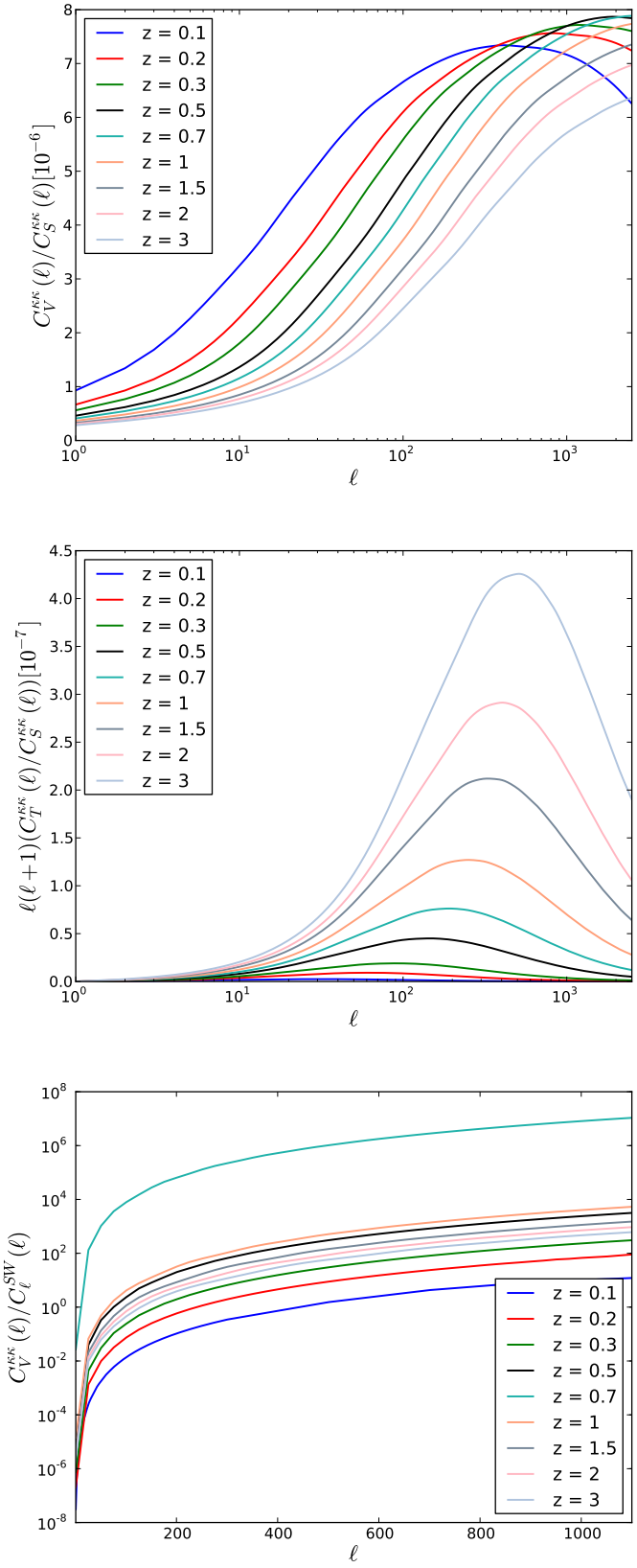

Figure 3.8: The convergence contributions from the vector mode background (top), gravitational wave background (middle) which are both relative to the scalar contribution and the vector modes contribution relative to the Sachs-Wolfe term (bottom). These are all plotted for the same source distributions at single redshifts, using the distribution in Eq. (3.69).

clustering. We then construct a redshift distribution that we paramaterise as

$$n(z) = A\frac{z^n}{(1+z)^m}\exp\left[-\frac{(a+bz)^2}{(1+z)^2}\right] \tag{3.71}$$

with best fit parameters $a = -1.806, b = 0.388, m = 2.482, n = 0.838$ and $A = 1.610$ and normalise the distribution at $z = 20$, which gives a description accurate to the percent level, which is good enough for our purposes. Note that this redshift distribution represents the very best case scenario since all sources from the simulation have been used in its construction, and no further observational cuts were included.

These source distributions can be used to compute the vector convergence spectrum for both surveys. Fig. 3.9 compares its amplitude to the standard scalar contribution, showing that it is typically 10^{-5} times smaller. Whereas compared to the Doppler contribution, its amplitude is about 10^2 larger and 10^{-2} smaller on small scales respectively for a SKA-like survey and for a Euclid-like survey – see Fig. 3.9. Interestingly, the vector contribution is subdominant for Euclid, for which the main correction arises from the Doppler term, while for SKA-like geometry the vector contribution is typically 1-100 times larger than the Doppler one for $\ell > 500$. On larger angular scales, the Doppler term always dominates – see Fig. 3.9, where on large angular scales the Doppler term totally prevails over the scalar contribution by about 5 orders of magnitude.

3.5 Conclusions

In this chapter we have evaluated the amplitude of relativistic contributions to the weak lensing power spectra. We have considered the gravitational wave and vector mode backgrounds which are sourced at second-order by density perturbations. The amplitude of these backgrounds are completely fixed once the normalisation of the scalar power spectrum in the linear regime is determined. As these are purely relativistic degrees of freedom they set the lower limit for all relativistic effects on cosmological modelling. While the gravitational wave background is very small in relation to the scalars, the vectors, which represent frame dragging in the metric, give corrections to the metric at nearly the percent level. The effect of these contributions on weak lensing convergence predictions have been computed in order to understand if they can either be detected, or bias the analysis of future weak lensing experiments, such as Euclid or SKA. We have compared them to the usual gravitational lensing contribution, the two Sachs-Wolfe contributions as well as the Doppler lensing con-

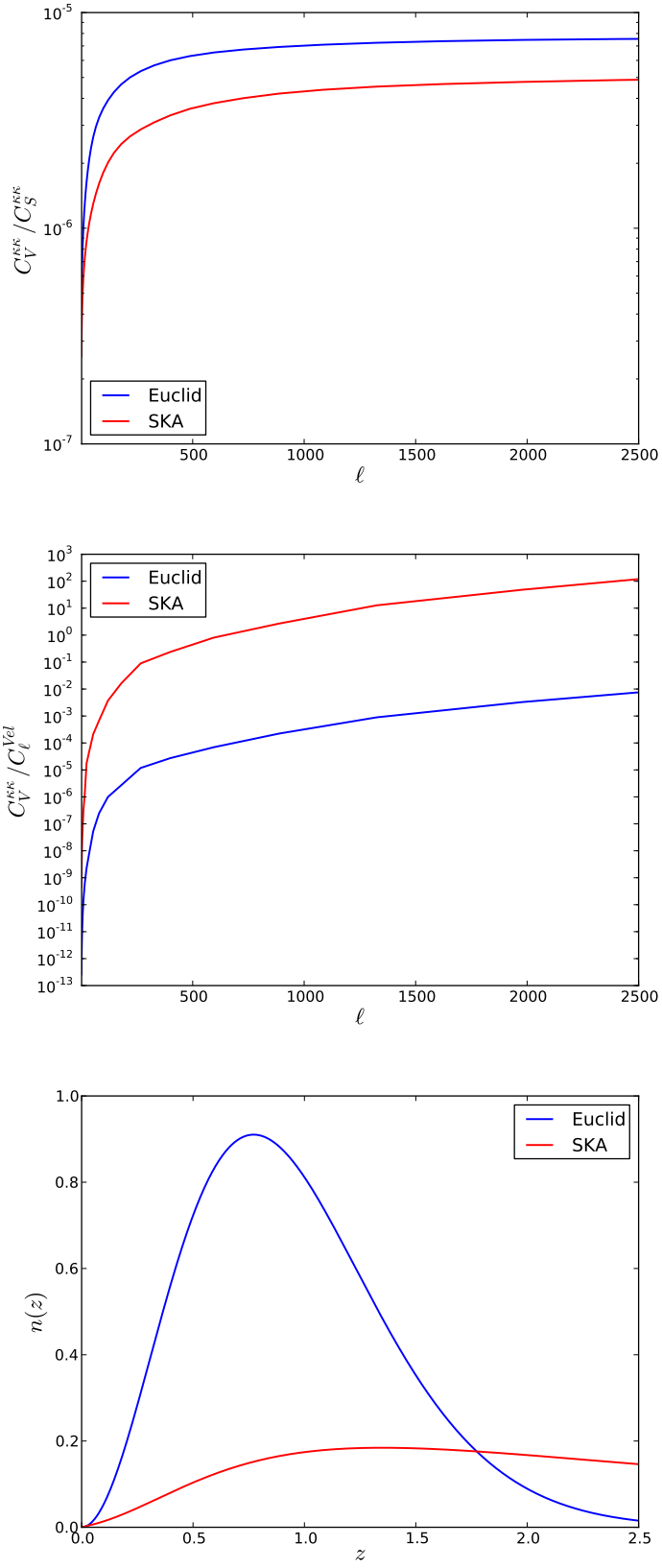

Figure 3.9: Ratio between the angular power spectra of the vectors $C_V^{\kappa\kappa}$ to scalars $C_S^{\kappa\kappa}$ (top) and to the doppler term C_ℓ^{Vel} (middle) as a function of multipole ℓ for two surveys, blue line (Euclid-like), red line (SKA-like). The survey geometries are shown (bottom).

tribution [165].

First, we have shown that even though the non-linear tensor mode background dominates over any possible primordial gravitational wave contribution, its effect on weak lensing is completely negligible, by 10 to 12 order of magnitudes (see Figs. 3.2 and 3.8).

Then, we have shown that the vector contribution to the convergence, while small, can dominate over the Doppler lensing at high redshift – but there it is swamped by gravitational lensing by density perturbations. We have shown this both for point sources and for two survey geometries. The vectors are actually more important than the Doppler term for SKA-like source distributions on small scales, but not for a Euclid like survey. For both of these surveys the vectors only reach about $10^{-3}\%$ that of the normal gravitational lensing contribution, and so can be safely neglected. Nevertheless, it is interesting that the vector contribution can be as important as some linear terms. It is worth noting that for Euclid, we observe more galaxies at low redshift compared to SKA therefore its corresponding Doppler term C_ℓ^{vel} is more enhanced which leads to a smaller amplitude of the ratio $C_V^{\kappa\kappa}/C_\ell^{vel}$. Whereas for SKA which probes at higher redshift, its corresponding lensing term $C_S^{\kappa\kappa}$ (which is an integrated effect) is a bit larger leading to a smaller amplitude of the ratio $C_V^{\kappa\kappa}/C_S^{\kappa\kappa}$.

We have also recovered that although the frame dragging effect is small, it becomes more important than both ISW and SW above $\ell \geq 50$. This comes to corroborate the fact that for observations, neglecting the 2 first order Sachs-Wolfe terms is a good approximation.

In this analysis, the non-linear effects of the metric perturbations have been described at second order while weak lensing was described assuming that the Born approximation still holds. In principle, one needs also to take into account second order effects on the geodesic deviation equation [166–170], as fully described in Refs. [171, 172].

There are a huge variety of second-order effects which come into the convergence. We have only considered two contributions which arise from non-linear dynamical effects which happen as structure forms. Many contributions appear when calculating the lensing convergence itself [77, 78, 158], and these also need to be analysed in a similar manner to that presented here to determine whether relativistic effects are important for future observations of magnification.

Chapter 4
Doppler lensing

4.1 Introduction

Light rays from distant sources are focused by overdensities (or defocused by underdensities) along the line of sight, leading to apparent magnification (or demagnification) of images. But besides this *gravitational lensing*, there is a further effect which appears to magnify or demagnify the images of objects in the Universe. This *Doppler lensing* effect arises from the peculiar velocity of the source, and was first highlighted and investigated in general by [88] (see also [76]). [89] then showed that the effect can dominate over gravitational lensing, and even reverse its effect, leading to an 'anti-lensing' phenomenon. Doppler lensing gives a new window into the peculiar velocity field in addition to the usual redshift space distortion measurements.

The effect is a consequence of the distortion introduced by mapping from redshift-space to real space, as illustrated in Fig. 4.1. Imagine we have three spherical galaxies with the same physical size, and (as an extreme case) the same measured redshift z_s. Galaxy A is at the centre of a spherical overdensity, and we ignore the contribution from gravitational lensing. A's redshift is purely cosmological, and its angular size is typical for objects at this redshift. Galaxy B is physically nearer to us, with a smaller cosmological redshift, but has a peculiar velocity away from us so that its net redshift is z_s. Its angular size is therefore larger than typical at this measured redshift. Finally, galaxy C has a larger cosmological redshift and is moving towards us, again with a net observed redshift z_s. Its angular size is therefore smaller than typical, as it is truly further away.

The contribution from Doppler lensing to (de)magnification can be summed up as follows: galaxies with peculiar velocity away from us appear magnified at a particular redshift, relative to typical objects at the same redshift. For galaxies behind an overdensity which are falling towards it, the effect has the opposite sign to gravitational lensing magnification, and is typically much larger than gravitational lensing in the infall region [89]. Similarly, objects behind a void appear magnified – opposite to the gravitational lensing contribution.

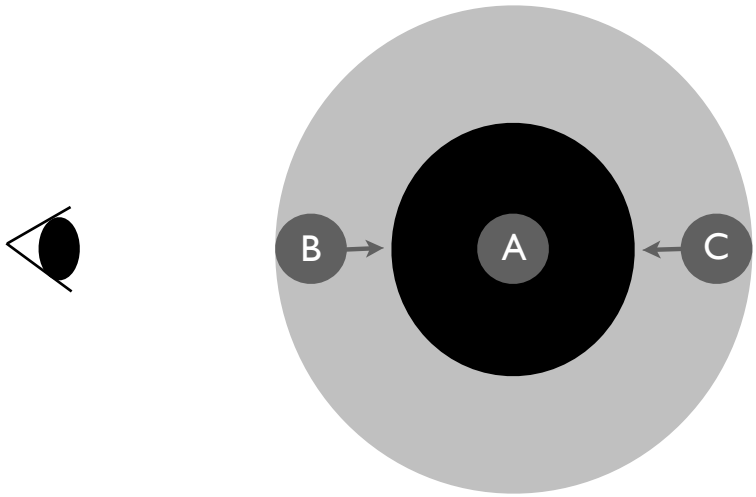

Figure 4.1: Three spherical galaxies of the same physical size and same observed redshift. A is at the centre of a spherical overdensity while B and C are falling towards the centre.

The Doppler lensing signal is a direct means of measuring velocities in the Universe, and therefore provides information about the growth rate of structure, a key quantity for discerning between dark energy models and for tests of gravity. In order to exploit the potential of this new probe, we need to find appropriate statistics to measure the effect, and examine the expected signal-to-noise for forthcoming surveys.

Doppler lensing causes a slight apparent change in size and magnitude for objects at a given observed redshift (throughout we will use the term 'size' to mean angular size). However, since these objects have an intrinsic range of sizes and magnitudes, to measure the effect it is necessary to measure size/magnitude for many objects in order to overcome this intrinsic noise. In addition, it is highly desirable to obtain spectroscopic redshifts for the sources, as Doppler lensing between two objects is present over relatively short separations in redshift ($\Delta z \simeq 0.02$), in contrast to gravitational lensing – which is integrated along the entire line of sight.

Here we suppose that well-calibrated estimates of size and magnitude are available for a catalogue of galaxy images in a survey, which can then be used to obtain noisy estimators of the magnification for each object. Most weak lensing studies so far have used galaxy ellipticities rather than sizes for probing the lensing field. However, size-magnitude estimators have been demonstrated as feasible, and the signal-to-noise for magnification measurements with these estimators is about half that of shear [20]. Once such estimates of magnification

have been obtained for a survey, it will be possible to apply the statistics and techniques we develop in this Chapter in order to measure and use the Doppler lensing effect.
The Chapter is organised as follows. In Section 4.2 we review the relevant theory for Doppler lensing, showing the redshift and wavenumber range over which the effect dominates over gravitational lensing. In Section 4.4 we introduce the survey configurations which we consider for our predictions. We then proceed to describe several applications of Doppler lensing: in Section 4.5, we examine the prospects for detecting the signal around stacked over/underdensities. In Section 4.6, we calculate suitable power spectra and correlation functions for Doppler lensing, showing that cross-correlation statistics can be measured with high signal-to-noise in future surveys. We consider the impact of intrinsic size correlations and gravitational lensing on these statistics.

4.2 Doppler lensing: theory

4.2.1 Derivation

The convergence κ includes both gravitational and Doppler lensing, as well as further terms (see Eq. (4.13) below); it causes an expansion or reduction of apparent size of an object. The shear γ arises principally from gravitational lensing; it causes a change in ellipticity of an object. The distorted apparent angular size of an object r_l is related to its undistorted angular size r_u by

$$r_l \simeq (1+\kappa) r_u, \tag{4.1}$$

while the lensed apparent magnitude of an object m_l is related to the unlensed apparent magnitude m_u by

$$m_l \simeq m_u + 5\log_{10}(1-\kappa). \tag{4.2}$$

A simple estimator for the convergence can be derived from an object's measured angular size r, which could be derived from fitted parameters(e.g. the square root of area, [182]) or measured using a quadrupole-moment method [183]. We can then obtain the mean log size $\langle \ln r \rangle$ at redshift z, after which a suitable estimator for convergence on a galaxy at redshift z will be

$$\hat{\kappa} = \ln r - \langle \ln r \rangle_z. \tag{4.3}$$

A more sophisticated estimator, combining size and magnitude, is provided by [20]. This estimator is able to take into account the lensing bias, where magnification can bring new

faint, small galaxies into the sample. Since galaxies intrinsically have a range of size and brightness, they find (their Figure 1) that the estimator has an intrinsic noise $\sigma_\kappa \simeq 0.3$, which is the value we adopt throughout this Chapter.

Now that we have introduced the lensing quantities, we will outline the derivation of the Doppler lensing contribution. The lensing convergence κ corrects the background angular diameter distance $\bar{D}_A$ for a source:

$$D_A(z_s, \boldsymbol{n}) = \bar{D}_A(z_s)\Big[1 - \kappa(z_s, \boldsymbol{n})\Big]. \tag{4.4}$$

The source is *observed* at redshift z_s in the perturbed model and in the direction $-\boldsymbol{n}$, i.e. $\boldsymbol{n}$ is the unit direction vector pointing from the source to the observer. The background area distance at any z is $\bar{D}_A(z) = \chi(z)/(1+z)$, where χ is the background comoving distance. The convergence κ may be found by solving the Sachs focusing equation, which follows from the geodesic deviation equation [125]:

$$\frac{d^2}{d\chi^2} D_A = -\frac{1}{2} R_{\mu\nu} k^\mu k^\nu \, D_A \tag{4.5}$$

(we neglect a second-order shear contribution). Here χ is the background comoving distance (used as affine parameter along the lightrays), the photon 4-momentum is $k^\mu = dx^\mu/d\chi$ and $R_{\mu\nu}$ is the Ricci tensor. We describe a perturbative correction to the angular diameter distance, relative to the background distance $\bar{D}_A$ at background redshift $\bar{z}$, by:

$$D_A(\bar{z}) = \bar{D}_A(\bar{z}) \left[1 + \frac{\delta D_A}{\bar{D}_A}\right] . \tag{4.6}$$

Solving Eq. (4.5), we find:

$$\left.\frac{\delta D_A}{\bar{D}_A}\right|_{\chi_s} = -\boldsymbol{v}_o \cdot \boldsymbol{n} - \Psi_s + \frac{1}{\chi_s} \int_0^{\chi_s} d\chi \Big[2\Psi + (\chi - \chi_s)\chi \nabla_\perp^2 \Psi\Big], \tag{4.7}$$

where s denotes source and o denotes observer, and $\boldsymbol{v}_o$ is the peculiar velocity of the observer. The transverse Laplacian (in the screen space orthogonal to the light ray) is given by[1]

$$\nabla_\perp^2 = \nabla^2 - (\boldsymbol{n} \cdot \boldsymbol{\nabla})^2 + 2\chi^{-1} \boldsymbol{n} \cdot \boldsymbol{\nabla} \, . \tag{4.8}$$

[1]There is a typo in the sign of the last term of Eq. (4.8) in [89]. The last term is neglected in [88], so that $\nabla_\perp^2$ as defined there is not the transverse Laplacian. This does not affect the final result, but it accounts for the difference in appearance between our expression and equation (31) of [88].

Eq. (4.7) contains Sachs-Wolfe and integrated SW contributions, together with the usual gravitational lensing term

$$\begin{aligned}\kappa_g &= \int_0^{\chi_s} d\chi(\chi_s-\chi)\frac{\chi}{\chi_s}\nabla_\perp^2\Psi \\ &\approx \frac{3}{2}H_0^2\Omega_m\int_0^{\chi_s} d\chi(\chi_s-\chi)\frac{\chi}{\chi_s}[1+z(\chi)]\delta,\end{aligned} \tag{4.9}$$

where the second line of Eq. (4.9) follows on the sub-Hubble scales of interest. Eq. (4.7) also includes a Doppler term from the observer's peculiar motion, but no Doppler term associated with the source.

The Doppler source term comes from the redshift perturbation; the redshift is distorted along a lightray by the volume expansion Θ and shear $\sigma_{\mu\nu}$ of the matter:

$$\frac{dz}{d\chi} = -\left[\frac{1}{3}\Theta + \sigma_{\mu\nu}n^\mu n^\nu\right](1+z)^2. \tag{4.10}$$

To linear order, this leads to

$$\left.\frac{\delta z}{1+\bar{z}}\right|_{\chi_s} = \left(\boldsymbol{v}_o - \boldsymbol{v}_s\right)\cdot\boldsymbol{n} + \Psi_o - \Psi_s - 2\int_0^{\chi_s} d\chi\,\Psi', \tag{4.11}$$

which contains SW and ISW terms, as well as the Doppler correction from the source's peculiar velocity $\boldsymbol{v}_s$. This term is the origin of the Doppler lensing contribution.

In Eqs. (4.7) and (4.11), $\chi_s = \chi(z_s)$ is the co-moving distance calculated in the background spacetime to the source which we infer from the *observed* redshift z_s, as opposed to the distance to the background redshift $\bar{z}$ which appears in Eq. (4.6). The difference between $\bar{z}$ and z_s does not affect first-order terms such as Eqs. (4.7) and (4.9) directly, as the relevant corrections are second-order. However, writing Eq. (4.6) in terms of z_s instead of $\bar{z}$ brings in important extra terms. The full perturbation to the angular diameter distance can be written in terms of the observed redshift of the source z_s by perturbatively expanding $\bar{z}$ in Eq. (4.6) and writing $a(\chi_s) = 1/(1+z_s)$ so that $H(z_s) = dz/d\chi\Big|_{\chi_s}$. We then find:

$$D_A(z_s) = \bar{D}_A(z_s)\left\{1 + \left.\frac{\delta D_A}{\bar{D}_A}\right|_{z_s} + \left[1 - \frac{1+z_s}{H(z_s)\chi_s(z_s)}\right]\left.\frac{\delta z}{1+\bar{z}}\right|_{z_s}\right\}. \tag{4.12}$$

Then the convergence for a source at observed redshift z_s follows from Eq. (4.4):

$$\kappa = \kappa_g + \kappa_v + \kappa_{\rm sw} + \kappa_{\rm isw}, \tag{4.13}$$

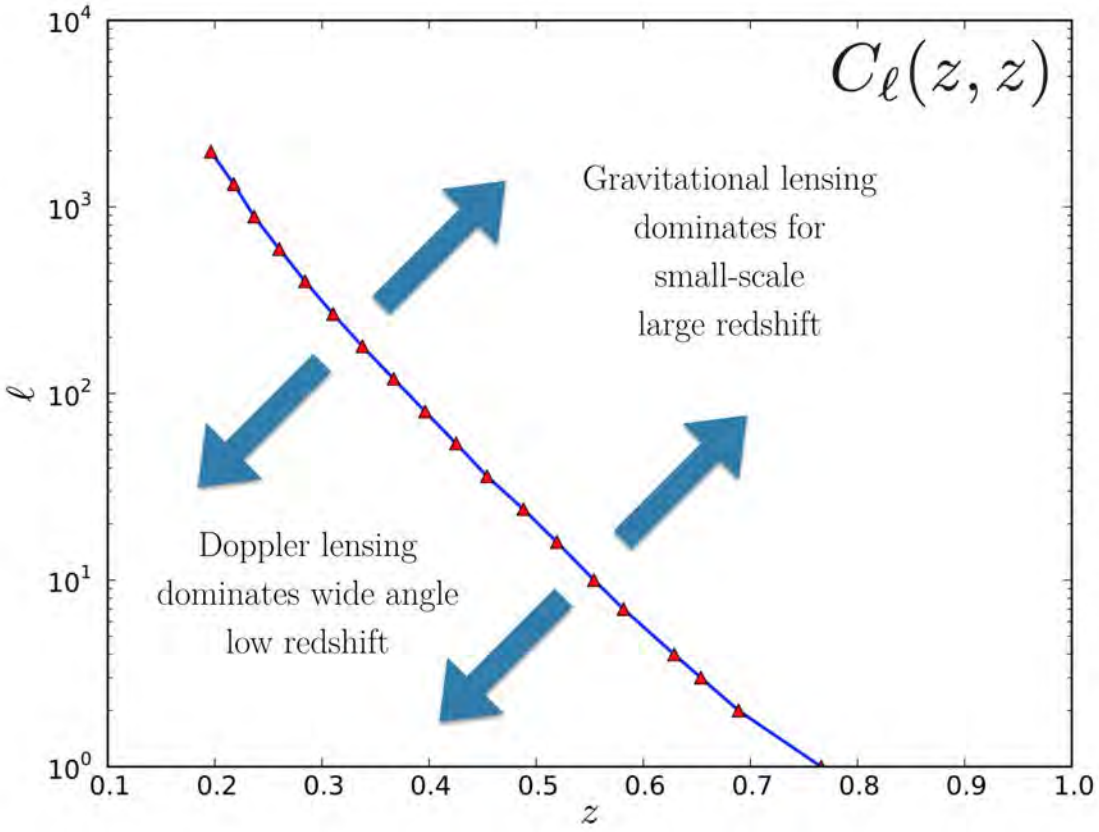

Figure 4.2: The curve shows where the power spectrum for an infinitesimal redshift slice of Doppler lensing (κ_v) equals that of standard gravitational lensing (κ_g). Doppler lensing dominates below the curve – on large scales (small ℓ) and small redshifts.

where we recall that the SW and ISW are given in Eqs. (3.12), (3.16),(3.18) and[2] and the gravitational lensing term κ_g is given by Eq. (4.9). The SW and ISW terms are generally sub-dominant to the other two contributions and can be neglected, so that

$$\kappa = \kappa_g + \kappa_v. \tag{4.15}$$

κ_v changes sign depending on whether objects are moving away from or towards us. Since $\boldsymbol{n}$ is the direction of photon propagation, $\boldsymbol{v}_s \cdot \boldsymbol{n} > 0$ for objects moving towards us and < 0 for objects moving away. At moderate redshift the term in brackets is negative; consequently,

- $\kappa_v < 0$ for objects moving towards us – implying that they appear smaller and dimmer

[2]In general, κ_v includes a term proportional to the peculiar velocity of the observer ($\boldsymbol{v}_o \cdot \boldsymbol{n}$)

$$\kappa_v = \frac{1+z_s}{H\chi_s}\boldsymbol{v}_o \cdot \boldsymbol{n} + \left(1 - \frac{1+z_s}{H\chi_s}\right)\boldsymbol{v}_s \cdot \boldsymbol{n}\,, \tag{4.14}$$

which leads to an overall dipole in the magnification. In all our calculations, we assume that this dipole is subtracted.

than typical objects at their observed redshift. Their angular distance is higher than inferred from the observed redshift.

- $\kappa_v > 0$ for objects moving away from us – they appear larger and brighter than typical objects at their observed redshift. Their angular distance is less than inferred from the observed redshift. In the case of objects at the far end of a void, this magnification is opposite to the demagnification from κ_g, leading to a significant anti-lensing effect [89].

With increasing redshift, the factor in brackets in Eq. (3.12) decreases in amplitude, so the magnitude of the Doppler lensing falls – while that of κ_g grows. The factor in brackets goes through zero at the maximum of $\bar{D}_A$, i.e. at $z \sim 1.5$ in ΛCDM. Therefore κ_v profiles change sign at high redshift; this is due to an effect which dominates at high redshift, in which the object's image experiences significantly more (or less) cosmic expansion than we inferred from its observed redshift.
On what scales is the Doppler lensing important? Using the estimate $|\boldsymbol{v}| \sim H_0\delta/k$, we expect the effect to be important on large scales. The factor in Eq. (4.30) is $\mathcal{O}(1)$ for $z \lesssim 1$, but its magnitude falls at high redshift. The region where the Doppler lensing dominates over standard gravitational lensing is shown in Fig. 4.2. This has been calculated as the points in wavenumber ℓ and redshift z where a Doppler lensing power spectrum equals that of a gravitational lensing power spectrum; see Section 6 for details of how we calculate the power spectrum (Eq. 4.53). We see that Doppler lensing dominates over gravitational lensing at medium-to-low redshifts and wavenumbers ($\ell \lesssim 1000$ at $z = 0.2$, and $\ell \lesssim 100$ at $z = 0.4$). As we will see in Section 6.3, the distinct redshift behaviour of Doppler lensing allows us to measure it at much higher redshifts as well.

4.3 Simulations

For the purpose of testing our Doppler lensing measurement techniques on observational data we construct two mock galaxy catalogues: 1) a wide-angle $50° \times 50°$ survey with galaxies having redshifts up to $z = 0.3$; and 2) a deep $10° \times 10°$ survey up to $z = 1$.

These mock catalogues were constructed using the data from the Millennium simulation [184, 185]. The Millennium simulation is an N-body simulation for a concordance cosmology ($\Omega_m = 0.25$, $\Omega_\Lambda = 0.75$, $H_0 = 73$ km s^{-1} Mpc $^{-1}$). It consists of approximately 10^9 particles of mass $8.6 \times 10^8 M_\odot h^{-1}$ within a cube of volume $(500h^{-1}$ Mpc$)^3$. The Millennium simulation is a pure dark matter simulation, but can be populated with galaxies using semi-analytic

galaxy formation models. For our mock catalogues we use the semi-analytic galaxies of [186]. Both data sets are accessible online[3].

The procedure for creating the mock catalogues is as follows: the observer is placed at the origin (X=0=Y=Z) of the Millennium box. Because of periodic boundary conditions, if the light ray exits the Millennium box, it enters the other side of the box with entry angles the same as the exit angles. The boundaries of the light cone are as follows: the angle between the X and Y axes is set to be between 36 and 86 deg, and the angle between the Z axis and XY plane is set to be between 2 and 52 deg. We then use the semi-analytic galaxies data of [186] (the SQL query `select snapnum, x,y,z,velX,velY,velZ,r_mag from Guo2010a..MR`). If a galaxy lies within the light cone boundaries (we check for single as well as multiple crossings of the Millennium box, and in addition we compare the time of propagation against the snapshot number) then we use the position and velocity data to calculate the cosmological distance, line of sight velocity, and redshifts (both the purely cosmological and the observed redshift affected by the peculiar velocity). Then using Eq. (3.12) we calculate the Doppler lensing. To calculate the gravitational lensing we using the dark matter distribution smoothed with a Gaussian kernel of $1.25h^{-1}$ Mpc (the SQL query `select snapnum, phkey, g1_25 from MField..MField`). The convergence κ_g is evaluated using Eq. (4.9). Finally, we calculate the observed magnitude

$$m = m_{\rm rest} + 5\log_{10} D_L + 25, \tag{4.16}$$

where

$$D_L(z_s) = (1+z_s)^2 \bar{D}_A(z_s)(1-\kappa_g-\kappa_v). \tag{4.17}$$

For the purpose of our studies we only select galaxies whose observed magnitude is brighter than 26 in the r SDSS band.

An example of a narrow light cone of 0.25 sq deg extracted from our mock catalogue is presented in Figs. 4.3 and 4.4. Fig. 4.3 shows the dark matter distribution and line of sight velocities of galaxies within this narrow light cone. We can see large variations in both distributions. The standard deviation of the line of sight velocities of all galaxies in the mock catalogue in the redshift range of 0 to 0.3 is approximately $v_{\rm rms} = 355$ km/s, while the average velocity (in any direction) is approximately $\bar{v} = 535$ km/s. As seen from the lower panel, most velocities of galaxies are within this range, with occasional spikes that are seen around large overdensities in the vicinity of large voids - for example at $z \approx 0.195$ and $z \approx 0.268$ where the density contrast is $\delta \approx 14.3$ and $\delta \approx 21.5$, respectively, and the line of

[3] `http://gavo.mpa-garching.mpg.de/MyMillennium`

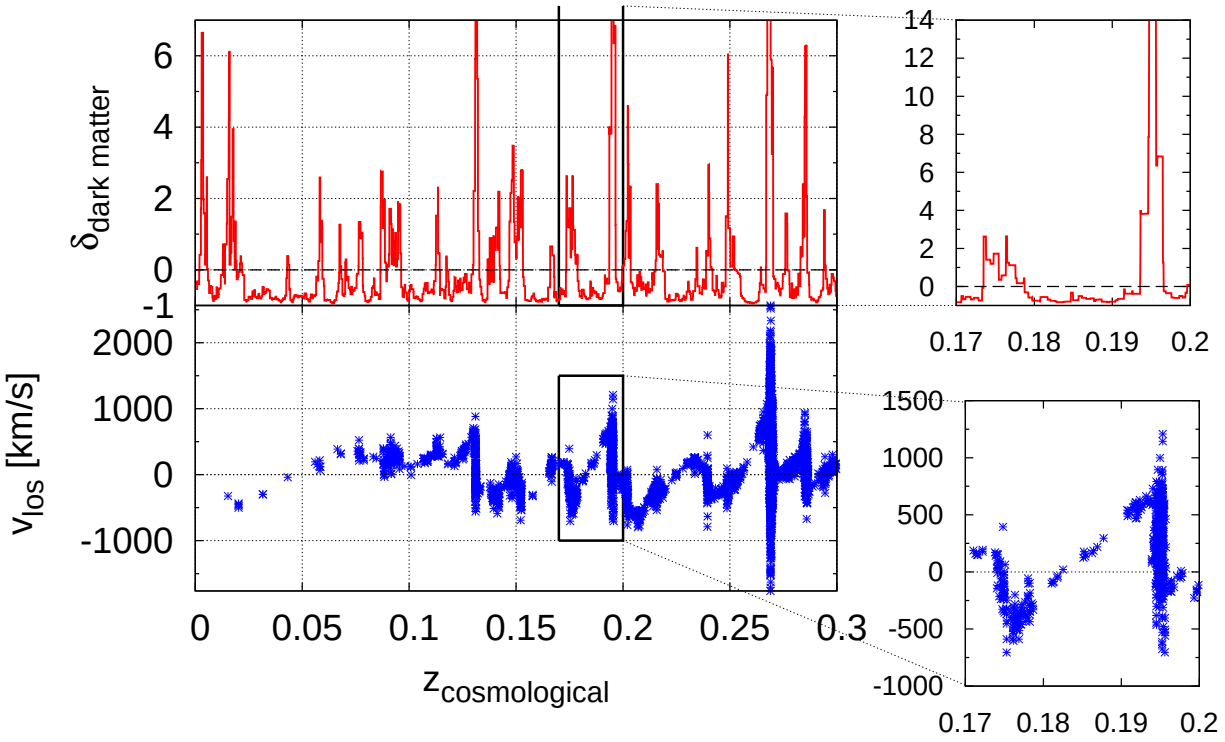

Figure 4.3: Dark matter distribution (δ) and the line of sight velocity ($v_{\rm los} = -\boldsymbol{v}\cdot\boldsymbol{n}$) within a narrow light cone of 0.25 sq deg, as a function of background cosmological redshift $z_{\rm cosmological} = \bar{z}$ (i.e. unaffected by the motion of galaxies).

sight velocity is $v_{\rm los} \approx 1200$ km/s and $v_{\rm los} \approx 2500$ km/s respectively.

As explained in Section 4.2, both the matter distribution along the line of sight and the peculiar velocities of galaxies contribute to convergence, and via convergence they affect the observed size and magnitude of galaxies. These effects are presented in Fig. 4.4. The gravitational lensing is an integrated effect, and so the induced gravitational convergence is a slowly varying function, without such a large variation as the Doppler convergence, which is a local phenomenon. We see that for redshifts below 0.3 the Doppler lensing dominates in the convergence, $\kappa \approx \kappa_v \gg \kappa_\delta$. Therefore, in this redshift range the convergence κ traces the local velocity field rather than the integrated density field along the line of sight, as is expected given the predictions presented in Fig. 4.2. We see that the Doppler lensing also significantly affects the change in magnitude of galaxies, which is presented in the lower panel of Fig. 4.4 and evaluated as

$$\Delta m = 5\log_{10}(1-\kappa_v-\kappa_\delta). \tag{4.18}$$

The shape and the amplitude of Δm around cosmic voids seen in Fig. 4.4 is comparable

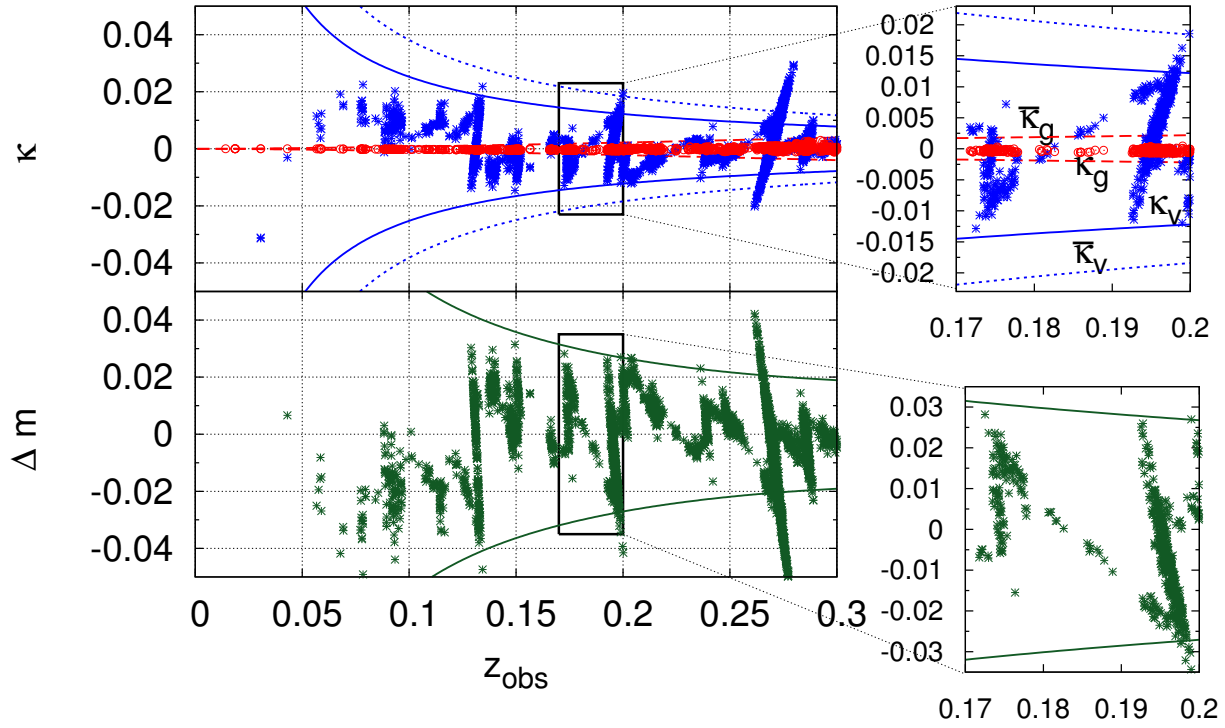

Figure 4.4: Observed convergence (κ) and the resulting change in magnitude (Δm), within a narrow light cone of 0.25 sq deg, as a function of the observed redshift (i.e. affected by the motion of galaxies). The convergence κ is presented in the upper panel; the Doppler convergence κ_v is shown using stars, and the gravitational convergence κ_g using open circles. The dashed line presents the predicted standard deviation of the gravitational lensing signal from Eq. (4.19), and the solid and dotted lines present the predicted variation of Doppler lensing evaluated from Eq. (3.12) with $v_s = 355$ km/s and $v_s = 535$ km/s respectively. The change in magnitude $\Delta m = 5\log_{10}(1 - \kappa_v - \kappa_g)$ is presented in the lower panel; the solid line show the predicted variation $\Delta\bar{m} = 5\log_{10}[1 - (\bar{\kappa}_v^2 + \bar{\kappa}_g^2)^{1/2}]$.

with that reported by [89], whose results were based on analytical models of single structures embedded in the otherwise homogeneous Universe. Note the behaviour of the convergence and magnitude around non-linear structures, where we obtain steep two-valued functions of redshift. This is caused by the conversion from background redshift to observed redshift (and is a contribution to the Doppler lensing effect which is not captured by our first order treatment in Section 4.2).

We also compare data from this narrow light cone with the expected amplitude of the Doppler lensing $\bar{\kappa}_v$ and gravitational lensing $\bar{\kappa}_g$. The predicted standard deviation of Doppler lensing is evaluated from Eq. (3.12) and is presented in the top panel of Fig. 4.4 with solid and dotted lines (for velocity $v = v_{\rm rms} = 355$ km/s and $v = \bar{v} = 535$ km/s respectively). The

predicted variation of gravitational lensing is evaluated from

$$\bar{\kappa}_g^2 = \frac{9}{4}\Omega_m^2 H_0^4 \int_0^{\chi_s} \mathrm{d}\chi \left[(1+z)\frac{\chi_s - \chi}{\chi_s}\chi\right]^2 \int_0^{\infty} \mathrm{d}k\ k\frac{P(k,z)}{2\pi}, \tag{4.19}$$

and this corresponds to the dashed curve in the upper panel of Fig. 4.4. Similarly, the expected variation of magnitude

$$\Delta\bar{m} = 5\log_{10}[1 - (\bar{\kappa}_v^2 + \bar{\kappa}_g^2)^{1/2}], \tag{4.20}$$

accurately predicts the variation in magnitude within the light cone. Both the convergence and the change in magnitude seen in the figure appear to be within reasonable observational limits, and therefore we might expect to measure them with prospective surveys. We will now turn to the issue of making predictions for the Doppler lensing effect with such surveys.

4.4 Prospective Surveys

In Sections 4.5 to 4.7 we will make predictions for measuring Doppler lensing signals with a selection of realistic cosmological survey configurations, representative of forthcoming surveys. We will examine the prospects with three imaging surveys of increasing size, each with dense spectroscopic follow-up:

(i) A 5000 square deg imaging survey, such as that being carried out with the Dark Energy Survey (DES)[4]. We suppose that convergence estimators will exist for all galaxies observed in redshift range $0.1 < z < 0.3$; we posit dense spectroscopic follow-up for $0.1 < z < 0.3$ from e.g. 2dF and SDSS overlap regions, plus further spectroscopic redshift campaigns. We assume a number density of objects in the spectroscopic sample of 0.7 per sq arcmin.

(ii) A 15000 square deg imaging survey, such as that planned with the Euclid space telescope[5] [180]. Again we include convergence estimators for a sub-sample of the photometrically observed galaxies, for which we assume we have spectroscopic redshifts, obtained with a dense follow-up survey. This subsample has redshifts $0.1 < z < 0.3$ with number density 0.7 per sq arcmin.

[4]http://www.darkenergysurvey.org/
[5]http://www.euclid-ec.org

(iii) A 30000 square degree imaging survey, such as the Phase I and/or II Square Kilometre Array (SKA, [187]) could achieve. We choose the same galaxy redshift range and density as before, and suppose that HI spectroscopic redshifts will be available for this galaxy catalogue.

In each of these three cases we assume the same convergence estimator intrinsic noise of $\sigma_\kappa = 0.3$ throughout the spectroscopic sample. Notice that in this Chapter, we are restricting ourselves to a survey in the redshift range $0.1 < z < 0.3$; this is very conservative, as there is a recoverable Doppler lensing signal at higher redshifts too (see Section 6.3). However, at these higher redshifts, one needs to disentangle the gravitational and Doppler lensing signals; while we sketch the way to achieve this in Section 6.3, we defer detailed predictions for this more complicated case to a future work.

We now turn to assessing the viability of detecting and utilising Doppler lensing with forthcoming surveys.

4.5 Measuring the signal around stacked overdensities

As an introductory example of Doppler lensing signals which can be measured, we consider the Doppler convergence in a spherical region around an over or under-density, e.g. a void or supercluster – this idealised case was shown to give significant Doppler lensing in [89].

Averaging the convergence κ_v over the objects in the spherical region will lead to a value close to zero, since the Doppler convergence in front of the over- or under-density centre will have the opposite sign to that behind the centre which shows the signal in front of and behind a void centre, and Figure 1 in [89].

To avoid this, we can instead average in the sphere the quantity $\kappa_v \cos\theta$, where θ is the angle between the line of sight and the line connecting the overdensity centre to the lensed galaxy. We will consider a spherically symmetric velocity profile $v(r)$, where r is the distance from the centre of the overdensity, which we assume is much smaller than its distance from the observer. Redshift space distortions will squeeze the sphere into an oblate spheroid in redshift space, but the ellipsoidality of this spheroid is less than 10% on 50Mpc scales and we neglect this distortion in our locus of averaging here. The component of velocity along the line of sight is $v(r)\cos\theta$, so $\kappa_v \cos\theta$ is proportional to $\cos^2\theta$. Averaging over all spherical

annuli of volume $2\pi r^2 \sin\theta d\theta dr$ out to radius R, we obtain

$$\langle \kappa_v \cos\theta \rangle \simeq \frac{A}{3} \int_0^R dr\, n(r) v(r) r^2 \Big/ \int_0^R dr\, n(r) r^2 \tag{4.21}$$

where $n(r)$ is the 3D number density of objects at radius r and $A = (1 - 1/a\chi H)$, assumed here to be approximately constant over the radius of the overdensity. The error on $\langle \kappa_v \cos\theta \rangle$ is given by

$$\langle \sigma^2 \rangle = \frac{\sigma_\kappa^2}{3} \Big/ \int_0^R dr\, n(r) r^2 \tag{4.22}$$

where σ_κ is the intrinsic dispersion on the convergence estimator for an object. In the simple case where the number density of objects is considered to be uniform throughout, denoted $\bar{n}$, the signal-to-noise for measuring $\kappa_v \cos\theta$ is

$$\frac{S}{N} = \frac{2\pi^{1/2} A}{3} \frac{\bar{v} R^{3/2} \bar{n}^{1/2}}{\sigma_\kappa} \tag{4.23}$$

where $\bar{v}$ is a typical velocity defined by the ratio of integrals in Eq. (4.21).

We show the resulting signal-to-noise for measuring the $\kappa_v \cos\theta$ signal around stacks of 100 over/under-densities in Fig. 4.5. Note that here we are examining an optimal situation where these voids are spherical and all of the same size and profile. We show the result for spherical averaging in a radius of 50Mpc, with $\bar{v} = 100\text{kms}^{-1}$; Eq. (4.23) shows how to scale for different choices of $\bar{v}$ and radius. We see that it may just be feasible to detect the Doppler lensing in this fashion, with acceptable S/N of > 5, and it is considerably easier to do this at low redshift (i.e. we do not have to stack so many overdensities). We also see that at no redshift is the measurement feasible for a single void or cluster; stacking would always be necessary. This naturally leads us on to consider other more powerful statistical approaches to measuring Doppler lensing.

4.6 Two point statistics

We now describe suitable two-point statistics for Doppler lensing, which can be measured with forthcoming surveys. We calculate the uncertainties on these statistics for the surveys described in Section 4.4, and show predictions for cosmological parameters from these statistics. We discuss the systematic effects which could afflict the Doppler lensing measurements, and describe how some of these can be mitigated.

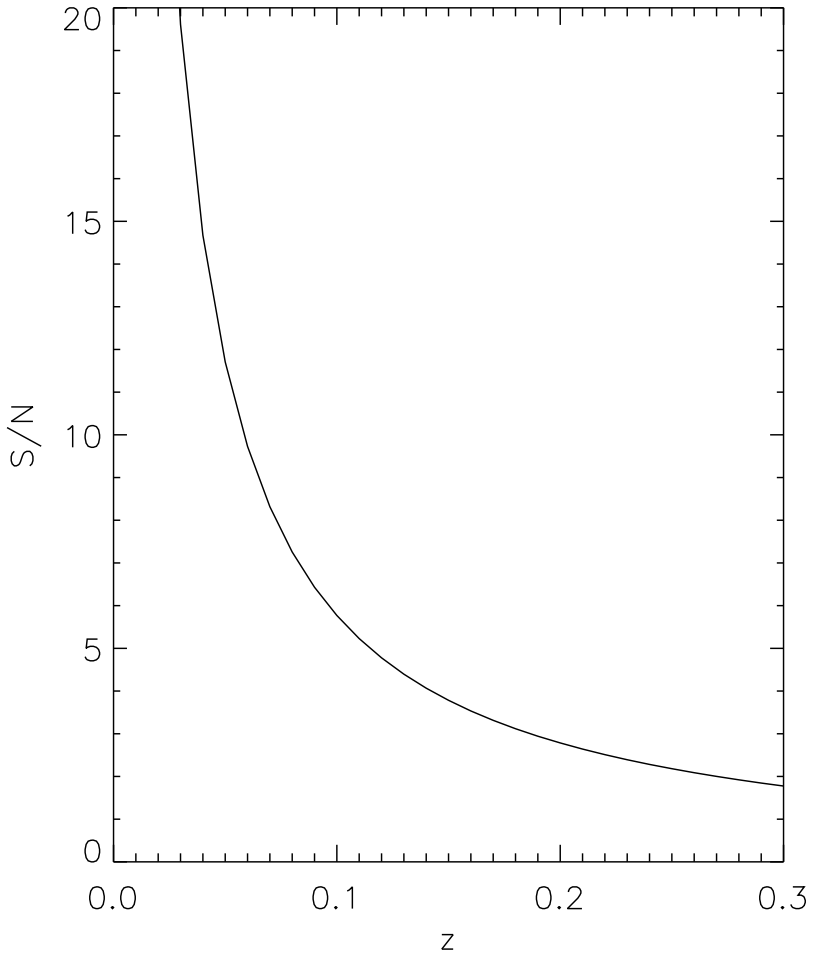

Figure 4.5: Signal-to-noise for measuring the signal for 100 stacked overdensities, with characteristic velocity $\bar{v} = 100\text{kms}^{-1}$ and radius $R = 50\text{Mpc}$, as a function of redshift.

4.6.1 Overdensity-convergence cross-correlation

We will first consider the cross-correlation between the overdensity δ and the Doppler convergence κ_v. We expect there to be a substantial cross-correlation between these quantities, as overdensities generate the gravitational potential wells which galaxies will fall into with some velocity - and velocity generates Doppler convergence. However, care needs to be taken in constructing a suitable statistic, as velocities from galaxies moving away from us could cancel with velocities moving towards us.

Both the density fluctuation and the Doppler convergence are, at a given redshift, scalar functions on the sky, so one can expand them in spherical harmonics. In direction on the sky $\boldsymbol{\theta} = -\boldsymbol{n}$ opposite to the photon direction, we have

$$\begin{aligned} \kappa_v(z,\boldsymbol{\theta}) &= \sum_{\ell m} \kappa^v_{\ell m}(z) Y_{\ell m}(\boldsymbol{\theta}) = -\kappa_v(z,\boldsymbol{n})\,, \\ \delta(z,\boldsymbol{\theta}) &= \sum_{\ell m} \delta_{\ell m}(z) Y_{\ell m}(\boldsymbol{\theta}) = \delta(z,\boldsymbol{n})\,. \end{aligned} \tag{4.24}$$

The coefficients $\delta_{\ell m}(z)$ and $\kappa^v_{\ell m}(z)$ are obtained from

$$\begin{aligned} \delta_{\ell m}(z) &= \int d\Omega_{\boldsymbol{\theta}} Y^*_{\ell m}(\boldsymbol{\theta}) \delta(z,\boldsymbol{\theta}), \\ \kappa^v_{\ell m}(z) &= \int d\Omega_{\boldsymbol{\theta}} Y^*_{\ell m}(\boldsymbol{\theta}) \kappa_v(z,\boldsymbol{\theta}). \end{aligned} \tag{4.25}$$

The angular cross-power spectrum $C_\ell^{\delta\kappa_v}$ can then be extracted from the average

$$\langle \delta_{\ell m}(z) \kappa^{v*}_{\ell' m'}(z') \rangle = C_\ell^{\delta\kappa_v}(z,z') \delta_{\ell\ell'} \delta_{mm'}\,. \tag{4.26}$$

We can also calculate the correlation function between two objects separated by angle θ:

$$\xi^{\delta\kappa_v}(z,z';\theta) = \sum_{\ell=0}^{\ell_{\rm max}} \frac{2\ell+1}{4\pi} C_\ell^{\delta\kappa_v}(z,z') P_\ell(\theta)\,, \tag{4.27}$$

where P_ℓ are the Legendre polynomials. In order to calculate the cross-power spectrum $C_\ell^{\delta\kappa_v}$, we need to obtain spherical harmonic decomposition coefficients for both the overdensity and the Doppler convergence. We use the same convention in Eq. (2.98) for the Fourier decomposition and Eq. (2.99) for the power spectrum. Taking the Fourier transform of Eq. (2.90), ignoring the sub-dominant term proportional to $(a\Psi)'$, and expanding the plane

wave in spherical harmonics, the galaxy overdensity reads

$$\delta_g(z,\boldsymbol{\theta}) = -\frac{2}{3H_0^2\Omega_m}a(z)b(z)4\pi\sum_{\ell m}\int\frac{d^3\boldsymbol{k}}{(2\pi)^{3/2}}k^2\Psi(\boldsymbol{k},\eta)i^\ell j_\ell(k\chi)Y_{\ell m}(\hat{\boldsymbol{k}})Y_{\ell m}(\boldsymbol{\theta}), \tag{4.28}$$

where we have expanded the exponential in terms of spherical Bessel functions j_ℓ in the usual way. In this equation we have introduced a linear bias $b(z)$ relating the galaxy overdensity to the total matter overdensity, $\delta_g(z) = b(z)\delta(z)$; from now on we will suppress the subscript g.

We now introduce a window function $W_1(z)$ over which we will consider the overdensity (this is the range of one tomographic bin). We can write the averaged overdensity in this thick redshift shell as

$$\delta(\boldsymbol{\theta}) = -\frac{8\pi}{3H_0^2\Omega_m}\sum_{\ell m}\int_{z_{\min}}^{z_{\max}}dzW_1(z)a(z)b(z)\int\frac{d^3\boldsymbol{k}}{(2\pi)^{3/2}}k^2\Psi(\boldsymbol{k},\eta)i^\ell j_\ell(k\chi)Y_{\ell m}(\hat{\boldsymbol{k}})Y_{\ell m}(\boldsymbol{\theta}). \tag{4.29}$$

We are then able to read off the coefficients for the spherical harmonic decomposition of $\delta(\boldsymbol{\theta})$,

$$\delta_{\ell m} = -\frac{8\pi}{3H_0^2\Omega_m}\int_{z_{\min}}^{z_{\max}}dzW_1(z)a(z)b(z)\int\frac{d^3\boldsymbol{k}}{(2\pi)^{3/2}}k^2\Psi(\boldsymbol{k},\eta)i^\ell j_\ell(k\chi)Y_{\ell m}(\hat{\boldsymbol{k}}).$$

Now we turn to the Doppler convergence which we recall

$$\kappa_v(z,\boldsymbol{\theta}) = -\left[1-\frac{1+z}{\chi H}\right]\boldsymbol{v}\cdot\boldsymbol{\theta} \tag{4.30}$$

and smoothing in redshift space yields

$$\kappa_v(\boldsymbol{\theta}) = \int_{z_{\min}}^{z_{\max}}dzW_2(z,z')\kappa_v(z,\boldsymbol{\theta}) \tag{4.31}$$

The weight function W_2 is specified in Eq. (4.42); it depends additionally upon the redshift z' of the δ bin which we will correlate with. The Fourier decomposition of the convergence reads

$$\kappa_v(\boldsymbol{\theta}) = \frac{2}{3\Omega_m H_0^2}\int_{z_{\min}}^{z_{\max}}dzW_2(z,z')a(z)\left[1-\frac{1}{\chi aH}\right]\int\frac{d^3\boldsymbol{k}}{(2\pi)^{3/2}}\Psi(\boldsymbol{k},\eta)\boldsymbol{\theta}\cdot\boldsymbol{\nabla}(e^{i\boldsymbol{k}\cdot\boldsymbol{x}}) \tag{4.32}$$

We expand the exponential in spherical harmonics while taking its spatial derivative along

the line of sight and obtain

$$\kappa_v(\boldsymbol{\theta}) = \frac{8\pi}{3\Omega_m H_0^2}\int_{z_{\rm min}}^{z_{\rm max}} dz W_2(z,z')a(z)\left[1-\frac{1}{\chi a H}\right]\sum_{\ell m}\int\frac{d^3\boldsymbol{k}}{(2\pi)^{3/2}}\Psi(\boldsymbol{k},\eta)i^\ell k j_\ell'(k\chi)Y_{\ell m}(\hat{\boldsymbol{k}})Y_{\ell m}(\boldsymbol{\theta}). \tag{4.33}$$

We can now read off the coefficients for the spherical harmonic decomposition of Doppler convergence,

$$\kappa^v_{\ell m} = \frac{8\pi}{3\Omega_m H_0^2}\int_{z_{\rm min}}^{z_{\rm max}} dz W_2(z,z')a(z)\left[1-\frac{1}{\chi a H}\right]\int\frac{d^3\boldsymbol{k}}{(2\pi)^{3/2}}\Psi(\boldsymbol{k},\eta)i^\ell k j_\ell'(k\chi)Y_{\ell m}(\hat{\boldsymbol{k}}). \tag{4.34}$$

The angular cross-power spectrum for a particular tomographic bin can now be easily deduced, as

$$\begin{aligned}\langle\delta_{\ell m}\kappa^{v*}_{\ell' m'}\rangle &= \delta_{\ell\ell'}\delta_{mm'}\frac{16\pi}{(3H_0^2\Omega_m)^2}\int_0^\infty dk k^2 T^2(k)\mathcal{P}_{\Psi_i}(k)\int_{z_{\rm min}}^{z_{\rm max}} dz W_1(z)a(z)b(z)j_\ell(k\chi(z))g(z)\\ &\times\int_{z_{\rm min}}^{z_{\rm max}} dz' W_2(z',z)\left[\frac{1}{\chi(z')H(z')}-a(z')\right]\mathcal{G}(z')j_\ell'(k\chi(z'))\end{aligned} \tag{4.35}$$

where we have used Eq. (2.99). In addition, we have written the potential power spectrum $\mathcal{P}_\Psi$ in terms of the primordial power spectrum $\mathcal{P}_{\Psi_i}(k)$,

$$\mathcal{P}_\Psi(k,\chi,\chi') = \mathcal{P}_{\Psi_i}(k)\tilde{T}(k,\chi)\tilde{T}(k,\chi') \tag{4.36}$$

where

$$\tilde{T}(k,\chi) = T(k)\mathcal{G}(\chi) \tag{4.37}$$

and

$$\mathcal{G}(\chi) = g'(\chi) + aHg(\chi) \tag{4.38}$$

where $g(\chi)$ is the growth suppression factor, and $T(k)$ is the transfer function. It is then straightforward to deduce $C_\ell^{\delta\kappa_v}$

$$\begin{aligned}C_\ell^{\delta\kappa_v}(z,z') &= \frac{16\pi}{\left(3H_0^2\Omega_m\right)^2}\int_0^\infty dk k^2 T^2(k)\mathcal{P}_{\Psi_i}(k)g(z)b(z)j_\ell(k\chi(z))\\ &\times\left[\left(\frac{1}{\chi(z')H(z')}-a(z')\right)\mathcal{G}(z')j_\ell'(k\chi(z'))\right]\end{aligned} \tag{4.39}$$

The definition of $\mathcal{G}(z)$ is provided by Eq. (4.38), $g(z)$ is the growth suppression factor, and $b(z)$ is the linear galaxy bias. In a real survey, we will examine the cross-correlation in redshift bins of finite width. This is taken into account using window functions W in the

radial direction. The cross-power spectrum for a particular tomographic bin from Eq. (4.26) and Eq. (4.35) then reads

$$\begin{aligned}\tilde{C}_\ell^{\delta\kappa_v} &= \frac{1}{N}\int_{z_{\min}}^{z_{\max}} dz' W_1(z') \int_{z_{\min}}^{z_{\max}} dz W_2(z,z') C_\ell^{\delta\kappa_v}(z',z) \\ &= \frac{16\pi}{N\left(3H_0^2\Omega_m\right)^2}\int_0^\infty dk k^2 T^2(k)\mathcal{P}_{\Psi_i}(k) \\ &\quad \times \int_{z_{\min}}^{z_{\max}} dz' W_1(z') g(z') b(z') j_\ell(k\chi(z')) \\ &\quad \times \int_{z_{\min}}^{z_{\max}} dz W_2(z,z') \left(\frac{1}{\chi(z)H(z)} - a(z)\right) \mathcal{G}(z) j_\ell'(k\chi(z))\end{aligned} \tag{4.40}$$

where N is a normalization factor. As realistic examples of what could be measured by a survey, we choose (i) a thick bin of width $\Delta z = 0.2$ between $z_{\min} = 0.1$ and $z_{\max} = 0.3$, and (ii) two thick tomographic bins of width $\Delta z = 0.1$ between $z_{\min} = 0.1$ and $z_{\max} = 0.3$. The Doppler lensing prevails over gravitational lensing at low and intermediate redshift, and we will therefore neglect the latter. We select the galaxy density fluctuations δ_g in these thick redshift bins using the window function

$$W_1(z) = n(z)\Theta(z - 0.1)(1 - \Theta(z - 0.3)) \tag{4.41}$$

and the equivalent for the tomographic bins; the galaxy redshift distribution in the bins is approximated as $n(z) \propto z^2$ where the proportionality constant is chosen to give the required galaxy density, and Θ is the Heaviside function.

We need to be careful in selecting appropriate objects with measured convergences to cross-correlate with these galaxy density fluctuations. Since an overdensity only generates infall velocities over a relatively small distance (or redshift range), we only consider count-convergence pairs for which the two points are within a redshift distance of each other $\Delta z = 0.02$. In addition, we need to avoid averaging Doppler convergences in front of and behind an overdensity, as these cancel each other out (c.f. Section 4.5). This is achieved by using a one-sided top hat function for the second window function,

$$W_2(z, z') = n(z)\Theta(z - z')(1 - \Theta(z - z' - 0.02)) \tag{4.42}$$

where z' is the redshift of the overdensity, in front of the convergence at redshift z. The cross-power for convergence in front of overdensities has the same amplitude and opposite sign, so we will average the absolute value of these two signals, reducing the noise on the power by a factor of $\sqrt{2}$.

As can be noticed from Eq. (4.40), the computation is quite expensive as it involves three integrals. To circumvent this issue, we subdivide each thick bin into thin shells, so the computation of the cross-correlation for each thin shell involves only two integrals. For each thin shell, we fix the redshift of the overdensities, then compute the two point function between this overdensity slice and the convergences behind it within a bin of width $\Delta z = 0.02$. The angular cross-power spectrum within a thin shell then reads

$$C_\ell^{\delta\kappa_v}(z') = \frac{1}{N(z')}\int_{z_{\min}}^{z_{\max}} dz W_2(z,z') C_\ell^{\delta\kappa_v}(z',z) \tag{4.43}$$

$$= \frac{16\pi}{N\left(3H_0^2\Omega_m\right)^2}\int_0^\infty dk T^2(k) k^2 \mathcal{P}_{\Psi_i} g(z') b(z') j_\ell(k\chi(z')) \times \int_{z_{\min}}^{z_{\max}} dz W_2(z,z') \left(\frac{1}{\chi(z)H(z)} - a(z)\right) \mathcal{G}(z) j_\ell'(k\chi(z)) \tag{4.44}$$

with the normalization factor

$$N(z') = \int_{z_{\min}}^{z_{\max}} dz W_2(z,z'). \tag{4.45}$$

(When we write $C_\ell^{\delta\kappa_v}$ with one argument (z) rather than two (z,z') we are referring to Eq. (4.44).) We finally take the average of all the $C_\ell^{\delta\kappa_v}(z)$ related to each thin shell to obtain the total angular cross-correlation within a thick bin,

$$\bar{C}_\ell^{\delta\kappa_v} = \frac{\sum z_i^2 C_\ell^{\delta\kappa_v}(z_i)}{\sum z_i^2}. \tag{4.46}$$

The average angular power spectrum $\bar{C}_\ell^{\delta\kappa_v}$ for $0.1 < z < 0.3$ is shown in Figure 4.6 (top panel). To account for the non-linear evolution of the potential on small scales, the cross-power was computed using the HALOFIT formula [173], modifying the growth and transfer function. In our calculations, the non-linear matter power spectrum was generated using CAMB [108, 188], then the effective growth suppression factor becomes dependent on both redshift and wavenumber due to non-linearity, and is computed as

$$g_{NL}(z,k) = (1+z)\sqrt{\frac{P_{NL}(z,k)}{P(k)}} \tag{4.47}$$

where $P_{NL}(z,k)$ is the non-linear matter power spectrum, and $P(k)$ is the present day linear matter power spectrum. At small k (large scales) we have $g_{NL}(z,k) \simeq g(z)$; the non-linear part of the growth suppression factor comes into play when k is large (small scales).

To assess the detectability of the signal, we have computed the error bars for the three different surveys in Section 4.4, with sky coverage $f_{sky} = 1/8, 3/8$, and $3/4$ respectively. The errors, including cosmic variance and Poisson noise, are estimated as [189]

$$\Delta\bar{C}_\ell^2 = \frac{1}{(2\ell+1)f_{sky}}\left[\left(\bar{C}_\ell^{\delta\kappa_v}\right)^2 + \left(\bar{C}_v^{\kappa_v\kappa_v} + \frac{\sigma_\kappa^2}{n_\kappa}\right)\left(\bar{C}_\ell^{\delta\delta} + \frac{1}{n_g}\right)\right] \tag{4.48}$$

where n_κ is the number density of the thin convergence bin and n_g is the number density of the thick bin in question. Fig. 4.6 (top panel) shows the errors (shaded area) corresponding to each survey. The signal can be measured over a wide range in wavenumber in all three survey configurations; note that the error is on each individual ℓ, so band averaging can be used to measure the signal to high ℓ. The errors are large on low ℓ modes due to cosmic variance, and are large at high ℓ due to the limited number of objects at small scales. In addition, we expect that gravitational lensing will dominate over the doppler lensing signal presented here for $\ell \gtrsim 1000$ (see Fig. 4.2).

We can now calculate the angular correlation function in real space, using Eq. (4.27). To compute the errors on this quantity, we use

$$\sigma_\xi^2(\theta_i, \Delta\theta) \simeq \sum_0^{\ell_{max}} \Delta\bar{C}_\ell^2 \left(\frac{2\ell+1}{4\pi}\right)^2 \frac{P_\ell(\theta_i) + P_\ell(\theta_{i+1})}{\Delta\theta^2} \tag{4.49}$$

where $\Delta\theta$ is the angular bin size; here we choose $\Delta\theta = 6'$. The correlation function and errors for different surveys, for one thick redshift slice $0.1 < z < 0.3$, are shown in the lower panel of Fig. 4.6; notice the small error bars on this statistic for each of our prospective surveys.

We can obtain from these statistics estimates of constraints on cosmological parameters, using the Fisher information matrix. This is given here by [189]

$$F_{\alpha\beta} = f_{\rm sky}\sum_\ell (2\ell+1)\frac{\partial\bar{C}_\ell^{\delta\kappa_v}}{\partial X_\alpha}\frac{\partial\bar{C}_\ell^{\delta\kappa_v}}{\partial X_\beta}\frac{1}{\Delta\bar{C}_\ell^2} \tag{4.50}$$

where X_α is the set of cosmological parameters we consider. Here we choose $\boldsymbol{X} = \{A, b, h, \Omega_b, \Omega_m, w_0\}$, where A is the primordial power spectrum amplitude, b is the linear galaxy bias, h is the Hubble parameter, Ω_b is the baryon density parameter, Ω_m is the total matter density parameter, and w_0 is the dark energy equation of state. We calculate this Fisher matrix using wavenumbers $1 < \ell < 1000$. Assuming the parameter likelihood is approximately a multivariate Gaussian around its peak, the Fisher matrix is the inverse of the covariance

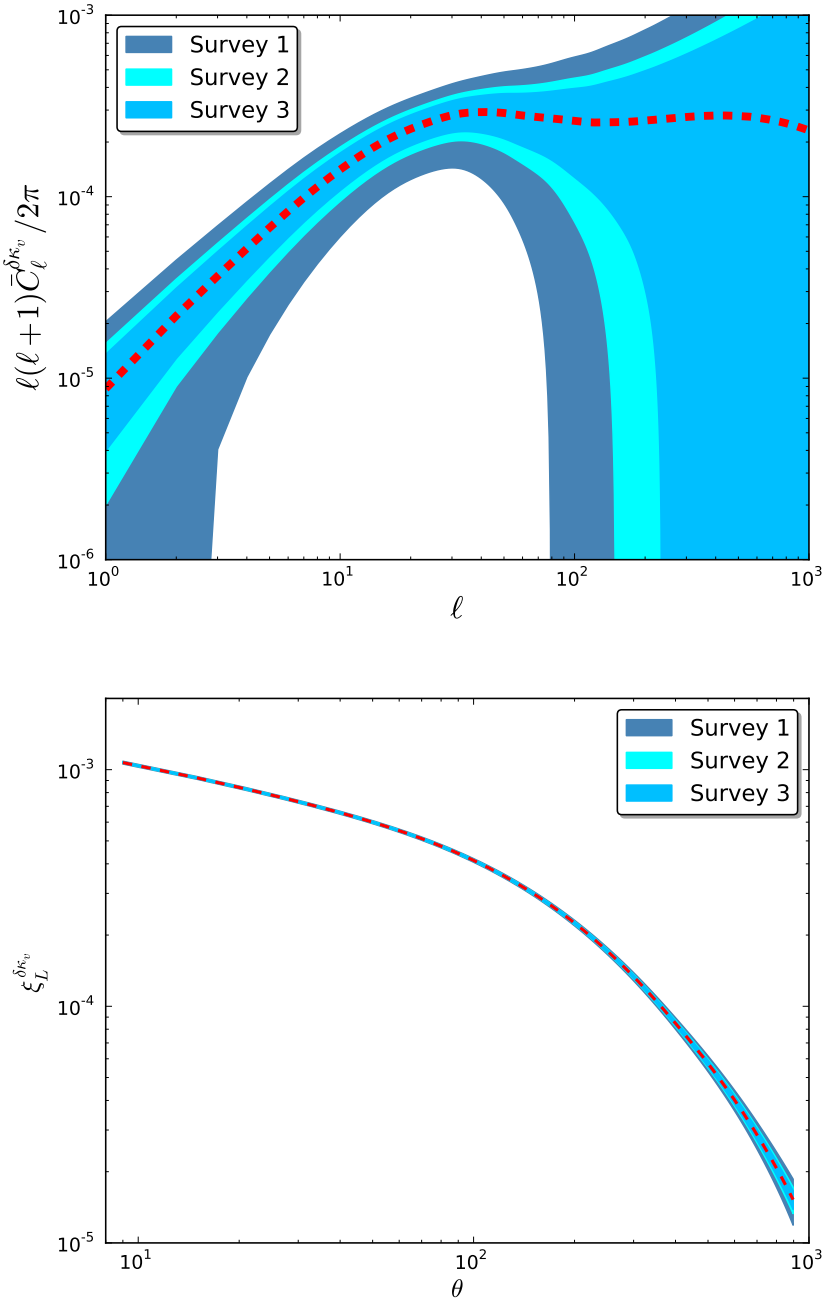

Figure 4.6: Top: average angular cross-power spectrum $\bar{C}^{\delta\kappa_v}$. The errors are computed by considering the three surveys with sky coverage $f_{\rm sky} = 1/8, 3/8, 3/4$ respectively. Doppler lensing dominates over gravitational lensing for $\ell \lesssim 1000$. Bottom: corresponding average angular cross-correlation $\xi^{\delta\kappa_v}$ in real space as a function of angle θ in arcmin, in angular bins of width $6'$.

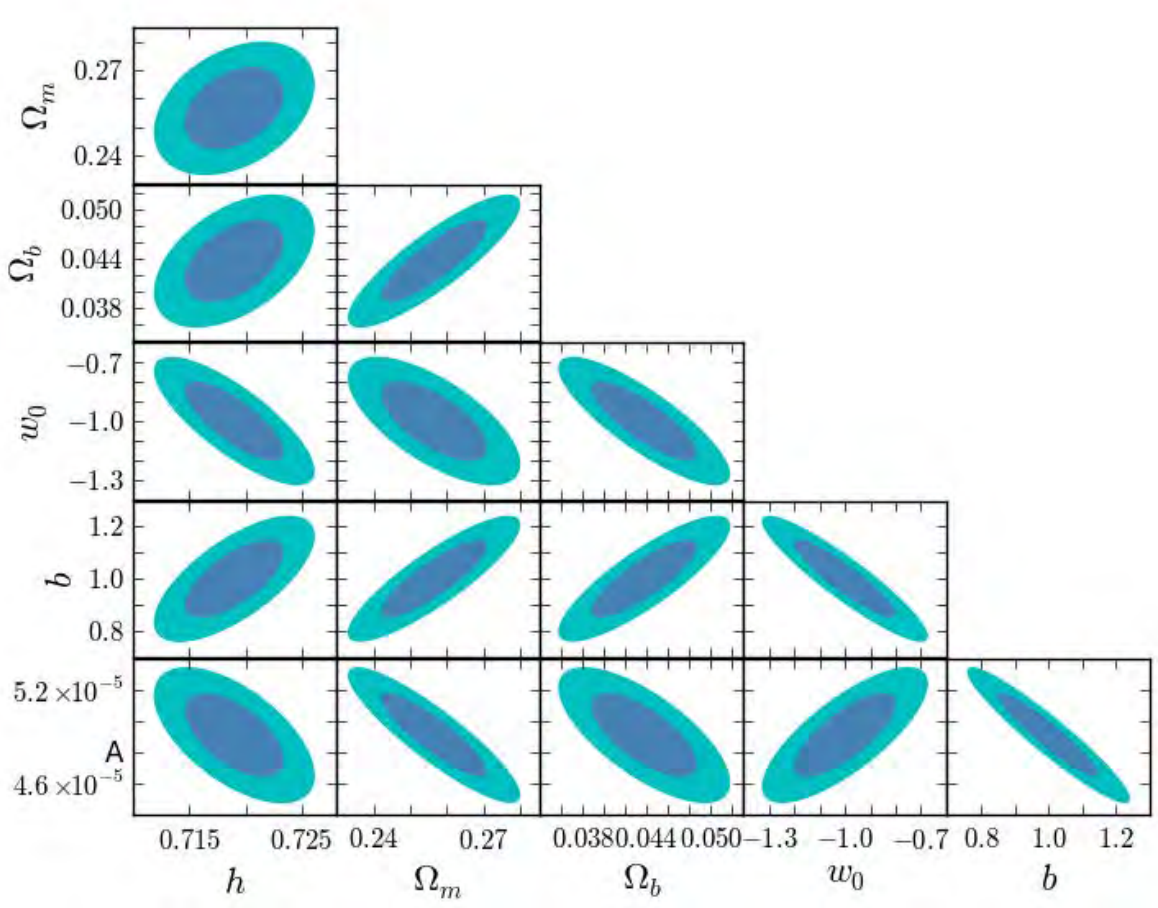

Figure 4.7: 68% (blue) and 95% (light blue) confidence ellipses for cosmological parameters. Here, survey (iii) is used to compute the Fisher matrix, with two low redshift tomographic bins.

matrix of the parameters; in Fig. 4.7, we show the resulting 68% and 95% CL ellipses for pairs of cosmological parameters, where the other cosmological parameters have been marginalised over. We show the results for the two tomographic bin case, for survey (iii) with no other cosmological information (e.g. Planck or supernovae priors). We see that the constraints are very promising, bearing in mind that this is for only two low redshift tomographic bins; we obtain marginalised error on dark energy equation of state of $\sigma_w = 0.13$. We pursue the question of whether we can push our measurements to high redshift in § 4.6.3.

In order to demonstrate the practicality of measuring this signal, we have measured the cross-correlation function $\xi^{\delta\kappa_v}$ in our $50^\circ \times 50^\circ$ simulated dataset (see Section 3). We use the same window functions as above: we include galaxies with redshifts $0.1 < z < 0.3$, dividing these into two bins with $0.1 < z < 0.2$ and $0.2 < z < 0.3$. We average the galaxy counts and Doppler convergence estimators in pixels with size 1° transversely and 0.001 in the redshift direction, calculating δ_g as the overdensity of counts in pixels. We then calculate the correlation function for the jth tomographic bin,

$$\xi^{\delta\kappa_v}(\theta_i, z_j) = \sum_A \delta(z, \boldsymbol{\theta})\kappa_v(z', \boldsymbol{\theta}') - \sum_B \delta(z, \boldsymbol{\theta})\kappa_v(z', \boldsymbol{\theta}') \tag{4.51}$$

where sum A is over δ pixels in the jth thick tomographic bin, and over κ_v pixels with $z' > z$, within 0.02 in redshift of the δ pixel in the pair, and with appropriate angular separation to be in the θ_i bin. Sum B is over δ pixels in the thick tomographic bin, and over κ_v pixels with $z' < z$, within 0.02 in redshift of the δ pixel in the pair, and with appropriate angular separation to be in the θ_i bin.

We show our resulting correlation function in two tomographic bins in Fig. 4.8. We see that the simulated measurements are similar in magnitude to our theoretical calculations, and are precisely measured even when splitting the signal tomographically. Deviations from our theoretical curves will be reduced in future by more detailed modelling of the nonlinear velocity field, and and taking into account the slope effect seen in Fig. 4.4.

4.6.2 Doppler convergence autocorrelation

Having calculated the cross-correlation between the overdensity δ and the Doppler convergence κ_v, it is also of interest to calculate the power spectrum and auto-correlation for

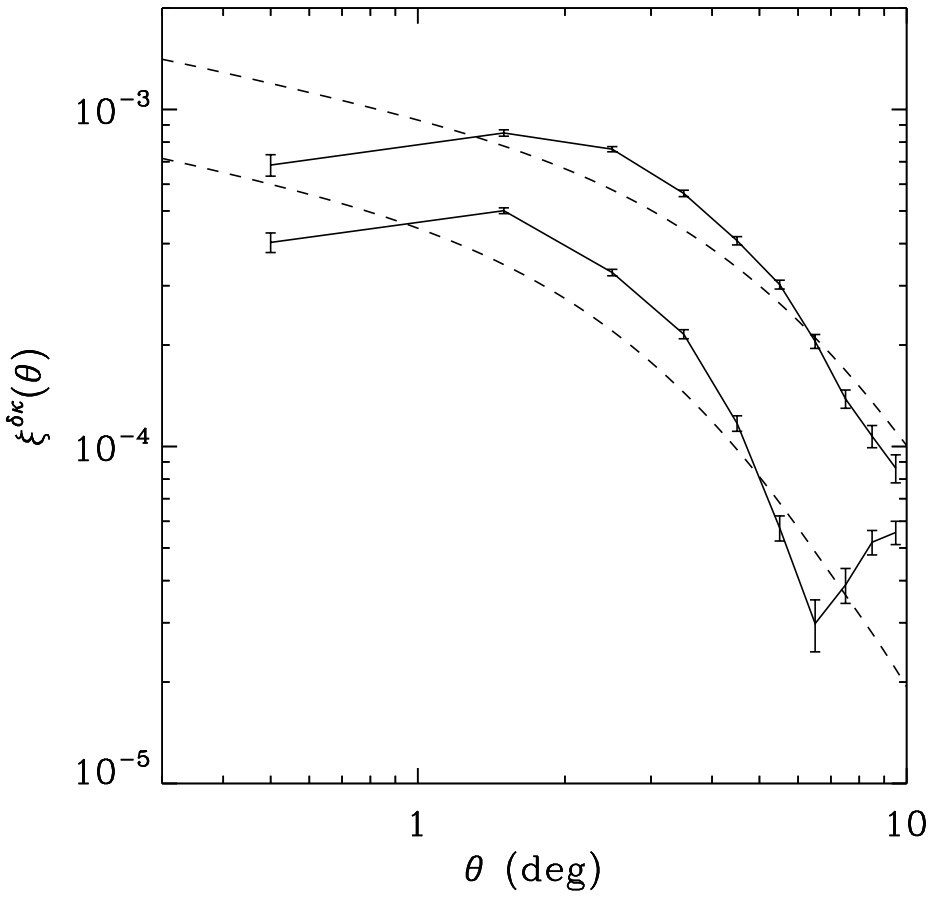

Figure 4.8: Overdensity - doppler convergence cross-correlation function as a function of separation angle. The solid lines show the correlation measurements for the tomographic bins $0.1 < z < 0.2$ (upper line) and $0.2 < z < 0.3$ (lower line), and the dashed lines show the theoretical predictions.

Doppler convergence. Using the definition

$$\langle \kappa^v_{\ell m}(z)\kappa^{v^*}_{\ell' m'}(z')\rangle = C^{\kappa_v\kappa_v}_\ell(z,z')\delta_{\ell\ell'}\delta_{mm'} \tag{4.52}$$

we find the Doppler convergence power spectrum to be (see Appendix B for derivations)

$$\begin{aligned}\bar{C}^{\kappa_v\kappa_v}_\ell &= \frac{16\pi}{N\left(3H_0^2\Omega_m\right)^2}\int_0^\infty dk k T^2(k)\mathcal{P}_{\Psi_i}(k)\left[\int_{z_{\rm min}}^{z_{\rm max}} dz\left(1-\frac{1}{\chi aH}\right)a(z)W_1(z)\mathcal{G}(z)j'_\ell(k\chi(z))\right]\\ &\times\left[\int_{z_{\rm min}}^{z_{\rm max}} dz'\left(1-\frac{1}{\chi aH}\right)a(z')W_2(z',z)\mathcal{G}(z')j'_\ell(k\chi(z'))\right].\end{aligned} \tag{4.53}$$

[88] used the continuity equation involving the density fluctuations to compute this Doppler convergence power spectrum, whereas in our case we have used the potential Φ and have recovered the same results.

To show the feasibility of measuring Doppler lensing correlations, we make calculations for the three surveys in Section 4, choosing the same thick redshift bins as in Section 6.1: (i) a thick bin of width $\Delta z = 0.2$ between $z_{\rm min} = 0.1$ and $z_{\rm max} = 0.3$, and (ii) two thick tomographic bins of width $\Delta z = 0.1$ between $z_{\rm min} = 0.1$ and $z_{\rm max} = 0.3$. We correlate all the objects at a given redshift z' with all the objects behind within a distance of $\Delta z = 0.02$, and we average over the thick bin in question. For these configurations, $W_1(z)$ has the same form as Eq. 4.41 and $W_2(z)$ is given by

$$W_2(z,z') = n(z)\Theta(z-z')(1-\Theta(z-z'-0.02)) \tag{4.54}$$

Again, since the computations are expensive due to the three integrals, we adopt the same approach we used for the cross-correlation function; the Doppler convergence power within a thin shell is given by

$$\begin{aligned}C^{\kappa_v\kappa_v}_\ell(z') &= \frac{16\pi}{N\left(3H_0^2\Omega_m\right)^2}\int_0^\infty dk k T^2(k)\mathcal{P}_{\Psi_i}(k)\left[\left(1-\frac{1}{\chi aH}\right)a(z')\mathcal{G}(z')j'_\ell(k\chi(z'))\right]\\ &\times\left[\int_{z_{\rm min}}^{z_{\rm max}} dz\left(1-\frac{1}{\chi aH}\right)a(z)W_2(z',z)\mathcal{G}(z)j'_\ell(k\chi(z))\right],\end{aligned} \tag{4.55}$$

with the normalization factor

$$N(z') = \int_{z_{\rm min}}^{z_{\rm max}} dz W_2(z,z'). \tag{4.56}$$

Then the average Doppler convergence power within a thick bin is found using

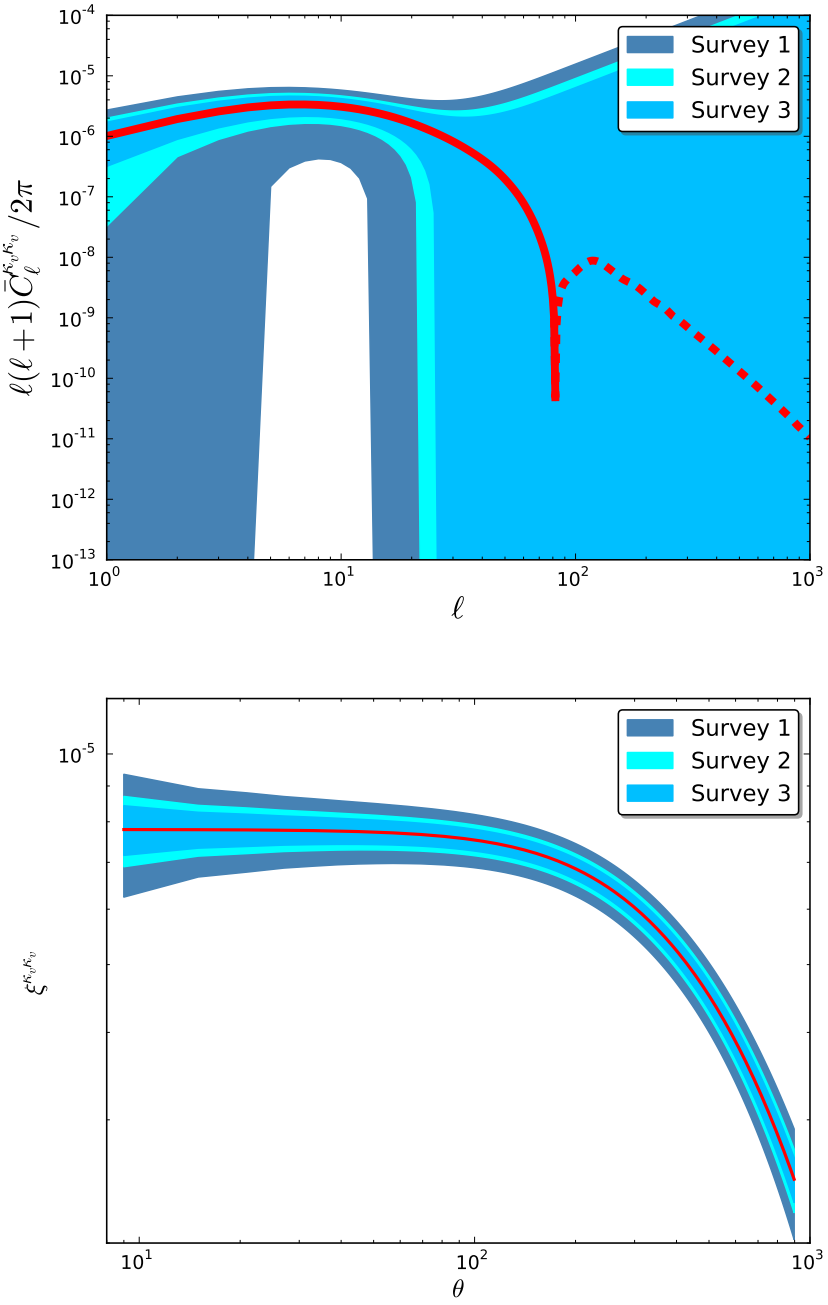

Figure 4.9: Top: Power spectrum of the Doppler convergence in harmonic space. The dashed line indicates negative values, whereas the solid line indicates positive values. Bottom: Correlation function of the Doppler convergence in real space.

$$\bar{C}_\ell^{\kappa_v\kappa_v} = \frac{\sum z_i^2 C_\ell^{\kappa_v\kappa_v}(z_i)}{\sum z_i^2}. \tag{4.57}$$

Fig. 4.9 shows the resulting angular power spectrum $\bar{C}_\ell^{\kappa_v\kappa_v}$ for redshift averaging (i). At low wavenumber (large physical scales), the signal is positive, indicating that most pairs at large separation in this redshift slice are on the same side of the nearest large-scale gravitational well, which may extend outside of the slice. At high wavenumber (small physical scales), we have negative values indicated by the dashed line; this is due to there being an excess of pairs in our sample on these scales which have velocities facing towards each other (due to there being many small-scale potential wells within the redshift slice for which pairs can exist on either side). We compute the errors in the power spectra for our three surveys; the errors in the $\bar{C}_\ell$ are given by

$$\Delta\bar{C}_\ell^2 = \frac{1}{(2\ell+1)f_{\rm sky}}\left(\bar{C}_\ell^{\kappa_v\kappa_v} + \frac{\sigma_\kappa^2}{n_{\rm thin}}\right)\left(\bar{C}_\ell^{\kappa_v\kappa_v} + \frac{\sigma_\kappa^2}{n_{\rm thick}}\right) \tag{4.58}$$

where $n_{\rm thin}$ and $n_{\rm thick}$ are the galaxy number densities of the thin shell and the thick bin respectively. We see in Fig. 4.9 that the Doppler convergence power spectrum can be measured on a range of scales; note again that the errors shown are for each individual ℓ, so averaging in band powers will lead to tighter error bars on each bin.

We have also computed the autocorrelation function $\xi^{\kappa_v\kappa_v}(\theta)$ in real space using the relation

$$\xi^{\kappa_v\kappa_v}(\theta) = \sum_{\ell=0}^{\ell_{\rm max}} \frac{2\ell+1}{4\pi}\bar{C}_\ell^{\kappa_v\kappa_v} P_\ell(\theta) \tag{4.59}$$

The bottom panel of Fig. 4.9 shows the Doppler convergence correlation in real space for redshift averaging (i). Again, the error bars are computed for the three surveys defined in Section 4.4, using Eq. (4.49), choosing a bin size $\Delta\theta = 6'$. We see that the autocorrelation function is measurable with each of the three surveys, but at lower signal-to-noise than the cross-correlation function $\xi^{\delta\kappa_v}$.

We use our $50^\circ \times 50^\circ$ simulated dataset (see Section 4.3) to attempt to measure the autocorrelation $\xi^{\kappa_v\kappa_v}$. We use the same window functions as above: we include two redshift bins with $0.1 < z < 0.2$ and $0.2 < z < 0.3$. Using the same pixelisation as in § 4.6.1, we calculate the correlation function for the jth tomographic bin,

$$\xi^{\kappa_v\kappa_v}(\theta_i, z_j) = \sum_A \kappa_v(z, \boldsymbol{\theta})\kappa_v(z', \boldsymbol{\theta'}) \tag{4.60}$$

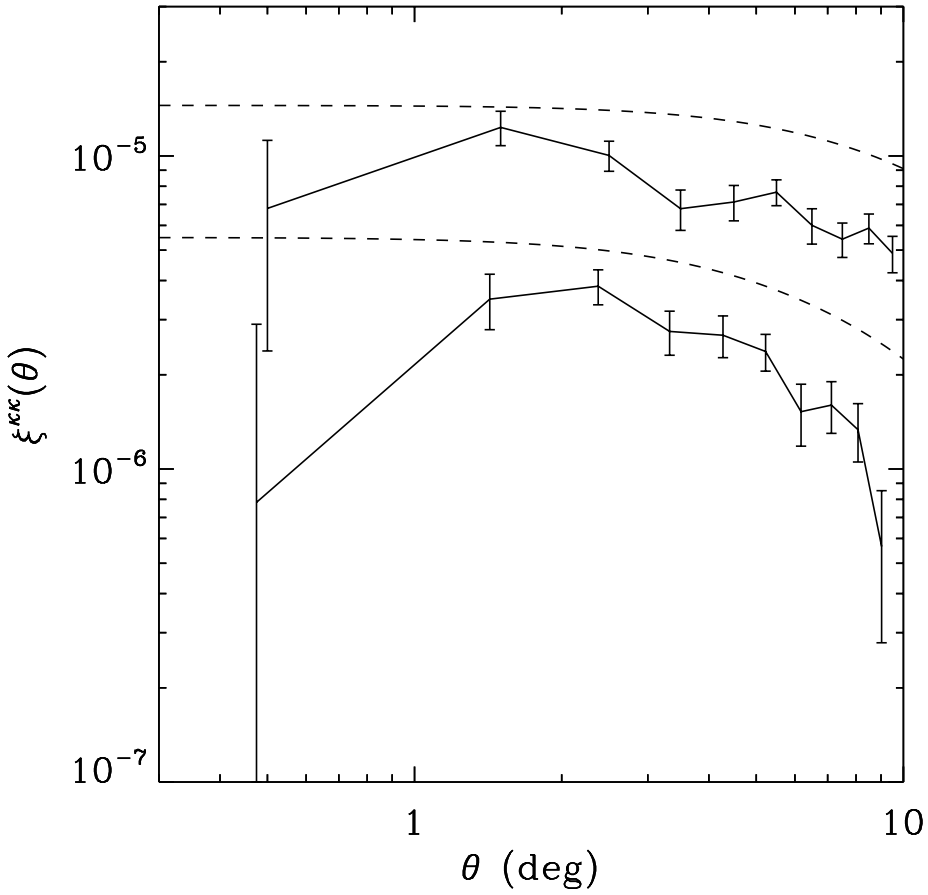

Figure 4.10: Doppler convergence autocorrelation function as a function of separation angle. The solid lines show the correlation measurements for the tomographic bins $0.1 < z < 0.3$ and $0.2 < z < 0.3$, and the dashed lines show the theoretical prediction.

where sum A is over κ_v pixels in the jth thick tomographic bin, and over κ_v pixels within 0.02 in redshift (either side) of the first pixel in the pair, and with appropriate angular separation to be in the θ_i bin.

We show our resulting correlation function in two tomographic bins in Fig. 4.10. We are able to measure the signal between 1° and 10° on this 2500 sq deg survey, in two low redshift bins. Our measurements are of a similar amplitude to the predicted values, but are somewhat suppressed in both tomographic bins; further modelling of the nonlinear velocities and the slope effect of Fig. 4.4 are clearly required for more accurate predictions

4.6.3 The impact of intrinsic size/brightness correlations and gravitational lensing

In the above analysis, we have neglected two potential contributors to our correlation functions: intrinsic size/brightness correlations between galaxies, and the gravitational lensing effect. Here we will discuss how these two effects impact our results. For simplicity, we will only discuss size throughout this section, although all the same arguments pertain for magnitude.

Intrinsic correlations

It is well known that gravitational lensing shear studies suffer from a systematic effect, the intrinsic alignment of galaxy ellipticities (see e.g. [190]). Two effects contribute: the 'II' effect where two background galaxies are physically aligned with each other, mimicking the gravitational shear signal; and the 'GI' effect where a background galaxy is lensed by a foreground halo, which is also affecting the orientation of a physically nearby galaxy.

It is plausible that similar intrinsic correlations exist for the size of objects. The equivalent of the 'II' effect is the possibility that galaxies which are near each other and in a similar environment may have correlated physical sizes. There are two effects equivalent to the 'GI' effect: the first is the idea that a background object may have gravitational lensing convergence because of a foreground halo, which is also contributing to an environmental dependence on another galaxy's size in its vicinity. The second is the idea that an object may have Doppler convergence due to a nearby halo, which is also contributing to an environmental dependence on another galaxy's size in its vicinity. Will these effects cause problems for Doppler lensing measurements?

We can analyse the issue symbolically in the following way. The excess size of an object can be described by a total estimated convergence,

$$\kappa = \kappa_{\rm int} + \kappa_v + \kappa_g \tag{4.61}$$

where $\kappa_{\rm int}$ is a measure of the fact that a galaxy may be intrinsically larger or smaller than usual. κ_v and κ_g are the Doppler and gravitational lensing convergence respectively.

If we autocorrelate the total convergence, we obtain

$$\langle\kappa\kappa\rangle = \langle\kappa_{\rm int}\kappa_{\rm int}\rangle + 2\langle\kappa_v\kappa_{\rm int}\rangle + 2\langle\kappa_g\kappa_{\rm int}\rangle + 2\langle\kappa_g\kappa_v\rangle + \langle\kappa_g\kappa_g\rangle + \langle\kappa_v\kappa_v\rangle \tag{4.62}$$

The first term here is the II term; the next two terms are the two GI terms; the sixth term is the Doppler auto-correlation that we are interested in. We will discuss the fourth and fifth terms in the next subsection.

Of the first three terms, we can immediately discount the third for the Doppler lensing statistics discussed above. The source of such a correlation would be a halo near a galaxy with $\kappa_{\rm int}$, which also gravitationally lenses the other galaxy in the correlation function pair. Our Doppler lensing auto- and cross-correlations are designed to only include pairs separated by a small distance in redshift ($\Delta z = 0.02$), over which distance the growth of gravitational lensing convergence is insignificant.

However, the first and second terms need not be small; as in gravitational lensing shear studies, it will be necessary to develop a model for intrinsic size correlations, and fit jointly for Doppler convergence and size correlation parameters when making cosmological constraints with the autocorrelation function.

The situation is much simpler in the case of the overdensity-Doppler cross-correlation. Here, the terms are

$$\langle\kappa\delta\rangle = \langle\kappa_{\rm int}\delta\rangle + \langle\kappa_v\delta\rangle + \langle\kappa_g\delta\rangle \tag{4.63}$$

The term we are interested in is the second term; we will consider the third term in the next subsection. The first term is the systematic intrinsic size term, which for some choices of correlation function could be large - the intrinsic size of galaxies plausibly depends on the density of their environment. However, we have chosen to average pairs with opposite signs depending on whether the κ-galaxy is in front of or behind the δ-galaxy. Since $\kappa_{\rm int}$ has no knowledge of whether it is in front of or behind an overdensity, this term averages to zero.

Hence our cross-correlation is not affected by intrinsic size correlations. The same is true of the statistic in Section 4.5, which again averages convergence with opposite signs in front of and behind an overdensity centre (via the $\cos\theta$ factor).

Gravitational lensing

In addition to the intrinsic size correlation, a further effect can mix with the Doppler lensing signal: gravitational lensing itself. We see this in Eq. (4.62), where the fourth and fifth terms involve gravitational lensing convergence.

The fourth term describes correlations between Doppler and gravitational lensing. This can be made large for some configurations - for instance if the average is over pairs selected to be where one object is just behind an overdensity (and hence Doppler lensed), and the other is far behind the same overdensity (and hence gravitationally lensed). However, for the average suggested in § 4.6.2, the term will be very small due to the thin $\Delta z = 0.2$ redshift shell - a halo causing Doppler convergence in a nearby galaxy cannot cause substantial gravitational lensing in such a thin shell.

The fifth term is negligible at low redshifts (c.f. Fig. 4.2), and hence does not impact on our calculations in § 4.6.2 made for $0 < z < 0.3$. However, at higher redshifts, this term will dominate over the Doppler autocorrelation. In this case, it is still possible to distinguish the gravitational lensing and Doppler lensing signals, due to the fact that while convergence is caused by Doppler and gravitational lensing, shear is only caused by gravitational lensing to a very good approximation [88]. In addition, the two point statistics of gravitational shear and gravitational convergence are identical [125]. Hence, if we have estimators for total convergence κ and shear γ for a set of objects, and if intrinsic alignments and intrinsic size correlations have been fully modeled and subtracted, we have

$$\langle\kappa\kappa\rangle = \langle\kappa_g\kappa_g\rangle + \langle\kappa_v\kappa_v\rangle \quad (4.64)$$

$$\langle\gamma\gamma\rangle = \langle\kappa_g\kappa_g\rangle \quad (4.65)$$

Therefore the shear correlation function gives us the pure gravitational lensing signal, and $\langle\kappa\kappa\rangle - \langle\gamma\gamma\rangle$ gives us the pure Doppler lensing signal.

Again the situation is much simpler with the cross-correlation, Eq. (4.63). While the third term here can be large for a thick redshift bin with uniform averaging, this is not the configuration chosen in § 4.6.1. There, the average is over a thin slice, and has opposite

signs depending on whether the κ object is in front of or behind the δ object. Hence we expect this term to average to a small value (the typical lensing due to an overdensity at a redshift separation < 0.02 behind the overdensity) even at high redshift, leaving only the second term which is the Doppler cross-correlation of interest.

We have measured the cross-correlation function given in Eq. (4.51), in a thick δ bin of $0.5 < z < 0.9$, with a thin κ region of $\Delta z = 0.02$, and opposite signs on the average when κ is in front of or behind δ. We measure the cross-correlation function for our simulation with gravitational lensing switched off, then with gravitational lensing present. The results for these two cases are shown in Fig. 4.11; we see that gravitational lensing does not appear to have a significant effect on this statistic, even at high redshift. Nevertheless, for future precision cosmological measurements, a joint model of Doppler and gravitational lensing will remove any remaining bias.

4.7 Maps

In addition to the two-point statistics above, Doppler lensing allows us to make spatially resolved maps of a quantity related to the gravitational potential. Combining equations the general relativistic Poisson equation which we recall

$$\delta = \frac{2a}{3H_0^2\Omega_m}[\nabla^2\Psi - 3aH(\Psi' + aH\Psi)] \tag{4.66}$$

and (3.12) we find that

$$\Psi' + aH\Psi = -\int d\chi \frac{3\Omega_m H_0^2}{2}\frac{\chi H}{\chi aH - 1}\kappa_v(z, \boldsymbol{n}). \tag{4.67}$$

Hence by combining our measured estimates of $\kappa_v(z, \boldsymbol{n})$ with models or measurements of the other quantities in the integral, we are able to map the quantity on the right hand side.

Alternatively, we could make a map of a quantity ϕ which is closer to the data, which we will call the Doppler lensing potential, being simply the integral of κ_v along the line of sight,

$$\phi(z, \boldsymbol{n}) = \int_0^z dz' \kappa_v(z', \boldsymbol{n}) \tag{4.68}$$

$$= -\int_0^\chi d\chi' \left[\frac{a\chi' H - 1}{\chi'}\right] \frac{2}{3\Omega_m H_0^2}\partial_\chi(\Psi' + aH\Psi) \tag{4.69}$$

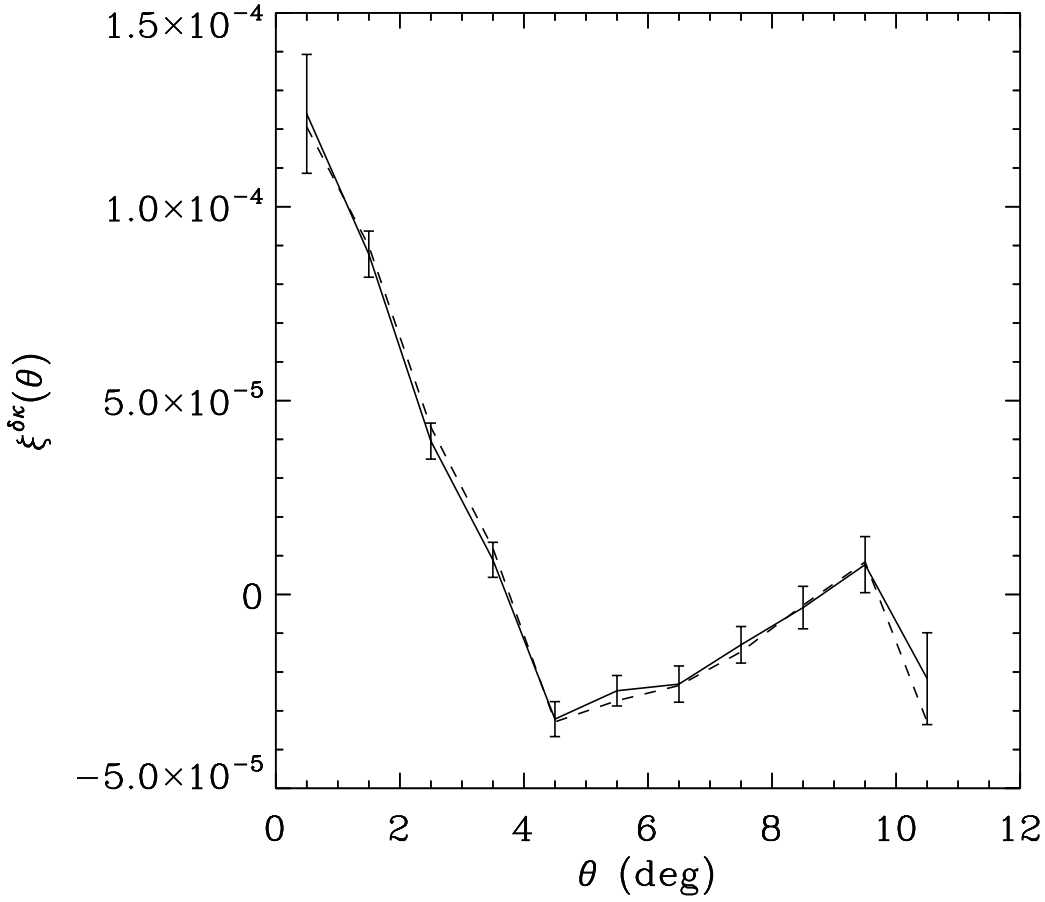

Figure 4.11: Overdensity - doppler convergence cross-correlation function as a function of separation angle, for a thick δ bin at $0.5 < z < 0.9$. Solid line shows the cross-correlation when gravitational lensing has not been added to the simulation; dashed line shows the cross-correlation including gravitational lensing.

which is a map combining information about geometry and potential; it is somewhat analogous to the lensing potential in gravitational lensing, which also includes an integral along the line of sight involving the gravitational potential and geometric factors. However, the two potentials behave differently: the gravitational lensing potential can be considered to be a 2-D projection of the gravitational potential, and varies only slowly with source redshift. On the other hand, the Doppler lensing potential is an integral of the derivative of quantities including the gravitational potential, so varies rapidly with source redshift in a similar way to the gravitational potential itself.

If we wish to consider the smoothed ϕ field, ϕ_s given by

$$\phi_s(z) = \int_0^\infty dz' \phi(z') W'(z' - z) \tag{4.70}$$

where W' is the convolving kernel, then integrating by parts and noting that $\kappa_v = \partial\phi/\partial z$, we find

$$\phi_s(z) = \int_0^\infty dz' \kappa_v(z') W(z' - z) \tag{4.71}$$

where W is the integral with respect to redshift of W'. Here we choose

$$W(z' - z) = (z' - z) \exp\left(-\frac{(z' - z)^2}{2\sigma_z^2}\right), \tag{4.72}$$

$$W'(z' - z) = \left(1 - \frac{(z' - z)^2}{\sigma_z^2}\right) \exp\left(-\frac{(z' - z)^2}{2\sigma_z^2}\right). \tag{4.73}$$

We make ϕ_s maps with our $50^\circ \times 50^\circ$ simulation (described in Section 3), for both the noise-free case and the case where κ_v has realistic noise on each galaxy. We choose a smoothing radius of $\sigma_z = 0.02$ for the radial convolving kernel above, and in addition smooth transversely with a Gaussian, with smoothing radius of 3°. An example slice at $z = 0.2$ of the true ϕ_s field is shown in the top panel of Fig. 4.12, together with the reconstructed ϕ_s field from noisy convergence data in the lower panel. We see that the reconstructed field bears a strong resemblance to the true ϕ_s field, with peaks and troughs in the field faithfully reproduced.

An alternative representation of the field is shown in Fig. 4.14; the top panel shows the true ϕ_s field in 3D, where an isocontour $\phi_s = 0.01$ has been drawn. The lower panel shows the reconstructed ϕ_s field, in the presence of realistic convergence noise. Again we see that the Doppler lensing potential appears to be well estimated in this large 3D volume.

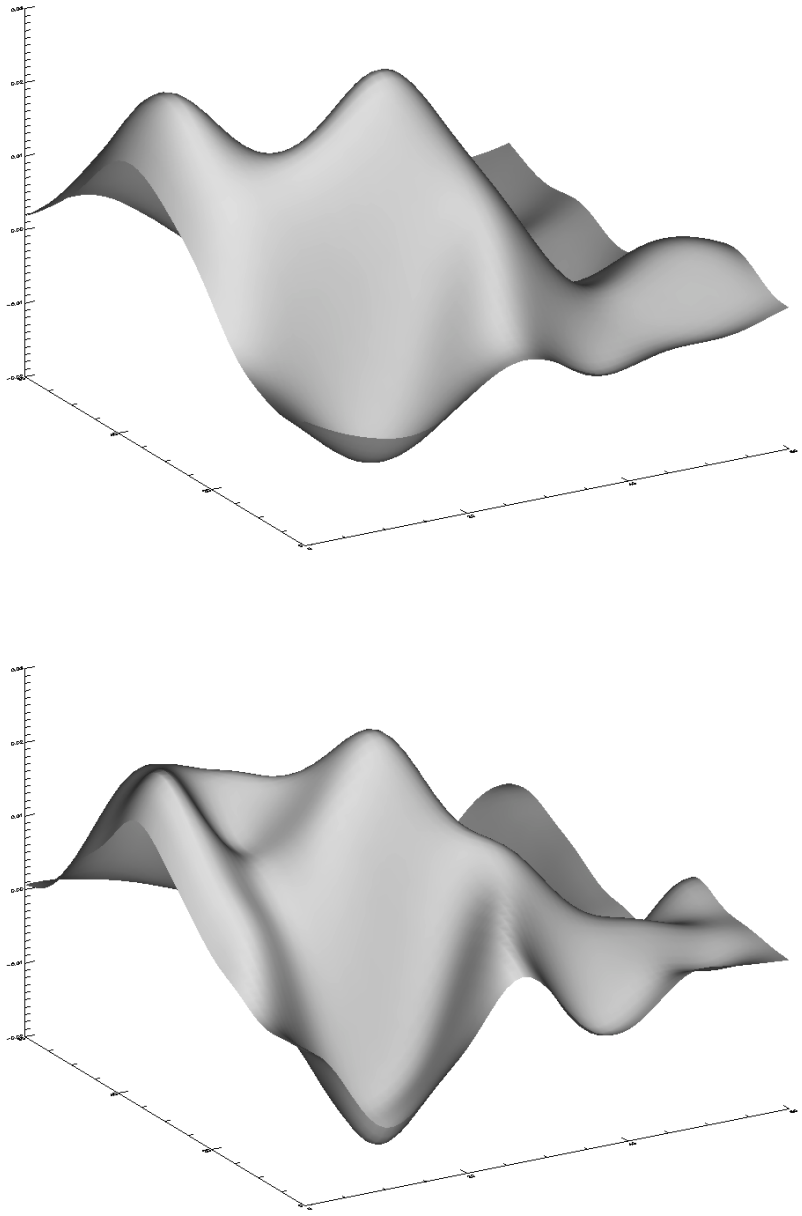

Figure 4.12: Top panel: Smoothed Doppler potential map for a slice at z=0.2. Here, no noise has been added to the Doppler convergence at each galaxy, so this represents the true field we seek to reconstruct. Bottom panel: Smoothed Doppler potential map for the same slice, now with noise added to the Doppler convergence at each galaxy.

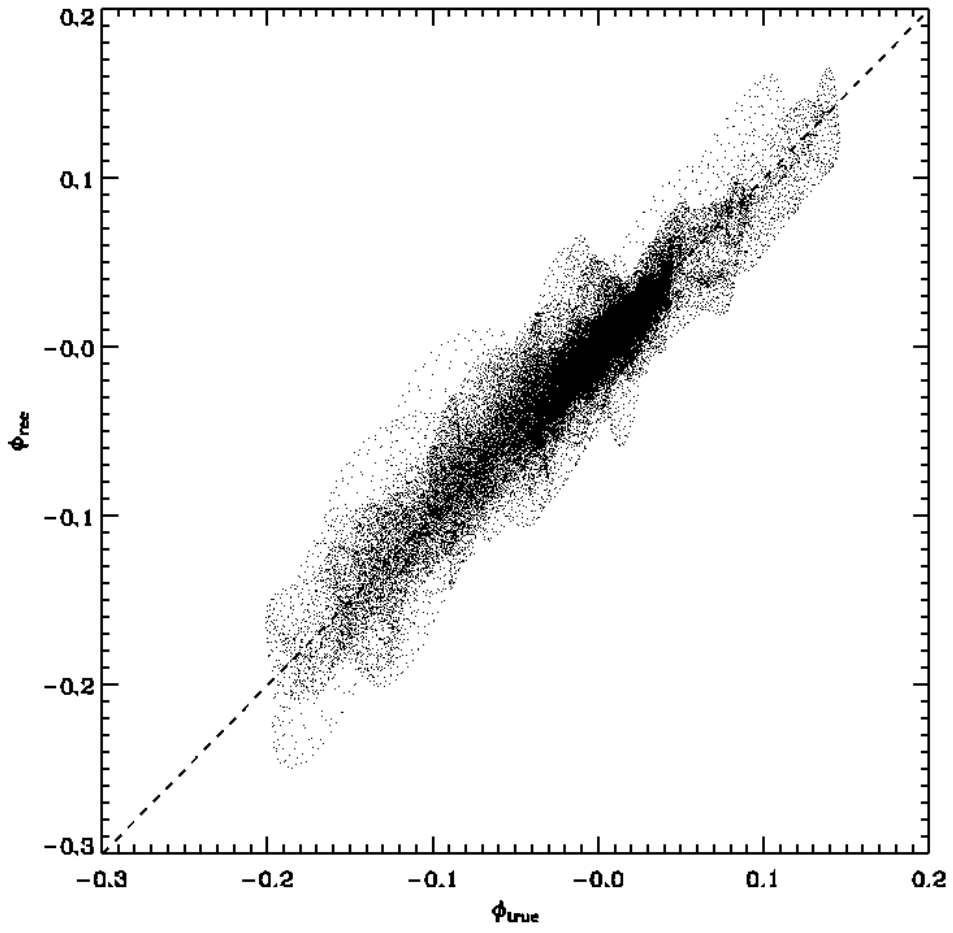

Figure 4.13: Reconstructed Doppler potential versus true Doppler potential for the wide field simulation, $0 < z < 0.3$.

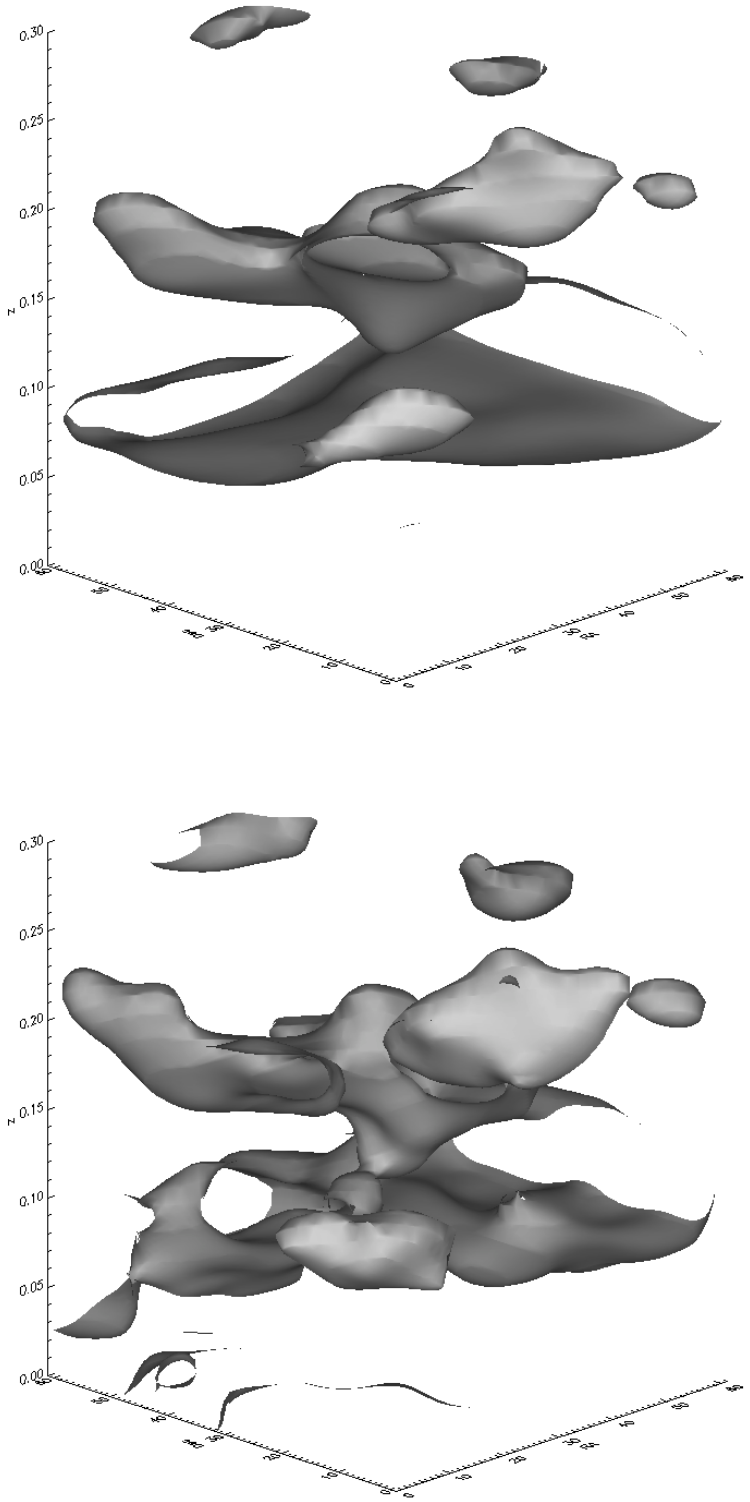

Figure 4.14: Top panel: Smoothed Doppler potential 3D map, at isocontour $\phi_s = 0.01$. Here, no noise has been added to the Doppler convergence at each galaxy. Bottom panel: Smoothed Doppler potential map for the same isocontour, now with realistic noise added to the Doppler convergence at each galaxy.

This is quantified for the full 3-D field in Fig. 4.13, which shows the Doppler lensing potential pixel values of the true versus reconstructed fields. The best fit line between these quantities is $\phi_{\rm rec} = 0.96\phi_{\rm true} - 3.8 \times 10^{-4}$, and the Pearson correlation coefficient is 0.95 for 1.2×10^5 pixels, which represents good agreement.

4.8 Conclusions

In this chapter we have investigated Doppler lensing as a probe of cosmology. This effect causes a slight change in the inferred physical size and brightness of objects at a given observed redshift; the magnitude of this effect is dependent on the peculiar velocities of galaxies, and so measurements of Doppler lensing are useful as a means of constraining the growth of structure and hence dark energy and gravitational physics.

As with gravitational lensing, the intrinsic range of sizes and magnitudes of galaxies leads to a substantial noise on Doppler lensing which needs to be overcome by using statistics which average over many galaxies.

A difference between gravitational and Doppler lensing is their behaviour as a function of radial distance from a 'lens'. Gravitational lensing convergence grows slowly behind a lens, whereas the amplitude of Doppler lensing rapidly rises then drops to zero both in front of and behind a lens (with different signs of the effect). Because of this, it is of great value to measure spectroscopic redshifts for sources when measuring Doppler lensing because of the rapid variation of the effect with redshift.

We have explained the theoretical background for the effect in Section 4.2, showing how it originates in the alteration of redshift due to peculiar velocity, together with the fact that we infer distances based on observed redshifts. We showed that Doppler lensing dominates over gravitational lensing at medium-low redshifts and wavenumbers ($\ell \lesssim 1000$ at $z = 0.2$, and $\ell \lesssim 100$ at $z = 0.4$).

We have examined the Doppler lensing effect in a series of simulations based on the Millennium simulation [184,185]. We have described these in Section 4.3, showing that they contain the expected Doppler lensing behaviour of having large convergence each side of a cluster or void, and of having a larger typical amplitude than gravitational lensing for $0 < z < 0.3$. We have defined three survey configurations (Section 4.4) typical of forthcoming surveys, covering a fraction of the sky ranging from 0.12 to 0.75, and including dense spectroscopic

redshift coverage for at least $0.1 < z < 0.3$.

We showed how one can measure the Doppler lensing convergence in spheres around stacked over- or under-densities (Section 4.5). We found that the signal is measurable with a stack of density peaks/voids, but is not detectable on individual objects.

We then calculated two point statistics for the cross-correlation overdensity-Doppler convergence , and the Doppler convergence autocorrelation (Section 4.6). In each case, we correlate pairs which are close to each other in redshift ($\Delta z < 0.02$) as it is on these scales that the Doppler lensing generates coherent convergence. We find that the two point correlations function can be measured with e.g. signal-to-noise $\simeq 80$ on $10'$ scales (survey 1), leading to useful constraints on cosmological parameters. We have discussed the potential systematic effects on the correlation functions due to intrinsic size correlations and gravitational lensing; for the cross-correlation we propose, we have shown that these systematics are small, while for the autocorrelation careful modelling of the intrinsic size correlation will be required.

Finally, we have shown how measurements of Doppler convergence can be used to make a 3D map of a potential field closely related to the gravitational potential. The reconstructed potential is strongly correlated with the true potential if smoothed on 50Mpc scales, despite the large noise term on convergence estimators.

In addition to the measurements proposed above, there are several further interesting areas for investigation with Doppler lensing. The effect gives us a direct way of estimating the peculiar velocity field at each galaxy, and therefore allows us to infer the velocity histogram for a volume of the Universe, and higher-point velocity statistics in addition to two-point statistics (redshift space distortions of the galaxy correlation function only provide the latter). Each of these quantities is sensitive to the evolution of large-scale structure, and can provide constraints on cosmology and gravitation.

Moreover, one could use Doppler convergence averaging around particular selections of clusters or galaxy types in order to probe the typical velocity field and gravitational potential field around these objects. This is equivalent to the cluster lensing and galaxy-galaxy lensing approaches well known in weak gravitational lensing studies.

Finally, one could combine the auto- and cross-correlation function of Doppler convergence with auto- and cross- correlation functions for galaxy counts and gravitational lensing. Fitting theory jointly to all of these correlations should provide improved constraints on bias and growth parameters.

To conclude, Doppler lensing affords a novel range of cosmological applications. Forthcoming surveys, furnished with spectroscopic redshifts, will be able to make the most out of this exciting new cosmological probe.

Chapter 5
Dipole modulation

Early works [191, 192] investigated the magnitude-distance relation and showed that the anisotropy of the luminosity distance $\delta D_L/\bar{D}_L$ (area distance) arises from the inhomogeneities of the intervening matter between the emitter and the observer. We recall from Eq. (1.21) that the perturbation of the luminosity distance (area distance) is $\delta D_L/\bar{D}_L = -\kappa$, where κ is the cosmic convergence which is an observable whose effect causes the change of apparent magnitude/observed size of distant object. As we mentioned in earlier Chapters, the convergence includes many terms like the integrated density fluctuations along the line of sight - the standard gravitational lensing - the Sachs-Wolfe effects, Shapiro time-delay, Doppler effects and many other non-linear terms like the vector/tensor mode contributions that we discussed in Chapter 3. It was also shown that the relative dominance of each term depends on both the scales of interest and redshift but overall, Doppler term dominates at low redshift and falls off with increasing redshift as opposed to the gravitational lensing - a cumulative effect - which dominates at hight redshift. In the previous Chapter, by using overdensity-size (of objects) correlator at low redshift, we were able to put good constraints - comparable to those obtained from *Planck* - on cosmological parameters [165]. Our approach also comes to corroborate the fact that peculiar motion constitutes a very good tool to study growth of structure and Dark energy. In this Chapter we propose a new way of measuring *Doppler magnification*. Although still based on the overdensity-size cross-correlation, this method is new in that the way we do the averaging differs from the one we had earlier. We first explain our method then develop the formalism upon which we build the new estimator and finally show the results obtained from applying our technique. We point out that this Chapter contains two main parts. In the first part, we use the statistical tool to constrain cosmological parameters describing the ΛCDM paradigm, whereas in the second part we investigate any departure from GR by using the same statistical tool.

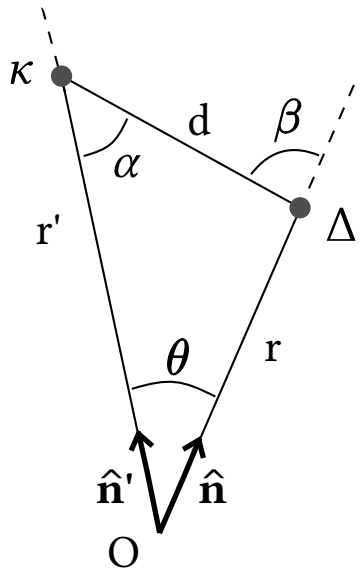

Figure 5.1: Schematic description of the Doppler dipole. It presents the coordinate system we adopt throughout this Chapter (courtesy: C. Bonvin).

5.1 Dipole modulation in ΛCDM

5.1.1 Theory

As discussed in the previous Chapter on Doppler magnification, we built our correlator upon the fact that we can observe a correlation between an overdensity Δ with the sizes of objects κ[1] surrounding it. But, there is a subtle difference in the new statistical tool we are developing now. Let's suppose an over-density Δ located at a distance r away from the observer (O) and an object with size κ at a distance r' away from O. The separation between κ and Δ is d; $\hat{\mathbf{n}}$ and $\hat{\mathbf{n}}'$ denote the directions of observations(see Fig. 5.1). We now want to correlate the overdensity with the sizes κ of all the objects at a separation distance d from Δ. The asymmetry of the cross-correlation which arises from the angle β dependence [2] of the correlator induces a dipole signal which we want to extract. To measure the amplitude of the dipole one must therefore average out the angle β.

[1]Here we refer to the convergence κ as size of object

[2]Noting also that objects that tend to run away from O are magnified and those moving towards O are demagnified

5.1.2 Formalism

As described above, we are particularly interested at the cross-correlation function between galaxy number count $\Delta(z, \hat{\mathbf{n}})$ and the cosmic convergence

$$\xi = \langle \Delta(z, \hat{\mathbf{n}}) \kappa(z', \hat{\mathbf{n}}') \rangle. \tag{5.1}$$

The galaxy number count reads [27, 28, 193]

$$\Delta(z, \hat{\mathbf{n}}) = b \cdot \delta - \frac{1}{\mathcal{H}} \partial_r (\boldsymbol{v} \cdot \hat{\mathbf{n}}) + (5s - 2) \int_0^r dr' \, \frac{r - r'}{2rr'} \Delta_\Omega (\Phi + \Psi) + \Delta^{\rm rel}(z, \hat{\mathbf{n}}) \,, \tag{5.2}$$

where the first term is just the galaxy overdensity δ_g - b being the bias - the second term is the redshift space distortion with ∂_r being the derivative along the line of sight, the third denotes the lensing magnification bias with s being the slope of the luminosity function, Φ and Ψ the two Bardeen potentials and Δ_Ω the angular part of the Laplacian

$$\Delta_\Omega = \cot\theta \, \partial_\theta + \partial_\theta^2 + \frac{1}{\sin^2\theta} \partial_\varphi^2 = r^2 \left(\nabla^2 - \hat{n}^i \hat{n}^j \partial_i \partial_j - \frac{2}{r} \hat{n}^i \partial_i \right) , \tag{5.3}$$

and finally the last term includes the so-called relativistic distortions. At first order, the expression of the convergence has been computed by [3] [76, 77]

$$\begin{aligned} \kappa(z, \hat{\mathbf{n}}) \;=\; & \frac{1}{2r} \int_0^r dr' \frac{r - r'}{r'} \Delta_\Omega (\Phi + \Psi) + \left(1 - \frac{1}{r\mathcal{H}} \right) \boldsymbol{v} \cdot \hat{\mathbf{n}} \\ & - \frac{2}{r} \int_0^r dr' \Psi + \left(1 - \frac{1}{r\mathcal{H}} \right) \int_0^r dr' (\dot{\Phi} + \dot{\Psi}) + \left(2 - \frac{1}{r\mathcal{H}} \right) \Psi \,. \end{aligned} \tag{5.4}$$

In our analysis, we only include the contribution from the matter density fluctuations and the redshift space distortion in the galaxy number count and select the gravitational lensing and Doppler term from the convergence. This is a good approximation for our purposes as we work at low redshift where the peculiar velocities are important. The cross-correlation thus reads

$$\xi = \left\langle \left(b \cdot \delta - \frac{1}{\mathcal{H}} \partial_r (\boldsymbol{v} \cdot \hat{\mathbf{n}}) \right) \cdot \left(\kappa_{\rm g} + \kappa_v \right) \right\rangle \,, \tag{5.5}$$

where we recall that the standard gravitational lensing and the Doppler term are

$$\kappa_{\rm g} \;=\; \frac{1}{2r} \int_0^r dr' \frac{r - r'}{r'} \Delta_\Omega (\Phi + \Psi) \,, \tag{5.6}$$

$$\kappa_v \;=\; \left(1 - \frac{1}{r\mathcal{H}} \right) \boldsymbol{v} \cdot \hat{\mathbf{n}} \,, \tag{5.7}$$

[3] Dot here denotes derivative with respect to conformal time η.

respectively.

5.1.3 Multipole expansion

To compute the quantity in Eq. (5.5) we need to expand each variable of interest in Fourier space using the convention

$$f(\boldsymbol{x},\eta) = \frac{1}{(2\pi)^3}\int d^3\boldsymbol{k}\, e^{-i\boldsymbol{k}\cdot\boldsymbol{x}} f(\boldsymbol{k},\eta)\,, \tag{5.8}$$

therefore throughout our calculations we adopt the following Fourier decomposition for the density contrast, the radial peculiar velocity and its derivative with respect to the comoving distance [4]

$$\delta(\hat{\mathbf{n}},z) = \frac{1}{(2\pi)^3}\int d^3\boldsymbol{k} e^{-i\boldsymbol{k}\cdot\boldsymbol{x}}\delta(\boldsymbol{k},z), \tag{5.9}$$

$$\boldsymbol{v}(\hat{\mathbf{n}},z)\cdot\hat{\mathbf{n}} = \frac{i}{(2\pi)^3}\int d^3\boldsymbol{k} e^{-i\boldsymbol{k}\cdot\boldsymbol{x}} v(\boldsymbol{k},z)(\hat{\boldsymbol{k}}\cdot\hat{\mathbf{n}}), \tag{5.10}$$

$$\partial_\chi(\boldsymbol{v}(\hat{\mathbf{n}},z)\cdot\hat{\mathbf{n}}) = \frac{1}{(2\pi)^3}\int d^3\boldsymbol{k} k e^{-i\boldsymbol{k}\cdot\boldsymbol{x}} v(\boldsymbol{k},z)(\hat{\boldsymbol{k}}\cdot\hat{\mathbf{n}})^2, \tag{5.11}$$

respectively, where $\hat{\boldsymbol{k}}\cdot\hat{\mathbf{n}}$ is the cosine between the wavevector $\hat{\boldsymbol{k}}$ and the direction of observation $\hat{\mathbf{n}}$. The density contrast in Fourier space is

$$\delta(\boldsymbol{k},z) = -\frac{2}{3\Omega_m} D_1(a)\left(\frac{k}{\mathcal{H}_0}\right)^2 T(k)\Psi_i(\boldsymbol{k}), \tag{5.12}$$

with $T(k)$ being the transfer function [112], Ψ_i the primordial potential and $D_1(a)$ the growth factor. The velocity potential reads

$$v(\boldsymbol{k},z) = \frac{2}{3\Omega_m}\frac{\mathcal{H}}{\mathcal{H}_0}\frac{k}{\mathcal{H}_0} f(a) D_1(a) T(k)\Psi_i(\boldsymbol{k}), \tag{5.13}$$

where again we have introduced the growth factor $f(a)$. Since we are at low redshift, the dominant term in the convergence is the Doppler term therefore we are mainly interested in the quantity

$$\xi_v = \left\langle \left(b\cdot\delta - \frac{1}{\mathcal{H}}\partial_r(\boldsymbol{v}\cdot\hat{\mathbf{n}})\right)\cdot\kappa_v \right\rangle . \tag{5.14}$$

[4] We interchangeably use either r or χ to denote the comoving distance

$$\xi_v = \frac{4}{9\Omega_m^2}\left(\frac{1}{\mathcal{H}(z')r'}-1\right)\frac{1}{(2\pi)^6}\int d^3\boldsymbol{k}\int d^3\boldsymbol{k}' e^{-i\boldsymbol{k}\cdot\boldsymbol{x}-i\boldsymbol{k}'\cdot\boldsymbol{x}'}D_1(a)D_1(a')i(\hat{\boldsymbol{k}}'\cdot\hat{\mathbf{n}}') \times\left(\frac{k}{\mathcal{H}_0}\right)^2\frac{k'}{\mathcal{H}_0}\frac{\mathcal{H}(a')}{\mathcal{H}_0}T(k)T(k')\Big(-b(a)-(\hat{\boldsymbol{k}}\cdot\hat{\mathbf{n}})^2 f(a)\Big)f(a')\langle\Psi_i(\boldsymbol{k})\Psi_i(\boldsymbol{k}')\rangle. \quad (5.15)$$

Defining the primordial power spectrum

$$\langle\Psi_i(\boldsymbol{k})\Psi_i(\boldsymbol{k}')\rangle = \frac{(2\pi)^3}{k^3}\mathcal{P}_{\Psi_i}(k)\delta_D(\boldsymbol{k}+\boldsymbol{k}'), \quad (5.16)$$

with

$$\mathcal{P}_{\Psi_i}(k) = A\left(\frac{k}{k_\lambda}\right)^{n_s-1}, \quad (5.17)$$

where A is the amplitude of the primordial curvature perturbation, n_s is the tilt and k_λ the pivot. Taking into account the definition Eq. (5.16) we get

$$\xi_v = \frac{4}{9\Omega_m^2}\left(\frac{1}{\mathcal{H}(a')r'}-1\right)\frac{1}{(2\pi)^3}D_1(a)D_1(a')f(a')\frac{\mathcal{H}(a')}{\mathcal{H}_0}\int d^3\boldsymbol{k}e^{id\boldsymbol{k}\cdot\boldsymbol{N}} \times\left(\frac{k}{\mathcal{H}_0}\right)^3 T(k)^2\Big(b(a)+\frac{f(a)}{3}+\frac{2}{3}f(a)P_2(\hat{\boldsymbol{k}}\cdot\hat{\mathbf{n}})\Big)iP_1(\hat{\boldsymbol{k}}\cdot\hat{\mathbf{n}})\mathcal{P}_{\Psi_i}(k), \quad (5.18)$$

where we have defined $\boldsymbol{x}'-\boldsymbol{x} = d\boldsymbol{N}$ (see Fig. 5.1) and introduced the Legendre polynomials

$$P_1(\hat{\boldsymbol{k}}\cdot\hat{\mathbf{n}}) = (\hat{\boldsymbol{k}}\cdot\hat{\mathbf{n}}), \quad (5.19)$$

$$P_2(\hat{\boldsymbol{k}}\cdot\hat{\mathbf{n}}) = \frac{3}{2}(\hat{\boldsymbol{k}}\cdot\hat{\mathbf{n}})^2-1. \quad (5.20)$$

To ease the computations, we first need to alleviate the notations by letting

$$\mathcal{F}(k) = \mathcal{P}_{\Psi_i}(k)T(k)^2\left(\frac{k}{\mathcal{H}_0}\right)^3, \quad (5.21)$$

such that the integral part of Eq. (5.18) becomes

$$\mathfrak{I} = \int\frac{d^3\boldsymbol{k}}{k^3}e^{id\hat{\boldsymbol{k}}\cdot\boldsymbol{N}}\mathcal{F}(k)i\Big(\Big[b(a)+\frac{f(a)}{3}\Big]P_1(\hat{\boldsymbol{k}}\cdot\hat{\mathbf{n}})+\frac{2}{3}f(a)P_2(\hat{\boldsymbol{k}}\cdot\hat{\mathbf{n}})P_1(\hat{\boldsymbol{k}}\cdot\hat{\mathbf{n}})\Big) \quad (5.22)$$

In Fig. 5.1, we now assume a cartesian coordinate system with the orthonormal basis $\{\boldsymbol{x}_1,\boldsymbol{x}_2,\boldsymbol{x}_3\}$ and an origin located at the observer, such that the configuration presented in Fig. 5.1 lies within the plane perpendicular to $\boldsymbol{x}_3$. We now choose a vector $\boldsymbol{N}$ on the line

segment d to be parallel to $\boldsymbol{x}_1$ such that $\boldsymbol{N} = (\pi/2, 0)$ where the first argument denotes the angle between $\boldsymbol{N}$ and $\boldsymbol{x}_3$ and the second is the angle between $\boldsymbol{N}$ and $\boldsymbol{x}_1$. It follows that $\hat{\mathbf{n}} = (\pi/2, \beta)$ and $\hat{\mathbf{n}}' = (\pi/2, \alpha)$. To go any further, we have to recall that the spherical harmonic expansions of the plane wave, P_1 and P_2. Thus

$$e^{id\hat{\boldsymbol{k}}\cdot\boldsymbol{N}} = 4\pi \sum_{LM} i^L j_L(kd) Y^*_{LM}(\hat{\boldsymbol{k}}) Y_{LM}(\boldsymbol{N}), \tag{5.23}$$

$$P_1(\hat{\boldsymbol{k}}\cdot\hat{\mathbf{n}}) = \frac{4\pi}{3} \sum_{m'=-1}^{1} Y^*_{1\,m'}(\hat{\boldsymbol{k}}) Y_{1\,m'}(\hat{\mathbf{n}}'), \tag{5.24}$$

$$P_2(\hat{\boldsymbol{k}}\cdot\hat{\mathbf{n}}) = \frac{4\pi}{5} \sum_{m=-2}^{2} Y^*_{2\,m}(\hat{\boldsymbol{k}}) Y_{2\,m}(\hat{\mathbf{n}}). \tag{5.25}$$

Exploiting the definition in Eqs. (5.24), (5.25), the first term in Eq. (5.22) becomes

$$\mathfrak{I}_1 = \left(b(a) + \frac{f(a)}{3}\right) \frac{(4\pi)^2}{3} \int \frac{dk}{k} \mathcal{F}(k) \sum_{LM} \sum_{m'=-1}^{1} i^{L+1} j_L(kd) Y_{LM}(\boldsymbol{N}) Y_{1\,m'}(\hat{\mathbf{n}}') \int d^2\hat{\boldsymbol{k}} Y^*_{LM}(\hat{\boldsymbol{k}}) Y^*_{1\,m'}(\hat{\boldsymbol{k}}). \tag{5.26}$$

Using the orthogonality relation of the spherical harmonic functions, the integral over the angle is

$$\int d^2\hat{\boldsymbol{k}} Y^*_{LM}(\hat{\boldsymbol{k}}) Y^*_{1\,m'}(\hat{\boldsymbol{k}}) = (-1)^{m'} \delta_{L\,1} \delta_{M\,(-m')}, \tag{5.27}$$

so that we get

$$\mathfrak{I}_1 = -\left(b(a) + \frac{f(a)}{3}\right) \frac{(4\pi)^2}{3} \int \frac{dk}{k} \mathcal{F}(k) \sum_{m'=-1}^{1} i^{L+1} j_L(kd) Y_{1\,(-m')}(\boldsymbol{N}) Y_{1\,m'}(\hat{\mathbf{n}}'). \tag{5.28}$$

By using the definition of the spherical harmonics and after simplifying

$$\mathfrak{I}_1 = -4\pi \left(b(a) + \frac{f(a)}{3}\right) \cos(\alpha) \int \frac{dk}{k} \mathcal{P}_{\Psi_i}(k) j_1(kd). \tag{5.29}$$

We now calculate the second term of the integral in Eq. (5.22)

$$\begin{aligned} \mathfrak{I}_2 = {} & \frac{2f(a)}{3} \frac{(4\pi)^3}{15} \int \frac{dk}{k} \mathcal{F}(k) \sum_{LM} \sum_{m'=-1}^{1} \sum_{m=-2}^{2} i^{L+1} j_L(kd) Y_{LM}(\boldsymbol{N}) Y_{2\,m}(\hat{\mathbf{n}}) Y_{1\,m'}(\hat{\mathbf{n}}') \\ & \times \int d^2\hat{\boldsymbol{k}} Y^*_{LM}(\hat{\boldsymbol{k}}) Y^*_{2\,m}(\hat{\boldsymbol{k}}) Y^*_{1\,m'}(\hat{\boldsymbol{k}}), \end{aligned} \tag{5.30}$$

where the integral over the angle of the product of three spherical harmonics involves the $3j$ Wigner symbols. After some algebra and combining everything we finally find the full-sky

expression of the cross-correlation

$$\begin{aligned}\xi_v &= -\frac{2}{9\Omega_m^2\pi^2}\frac{\mathcal{H}(z')}{\mathcal{H}_0}f(z')D_1(z)D_1(z')\left(1-\frac{1}{\mathcal{H}(z')r'}\right)\Bigg\{\Bigg[\left(b(z)+\frac{2f(z)}{5}\right)\nu_1(d)\\ &\quad -\frac{f(z)}{10}\nu_3(d)\Bigg]\cos\alpha+\frac{f(z)}{5}\Big[\nu_1(d)-\frac{3}{2}\nu_3(d)\Big]\cos\alpha\cos 2\beta+\frac{f(z)}{5}\Big[\nu_1(d)+\nu_3(d)\Big]\\ &\quad \times\sin\alpha\sin 2\beta\Bigg\},\end{aligned} \tag{5.31}$$

where we have defined

$$\nu_\ell(d)=\int\frac{dk}{k}\mathcal{F}(k)j_\ell(kd)\,,\ \ell=1,3\,. \tag{5.32}$$

The comoving distance to κ, r', and the angle α can be explicitly written in terms of (r,d,β)

$$r' = \sqrt{r^2+2dr\cos\beta+d^2}\,, \tag{5.33}$$

$$\cos\alpha = \frac{d+r\cos\beta}{\sqrt{r^2+2dr\cos\beta+d^2}}\,, \tag{5.34}$$

$$\sin\alpha = \frac{r\sin\beta}{\sqrt{r^2+2dr\cos\beta+d^2}}\,. \tag{5.35}$$

Eqs. (5.31) to (5.35) provide the general expression (valid at all scales) for the cross-correlation between the galaxy number count and the Doppler magnification, as a function of the three variables (r,d,β). Using the distant-observer approximation, i.e in the regime $d/r\ll 1$,

$$r' = r+\mathcal{O}\left(\frac{d}{r}\right)\,, \tag{5.36}$$

$$\cos\alpha = \cos\beta+\mathcal{O}\left(\frac{d}{r}\right)\,, \tag{5.37}$$

$$\sin\alpha = \sin\beta+\mathcal{O}\left(\frac{d}{r}\right), \tag{5.38}$$

and Taylor expanding all functions $F(z')$ of $z'\equiv z(r')$, to lowest order in d/r

$$F(z')=F(r')=F(r)+\mathcal{O}\left(\frac{d}{r}\right)\,, \tag{5.39}$$

we finally obtain the flat-sky expression of number count - Doppler term cross-correlation

$$\xi_v(r,d,\beta) = \frac{2}{9\Omega_m^2\pi^2}\frac{\mathcal{H}(z)}{\mathcal{H}_0}D_1^2(a)f(z)\left(1-\frac{1}{\mathcal{H}(z)r}\right)\Bigg[\left(b(z)+\frac{3f(z)}{5}\right)\nu_1(d)P_1(\cos\beta) - \frac{2f(z)}{5}\nu_3(d)P_3(\cos\beta)\Bigg] \tag{5.40}$$

It can be seen that the cross-correlation in Eq. (5.40) is a function of a dipole, P_1 term, and an octupole, P_3 term. To extract the amplitude of the dipole and octupole we weight the correlator by the appropriate Legendre polynomial[5] and integrate over β - more precisely $\mu = \cos(\beta)$. Therefore the amplitude of the dipole is

$$\begin{aligned}\xi_{\rm dip}(d,r) &= \frac{3}{2}\int_{-1}^{1} d\mu \xi_v(d,r,\beta)P_1(\mu) \\ &= \frac{2}{9\Omega_m^2\pi^2}\frac{\mathcal{H}(z)}{\mathcal{H}_0}D_1^2(z)f(z)\left(1-\frac{1}{\mathcal{H}(z)r}\right)\left(b(z)+\frac{3f(z)}{5}\right)\nu_1(d),\end{aligned} \tag{5.41}$$

and that of the octupole

$$\begin{aligned}\xi_{\rm oct}(d,r) &= \frac{7}{2}\int_{-1}^{1} d\mu \xi_v(d,r,\beta)P_3(\mu) \\ &= -\frac{2}{9\Omega_m^2\pi^2}\frac{\mathcal{H}(z)}{\mathcal{H}_0}D_1^2(z)f(z)\left(1-\frac{1}{\mathcal{H}(z)r}\right)\frac{2f(z)}{5}\nu_3(d).\end{aligned} \tag{5.42}$$

5.1.4 Estimator

We now propose the following estimator to measure the amplitude of the dipole

$$\hat{\xi}_{\rm dip}(d) = a_{\rm N}\sum_{ij}\Delta_i\kappa_j\cos\beta_{ij}\delta_K(d_{ij}-d), \tag{5.43}$$

where we have isolated the dipole contribution by weighting the cross-correlation by $\cos(\beta)$, similar to what we did in order to obtain its amplitude in Eq. (5.41) from the flat-sky expression in Eq. (5.40). Similarly, an obvious choice to build an estimator of the octupole is to weight the cross-correlation by $P_3(\cos(\beta))$ i.e

$$\hat{\xi}_{\rm oct}(d) = b_{\rm N}\sum_{ij}\Delta_i\kappa_j P_3(\cos\beta_{ij})\delta_K(d_{ij}-d). \tag{5.44}$$

[5]The choice of P_ℓ is based on the orthogonality relation of the Legendre polynomials

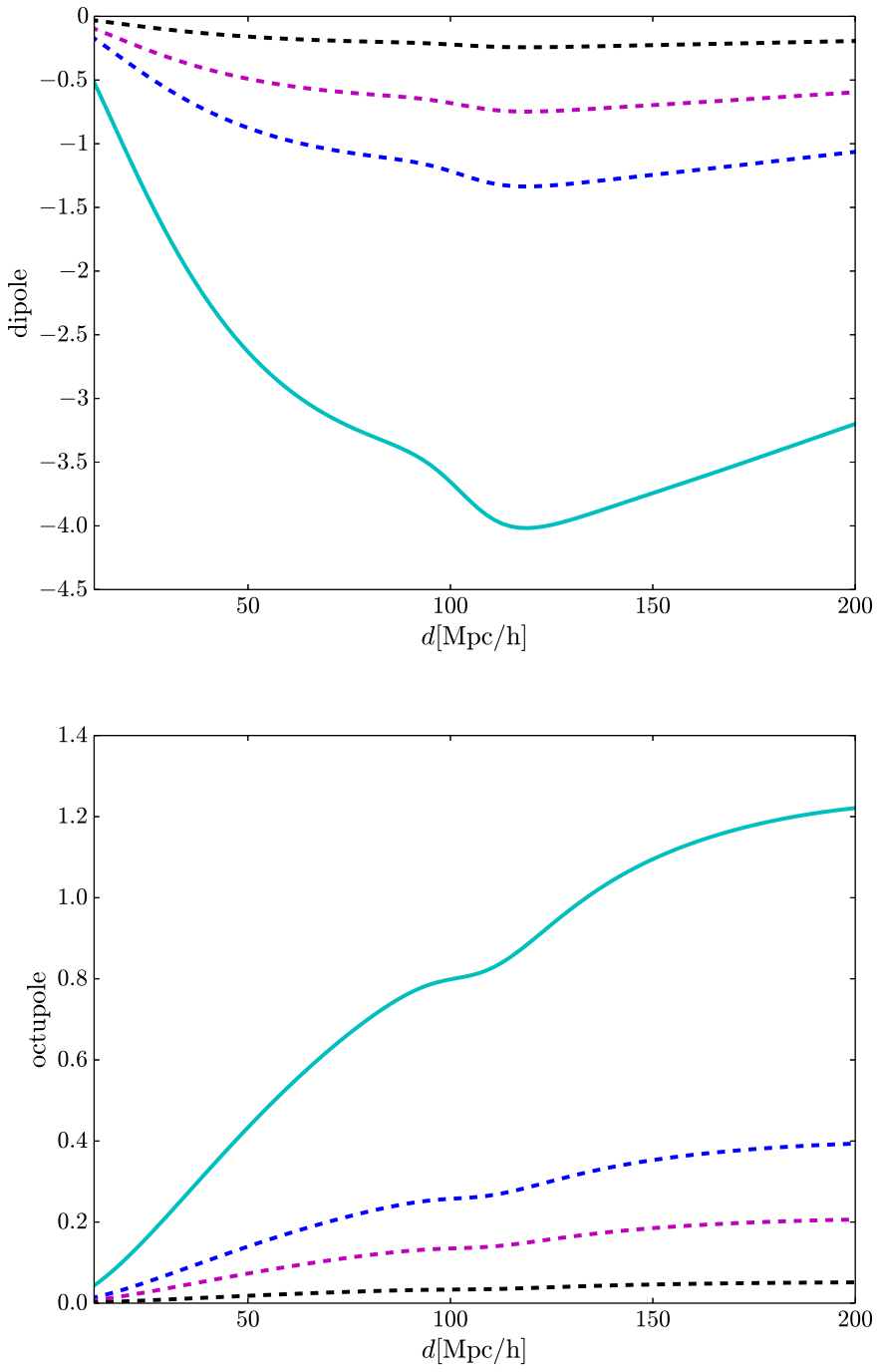

Figure 5.2: *Top panel*: mean of the estimator of the dipole (Eq. (5.50)) as a function of separation d at different redshifts z: $z = 0.1$ (blue solid), $z = 0.3$ (magenta dashed), $z = 0.5$ (black dotted) and $z = 1$ (cyan dash-dotted). *Bottom panel*: mean of the estimator of the octupole (Eq. (5.51)) as a function of separation d at different redshifts z (same as those of the dipole case).

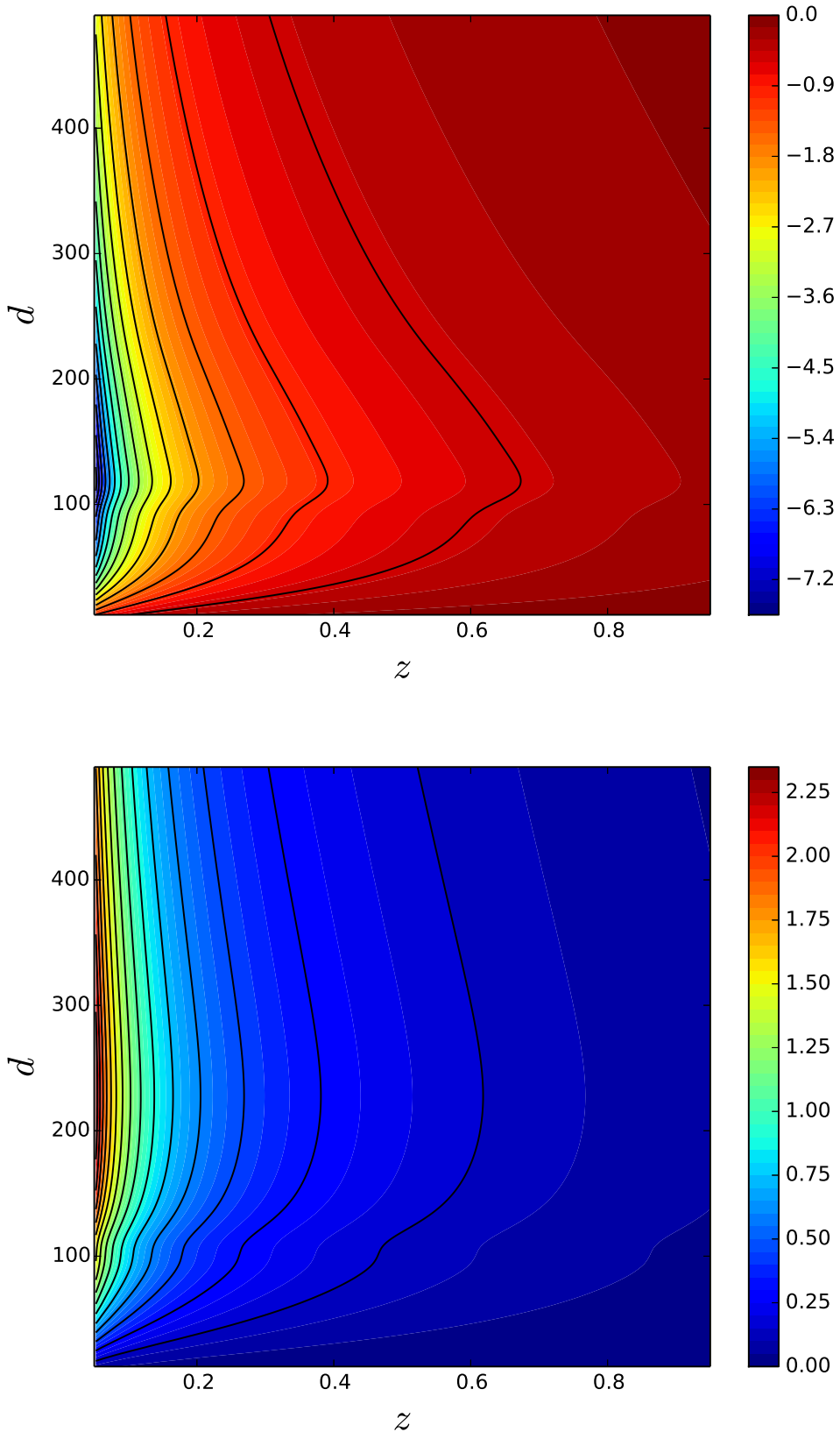

Figure 5.3: *Top panel*: Variation of the magnitude of the dipole in (z, d) space. *Bottom panel*: Variation of the magnitude of the octupole in (z, d) space.

The i and j indices are the pixel number where the number count and the convergence are measured respectively and a_N and b_N are the normalisation factors. For the dipole case, in the continuous limit of Eq. (5.43)

$$\langle\hat{\xi}_{\rm dip}\rangle(d) = a_N \frac{\ell_p}{\ell_p^6}\int d^3\boldsymbol{x}_i \int d^3\boldsymbol{x}_j \langle\Delta_i\kappa_j\rangle \cos\beta_{ij}\delta_D(d_{ij}-d), \tag{5.45}$$

in which the sum over pixel and the dirac delta function become

$$\sum_i = \frac{1}{\ell_p^3}\int d^3\boldsymbol{x}_i \quad , \quad \delta_K(d_{ij}-d) = \ell_p\delta_D(d_{ij}-d), \tag{5.46}$$

ℓ_p being the size of a cubic cell (of volume $V = \ell_p^3$). To compute the integral over $\boldsymbol{x}_i$ one can simply fix the position of the pixel i then multiply by its volume V, which is a good approximation since the universe is statistically homogeneous and isotropic. Then the inner integral can be computed by using spherical coordinates, recalling that by isotropy the correlator does not depend on the azimuthal angle φ, thus

$$\langle\hat{\xi}_{\rm dip}\rangle(d) = a_N \frac{2\pi V d^2\ell_p}{\ell_p^6}\int_0^\pi d\beta \sin\beta\cos\beta\langle\Delta\kappa\rangle. \tag{5.47}$$

Now, inserting the expression of $\langle\Delta\kappa\rangle$ and computing the integral over β yield the mean of the estimator of the dipole as a function of separation d at different redshift z

$$\langle\hat{\xi}_{\rm dip}\rangle(d) = \frac{4\pi V\ell_p d^2}{3\ell_p^6}\frac{2}{9\Omega_m^2\pi^2}\frac{\mathcal{H}(z)}{\mathcal{H}_0}f(z)\left(1-\frac{1}{\mathcal{H}(z)r}\right)\left(b(z)+\frac{3f(z)}{5}\right)\nu_1(d). \tag{5.48}$$

The normalisation factor is therefore

$$a_{\rm N} = \frac{3}{4\pi}\frac{\ell_p^6}{V\ell_p}, \tag{5.49}$$

and the mean of the estimator

$$\langle\hat{\xi}_{\rm dip}\rangle(d) = \frac{2}{9\Omega_m^2\pi^2}\frac{\mathcal{H}(z)}{\mathcal{H}_0}D_1^2(z)f(z)\left(1-\frac{1}{\mathcal{H}(z)r}\right)\left(b(z)+\frac{3f(z)}{5}\right)d^2\nu_1(d). \tag{5.50}$$

Similiar calculations for the case of octupole give

$$\langle\hat{\xi}_{\rm oct}\rangle(d) = -\frac{2}{9\Omega_m^2\pi^2}\frac{\mathcal{H}(z)}{\mathcal{H}_0}D_1^2(z)f(z)\left(1-\frac{1}{\mathcal{H}(z)r}\right)\frac{2f(z)}{5}d^2\nu_3(d) \tag{5.51}$$

with

$$b_{\rm N} = \frac{7}{4\pi}\frac{\ell_p^6}{V\ell_p}. \tag{5.52}$$

In Fig. 5.2, by choosing the set of cosmological parameters $h = 0.68$, $n_s = 0.96$, $\Omega_{cdm} = 0.2548$, $\Omega_b = 0.048$ and $A = 2.2 \times 10^{-9}$ in ΛCDM universe, with the bias evolving according to [2]

$$b(z) = c_4 \exp(c_5 z), \tag{5.53}$$

where c_4 and c_5 are free parameters, we show the mean of the dipole Eq. (5.50), and that of the octupole Eq. (5.51) as a function of the separation d for different values of z. Another way of viewing how both the dipole and octupole vary with respect to both the separation and the redshift, we show the maps in Fig. 5.3. We clearly see that in eah case (dipole and octupole) the overall amplitute drops off with an increasing redshift. This can be explained by the fact that the doppler term decreases as we go at higher redshift. Since the dipole amplitude is roughly three times larger than that of the octupole, in what follows we will only focus on the dipole.

5.1.5 Variance and signal-to-noise

We can now compute the variance of the signal with the expression

$$\mathrm{var}\left(\hat{\xi}_{\rm dip}\right) = \left\langle \left(\hat{\xi}_{\rm dip}\right)^2 \right\rangle - \left\langle \hat{\xi}_{\rm dip} \right\rangle^2. \tag{5.54}$$

Taking Eq. (5.43) into account gives

$$\mathrm{var}\left(\hat{\xi}_{\rm dip}\right) = a_{\rm N}^2 \sum_{ij}\sum_{ab}\Big[\langle \Delta_i\kappa_j\Delta_a\kappa_b\rangle - \langle\Delta_i\kappa_j\rangle\langle\Delta_a\kappa_b\rangle\Big]\cos\beta_{ij}\cos\beta_{ab}\delta_K(d_{ij}-d)\delta_K(d_{ab}-d'), \tag{5.55}$$

and by Wick's theorem we finally get

$$\mathrm{var}\left(\hat{\xi}_{\rm dip}\right) = a_{\rm N}^2 \sum_{ij}\sum_{ab}\Big[\langle \Delta_i\Delta_a\rangle\langle\kappa_j\kappa_b\rangle + \langle\Delta_i\kappa_b\rangle\langle\Delta_a\kappa_j\rangle\Big]\cos\beta_{ij}\cos\beta_{ab}\delta_K(d_{ij}-d)\delta_K(d_{ab}-d'). \tag{5.56}$$

The $\langle\Delta_i\Delta_a\rangle$ contribution to Eq. (5.56) is composed of a Poisson noise, which accounts for the finite number of galaxies, and the cosmic variance, i.e

$$\langle\Delta_i\Delta_a\rangle = \frac{1}{d\bar{n}}\delta_{ia} + C^{\Delta}(d_{ia},\beta_{ia}), \tag{5.57}$$

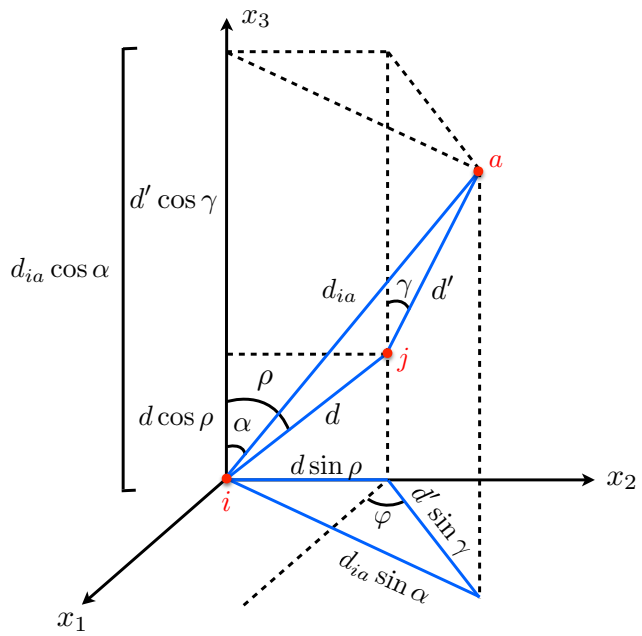

Figure 5.4: Configuration used to calculate the second term in Eq. (5.61) (courtesy: C. Bonvin).

where $d\bar{n}$ is the mean number of galaxies per pixel. The cosmic variance is given by

$$C^{\Delta}(d_{ia}, \beta_{ia}) = \left(b^2 + \frac{2bf}{3} + \frac{f^2}{5}\right) C_0(d_{ia}) - \left(\frac{4bf}{3} + \frac{4f^2}{7}\right) C_2(d_{ia}) P_2(\cos\beta_{ia}) + \frac{8f^2}{35} C_4(d_{ia}) P_4(\cos\beta_{ia}), \tag{5.58}$$

with

$$C_\ell(d_{ia}) = \frac{1}{2\pi^2} \int dk k^2 P(k, z) j_\ell(k d_{ia}) \quad \ell = 0, 2, 4. \tag{5.59}$$

The $\langle \kappa_j \kappa_b \rangle$ contribution contains an intrinsic error on the measurement of the galaxy's size and a cosmic variance contribution C^κ

$$\langle \kappa_j \kappa_b \rangle = \sigma_\kappa^2 \delta_{jb} + C^\kappa(d_{jb}, \beta_{jb}). \tag{5.60}$$

The uncertainety on the size measurement σ_κ depends on both the galaxy type and systematics related to the instruments [194]. It ranges from $\sigma_\kappa = 0.2 - 0.8$. The cosmic variance C^κ is at most of the order 10^{-4} in the range of redshifts we are interested in, it can therefore be safely neglected with respect to the first term in Eq. (5.60). Inserting Eqs. (5.57) and

(5.60) into Eq. (5.56) gives

$$\mathrm{var}\left(\hat{\xi}_{\rm dip}\right) = a_{\rm N}^2\left[\frac{\sigma_\kappa^2}{d\bar{n}}\sum_{ij}\cos^2\beta_{ij}\delta_K(d_{ij}-d)+\sigma_\kappa^2\sum_{ija}C^\Delta(d_{ia},\beta_{ia})\cos\beta_{ij}\cos\beta_{aj}\delta_K(d_{ij}-d)\delta_K(d_{aj}-d')\right], \tag{5.61}$$

where, again the first term var_1 can be computed in the continuous limit by fixing the position of the pixel i and integrating over j

$$\mathrm{var}_1 = \frac{3}{4\pi}\ell_p^2 d^2\frac{\sigma_\kappa^2}{N_{\rm tot}}. \tag{5.62}$$

We use the continuous limit to compute the second term var_2 in Eq. (5.61) and by homogeneity and isotropy we fix the position of the pixel i and multiply the result by V to account for the integral over $\boldsymbol{x}_i$. Without loss of generality we choose the position of the pixel j in the plane x_2-x_3 (see Fig. 5.4). The result is invariant under rotation of j around the x_3-axis so we multiply by 2π to account for this. We obtain

$$\begin{aligned}\mathrm{var}_2 &= a_N^2\sigma_\kappa^2\frac{2\pi\ell_p^2 V}{\ell_p^9}\int_0^\pi d\rho\sin\rho\int_0^\infty ds_1 s_1^2\int_0^{2\pi}d\varphi\int_0^\pi d\gamma\sin\gamma\\ &\quad\times\int_0^\infty ds_2 s_2^2 C^\Delta(d_{ia},\beta_{ia})\cos\rho\cos(\pi+\gamma)\delta_D(s_1-d)\delta_D(s_2-d').\end{aligned} \tag{5.63}$$

By setting $\mu=\cos\rho$ and $\nu=\cos\gamma$ and symplifying, we finally get the expression of the second term

$$\mathrm{var}_2 = -\frac{9}{8\pi}\frac{\ell_p^3}{V}\sigma_\kappa^2 d^2 d'^2\int_{-1}^1 d\mu\mu\int_{-1}^1 d\nu\nu\int_0^{2\pi}d\varphi C^\Delta(d_{ia},\beta_{ia}). \tag{5.64}$$

From Fig. 5.4 we have

$$d_{ia}^2 = d^2+d'^2+2dd'\left(\mu\nu+\sqrt{(1-\mu^2)(1-\nu^2)}\sin\varphi\right), \tag{5.65}$$

$$\cos\beta_{ia} = \frac{d\mu+d'\nu}{d_{ia}}. \tag{5.66}$$

We can now compute the signal to noise ratio to see if the signal is detectable when considering a specific experiment. The expression of S/N as a function of separation is given

$$\frac{S}{N}(d) = \frac{\langle\hat{\xi}_{\rm dip}\rangle(d)}{\sqrt{\mathrm{var}(d)}}, \tag{5.67}$$

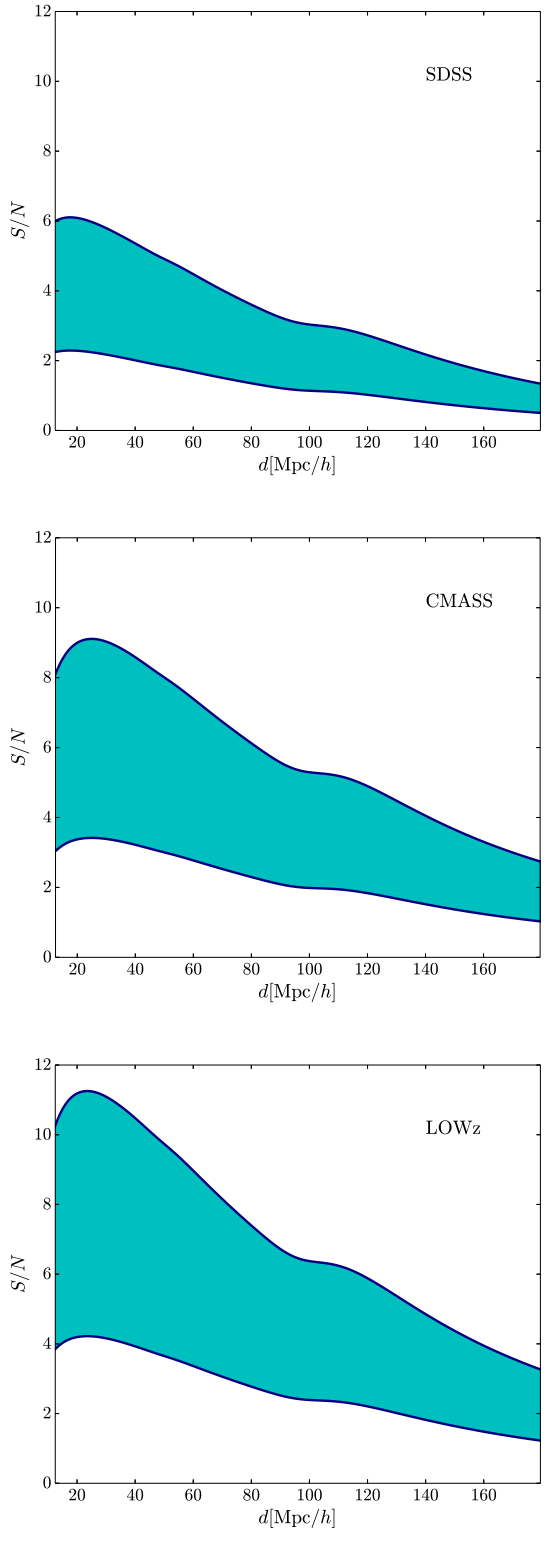

Figure 5.5: Signal to noise ratio as a function of separation for three optical surveys, namely SDSS (*top panel*), CMASS (*middle panel*) and LOWz (*bottom panel*). In each case, the upper bound is the optimistic case where the uncertainty in the size measurement $\sigma_\kappa = 0.3$ and in the lower bound we have $\sigma_\kappa = 0.8$.

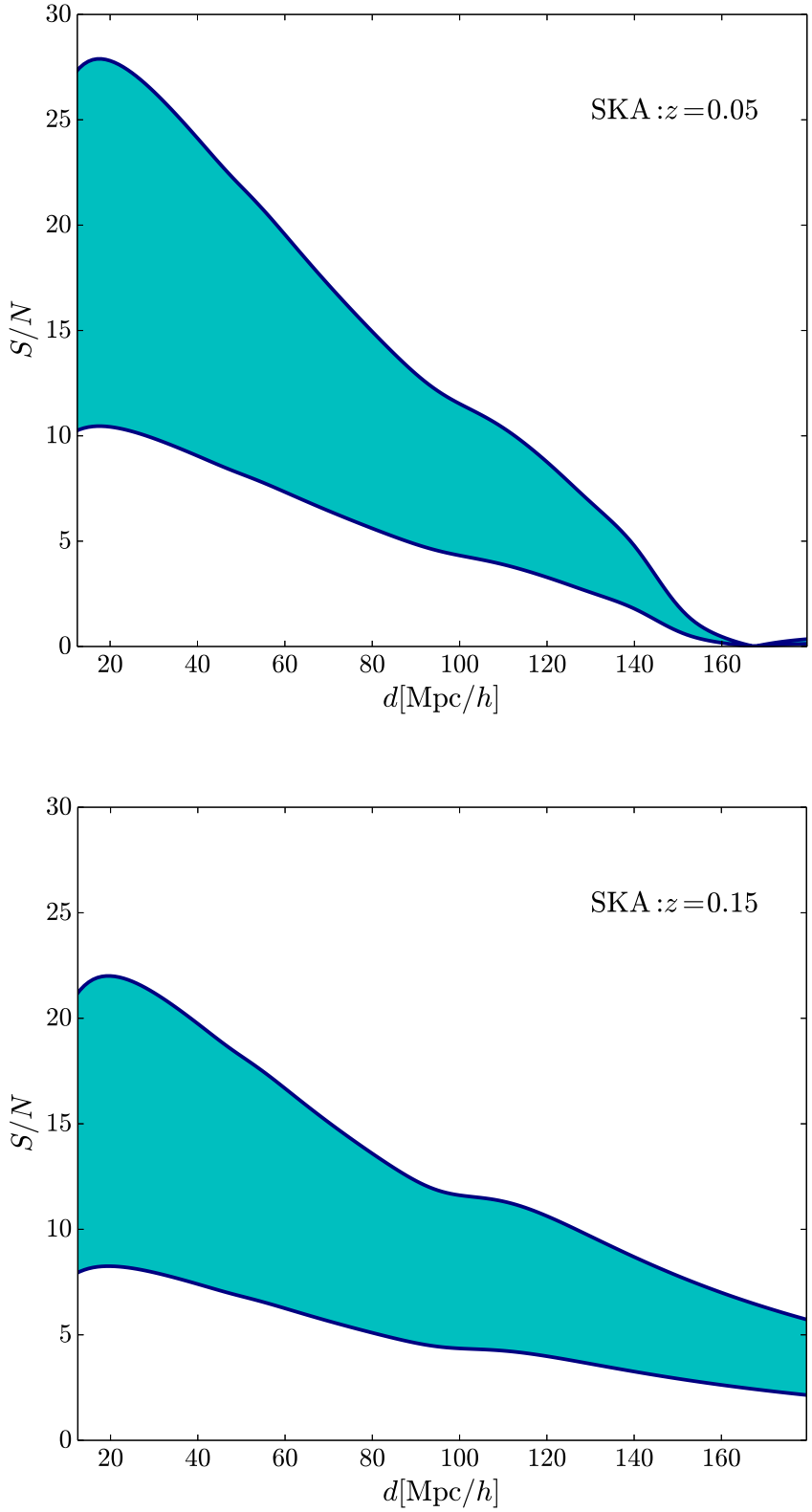

Figure 5.6: Signal to noise ratio as a function of separation for future radio survey SKA1-Mid for two different redshifts, $z = 0.05$ (*top panel*) and $z = 0.15$ (*bottom panel*). Here also for the upper limit $\sigma_\kappa = 0.3$ and for lower limit $\sigma_\kappa = 0.8$.

where the signal is given in Eq. (5.50) and the noise by Eqs. (5.62), (5.64). As shown in Fig. 5.5, we compute the S/N for three current optical surveys which are SDSS galaxies at $z \leq 0.2$, LOWz and CMASS. The characteristics of each of those three surveys are given in Table. 5.2 (taken from [195,196]). In this analysis, unlike in the previous one (see Chapter 4), we consider an optimistic case where $\sigma_\kappa = 0.3$ which results in the upper bounds in Fig. 5.5 and a pessimistic case with $\sigma_\kappa = 0.8$ giving the lower bound. The choice of $\sigma_\kappa = 0.8$ is based on the estimation of the typical dispersion on κ presented in [194] where they developed a Bayesian approach using measurements of sizes, magnitudes and redshifts of galaxy samples. In principle, assuming a lower intrinsic error in the size measurement $\sigma_\kappa = 0.3$, the Doppler magnification can be detected with the current optical surveys as illustrated in Fig. 5.5. We check the detectability of the signal with future radio surveys like SKA. To do so, we then compute S/N for two redshift bins $z = 0.05, 0.15$ by considering SKA1-Mid experiment whose characteristics are given in Table. 5.1 (taken from [3]).

$z_{\rm min}$	$z_{\rm max}$	$n(z)[{\rm Mpc}^{-3}]$	$b(z)$	$S_{\rm rms}[\mu{\rm Jy}]$
0.0	0.1	2.73×10^{-2}	0.657	117.9
0.1	0.2	4.93×10^{-3}	0.714	109.6
0.2	0.3	9.49×10^{-4}	0.789	102.9
0.3	0.4	2.23×10^{-4}	0.876	97.5
0.4	0.5	6.44×10^{-5}	0.966	93.1

Table 5.1: Number density $n(z)$, bias $b(z)$ and flux sensitivity $S_{\rm rms}$ per redshift bin for SKA1-Mid where a sky coverage of 5000 square degree is assumed.

	$z_{\rm mean}$	Ntot	V $[({\rm Mpc/h})^3]$
SDSS	0.1	444 475	0.657×10^6
LOWz	0.32	148 833	0.714×10^8
CMASS	0.57	380 899	0.789×10^9

Table 5.2: Total number of galaxies (Ntot) and survey volume (V) for each optical survey at a particular redshift.

We plot in Fig. 5.6 the signal to noise ratio assuming both the optimistic and pessimistic case again. The overall signal drops with increasing redshift. We also find that the signal will be measured by SKA. The cumulative signal-to-noise over all separations can be calculated accounting for the fact that the signal at different separation is correlated

$$\left(\frac{S}{N}\right)^2_{\rm c} = \sum_{ab} \langle\hat{\xi}_{\rm dip}\rangle(d_a) {\rm var}^{-1}(d_a, d_b) \langle\hat{\xi}_{\rm dip}\rangle(d_b)\,. \tag{5.68}$$

By choosing a range of separation $12 \leq d \leq 180$ Mpc/h we find for the optimistic case the cumulative signal-to-noise is $10.2, 22.5, 19.5$ for SDSS, LOWz and CMASS respectively and is $3.8, 8.4, 7.3$ for SDSS, LOWz and CMASS respectively for the pessimistic case. Assuming that the three samples are uncorrelated, we reach a total signal-to-noise of 31.4 in the optimistic case and of 11.8 in the pessimistic case. This comes to corroborate the fact that the Doppler magnification is detectable with those three optical surveys. For SKA experiment, we find that the cumulative signal-to-noise over the same range of separation combining redshifts $0 \leq z \leq 0.5$ (assuming that the redshift bins are uncorrelated) is 48.7 in the optimistic case and 18.3 in the pessimistic case.

5.1.6 Forecasts

As the Doppler magnification can be detected with the current optical surveys and future radio survey SKA, we want to know well the cosmological parameters can be constrained using those surveys. Considering each type of survey, we then carry out Fisher forecast analyses using the standard formula to construct the Fisher matrices

$$F_{\alpha\beta} = \sum_{ab} \frac{\partial \langle \hat{\xi}_{\rm dip} \rangle}{\partial p_\alpha}(d_a) \mathrm{var}^{-1}(d_a, d_b) \frac{\partial \langle \hat{\xi}_{\rm dip} \rangle}{\partial p_\beta}(d_b), \tag{5.69}$$

where p_α denotes all the free parameters in a model and var is the variance given in Eq. (5.61).

Optical surveys

For the optical surveys, we have three samples SDSS, LOWz and CMASS at three tomographic bins, $z = 0.1, 0.32, 0.57$ respectively. While accounting for correlations between separation using the full covariance matrix Eq. (5.61) we assume that the three samples are uncorrelated such that the three Fisher matrices related to the three bins can be combined. In our analyses we avoid non-linearities by choosing the lowest separation to be 12 Mpc/h. We examine different cases depending on whether the bias b is known and the growth index is chosen to be a free parameter.

We first consider that the bias in each tomographic bin is known and the value of the growth index is fixed to $\gamma = 0.55$(as in ΛCDM). The error contours for the joint constraints between all the free parameters are plotted in Fig. 5.7. For the optimistic case with $\sigma_\kappa = 0.3$, we find that the marginalised error for equation of state parameter w_0 is $\sigma_{w_0} = 0.13$, which is

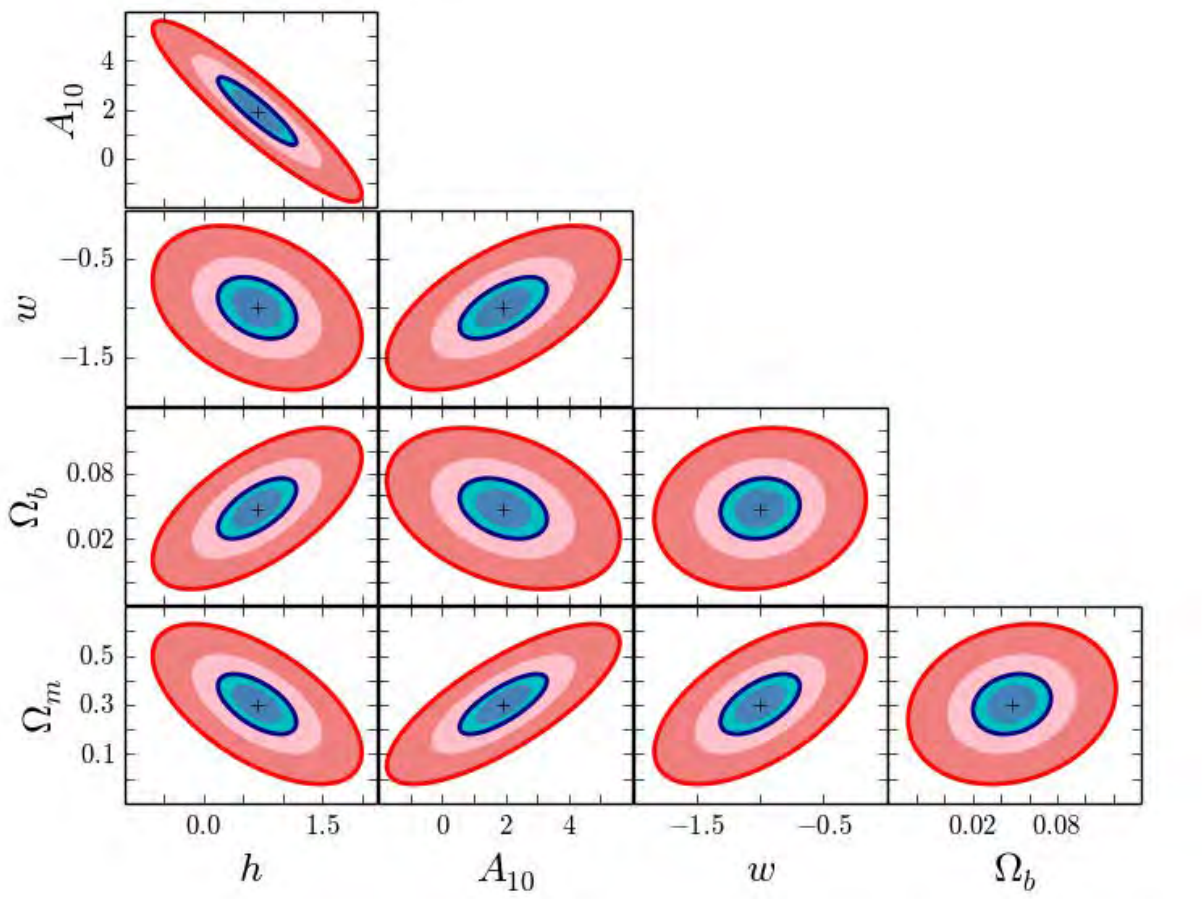

Figure 5.7: Joint constraints between all the free parameters in the model. Here we consider optical surveys (see text) and three redshift bins for our analysis. The value of growth index γ is fixed and the bias is assumed to be completely known. The blue ellipses are for the optimistic case $\sigma_\kappa = 0.3$ (68% blue and 95% light blue) and the red ones are for $\sigma_\kappa = 0.8$ (68% light red and 95% red).

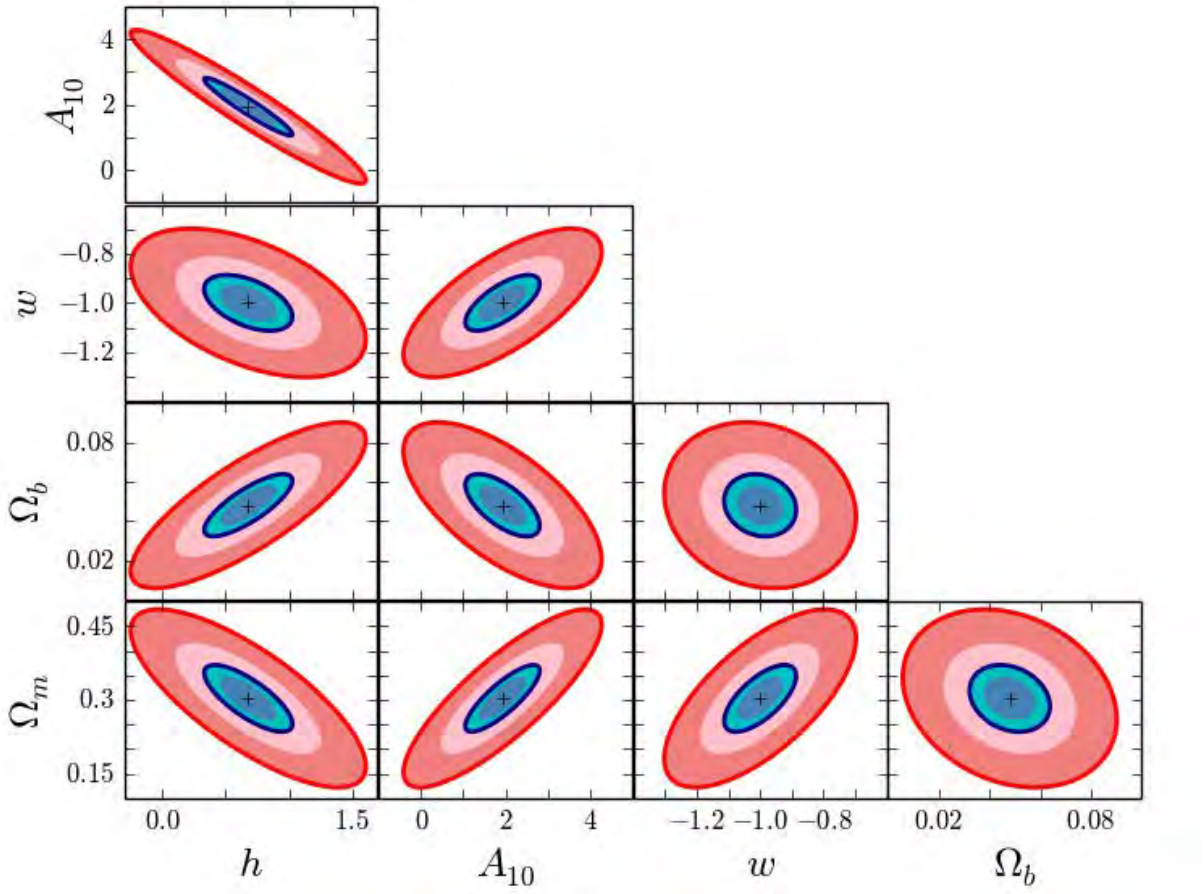

Figure 5.8: Joint constraints between all the free parameters in the model. Here we consider radio survey, SKA1-Mid (see text) and five redshift bins for our analysis. The value of growth index γ is fixed and the bias is assumed to be completely known. The blue ellipses are for the optimistic case $\sigma_\kappa = 0.3$ (68% blue and 95% light blue) and the red ones are for $\sigma_\kappa = 0.8$ (68% light red and 95% red)

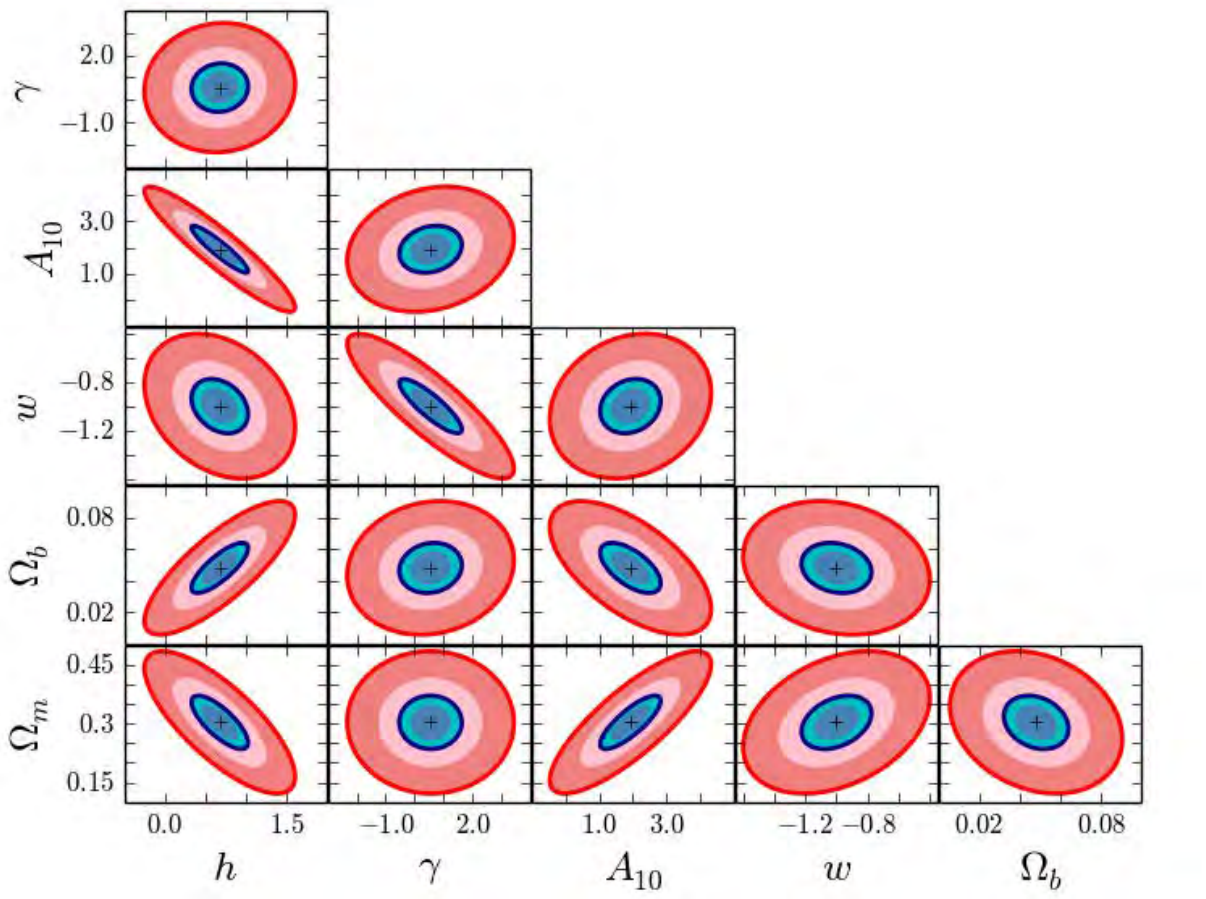

Figure 5.9: Joint constraints between all the free parameters in the model. Here we consider radio survey, SKA1-Mid (see text) and five redshift bins for our analysis. The bias is assumed to be completely known. The blue ellipses are for the optimistic case $\sigma_\kappa = 0.3$ (68% blue and 95% light blue) and the red ones are for $\sigma_\kappa = 0.8$ (68% light red and 95% red)

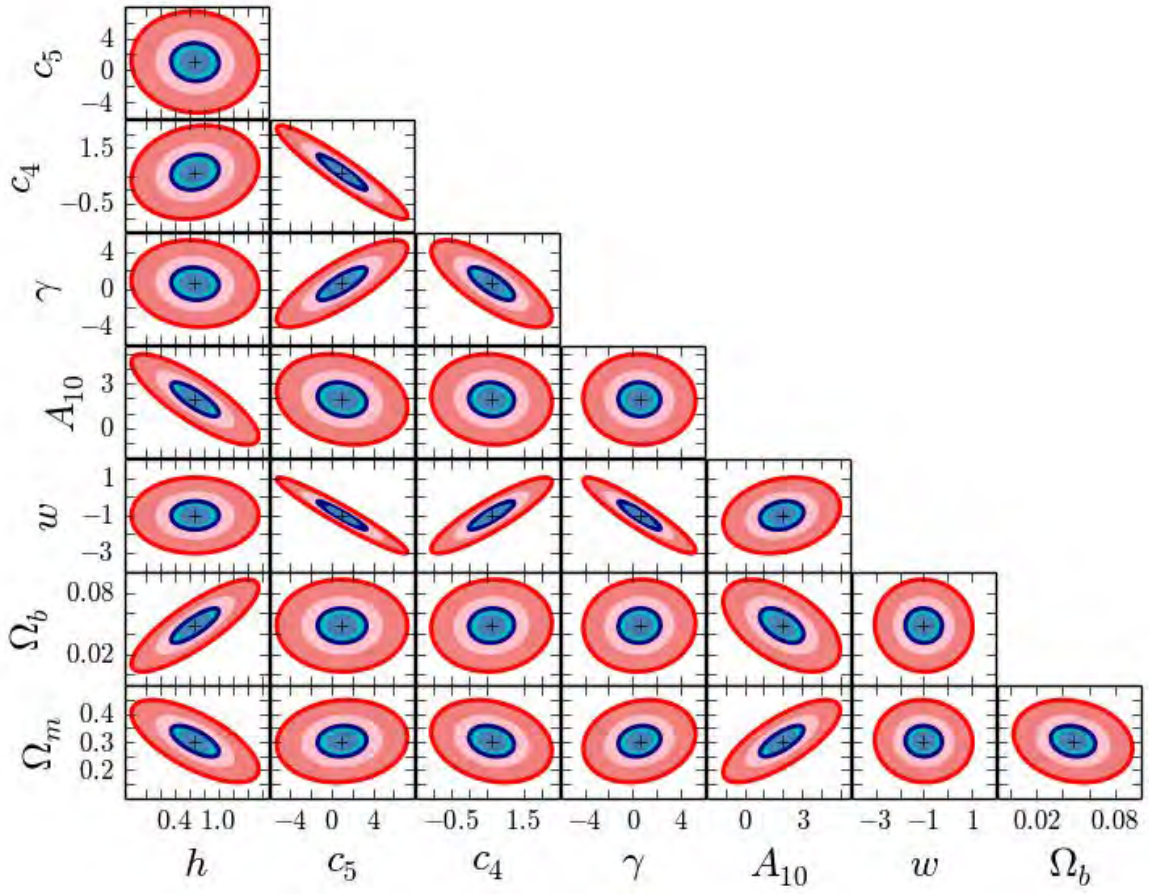

Figure 5.10: Joint constraints between all the free parameters in the model. Here we consider radio survey, SKA1-Mid (see text) and five redshift bins for our analysis. We assume a bias model defined by two free parameters c_4 and c_5. The blue ellipses are for the optimistic case $\sigma_\kappa = 0.3$ (68% blue and 95% light blue) and the red ones are for $\sigma_\kappa = 0.8$ (68% light red and 95% red)

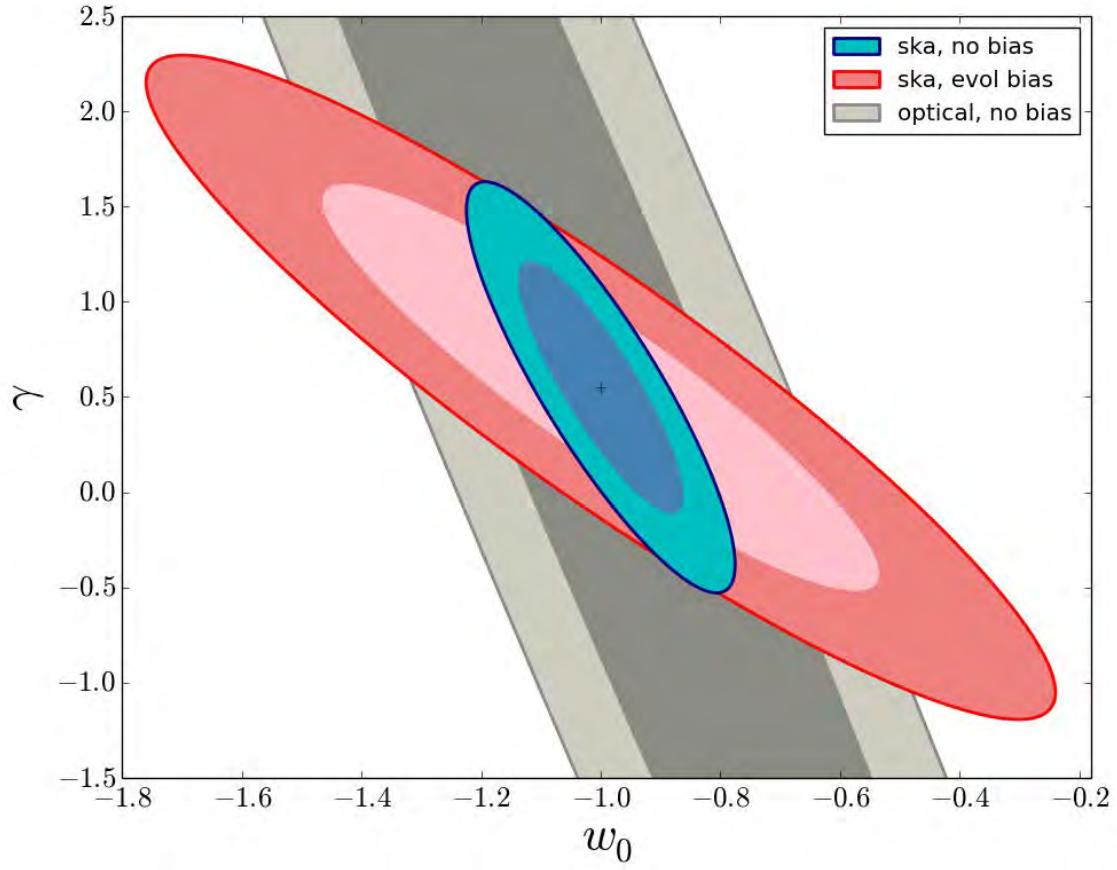

Figure 5.11: Joint constraints w_0-γ for three cases. Blue: we consider SKA1-Mid survey while assuming that the bias is completely known, red: we have SKA1-Mid with an evolving bias [2] and grey: we consider optical surveys (SDSS, LOWz and CMASS) while assuming the bias is completely known. In each case we have set $\sigma_\kappa = 0.3$ and plotted 1-σ and 2-σ confidence levels.

relatively good and that of the pessimistic case is $\sigma_{w_0} = 0.34$. It can be clearly seen how the uncertainty on the size measurement impacts on the constraints.

We now assume that we have no knowledge about the bias, by letting it be a free parameter in each tomographic bin. We find that under such conditions it is impossible to constrain dark energy as the marginalised error gets worse by several orders of magnitude in either pessimistic or optimistic case.

When we add another degree of freedom by allowing the growth index to vary while assuming the bias is completely known, we find that the constraint on dark energy is looser ($\sigma_{w_0} = 0.63$ for optimistic case and $\sigma_{w_0} = 1.70$ for pessimistic case) compared to the case where γ is fixed. This is expected since by adding more degrees of freedom, the constraints become loosened.

Radio survey, SKA1-Mid

For the future radio survey, SKA1-Mid, we choose five tomographic bins as prescribed in [3]. As in the case of optical surveys, we start our analysis by assuming that the bias is known and the growth index is fixed. We obtain a tight constraint on dark energy $\sigma_{w_0} = 0.04$ for the optimistic case and a constraint $\sigma_{w_0} = 0.12$ for the pessimistic case (see Fig. 5.8). When allowing devitations from ΛCDM, by letting γ vary, the constraint in each case is loosened a bit but still relatively tight compared to that of obtained from optical surveys (see Fig. 5.9).

When we assume that the bias is unknown, constraining dark energy turns out to be quite hard, as expected. The marginalised error σ_{w0} increases by several orders of magnitude. We now consider an evolution of the bias [2]. We find that the constraints on dark energy are promising either we allow some departure from ΛCDM or not. However the case with fixed growth index offers tighter constraints with $\sigma_{w_0} = 0.12$ against $\sigma_{w_0} = 0.30$ when γ is a free parameter[6]. In Fig. 5.10 we plot the ellipse contours of the model including γ as a free parameter. In Fig. 5.11, we compare the joint constraints w_0, γ obtained from three cases, SKA1-Mid with a known bias, SKA1-Mid with an evolving bias and optical survey with a known bias. The fact that SKA1-Mid survey with an evolving bias offers constraints tighter than that of obtained from an optical survey with a full knowledge of the bias clearly suggests that radio survey has far more constraining power. Fig. 5.11 also highlights the fact that a good knowledge of the bias is crucial to constraining dark energy.

[6]This is for the optimistic case, for the pessimistic case, the constraint with fixed γ is still tighter than that of with γ as a free parameter but both are a bit worse than that of optimistic case.

It is worth mentioning that in all our calculations leading to the Forecasts in Figs. 5.7, 5.8, 5.9, 5.10, 5.11, we have not used any priors from other experiments like *Planck* for example. The reason is that we want to investigate whether the new statistical tool presented in this Chapter is better than the one we used in the previous Chapter. However, by breaking the degeneracy by combining with data sets from different experiments, the constraints presented here will greatly improve.

5.2 Dipole modulation in Modified gravity

In order to explain the growth of structure and the acceleration of the expansion that the universe has recently undergone, lots of efforts have been made towards finding new alternative theories of gravity without resorting to a cosmological constant Λ. Among the more often used models is the Dvali-Gabadadze-Porrati (DGP) brane world [197, 198], where the acceleration is induced by the gravity leaking off the 5-D Minkowski space-time. Another alternative theory also consists of modifying the Einstein-Hilbert action by adopting a function of the Ricci scalar $f(R)$ instead of the Ricci scalar used in General Relativity (GR). A well studied model of $f(R)$ is the Hu and Sawicki model which was shown to respect the stringent constraints in high density environment [199]. This $f(R)$ model has the phenomenology of ΛCDM as a limiting case.

In an attempt to distinguish GR from modified gravity, [200] developed a technique to compute the non-linear power spectrum while taking into account the mechanism that allows the model to recover GR on small scales.

Peculiar velocity which is directly related to density perturbations via the conservation equation is also an important tool to probe the growth of structure and the nature of Dark Energy. In [165], by exploiting Doppler magnification, they obtained constraints on cosmological parameters that really look promising. Some previous works also highlighted how the use of peculiar velocities can help detect any departure from GR. In Section 5.1, we have investigated some departure from GR using the parametrisation

$$\frac{d\,\ln D(a)}{d\,\ln a} = \Omega(z)^{\gamma}. \tag{5.70}$$

In [74], they investigated the viability of some modified gravity theory by resorting to mean pairwise velocity.

Our motivation in this section is to elaborate a new method that potentially allows us to probe any modified gravity signature.

In this part of the work, we work within the parameterised post-Friedmann (PPF) framework which was first introduced by [201]. It is a general approach which was developed to describe the three regimes of modified gravity theories and consists of introducing a scale and time dependent parameter $\eta(k,z)$ relating the two Bardeen potentials and another parameter $\mu(k,z)$ which modifies the standard Poisson equation in ΛCDM paradigm in order to control the transition from quasi-linear regime to the non-linear one where GR should be recovered. The theories covered by this parameterisation, like a cosmological constant with a negative pressure, allows one to account for the late-time acceleration. We consider linear regime in sub-horizon scales in all our calculations.

In § 5.2.1 we develop the formalism where we derive the velocity potential in PPF. We also compute the suitable correlation function that allows us to constrain the parameters used in the model via a Fisher forecast analysis. We present our predictions in § 5.2.5 and finally conclude.

5.2.1 Velocity and growth suppression factor

Poisson's equation from Einstein field equation is modified and the two Bardeens potentials are no longer the same thus, for consistency, the velocity potential takes a new form accordingly. In this section, we present the resulting expression of the velocity within the context of PPF. In what follows, we assume that the expansion history is the same as ΛCDM and the relevant scales are sub-horizon in linear regime. We now consider the line element in Newtonian gauge

$$ds^2 = a^2\left[-(1+2\Psi)d\eta^2 + (1-2\Phi)dx_i dx^i\right]. \tag{5.71}$$

It is worth mentioning that from now on, we choose Ψ as the time-time component and Φ the space-space component. Modifying Poisson's equation consists of introducing a generic function which is both scale and time dependent [179, 202]

$$-k^2\Psi = 4\pi G a^2 \bar{\rho}\mu(a,k)\Delta_M, \tag{5.72}$$

where Δ_M is defined as the gauge invariant comoving density perturbation

$$\Delta_M = \delta + 3\mathcal{H}v/k. \tag{5.73}$$

and $\mu(a,k)$ is a function both scale and time dependent. The second modification is the relationship between the two Bardeen potentials [179, 202]

$$\Phi = \eta(a,k)\Psi, \tag{5.74}$$

$\eta(a,k)$ being known as the gravitational slip. Exploiting the two conservation equations ($T^{\mu}_{\nu;\mu} = 0$)

$$\delta' = -kv + 3\Phi', \tag{5.75}$$

$$v' = -\mathcal{H}v + k\Psi, \tag{5.76}$$

and taking into account Eqs. (5.72),(5.73) and (5.74), we arrive at the modified form of the velocity potential.

$$v = \left[\Psi'\left(3\eta + \frac{2ak^2}{3\mu\mathcal{H}_0^2\Omega_m}\right) + \Psi\mathcal{H}\left(3\left[1+\frac{\eta'}{\mathcal{H}}\right] + \frac{2ak^2}{3\mu\mathcal{H}_0^2\Omega_m}\left[1-\frac{\mu'}{\mathcal{H}\mu}\right]\right)\right]\frac{k}{(k^2+3(\mathcal{H}^2-\mathcal{H}'))}. \tag{5.77}$$

This expression involving the two generic functions is a bit complicated but on sub-horizon scales ($k \gg \mathcal{H}$) we can use the following approximation

$$v = \frac{2ak}{3\mu\mathcal{H}_0^2\Omega_m}\left[\Psi' + \Psi\mathcal{H}\left(1-\frac{\mu'}{\mathcal{H}\mu}\right)\right]. \tag{5.78}$$

One can clearly see that the ΛCDM version of the velocity is recovered by letting $\mu = 1$ in Eq. (5.78). The resulting Bardeen equation on sub-horizon scales from the modifications reads [179, 202]

$$\Delta_M'' + \left[2 + \frac{\mathcal{H}'}{\mathcal{H}}\right]\Delta_M' = \frac{3}{2}\Omega_M(a)\mu\Delta_M, \tag{5.79}$$

where primes here are derivatives with respect to ln(a). The growth suppression factor is computed by solving Eq. (5.79) numerically. It is worth noting that, the modified quantities, namely the velocity potential and the growth suppression factor are only dependent on $\mu(a,k)$, therefore on small scales, we can only constrain the parameters used to define $\mu(a,k)$.

5.2.2 Cross-correlation between galaxy overdensity and doppler convergence

In order to constrain modified gravity using peculiar velocity, the approach consists of using the cross-correlation of the Doppler magnification and galaxy number count as in ΛCDM (see Eq. 5.1),

$$\xi^{MG} = \langle \Delta(\hat{\mathbf{n}}, z)\kappa(\hat{\mathbf{n}}', z')\rangle, \tag{5.80}$$

where $\Delta(\hat{\mathbf{n}}, \mathrm{z})$ is the galaxy overdensity, $\kappa(\hat{\mathbf{n}}, \mathrm{z})$ the Doppler convergence, z is the redshift and $\hat{\mathbf{n}}$ is the unit vector pointing in the direction of observations. Here also, to leading order, we choose

$$\Delta(\hat{\mathbf{n}}, \mathrm{z}) = b \cdot \delta - \frac{1}{\mathcal{H}}\partial_\chi(\mathbf{V} \cdot \hat{\mathbf{n}}). \tag{5.81}$$

Similar to the ΛCDM case, we only take into account the doppler term in the convergence. Using $\bar{\rho} = 3\Omega_m\mathcal{H}_0^2/(8\pi G a^3)$ and Eq. (5.72), the density becomes

$$\delta(\hat{\boldsymbol{k}}, z) = -\frac{2}{3}\left(\frac{k}{\mathcal{H}_0}\right)^2 \frac{a}{\Omega_m \mu(z,k)} T(k) g_{MG}(z,k)\Psi(\hat{\boldsymbol{k}}) \tag{5.82}$$

where the subscript MG means modified gravity counterpart of a variable. Here $T(k)$ is the transfer function in ΛCDM since modified gravity, within this class of theories, comes into play well after equality and $g_{MG}(z,k)$ is the growth suppression factor which is now both scale and time dependent. Using $\Psi(\hat{\mathbf{k}}, z) = T(k)g_{MG}(k,z)\Psi_i(\hat{\mathbf{k}})$ at linear order, the velocity becomes

$$v(\hat{\boldsymbol{k}}, z) = \mathcal{G}_{MG}(k,z)T(k)\Psi(\hat{\boldsymbol{k}}). \tag{5.83}$$

Where prime denotes derivatives with respect to conformal time. To alleviate the notations, we let

$$\mathcal{G}_{MG}(k,z) = \frac{2ak}{3\mu\mathcal{H}_0^2\Omega_m}\left[g_{MG}(k,z)' + g_{MG}(k,z)\mathcal{H}\left(1 - \frac{\mu'}{\mathcal{H}\mu}\right)\right]. \tag{5.84}$$

The correlation then reads

$$\begin{aligned}\xi^{MG} &= \left(\frac{1}{\mathcal{H}(z')\chi(z')}-1\right)\int\frac{d^3\boldsymbol{k}}{(2\pi)^3}\int\frac{d^3\boldsymbol{k}'}{(2\pi)^3}e^{-i\mathbf{k}\cdot\mathbf{x}}e^{-i\mathbf{k}'\cdot\mathbf{x}'}i(\hat{\boldsymbol{k}}\cdot\hat{\mathbf{n}}') \\ &\times\left(-\frac{2b}{3}\left(\frac{k}{\mathcal{H}_0}\right)^2\frac{a}{\Omega_M\mu(z,k)}T(k)g_{MG}(z,k)-(\hat{\boldsymbol{k}}\cdot\hat{\mathbf{n}})^2\frac{k}{\mathcal{H}}\mathcal{G}_{MG}(k,z)T(k)\right) \\ &\times(\mathcal{G}_{MG}(k',z')T(k'))\,\langle\Psi(\hat{\boldsymbol{k}})\Psi(\hat{\boldsymbol{k}}')\rangle.\end{aligned} \tag{5.85}$$

Using the definition in Eq. (5.16) yields

$$\begin{aligned}\xi^{MG} &= \left(\frac{1}{\mathcal{H}(z')\chi(z')}-1\right)\int\frac{d^3\boldsymbol{k}}{(2\pi)^3}e^{i\hat{\boldsymbol{k}}\cdot(\mathbf{x}'-\mathbf{x})}i(\hat{\boldsymbol{k}}\cdot\hat{\mathbf{n}}') \\ &\times\left(\frac{2b}{3}\left(\frac{k}{\mathcal{H}_0}\right)^2\frac{a}{\Omega_M\mu(z,k)}T(k)g_{MG}(z,k)+(\hat{\boldsymbol{k}}\cdot\hat{\mathbf{n}})^2\frac{k}{\mathcal{H}}\mathcal{G}_{MG}(k,z)T(k)\right) \\ &\times(\mathcal{G}_{MG}(k,z')T(k))\,P_\Psi(k).\end{aligned} \tag{5.86}$$

Using the same approach as in the ΛCDM case (Section 5.1), we finally get the expression of the cross-correlation in full sky

$$\begin{aligned}\xi^{MG} &= \frac{1}{(2\pi)^3}\left(\frac{1}{\mathcal{H}(z')\chi(z')}-1\right)\Bigg\{-4\pi\cos\alpha\left[\lambda_1(d)+\frac{1}{15}\nu_1(d)-\frac{1}{10}\nu_3(d)\right] \\ &-\frac{4\pi}{5}\cos(\alpha)\cos(2\beta)\left[\nu_1(d)-\frac{3}{2}\nu_3(d)\right]-\frac{4\pi}{5}\sin(\alpha)\sin(2\beta)\left[\nu_1(d)+\nu_3(d)\right]\Bigg\}\end{aligned} \tag{5.87}$$

letting

$$\nu_\ell(d)=\int dk\,k^2\mathcal{F}_{1,2}(k,z,z')j_\ell(kd) \tag{5.88}$$

with $\ell=1,3$ and

$$\lambda_\ell(d)=\int dk\,k^2\mathcal{F}_1(k,z,z')j_\ell(kd). \tag{5.89}$$

where $\ell=1$. Here we have set

$$\mathcal{F}_1(k,z,z')=\left(\frac{2b}{3}\left(\frac{k}{\mathcal{H}_0}\right)^2\frac{a}{\Omega_M\mu(z,k)}g_{MG}(z,k)+\frac{k}{3\mathcal{H}}\mathcal{G}_{MG}(k,z)\right)\mathcal{G}_{MG}(k,z')T^2(k)P_\Psi(k), \tag{5.90}$$

$$\mathcal{F}_{1,2}(k,z,z')=\frac{k}{\mathcal{H}}\mathcal{G}_{MG}(k,z)\mathcal{G}_{MG}(k,z')T^2(k)P_\Psi(k). \tag{5.91}$$

The expression of the correlation function in the distant observer approximation reads

$$\xi^{MG} = \frac{1}{(2\pi)^3}\left(1-\frac{1}{\mathcal{H}\chi}\right)\left[\left(\frac{16\pi}{15}\nu_1 + 4\pi\lambda_1\right)P_1(\cos(\beta)) - \frac{8\pi}{5}P_3(\cos(\beta))\nu_3\right], \tag{5.92}$$

where the dipole is

$$\xi^{MG}_{\rm dip} = \frac{1}{(2\pi)^3}\left(1-\frac{1}{\mathcal{H}\chi}\right)\left(\frac{16\pi}{15}\nu_1 + 4\pi\lambda_1\right), \tag{5.93}$$

and the octupole

$$\xi^{MG}_{\rm oct} = -\frac{1}{5\pi^2}\left(1-\frac{1}{\mathcal{H}\chi}\right)\nu_3. \tag{5.94}$$

It is noted that by setting $\mu = 1$ in Eqs. (5.93),(5.94), we recover Eq. (5.41),(5.42) respectively.

5.2.3 Parametrisation

In the phenomenological approach of modifying Einstein's GR, there exists a variety of functional forms of $\mu(k,a)$ but they all share the common feature of mimicking the apparent acceleration of the cosmic expansion at both specific scales and times. In our analysis, whose main objective is to highlight the great potential that our statistical tool provides in terms of contraining modified gravity, we choose the following parametrisation derived from $f(R)$ theories [203]

$$\mu(k,a) = \frac{1+\beta_1\lambda_1^2k^2a^s}{1+\lambda_1^2k^2a^s}, \tag{5.95}$$

where β_1 is a dimensionless couplings, λ_1^2 has length squared unit. We also consider another type of parametrisation [204, 205]

$$\mu(a,k) = 1 + f_1(a)\frac{1+c_1(\lambda H/k)^2}{1+(\lambda H/k)^2}, \tag{5.96}$$

where the time dependence $f_1(a) = E_{11}\Omega_\Lambda(a)$. In the large scales limit we have $\mu \sim 1 + f_1(a)c_1$ whereas for small scales $\mu \sim 1 + f_1(a)$. As pointed out in the papers of the *Planck* collaboration [205], there is no significant difference in terms of constraint by adding extra degree of freedom to account for the scale-dependence of this type of parametrisation, therefore we follow their prescription by choosing a time dependent $\mu(a)$ i.e $\mu \sim 1 + f_1(a)$.

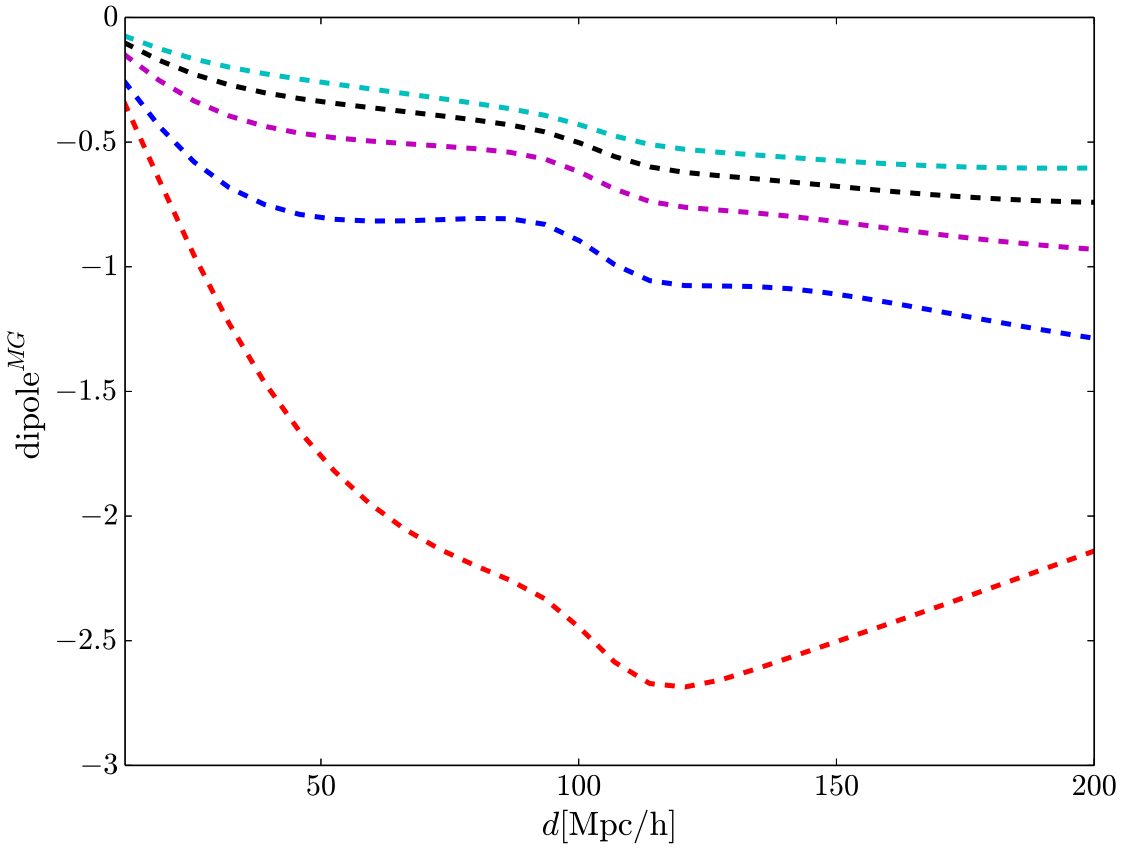

Figure 5.12: Mean estimator of the dipole in modified gravity related to the parametrisation in Eq. (5.95) at different redshifts: $z = 0.15$ (blue dashed), $z = 0.25$ (magenta dashed), $z = 0.35$ (black dashed), $z = 0.45$ (cyan dashed). We choose the fiducial values $s = 4$, $\beta_1 = 4/3$ and $\log(\beta_1\lambda_1^2/\mathrm{Mpc}^2) = 4$ and the bias b at each redshift bin is given in [3]. For comparison, dipole in ΛCDM is also plotted at $z = 0.15$ (red dashed)

5.2.4 Estimator

In this analysis, we propose to use the same estimator as in ΛCDM which we recall

$$\hat{\xi}^{MG}_{\mathrm{dip}}(d) = a_{\mathrm{N}} \sum_{ij} \Delta_i \kappa_j \cos\beta_{ij} \delta_K(d_{ij} - d), \tag{5.97}$$

for which the variance is the exact same form of Eq. (5.61). The only difference lies in that the growth factor is in general both time and scale dependent, therefore we need to recompute the cosmic variance C^{Δ} for modified gravity. Thus, we first need give the following

definitions to alleviate the notations

$$\mathcal{T}_v(z,k) = \mathcal{G}_{MG}(k,z)T(k), \tag{5.98}$$

$$\mathcal{T}_\Delta(k,z) = -\frac{2}{3}\left(\frac{k}{\mathcal{H}_0}\right)^2 \frac{a}{\Omega_M \mu(z,k)} T(k) g_{MG}(z,k), \tag{5.99}$$

so that

$$v(\hat{\boldsymbol{k}},z) = \mathcal{T}_v(k,z)\Psi(\hat{\boldsymbol{k}}), \tag{5.100}$$

and

$$\Delta(\hat{\boldsymbol{k}},z) = \mathcal{T}_\Delta(k,z)\Psi(\hat{\boldsymbol{k}}). \tag{5.101}$$

We also let the cosine between the wavevector and the direction of observation

$$u = (\hat{\boldsymbol{k}}\cdot\hat{\mathbf{n}}). \tag{5.102}$$

The correlator becomes

$$\begin{aligned}\langle\Delta(\hat{\mathbf{n}},z)\Delta(\hat{\mathbf{n}}',z')\rangle &= \int \frac{d^3\boldsymbol{k}}{(2\pi)^3}\int \frac{d^3\boldsymbol{k}'}{(2\pi)^3} e^{-i\boldsymbol{k}\cdot\boldsymbol{x}} e^{-i\boldsymbol{k}'\cdot\boldsymbol{x}'}\left[b\mathcal{T}_\Delta(k,z) - \frac{1}{\mathcal{H}}\mathcal{T}_v(k,z)u^2\right] \\ &\times\left[b\mathcal{T}_\Delta(k',z') - \frac{1}{\mathcal{H}}\mathcal{T}_v(k',z')u'^2\right]\langle\Psi(\hat{\boldsymbol{k}})\Psi(\hat{\boldsymbol{k}}')\rangle,\end{aligned} \tag{5.103}$$

which in a distant observer approximation yields

$$\langle\Delta(\boldsymbol{x})\Delta(\boldsymbol{x}')\rangle = \int \frac{d^3\boldsymbol{k}}{(2\pi)^3} e^{i\boldsymbol{k}\cdot(\boldsymbol{x}'-\boldsymbol{x})}\left[b\mathcal{T}_\Delta(k,z) - \frac{1}{\mathcal{H}}\mathcal{T}_v(k,z)u^2\right]^2 P(k). \tag{5.104}$$

Now further simplifying the notations

$$b_{MG}(z,k) = b\mathcal{T}_\Delta(k,z), \tag{5.105}$$

$$f_{MG}(z,k) = -\frac{1}{\mathcal{H}}\mathcal{T}_v(k,z), \tag{5.106}$$

such that

$$\langle\Delta(\boldsymbol{x})\Delta(\boldsymbol{x}')\rangle = \int \frac{d^3\boldsymbol{k}}{(2\pi)^3} e^{i\boldsymbol{k}\cdot(\boldsymbol{x}'-\boldsymbol{x})}\left[b_{MG}(k,z) + f_{MG}(k,z)u^2\right]^2 P(k). \tag{5.107}$$

After some algebra we obtain

$$C^\Delta_{MG}(d_{ia},\beta_{ia}) = C_0^{MG}(d_{ia}) - C_2^{MG}(d_{ia})P_2(\cos\beta_{ia}) + C_4^{MG}(d_{ia})P_4(\cos\beta_{ia}), \tag{5.108}$$

with

$$C_0^{MG}(d_{ia}) = \frac{1}{2\pi^2}\int dk k^2 \left(b_{MG}^2 + \frac{2b_{MG}f_{MG}}{3} + \frac{f_{MG}^2}{5}\right) P(k,z) j_0(kd_{ia}), \tag{5.109}$$

$$C_2^{MG}(d_{ia}) = \frac{1}{2\pi^2}\int dk k^2 \left(\frac{4b_{MG}f_{MG}}{3} + \frac{4f_{MG}^2}{7}\right) P(k,z) j_2(kd_{ia}), \tag{5.110}$$

and

$$C_4^{MG}(d_{ia}) = \frac{4}{35\pi^2}\int dk k^2 f_{MG}^2 P(k,z) j_4(kd_{ia}). \tag{5.111}$$

In Fig. 5.12, we plot the mean estimator of the dipole for modified gravity, the $f(R)$ motivated parametrisation in Eq. (5.95), at different redshifts. As expected, the amplitude of the signal drops with an increasing redshift. We can see that at the same redshift, the dipole in ΛCDM (red dashed in Fig. 5.12) is more enhanced at small and moderate scales than that of $f(R)$.

5.2.5 Forecasts

We consider the same radio survey SKA1-Mid with five tomographic bins in redshift and assume that the bias is completely known. The range of separation d is also $12 \leq d \leq 180$ Mpc/h so as to avoid non-linearities. We also select two values of the uncertainty in the size measurement $\sigma_\kappa = 0.3, 0.8$. In the first parametrisation Eq. (5.95), we consider the $f(R)$ motivated case where the fiducial values[7] of the free parameters $\{s, \lambda_1^2, \beta_1\}$ are $s = 4$, $\beta_1 = 4/3$ and $\log(\beta_1\lambda_1^2/\mathrm{Mpc}^2) = 4$. We obtain the 68% (blue for the optimistic case and light red for the pessimistic case) and 95% (light blue for the optimistic case and red for the pessimistic case) confidence contours in Fig. 5.13. In general, the constraints are comparable - if not tighter - to those obtained in [203]. This exhibits the constraining power of our statistical tool.

As for the second parametrisation in Eq. (5.96), the free parameters to constrain are $\{h, \Omega_m, \Omega_b, A_{10}, E_{11}\}$ whose fiducial values are those of ΛCDM: $h = 0.68, \Omega_m = 0.3028, \Omega_b = 0.048, A_{10} = 1.93, E_{11} = 0.0$. For the optimistic case and the pessimistic case we find the marginalised errors on E_{11} are $\sigma_{E11} = 0.19$ and $\sigma_{E11} = 0.51$ respectively which are consistent with the results of *Planck* [205]. In Fig. 5.14, we plot the error contours for 68% and 95% confidence levels.

[7]Ideally, to look for any departure from GR, one wants to constrain $\{s, \lambda_1^2, \beta_1\}$ by choosing their corresponding GR values as fiducial ones but this turns out to be quite hard to deal with.

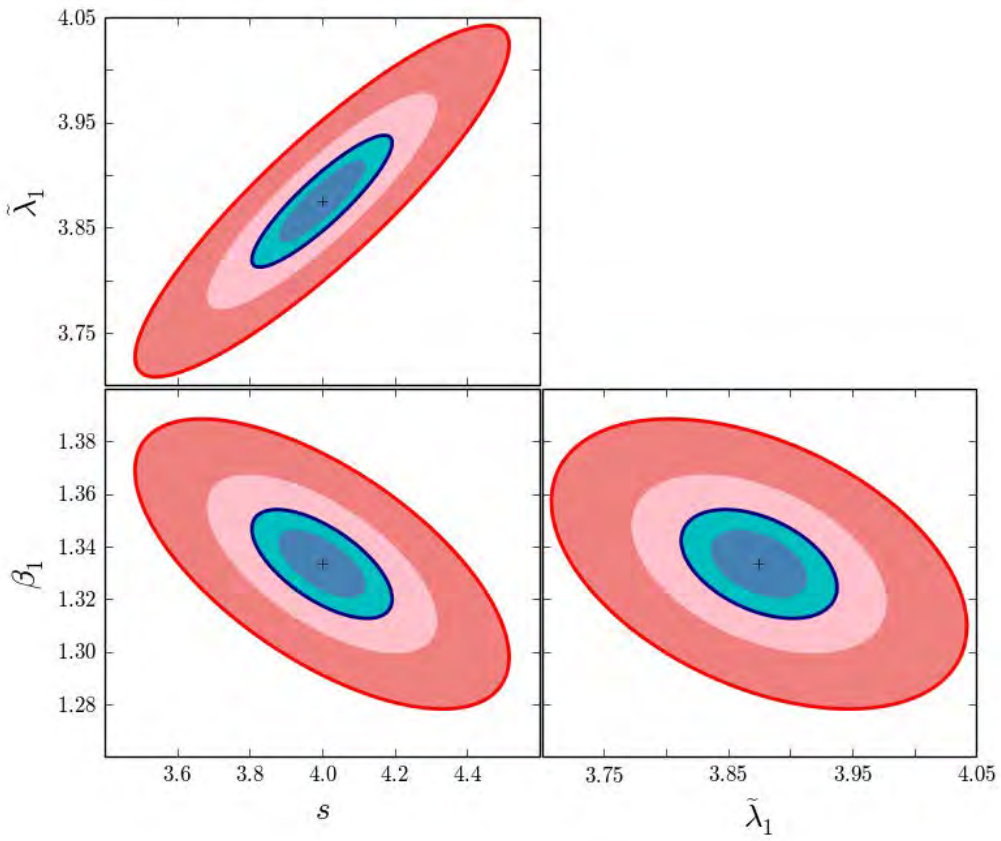

Figure 5.13: Joint constraints between all the free parameters in the parameterisation defined in Eq. 5.95. Here we consider radio survey, SKA1-Mid (see text) and five redshift bins for our analysis. The bias is assumed to be completely known. The blue ellipses are for the optimistic case $\sigma_\kappa = 0.3$ (68% blue and 95% light blue) and the red ones are for $\sigma_\kappa = 0.8$ (68% light red and 95% red)

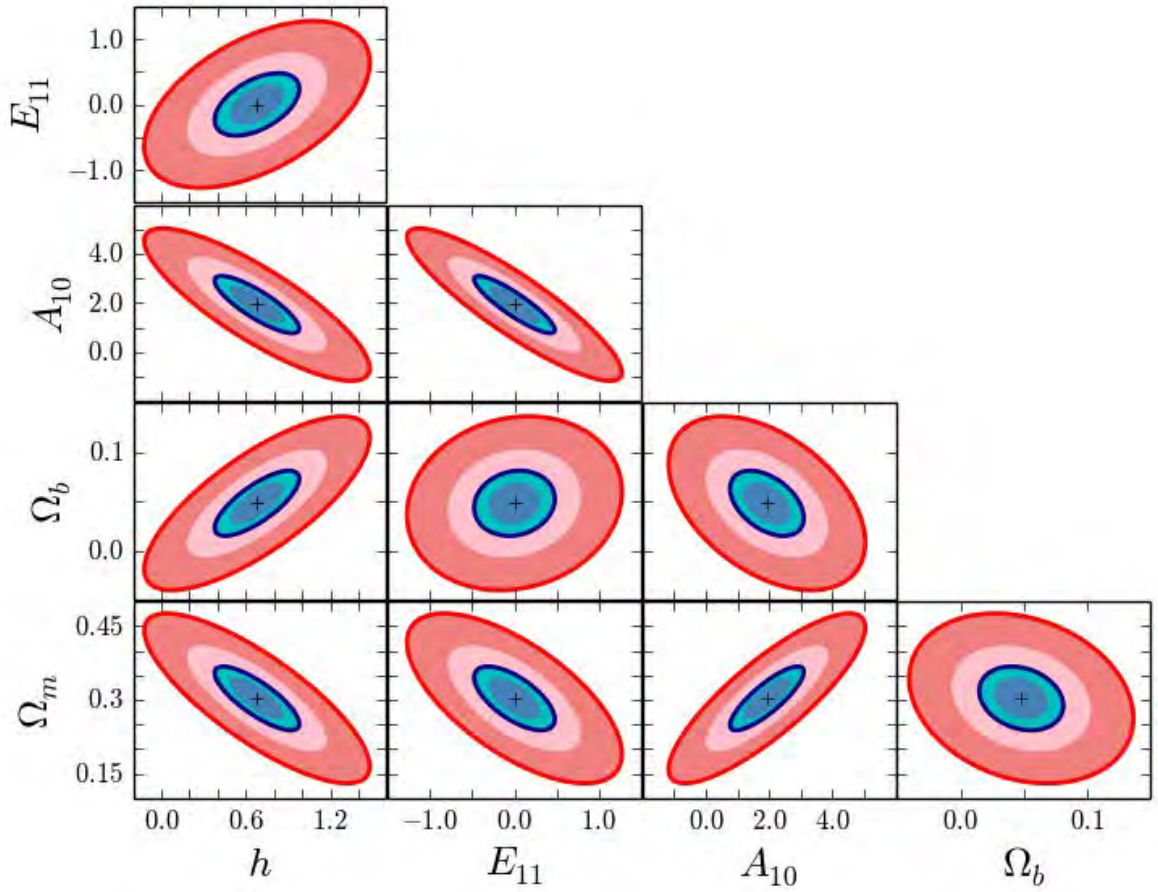

Figure 5.14: Joint constraints between all the free parameters in the model Eq. (5.96). Here we consider radio survey, SKA1-Mid (see text) and five redshift bins for our analysis. The bias is assumed to be completely known. The blue ellipses are for the optimistic case $\sigma_\kappa = 0.3$ (68% blue and 95% light blue) and the red ones are for $\sigma_\kappa = 0.8$ (68% light red and 95% red)

5.3 Conclusions

In this Chapter, we have proposed a new way to measure the Doppler magnification which is a lensing-like effect arising from peculiar motions of objects. The technique developed in this Chapter is different from the one proposed in Chapter 4 in that it extracts the dipole signal that results from the angle dependence of the cross-correlation between a galaxy number count and all the sizes of objects located at a distance d from it.

In our approach, we have computed the full-sky cross-correlation between galaxy number count which to leading order includes the matter fluctuations and the redshift space distortion term; and the Doppler term - used as proxy for size of object - which is the dominant term of the cosmic convergence at low and intermediate redshifts. We have shown that in the distant observer approximation, the correlator is composed of a dipole term and an octupole term.

We have then proposed new estimators of both the dipole and octupole and found that the dipole contribution is roughly one order of magnitude larger than that of the octupole. Therefore we have decided to only focus on the dipole.

After calculating the variance of the signal where the correlation between bins in separation has been properly taken into account, we have computed the signal to noise ratio for optical (SDSS, LOWz and CMASS) and future radio (SKA1-Mid) surveys. With relatively large S/N's, it has been concluded that for both types of survey the Dipole magnification can be detected, which looks really promising.

Equipped with our new statistical tool, we have also carried out Fisher forecasts analyses to constrain cosmological parameters in the ΛCDM paradigm. Choosing both optical and radio surveys, we have identified cases where the bias b is unknown, completely known and evolving. Cases with both fixed and varying growth index γ have been considered as well. All our results depend on the uncertainty of the size measurements where for simplicity two values have been chosen, $\sigma_\kappa = 0.3, 0.8$ (optimistic case and pessimistic one respectively). For optical surveys, by assuming that the bias is known with the growth index fixed, the constraint on dark energy w_0 is relatively good with a marginalised error of $\sigma_{w_0} = 0.13$ for the optimistic case. Whereas with the case where the bias is a free parameter, it is quite hard to constrain w_0. As expected, by adding γ as a free parameter, the constraints gets looser than the case where it is fixed. For radio survey, similar to the optical case, the constraints get better or worse according to both our knowledge of the bias and whether we choose γ as

a free parameter. We have also adopted an evolving bias while allowing some departure from GR for the radio survey and found that the constraint on dark energy is comparable to that of optical surveys with known bias and fixed γ. The constraining power of the future radio survey SKA1-Mid will still strongly depend on both how precise the size measurements are in the near future and the knowledge of the bias.

In addition, we have investigated the possibility of constraining some modified gravity models with this new correlator. For our purposes, we have considered parametrised models that account for the late time acceleration of the cosmic expansion by introducing some functional forms $\mu(k, a)$ which modify the Poisson equation and the relation between the two Bardeen potentials, time-time and space-space components.

We have first derived the new form of the velocity potential while assuming sub-horizon scales then computed the modified growth suppression factor using the Bardeen equation. Then we have calculated the expression of the cross-correlation function in the modified gravity context. We have chosen a $f(R)$ motivated parametrisation where $\mu(k, a)$ is both scale and time dependent and another parametrisation - dark energy related - where $\mu(a)$ is only time dependent.

The form of the estimator in the modified gravity case is the same as in the ΛCDM case. However with the modified growth factor, the computation of the cosmic variance C^{Δ} has been required.

In our Fisher forecast analyses, we have only considered SKA1-Mid experiment. In the first parametrisation in which there are three free parameters whose fiducial values have been chosen from [203], we have found that the constraints are comparable or even tighter than those obtained in [203]. For the second parametrisation, we have five free parameters whose fiducial values are those of GR. Our results are consistent with those obtained in *Planck*.

We can conclude that our new statistical tool offers a great potential which will help us better understand the structure growth and the nature of gravity. In the near future where the size measurements of objects will be greatly improved and the knowledge of the bias will be more precise, the constraining power of this new probe will reach its maximum.

Chapter 6
General conclusion

6.1 Summary and discussions

In general, when interpreting weak lensing data, the cosmic convergence is often approximated by the standard gravitational lensing – the line of sight integration of the density fluctuations. However, with the future advanced experiments like Euclid and SKA, where measurements will be achieved with an unprecedented precision, full analyses of those future data should be done carefully. Precisely our motivation in this thesis, where we have looked at some general relativistic contributions to weak lensing convergence, is to investigate under which conditions the approximation $\kappa \approx \kappa_g$ is valid and see whether the relativistic treatment of the cosmic convergence – crucial to future weak lensing experiments – will offer us a new way to probe the structure growth and address the dark energy problem.

In Chapter 2, we have looked at the cosmological perturbation theory, foundation of modern cosmology. We have seen how gauge invariant quatities, which are what we observe, can be constructed and the physics of how the second-order vector modes and tensor modes are generated. The basics of gravitational lensing, where we have looked at the physics of lensing phenomena and the detailed derivation of the standard lensing formula, has been very useful to us.

In Chapter 3, we have presented the non-linear relativistic contributions of the secondary vector and tensor modes to weak lensing convergence. Early work has considered the effects of these two modes on the polarisation of the Cosmic Microwave Background [81]. We have worked in Poisson gauge, by only considering first order scalar perturbation and second-order vector and tensor perturbations – a reasonable choice since we have only focused on scalar induced secondary modes. using SVT decomposition and assuming that the Born approximation still holds at second order, we have first derived a formalism which allows us to compute the angular power spectra of these second order effects. For the sake of completeness, we have also computed first order contributions, such as Sachs-Wolfe and Integrated Sachs-Wolfe and velocity term, in our analyses. We have found that the secondary

vector modes contribution to the convergence is small compared to that of the standard formula κ_g and although the secondary tensor modes can dominate primordial gravitational waves [118], their effect on weak lensing can be completely neglected. What is quite interesting in our findings is the fact that, despite its relatively small contribution to the cosmic convergence, the frame dragging effect, a second order quatity, can dominate first order term like the Doppler term at high redshift; it also prevails over both ISW and SW terms above $\ell \geq 50$. This then suggests that for observations, the secondary modes effects and the two Sachs-Wolfe terms can be safely neglected.

In Chapter 4, we have carried out a careful analysis of the effect of the Doppler term κ_v, dubbed *Doppler lensing/magnification*, on weak lensing convergence. *Doppler magnification* is not like the standard integrated effect of gravitational lensing, but its effect on the magnification of objects arises from the line of sight peculiar velocity which affects the observed redshift in such a way that by using the distance-redshift relation, the distance of an object is underestimated or overestimated – according to whether the line of sight velocity is pointing away or towards the observer respectively. We have first looked at how the Doppler term arises in the area distance anisotropies (see also [76, 90, 91]). We have seen that the Doppler term is more significant than the standard lensing term at low redshift on large scales (see Fig. 4.2). In order to isolate the effect of the peculiar velocity on weak lensing at low redshift, we have then computed the cross-correlation function between the size of objects – used as a proxy for the velocity – with galaxy over-densities and the Doppler convergence auto-correlation. We have compared our theoretical predictions with simulated measurements and found that they are roughly the same but the discrepancies can be accounted for by the fact that in our calculations we have neither considered non-linear velocity field nor taken into account the slope effect. The key point in our analysis is our ability to turn this Doppler effect, considered as systematics to be accounted for in supernova survey (see [91–93]) into a useful signal. We have then conducted a Fisher forecast analysis, by considering a specific geometrical configuration and three different types of surveys namely DES-like, Euclid-like and SKA-like surveys, to constrain cosmological parameters. Without using any priors in our analysis, our results suggest that our statistical tool can be used to study structure growth and dark energy, with a marginalised error on dark energy $\sigma_{w_0} = 0.13$. In addition, we have shown that the *Doppler magnification* also offers us a new way of mapping the velocity field of galaxies at low and intermediate redshifts.

In an attempt to further analyse the effect of peculiar velocity on weak lensing and measure it in a different way, we have built up a new statistical tool by considering another geometrical configuration in Chapter 5. Unlike in the Chapter 4, we have looked at the dependence

of the cross-correlation function, between the size of objects located at a distance d away from an over-density Δ, which gives rise to a dipole signal. In our formalism, we have only considered the matter fluctuations and the redshift space distortion term in the expression of the galaxy number counts, and the Doppler term κ_v for the cosmic convergence, sufficient enough for our purposes. We have computed the full sky expression of the cross-correlation function and found that for a distant observer approximation it is composed of a dipole term and an octupole term. We have then proposed an estimator for each of them but after comparing the two terms we have found that the dipole term is relatively large, by one order of magnitude, compared to the octupole which we have therefore neglected in the remaining analysis. By considering three optical surveys, SDSS, LOWz and CMASS, and the future radio survey SKA1-Mid, we have shown that a direct detection of the *Doppler magnification* is possible, with a reasonably good signal to noise ratio. In our Fisher forecast analyses, we have adopted several cases where we have treated the bias as a free parameter, evolving or completely known in each redshift bin. We have also looked at the cases where a departure from GR is allowed – treating the growth index γ as a free parameter. Since our calculations depend on the value of the uncertainty of size measurements σ_κ we have opted for two extreme cases; the pessimistic case with $\sigma_\kappa = 0.8$ and the optmistic case with $\sigma_\kappa = 0.3$. As expected, constraints on cosmological parameters (here for ΛCDM model) get worse as the number of free parameters increase, e.g γ fixed with a known bias gives $\sigma_{w_0} = 0.13$ against γ as free parameter with known bias giving $\sigma_{w_0} = 0.63$ (for optical surveys and optimistic case). Considering SKA1-Mid, we have obtained strong constraints on dark energy with $\sigma_{w_0} = 0.04$ (optimistic case) comparable to current constraints from other experiments like *Planck* for example. As a whole, the constraining power of SKA1-Mid is much better than those optical surveys.

In addition to that, in Chapter 5, we have investigated the possible constraints we can put on some parametrised models of modified gravity. At small scales, a both time and scale dependent function $\mu(k, a)$ is then introduced in Poisson equation to account for the apparent late time acceleration of the expansion of the universe. We have selected the functional forms prescribed in [203], $f(R)$ motivated model, and [204], dark energy related model. In order to recompute the dipole estimator in modified gravity, the modified velocity has been computed. In our Fisher forecasts, where again both pessimistic and optimistic cases are considered, we have found that the constraints obtained for $f(R)$ model are tighter than those from [203]. For the dark energy related model, our results are consistent with those obtained in *Planck*.

We have found in the *Doppler magnification* a novel way, with great potential, to better understanding the nature of dark energy and gravity. There is still a variety of applications

which will allow us to corroborate all these results we have found so far, such as simulations, and further exploit this effect to study the evolution of the neutral hydrogen in our universe for example.

6.2 Future work

Non-linearities

How significantly would our current results change by taking into account the non-linear velocity? We expect that accounting for non-linearities of the velocity, using one-loop corrections to the power spectrum which are more accurate [206], will reduce considerably the discrepancies between the simulated measurements and our theoretical calculations.

Relativistic ray-tracing simulation

Usually in a weak lensing simulation which consists of tracing the light ray propagation from the observer to the source. It was pioneered by [207–209] and has been an incredible tool to both do predictions and interpret the measurements. The cumulated deflections and distortions along the light path will help us understand the distribution of the intervening matter between the observer and the source. We can study the influence of implementing corrections (first and second order) to the standard gravitational lensing in a ray-tracing simulation.

HI intensity mapping

HI intensity mapping [210, 211] consists of measuring the total emission of the neutral hydrogen, which is mostly found in galaxies, via the spin-flip transition at a rest wavelength of 21 cm without having to resolve the individual galaxies in large angular scales. The great potential of HI intensity mapping in cosmology has been examined [211–214]. A variety of studies has already looked into the possibilities of measuring the lensing of HI [213] by taking into account the discreetness of galaxies. We can then make use of the *Doppler magnification* and constraining power of HI to analyse the structure formation. This, we believe, will give stronger constraints on the cosmological parameters. There are many possibilities but one approach could be for example the cross-correlation between size of HI blobs with galaxy number counts.

Appendix A
Useful relations and functions

A.1 Spherical harmonics

Any quantities on the screen space (or 2 sphere) can be decomposed as functions of the spherical harmonics which are the basis functions, the eigenfunctions of the 2 dimensional Laplacian in spherical coordinates

$$\left(\frac{\partial^2}{\partial\theta^2} + \cot\theta\frac{\partial}{\partial\theta} + \frac{1}{\sin^2\theta}\frac{\partial^2}{\partial\varphi^2}\right) Y_\ell^m = -\ell(\ell+1)Y_\ell^m. \tag{A. 1}$$

The conjugate of a spherical harmonic is

$$Y^*_{\ell m}(\theta,\varphi) = (-1)^m Y_{\ell\ -m}(\theta,\varphi) = Y_{\ell m}(\theta,-\varphi), \tag{A. 2}$$

and the orthogonality relation gives

$$\int_0^{2\pi} d\varphi \int_0^{\pi} d\theta \sin\theta Y^*_{\ell m}(\theta,\varphi) Y_{\ell' m'}(\theta,\varphi) = \delta_{\ell\ell'}\delta_{mm'}. \tag{A. 3}$$

Let's suppose we have a function $f(\hat{\mathbf{n}})$ (alternatively $f(\theta,\varphi)$) defined on the 2-sphere, its decomposition is then

$$f(\hat{\mathbf{n}}) = \sum_{\ell m} f_{\ell m} Y_{\ell m}(\hat{\mathbf{n}}), \tag{A. 4}$$

where the $f_{\ell m}$ are the coefficients of the expansion. A plane wave for example can be decomposed in spherical harmonics as

$$\exp(\mathrm{i}\boldsymbol{k}\cdot\boldsymbol{x}) = 4\pi\sum_{\ell m}\mathrm{i}^\ell j_\ell(kx) Y_{\ell m}(\hat{\boldsymbol{k}}) Y_{\ell m}(\hat{\boldsymbol{x}})\,, \tag{A. 5}$$

where the j_ℓ are the spherical Bessel functions whose definition will be given below and $\hat{\boldsymbol{k}} = (\theta_k,\varphi_k)$, $\hat{\boldsymbol{x}} = (\theta_x,\varphi_x)$. A very useful relation, needed in the computation of vector and

tensor modes angular power spectra, is the integral of three spherical harmonics

$$\begin{aligned}\mathcal{G}^{\ell_3 m_3}_{\ell_1 m 1 \ell_2 m 2} &= \int d^2\boldsymbol{n} Y_{\ell_1 m_1} Y_{\ell_2 m_2} Y^*_{\ell_3 m_3} \qquad \text{(A. 6)}\\ &= \sqrt{\frac{(2\ell_1+1)(2\ell_2+1)(2\ell_3+1)}{4\pi}}(-1)^{m_3}\begin{pmatrix}\ell_1 & \ell_2 & \ell_3\\ m_1 & m_2 & -m_3\end{pmatrix}\begin{pmatrix}\ell_1 & \ell_2 & \ell_3\\ 0 & 0 & 0\end{pmatrix}.\end{aligned}$$

The $3j$-Wigner symbols $\begin{pmatrix}\ell_1 & \ell_2 & \ell_3\\ m_1 & m_2 & m_3\end{pmatrix}$ are non-zero when $|\ell_1 - \ell_2| \leq \ell_3 \leq \ell_1 + \ell_2$, $m_1 + m_2 + m_3 = 0$. We finally give the values of the spherical harmonics for low $\ell = 0, 1, 2$

$$Y_{00} = -\frac{1}{\sqrt{4\pi}}, \text{ for } \ell = 0, \qquad \text{(A. 7)}$$

$$\begin{aligned}Y_{10} &= \sqrt{\frac{3}{4\pi}}\cos\theta\\ Y_{11} &= -\sqrt{\frac{3}{8\pi}}\sin\theta e^{i\varphi}, \text{ for } \ell = 1, \qquad \text{(A. 8)}\\ Y_{20} &= \sqrt{\frac{5}{4\pi}}\left(\frac{3}{2}\cos^2\theta - \frac{1}{2}\right)\\ Y_{21} &= -\sqrt{\frac{15}{8\pi}}\sin\theta\cos\theta e^{i\varphi}\\ Y_{22} &= \sqrt{\frac{15}{32\pi}}\sin^2\theta e^{2i\varphi}, \text{ for } \ell = 2 \qquad \text{(A. 9)}\end{aligned}$$

A.2 Spherical Bessel function

The spherical Bessel functions $j_\ell(x)$ are solutions to the second order differential equation

$$x^2\frac{d^2 f}{dx^2} + 2x\frac{df}{dx} + (x^2 - \ell(\ell+1))f = 0, \qquad \text{(A. 10)}$$

where ℓ is an integer. They obey the recursion relations

$$\begin{aligned}j_\ell(x) &= \frac{x}{2\ell+1}\Big(j_{\ell-1}(x) + j_{\ell+1}(x)\Big), \qquad \text{(A. 11)}\\ j'_\ell(x) &= \frac{\ell}{2\ell+1}\Big(j_{\ell-1}(x) - \frac{\ell+1}{\ell}j_{\ell+1}\Big), \qquad \text{(A. 12)}\\ j'_\ell(x) &= j_{\ell-1}(x) - \frac{\ell+1}{x}j_\ell(x). \qquad \text{(A. 13)}\end{aligned}$$

They also satisfy the property

$$\frac{j_\ell(x)}{x^2} = \frac{1}{(2\ell-1)(2\ell+1)(2\ell+3)}\Big[(2\ell+3)j_{\ell-2}(x)+2(2\ell+1)j_\ell(x)+j_{\ell+2}(x)(2\ell-1)\Big]. \quad \text{(A. 14)}$$

A.3 Legendre Polynomial

The Legendre polynomials are solutions to the following second order differential equation

$$(1-x^2)\frac{d^2f}{dx^2} - 2x\frac{df}{dx} + \ell(\ell+1)f = 0, \quad \text{(A. 15)}$$

and satisfy the normalisation condition

$$\int_{-1}^{1} dx P_\ell(x) P_{\ell'}(x) = \frac{2}{2\ell+1}\delta_{\ell\ell'}. \quad \text{(A. 16)}$$

The polynomials at each order can be constructed from the Rodrigues' formula

$$P_\ell = \frac{1}{2^\ell \ell!}\frac{d^\ell}{dx^\ell}(x^2-1)^\ell, \quad \text{(A. 17)}$$

for example for $\ell = 0, 1, 2$ we have

$$P_0 = 1, \quad \text{(A. 18)}$$

$$P_1 = x, \quad \text{(A. 19)}$$

$$P_2 = \frac{1}{2}(3x^2-1). \quad \text{(A. 20)}$$

Appendix B
Angular power spectra of some first order quantities

B.1 Doppler term

We start with Eq. (3.18) for the convergence associated to the Doppler effect in which v_i is given by

$$v_i = -\frac{2a(\eta)}{3\Omega_{\rm m}H_0^2}[g(\eta)' + \mathcal{H}g(\eta)]\partial_i\Psi. \tag{B. 1}$$

Then decompose the gravitational potential in Fourier mode as in Eq. (2.98), with the definition of its power spectrum given in Eq. (2.99), one gets

$$\kappa(\boldsymbol{n}) = A\int_0^\infty d\chi n_s(\chi)a(\chi)\left(1-\frac{1}{\chi\mathcal{H}(\chi)}\right)\int\frac{d^3\boldsymbol{k}}{(2\pi)^{3/2}}\Psi(\boldsymbol{k},\eta)n^i\partial_i\left(e^{\mathrm{i}\boldsymbol{k}.\boldsymbol{x}}\right) \tag{B. 2}$$

where the coefficient A is given by

$$A = \frac{2}{3\Omega_{\rm m}H_0^2}.$$

Now, using that

$$n^i\partial_i\left(\exp(\mathrm{i}\boldsymbol{k}\cdot\boldsymbol{x})\right) = 4\pi\sum_{\ell m}\mathrm{i}^\ell kj'_\ell(k\chi)Y_{\ell m}(\hat{\boldsymbol{k}})Y_{\ell m}(\boldsymbol{n})\ , \tag{B. 3}$$

with a prime on the spherical Bessel function denoting the derivative with respect to its argument, Eq. (B. 2) becomes

$$\kappa(\boldsymbol{n}) = 4\pi A\int_0^\infty d\chi n_s(\chi)a(\chi)\left(1-\frac{1}{\chi\mathcal{H}(\chi)}\right)\int\frac{d^3\boldsymbol{k}}{(2\pi)^{3/2}}\Psi(\boldsymbol{k},\eta)\sum_{\ell m}\mathrm{i}^\ell kj'_\ell(k\chi)Y_{\ell m}(\hat{\boldsymbol{k}})Y_{\ell m}(\boldsymbol{n}) \tag{B. 4}$$

from which we can extract the components

$$\kappa_{\ell m} = 4\pi A\int_0^\infty d\chi n_s(\chi)a(\chi)\left(1-\frac{1}{\chi\mathcal{H}(\chi)}\right)\int\frac{d^3\boldsymbol{k}}{(2\pi)^{3/2}}\Psi(\boldsymbol{k},\eta)\mathrm{i}^\ell kj'_\ell(k\chi)Y_{\ell m}(\hat{\boldsymbol{k}}). \tag{B. 5}$$

Its correlator is then given by

$$\langle \kappa_{\ell m} \kappa^*_{\ell' m'} \rangle = 4\pi A^2 \int_0^\infty d\chi F(\chi) j'_\ell(k\chi) \int_0^\infty d\chi' F(\chi') j'_\ell(k\chi') \int_0^\infty \frac{dk}{k} \mathcal{P}_v(k,\chi,\chi') \delta_{\ell\ell'} \delta_{mm'} \quad \text{(B. 6)}$$

with

$$\mathcal{P}_v(k,\chi,\chi') \equiv k^2 \mathcal{P}_\Psi(k,\chi,\chi') \quad \text{(B. 7)}$$

and where

$$F(\chi) \equiv n_s(\chi) a(\chi) \left(1 - \frac{1}{\chi \mathcal{H}(\chi)}\right). \quad \text{(B. 8)}$$

We finally get the formula of the angular power spectrum convergence associated to the Doppler contribution as

$$C_\ell^v = 4\pi A^2 \int_0^\infty d\chi F(\chi) \int_0^\infty d\chi' F(\chi') \int_0^\infty \frac{dk}{k} \mathcal{P}_v(k,\chi,\chi') j'_\ell(k\chi) j'_\ell(k\chi') \,. \quad \text{(B. 9)}$$

Since $\mathcal{P}_\Psi(k,\chi,\chi') = \mathcal{P}_{\Psi_i}(k) \tilde{T}(k,\chi) \tilde{T}(k,\chi')$ with

$$\tilde{T}(k,\chi) = T(k) \left[g'(\chi) + \mathcal{H} g(\chi)\right]$$

the angular spectrum reduces to

$$C_\ell^v = 4\pi A^2 \int_0^\infty \frac{dk}{k} \mathcal{P}_{v_i}(k) \left[\int_0^\infty d\chi F(\chi) j'_\ell(k\chi) \tilde{T}(k,\chi)\right]^2 . \quad \text{(B. 10)}$$

B.2 Integrated Sachs-Wolfe term

As discussed in the text, the Integrated Sachs-Wolfe terms also contribute to the cosmic convergence at first order

$$\kappa_{\rm isw}(\boldsymbol{n}) = 2 \int_0^\infty d\chi \; \hat{g}_{\rm isw1}(\chi) \Psi'(\boldsymbol{n},\chi) + 2 \int_0^\infty d\chi \hat{g}_{\rm isw2}(\chi) \Psi(\boldsymbol{n},\chi) \quad \text{(B. 11)}$$

with both $\hat{g}_{\rm isw2}$ and $\hat{g}_{\rm isw1}$ defined in the text. The harmonic expansions of both the first and the second terms, which we call $\kappa_{\rm isw1}$ and $\kappa_{\rm isw2}$ respectively give

$$\kappa_{\rm isw1}(\boldsymbol{n}) = 8\pi \int_0^\infty d\chi \hat{g}_{\rm isw1}(\chi) \int \frac{d^3\boldsymbol{k}}{(2\pi)^{3/2}} \Psi'(\boldsymbol{k},\eta) \sum_{\ell m} \mathrm{i}^\ell j_\ell(k\chi) Y_{\ell m}(\hat{\boldsymbol{k}}) Y_{\ell m}(\boldsymbol{n}). \quad \text{(B. 12)}$$

The second term

$$\kappa_{\rm isw2}(\boldsymbol{n}) = -8\pi \int_0^\infty d\chi \hat{g}_{\rm isw2}(\chi) \int \frac{d^3\boldsymbol{k}}{(2\pi)^{3/2}} \Psi(\boldsymbol{k},\eta) \sum_{\ell m} \mathrm{i}^\ell j_\ell(k\chi) Y_{\ell m}(\hat{\boldsymbol{k}}) Y_{\ell m}(\boldsymbol{n}). \tag{B. 13}$$

It follows that the correlator contains three terms

$$\langle \kappa^{\rm isw}_{\ell m} \kappa^{\rm isw^*}_{\ell' m'} \rangle = \langle \kappa^{\rm isw1}_{\ell m} \kappa^{\rm isw1^*}_{\ell' m'} \rangle + \langle \kappa^{\rm isw2}_{\ell m} \kappa^{\rm isw2^*}_{\ell' m'} \rangle + 2\langle \kappa^{\rm isw1}_{\ell m} \kappa^{\rm isw2^*}_{\ell' m'} \rangle \tag{B. 14}$$

thus

$$\langle \kappa^{\rm isw1}_{\ell m} \kappa^{\rm isw1^*}_{\ell' m'} \rangle = 16\pi \int_0^\infty d\chi \int_0^\infty d\chi' \int_0^\infty \frac{dk}{k}\ \hat{g}_{\rm isw1}(\chi) \hat{g}_{\rm isw1}(\chi') j_\ell(k\chi) j_\ell(k\chi') \mathcal{P}_\Psi(k,\chi,\chi') \delta_{\ell\ell'} \delta_{mm'} \tag{B. 15}$$

where

$$\mathcal{P}_\Psi(k,\chi,\chi') = \mathcal{P}_{\Psi_i}(k) T_{\rm isw1}(k,\chi) T_{\rm isw1}(k,\chi')$$

and

$$T_{\rm isw1}(k,\chi) = T(k) g'(\chi)$$

$g'(\chi)$ being the derivative of the growth suppression factor with respect to conformal time η. The second term that constitutes to the correlator

$$\langle \kappa^{\rm isw2}_{\ell m} \kappa^{\rm isw2^*}_{\ell' m'} \rangle = 16\pi \int_0^\infty d\chi \int_0^\infty d\chi' \int_0^\infty \frac{dk}{k}\ \hat{g}_{\rm isw2}(\chi) \hat{g}_{\rm isw2}(\chi') j_\ell(k\chi) j_\ell(k\chi') \mathcal{P}_\Psi(k,\chi,\chi') \delta_{\ell\ell'} \delta_{mm'} \tag{B. 16}$$

with

$$\mathcal{P}_\Psi(k,\chi,\chi') = \mathcal{P}_{\Psi_i}(k) T_{\rm isw2}(k,\chi) T_{\rm isw2}(k,\chi')$$

and

$$T_{\rm isw2}(k,\chi) = T(k) g(\chi).$$

And the last term yields

$$\langle \kappa^{\rm isw1}_{\ell m} \kappa^{\rm isw2^*}_{\ell' m'} \rangle = -16\pi \int_0^\infty d\chi \int_0^\infty d\chi' \int_0^\infty \frac{dk}{k}\ \hat{g}_{\rm isw1}(\chi) \hat{g}_{\rm isw2}(\chi') j_\ell(k\chi) j_\ell(k\chi') \mathcal{P}_\Psi(k,\chi,\chi') \delta_{\ell\ell'} \delta_{mm'} \tag{B. 17}$$

letting

$$\mathcal{P}_\Psi(k,\chi,\chi') = \mathcal{P}_{\Psi_i}(k) T_{\rm isw1}(k,\chi) T_{\rm isw2}(k,\chi').$$

So, the total contribution of the Integrated Sachs-Wolfe term ($C_\ell^{\rm isw}$) to the convergence is thus given by the sum of each $C'_\ell s$ extracted from each of the terms that composes the

correlator i.e

$$C_\ell^{\rm isw} = C_\ell^{\rm isw1,isw1} + C_\ell^{\rm isw2,isw2} - 2C_\ell^{\rm isw1,isw2}. \tag{B. 18}$$

B.3 Sachs-Wolfe term

The contribution to the convergence of the Sachs-Wolfe term reads

$$\kappa_{\rm sw}(\boldsymbol{n}) = \int_0^\infty d\chi n_s(\chi) \left(2 - \frac{1}{\mathcal{H}\chi}\right) \Psi(\boldsymbol{n}, \chi). \tag{B. 19}$$

Using the Fourier decomposition of the potential and expanding the plane waves we arrive at

$$\kappa_{\rm sw}(\boldsymbol{n}) = 4\pi \int_0^\infty d\chi n_s(\chi) \left(2 - \frac{1}{\chi\mathcal{H}(\chi)}\right) \int \frac{d^3\boldsymbol{k}}{(2\pi)^{3/2}} \Psi(\boldsymbol{k}, \eta) \sum_{\ell m} \mathrm{i}^\ell j_\ell(k\chi) Y_{\ell m}(\hat{\boldsymbol{k}}) Y_{\ell m}(\boldsymbol{n}) \tag{B. 20}$$

and the coefficients $\kappa_{\ell m}^{\rm sw}$ are given by

$$\kappa_{\ell m}^{\rm sw} = 4\pi \int_0^\infty d\chi n_s(\chi) \left(2 - \frac{1}{\chi\mathcal{H}(\chi)}\right) \int \frac{d^3\boldsymbol{k}}{(2\pi)^{3/2}} \Psi(\boldsymbol{k}, \eta) \mathrm{i}^\ell j_\ell(k\chi) Y_{\ell m}(\hat{\boldsymbol{k}}) \tag{B. 21}$$

so that

$$\langle \kappa_{\ell m}^{\rm sw} \kappa_{\ell' m'}^{\rm sw^*} \rangle = 4\pi \int_0^\infty d\chi \int_0^\infty d\chi' \int_0^\infty \frac{dk}{k}\ \hat{g}_{\rm sw}(\chi) \hat{g}_{\rm sw}(\chi') j_\ell(k\chi) j_\ell(k\chi') \mathcal{P}_\Psi(k, \chi, \chi') \delta_{\ell\ell'} \delta_{mm'} \tag{B. 22}$$

where we define

$$\hat{g}_{\rm sw}(\chi) = n_s(\chi) \left(2 - \frac{1}{\mathcal{H}\chi}\right).$$

Extracting $C_\ell^{\rm sw}$ from (B. 22) is straightforward.

Appendix C
Correlation function

C.1 Gravitational lensing convergence

The standard gravitational lensing term is given by the first line of Eq. (4.9). The second line of Eq. (4.9) follows under the approximations $\nabla_\perp^2 \approx \nabla^2$ and $\nabla^2\Psi = 3H_0^2\Omega_m\delta/(2a)$, which are based on the sub-Hubble limit of Eqs. (4.8) and (2.90) respectively. With

$$\boldsymbol{n}\cdot\boldsymbol{\nabla} = -\frac{d}{d\chi} - \frac{\partial}{\partial\eta}, \tag{C. 1}$$

Eq. (4.8) implies

$$\nabla_\perp^2\Psi = \nabla^2\Psi - \frac{d\Psi}{d\chi^2} - 2\frac{d\Psi}{d\chi} - \Psi'' + \frac{2}{\chi}\left(\Psi' + \frac{d\Psi}{d\chi}\right). \tag{C. 2}$$

On sub-Hubble scales we can neglect all terms on the right after the first. On these scales, the Poisson equation (2.90) reduces to its Newtonian form, since we can neglect the Φ and Φ' terms. This then leads to the usual lensing magnification in the second line of Eq. (4.9) – as an integral over the density contrast along a line of sight.

C.2 Auto-correlation $C_\ell^{\kappa_v\kappa_v}$

The Doppler lensing power spectrum $C_\ell^{\kappa_v\kappa_v}$ has already been calculated in B.1, except that here we introduce some weight functions which take into account the geometry of the survey. Now, from Eq. (4.34) we obtain

$$\begin{aligned}\langle\kappa_{\ell m}\kappa^*_{\ell' m'}\rangle &= 4\pi\left(\frac{2}{3H_0^2\Omega_m}\right)^2\int_0^\infty dk k T^2(k)\mathcal{P}_{\Psi_i}(k)\int_{z_{\min}}^{z_{\max}} dz W_1(z)\left[a(z) - \frac{1}{\chi(z)H(z)}\right] \\ &\times\mathcal{G}(z)j'_\ell(k\chi(z))\int_{z_{\min}}^{z_{\max}} dz' W_2(z',z)\left[a(z') - \frac{1}{\chi(z')H(z')}\right]\mathcal{G}(z')j'_\ell(k\chi(z'))\delta_{\ell\ell'}\delta_{mm'}\end{aligned} \tag{C. 3}$$

where we have again used Eq. (2.99). The fact that we use two different window functions (W_1, W_2) is explained in Section 4.6. By carrying out the similar calculations as before we get

$$\begin{aligned} C_\ell^{\kappa_v\kappa_v} &= \frac{16\pi}{N\left(3H_0^2\Omega_m\right)^2}\int_0^\infty dk k T^2(k)\mathcal{P}_{\Psi_i}(k)\left[\int_{z_{\min}}^{z_{\max}} dz W_1(z)\left(a-\frac{1}{\chi H}\right)\mathcal{G}(z)j_\ell'(k\chi(z))\right] \\ &\quad\times\left[\int_{z_{\min}}^{z_{\max}} dz' W_2(z',z)\left(a-\frac{1}{\chi H}\right)\mathcal{G}(z')j_\ell'(k\chi(z'))\right] \end{aligned} \tag{C. 4}$$

References

[1] M. Feix, A. Nusser, and E. Branchini, "Growth Rate of Cosmological Perturbations at $z \sim 0.1$ from a New Observational Test." *Phys. Rev. Lett.* **115** (2015), no. 1 011301, [arXiv:1503.05945].

[2] S. Yahya, P. Bull, M. G. Santos, M. Silva, R. Maartens, P. Okouma, and B. Bassett, "Cosmological performance of SKA HI galaxy surveys." *Mon. Not. Roy. Astron. Soc.* **450** (2015), no. 3 2251–2260, [arXiv:1412.4700].

[3] P. Bull, "Extending cosmological tests of General Relativity with the Square Kilometre Array." *Astrophys. J.* **817** (2016), no. 1 26, [arXiv:1509.07562].

[4] D. Clowe, M. Bradac, A. H. Gonzalez, M. Markevitch, S. W. Randall, C. Jones, and D. Zaritsky, "A direct empirical proof of the existence of dark matter." *Astrophys. J.* **648** (2006) L109–L113, [astro-ph/0608407].

[5] M. Persic, P. Salucci, and F. Stel, "The Universal rotation curve of spiral galaxies: 1. The Dark matter connection." *Mon. Not. Roy. Astron. Soc.* **281** (1996) 27, [astro-ph/9506004].

[6] E. Corbelli and P. Salucci, "The Extended Rotation Curve and the Dark Matter Halo of M33." *Mon. Not. Roy. Astron. Soc.* **311** (2000) 441–447, [astro-ph/9909252].

[7] V. Mukhanov, *Physical Foundations of Cosmology*. Cambridge University Press, Oxford, 2005.

[8] R. Durrer, *The cosmic microwave background*, vol. 401. Cambridge University Press Cambridge, 2008.

[9] Planck Collaboration, P. A. R. Ade et al., "Planck 2015 results. XIII. Cosmological parameters." arXiv:1502.01589.

[10] S. Colgate, "Supernovae as a standard candle for cosmology." *The Astrophysical Journal* **232** (1979) 404–408.

[11] S. Dodelson, *Modern Cosmology*. Academic Press, Amsterdam, 2003.

[12] Supernova Search Team Collaboration, A. G. Riess et al., "Observational evidence from supernovae for an accelerating universe and a cosmological constant." *Astron. J.* **116** (1998) 1009–1038, [astro-ph/9805201].

[13] Supernova Cosmology Project Collaboration, S. Perlmutter et al., "Measurements of Omega and Lambda from 42 high redshift supernovae." *Astrophys. J.* **517** (1999) 565–586, [astro-ph/9812133].

[14] Supernova Search Team Collaboration, B. P. Schmidt et al., "The High Z supernova search: Measuring cosmic deceleration and global curvature of the universe using type Ia supernovae." *Astrophys. J.* **507** (1998) 46–63, [astro-ph/9805200].

[15] SDSS Collaboration, D. J. Eisenstein et al., "Detection of the baryon acoustic peak in the large-scale correlation function of SDSS luminous red galaxies." *Astrophys. J.* **633** (2005) 560–574, [astro-ph/0501171].

[16] D. J. Schlegel et al., "BigBOSS: The Ground-Based Stage IV Dark Energy Experiment." arXiv:0904.0468.

[17] C. Wagner, V. Muller, and M. Steinmetz, "Constraining dark energy via baryon acoustic oscillations in the (an)isotropic light-cone power spectrum." *Astron. Astrophys.* **487** (2008) 63–74, [arXiv:0705.0354].

[18] M. Lopez-Corredoira, "Alcock-Paczynski cosmological test." *Astrophys. J.* **781** (2014), no. 2 96, [arXiv:1312.0003].

[19] D. J. Bacon, A. R. Refregier, and R. S. Ellis, "Detection of weak gravitational lensing by large-scale structure." *Mon. Not. Roy. Astron. Soc.* **318** (2000) 625, [astro-ph/0003008].

[20] F. Schmidt, A. Leauthaud, R. Massey, J. Rhodes, M. R. George, A. M. Koekemoer, A. Finoguenov, and M. Tanaka, "A Detection of Weak Lensing Magnification using Galaxy Sizes and Magnitudes." *Astrophys. J.* **744** (2012) L22, [arXiv:1111.3679].

[21] M. Shirasaki, T. Hamana, and N. Yoshida, "Probing cosmology with weak lensing selected clusters II: Dark energy and f(R) gravity models." arXiv:1508.02104.

[22] M. Takada and S. Bridle, "Probing dark energy with cluster counts and cosmic shear power spectra: including the full covariance." *New J. Phys.* **9** (2007) 446, [arXiv:0705.0163].

[23] W.-J. Fang and Z. Haiman, "Constraining Dark Energy by Combining Cluster Counts and Shear-Shear Correlations in a Weak Lensing Survey." *Phys. Rev.* **D75** (2007) 043010, [astro-ph/0612187].

[24] L. Marian and G. M. Bernstein, "Dark energy constraints from lensing-detected galaxy clusters." *Phys. Rev.* **D73** (2006) 123525, [astro-ph/0605746].

[25] E. V. Linder, "Cosmic growth history and expansion history." *Phys. Rev.* **D72** (2005) 043529, [astro-ph/0507263].

[26] P. J. E. Peebles, *Principles of physical cosmology.* Princeton University Press, 1993.

[27] J. Yoo, A. L. Fitzpatrick, and M. Zaldarriaga, "A New Perspective on Galaxy Clustering as a Cosmological Probe: General Relativistic Effects." *Phys. Rev.* **D80** (2009) 083514, [arXiv:0907.0707].

[28] C. Bonvin and R. Durrer, "What galaxy surveys really measure." *Phys. Rev.* **D84** (2011) 063505, [arXiv:1105.5280].

[29] N. Kaiser, "Clustering in real space and in redshift space." *Mon. Not. Roy. Astron. Soc.* **227** (1987), no. 1 1–21.

[30] R. B. Tully and J. R. Fisher, "A new method of determining distances to galaxies." *Astronomy and Astrophysics* **54** (1977) 661–673.

[31] M. A. Strauss and J. A. Willick, "The Density and peculiar velocity fields of nearby galaxies." *Phys. Rept.* **261** (1995) 271–431, [astro-ph/9502079].

[32] A. Dekel, "Dynamics of cosmic flows." *Ann. Rev. Astron. Astrophys.* **32** (1994) 371–418, [astro-ph/9401022].

[33] C. M. Springob, K. L. Masters, M. P. Haynes, R. Giovanelli, and C. Marinoni, "SFI++ II: A New I-band Tully-Fisher Catalog, Derivation of Peculiar Velocities and Dataset Properties." *Astrophys. J. Suppl.* **172** (2007) 599–614, [arXiv:0705.0647]. [Erratum: Astrophys. J. Suppl.182,474(2009)].

[34] S. M. Faber and R. E. Jackson, "Velocity dispersions and mass to light ratios for elliptical galaxies." *Astrophys. J.* **204** (1976) 668.

[35] P. L. Schechter, "Mass-to-light ratios for elliptical galaxies." *Astrophys. J.* **85** (1980) 801–811.

[36] J. L. Tonry and M. Davis, "Velocity dispersions of elliptical and S0 galaxies. I - Data and mass-to-light ratios. II - Infall of the local group to Virgo." *Astrophys. J.* **246** (1981) 666–695.

[37] S. Djorgovski and M. Davis, "Fundamental properties of elliptical galaxies." *The Astrophysical Journal* **313** (1987) 59–68.

[38] C. M. Springob, C. Magoulas, M. Colless, J. Mould, P. Erdogdu, D. H. Jones, J. R. Lucey, L. Campbell, and C. J. Fluke, "The 6dF Galaxy Survey: Peculiar Velocity Field and Cosmography." *Mon. Not. Roy. Astron. Soc.* **445** (2014), no. 3 2677–2697, [arXiv:1409.6161].

[39] D. Lynden-Bell, S. M. Faber, D. Burstein, R. L. Davies, A. Dressler, R. J. Terlevich, and G. Wegner, "Spectroscopy and photometry of elliptical galaxies. V - Galaxy streaming toward the new supergalactic center." *Astrophys. J.* **326** (1988) 19.

[40] M. M. Phillips, "The absolute magnitudes of Type IA supernovae." *Astrophys. J.* **413** (1993) L105–L108.

[41] A. G. Riess, W. H. Press, and R. P. Kirshner, "A Precise distance indicator: Type Ia supernova multicolor light curve shapes." *Astrophys. J.* **473** (1996) 88, [astro-ph/9604143].

[42] SNLS Collaboration, J. Guy et al., "SALT2: Using distant supernovae to improve the use of Type Ia supernovae as distance indicators." *Astron. Astrophys.* **466** (2007) 11–21, [astro-ph/0701828].

[43] S. J. Turnbull, M. J. Hudson, H. A. Feldman, M. Hicken, R. P. Kirshner, and R. Watkins, "Cosmic flows in the nearby universe from Type Ia Supernovae." *Mon. Not. Roy. Astron. Soc.* **420** (2012) 447–454, [arXiv:1111.0631].

[44] M. G. Lee, W. L. Freedman, and B. F. Madore, "The Tip of the Red Giant Branch as a Distance Indicator for Resolved Galaxies." *Astrophys. J.* **417** (1993) 553.

[45] M. Feast, "Cepheids as distance indicators: some current problems." astro-ph/0110360.

[46] M. Feast, "Cepheids as distance indicators." *Publications of the Astronomical Society of the Pacific* **111** (1999), no. 761 775.

[47] M. Feast, "Local distance indicators." astro-ph/0010590.

[48] D. J. Majaess, D. G. Turner, and D. J. Lane, "Type II Cepheids as Extragalactic Distance Candles." *Acta Astron.* **59** (2009) 403, [arXiv:0909.0181].

[49] A. C. Layden, R. B. Hanson, S. L. Hawley, A. R. Klemola, and C. J. Hanley, "The Absolute Magnitude and Kinematics of RR Lyrae Stars via Statistical Parallax." *Astron. J.* **112** (1996) 2110–2131, [astro-ph/9608108].

[50] D. J. Majaess, "RR Lyrae and Type II Cepheid Variables Adhere to a Common Distance Relation." *J. Am. Assoc. Var. Star Obs.* **38** (2010) 100–112, [arXiv:0912.2928].

[51] A. Sandage, A. Saha, G. A. Tammann, L. Labhardt, N. Panagia, and F. D. Macchetto, "Cepheid Calibration of the Peak Brightness of Type IA Supernovae: Calibration of SN 1990N in NGC 4639 Averaged with Six Earlier Type IA Supernova Calibrations to Give H_0 Directly." *Astrophys. J. Lett* **460** (1996) L15.

[52] A. Nusser and M. Davis, "Estimation of peculiar velocity from the inverse tully-fisher relation." *Mon. Not. Roy. Astron. Soc.* **276** (1995) 1391, [astro-ph/9407100].

[53] R. Watkins and H. A. Feldman, "An Unbiased Estimator of Peculiar Velocity with Gaussian Distributed Errors for Precision Cosmology." *Mon. Not. Roy. Astron. Soc.* **450** (2015), no. 2 1868–1873, [arXiv:1411.6665].

[54] F. Beutler, C. Blake, M. Colless, D. H. Jones, L. Staveley-Smith, L. Campbell, Q. Parker, W. Saunders, and F. Watson, "The 6dF Galaxy Survey: Baryon Acoustic Oscillations and the Local Hubble Constant." *Mon. Not. Roy. Astron. Soc.* **416** (2011) 3017–3032, [arXiv:1106.3366].

[55] J. G. Sorce, "Minimization of biases in galaxy peculiar velocity catalogues." *Mon. Not. Roy. Astron. Soc.* **450** (2015), no. 3 2644–2657, [arXiv:1504.06968].

[56] R. B. Tully et al., "Cosmicflows-2: The Data." *Astron. J.* **146** (2013) 86, [arXiv:1307.7213].

[57] A. Hamilton, "Omega from the anisotropy of the redshift correlation function in the iras 2 jansky survey." *The Astrophysical Journal* **406** (1993) L47–L50.

[58] J. N. Fry and E. Gaztanaga, "Biasing and hierarchical statistics in large scale structure." *Astrophys. J.* **413** (1993) 447–452, [astro-ph/9302009].

[59] P. J. E. Peebles, *The large-scale structure of the universe.* 1980.

[60] K. B. Fisher, M. Davis, M. A. Strauss, A. Yahil, and J. P. Huchra, "Clustering in the 1.2-Jy IRAS Galaxy Redshift Survey–II. Redshift distortions and $\xi(r_p, \pi)$." *Mon. Not. Roy. Astron. Soc.* **267** (1994) 927, [astro-ph/9308013].

[61] J. Koda, C. Blake, T. Davis, C. Magoulas, C. M. Springob, M. Scrimgeour, A. Johnson, G. B. Poole, and L. Staveley-Smith, "Are peculiar velocity surveys competitive as a cosmological probe?." *Mon. Not. Roy. Astron. Soc.* **445** (2014), no. 4 4267–4286, [arXiv:1312.1022].

[62] J. Carrick, S. J. Turnbull, G. Lavaux, and M. J. Hudson, "Cosmological parameters from the comparison of peculiar velocities with predictions from the 2M++ density field." *Mon. Not. Roy. Astron. Soc.* **450** (2015), no. 1 317–332, [arXiv:1504.04627].

[63] R. W. Pike and M. J. Hudson, "Cosmological parameters from the comparison of the 2mass gravity field with peculiar velocity surveys." *Astrophys. J.* **635** (2005) 11–21, [astro-ph/0511012].

[64] M. Davis, A. Nusser, K. Masters, C. Springob, J. P. Huchra, and G. Lemson, "Local Gravity versus Local Velocity: Solutions for β and nonlinear bias." *Mon. Not. Roy. Astron. Soc.* **413** (2011) 2906, [arXiv:1011.3114].

[65] E. Branchini, M. Davis, and A. Nusser, "The velocity field of 2MRS Ks=11.75 galaxies: constraints on beta and bulk flow from the luminosity function." *Mon. Not. Roy. Astron. Soc.* **424** (2012) 472–481, [arXiv:1202.5206].

[66] G. Lavaux and M. J. Hudson, "The 2M++ galaxy redshift catalogue." *Mon. Not. Roy. Astron. Soc.* **416** (2011) 2840–2856, [arXiv:1105.6107].

[67] A. Nusser, E. Branchini, and M. Davis, "A new method for the determination of the growth rate from galaxy redshift surveys." *Astrophys. J.* **744** (2012) 193, [arXiv:1106.6145].

[68] SDSS Collaboration, K. N. Abazajian et al., "The Seventh Data Release of the Sloan Digital Sky Survey." *Astrophys. J. Suppl.* **182** (2009) 543–558, [arXiv:0812.0649].

[69] P. G. Ferreira, R. Juszkiewicz, H. A. Feldman, M. Davis, and A. H. Jaffe, "Streaming velocities as a dynamical estimator of omega." *Astrophys. J.* **515** (1999) L1–L4, [astro-ph/9812456].

[70] S. Bhattacharya, A. Kosowsky, J. A. Newman, and A. R. Zentner, "Galaxy Peculiar Velocities From Large-Scale Supernova Surveys as a Dark Energy Probe." *Phys. Rev.* **D83** (2011) 043004, [arXiv:1008.2560].

[71] SNLS Collaboration, J. D. Neill, M. J. Hudson, and A. J. Conley, "The Peculiar Velocities of Local Type Ia Supernovae and their Impact on Cosmology." *Astrophys. J.* **661** (2007) L123, [arXiv:0704.1654].

[72] W. A. Hellwing, A. Barreira, C. S. Frenk, B. Li, and S. Cole, "A clear and measurable signature of modified gravity in the galaxy velocity field." *Phys. Rev. Lett.* **112** (2014) 221102, [arXiv:1401.0706].

[73] A. Johnson, C. Blake, J. Dossett, J. Koda, D. Parkinson, and S. Joudaki, "Searching for Modified Gravity: Scale and Redshift Dependent Constraints from Galaxy Peculiar Velocities." arXiv:1504.06885.

[74] A. Kosowsky and S. Bhattacharya, "A Future Test of Gravitation Using Galaxy Cluster Velocities." *Phys. Rev.* **D80** (2009) 062003, [arXiv:0907.4202].

[75] A. Johnson et al., "The 6dF Galaxy Velocity Survey: Cosmological constraints from the velocity power spectrum." *Mon. Not. Roy. Astron. Soc.* **444** (2014) 3926, [arXiv:1404.3799].

[76] C. Bonvin, R. Durrer, and M. A. Gasparini, "Fluctuations of the luminosity distance." *Phys. Rev.* **D73** (2006) 023523, [astro-ph/0511183]. [Erratum: Phys. Rev.D85,029901(2012)].

[77] O. Umeh, C. Clarkson, and R. Maartens, "Nonlinear relativistic corrections to cosmological distances, redshift and gravitational lensing magnification: I. Key results." *Class. Quant. Grav.* **31** (2014) 202001, [arXiv:1207.2109].

[78] O. Umeh, C. Clarkson, and R. Maartens, "Nonlinear relativistic corrections to cosmological distances, redshift and gravitational lensing magnification. II - Derivation." *Class. Quant. Grav.* **31** (2014) 205001, [arXiv:1402.1933].

[79] J. Crowder and N. J. Cornish, "Beyond LISA: Exploring future gravitational wave missions." *Phys. Rev.* **D72** (2005) 083005, [gr-qc/0506015].

[80] C. Cutler and D. E. Holz, "Ultra-high precision cosmology from gravitational waves." *Phys. Rev.* **D80** (2009) 104009, [arXiv:0906.3752].

[81] S. Mollerach, D. Harari, and S. Matarrese, "CMB polarization from secondary vector and tensor modes." *Phys. Rev.* **D69** (2004) 063002, [astro-ph/0310711].

[82] M. Kamionkowski, A. Kosowsky, and A. Stebbins, "A Probe of primordial gravity waves and vorticity." *Phys. Rev. Lett.* **78** (1997) 2058–2061, [astro-ph/9609132].

[83] S. Mollerach and S. Matarrese, "Cosmic microwave background anisotropies from second order gravitational perturbations." *Phys. Rev.* **D56** (1997) 4494–4502, [astro-ph/9702234].

[84] K. Tomita, "Relativistic second-order perturbations of nonzero-lambda flat cosmological models and CMB anisotropies." *Phys. Rev.* **D71** (2005) 083504, [astro-ph/0501663].

[85] R. Durrer, "Light deflection in perturbed Friedmann universes." *Phys. Rev. Lett.* **72** (1994) 3301–3304, [astro-ph/9401033].

[86] T. H.-C. Lu, K. Ananda, and C. Clarkson, "Vector modes generated by primordial density fluctuations." *Phys. Rev.* **D77** (2008) 043523, [arXiv:0709.1619].

[87] K. N. Ananda, C. Clarkson, and D. Wands, "The Cosmological gravitational wave background from primordial density perturbations." *Phys. Rev.* **D75** (2007) 123518, [gr-qc/0612013].

[88] C. Bonvin, "Effect of Peculiar Motion in Weak Lensing." *Phys. Rev.* **D78** (2008) 123530, [arXiv:0810.0180].

[89] K. Bolejko, C. Clarkson, R. Maartens, D. Bacon, N. Meures, and E. Beynon, "Antilensing: The Bright Side of Voids." *Phys. Rev. Lett.* **110** (2013), no. 2 021302, [arXiv:1209.3142].

[90] N. Sugiura, N. Sugiyama, and M. Sasaki, "Anisotropies in Luminosity Distance." *Progress of Theoretical Physics* **101** (Apr., 1999) 903–922.

[91] L. Hui and P. B. Greene, "Correlated Fluctuations in Luminosity Distance and the (Surprising) Importance of Peculiar Motion in Supernova Surveys." *Phys. Rev.* **D73** (2006) 123526, [astro-ph/0512159].

[92] A. Cooray and R. R. Caldwell, "Large-scale bulk motions complicate the hubble diagram." *Phys. Rev.* **D73** (2006) 103002, [astro-ph/0601377].

[93] T. M. Davis et al., "The effect of peculiar velocities on supernova cosmology." *Astrophys. J.* **741** (2011) 67, [arXiv:1012.2912].

[94] C. Clarkson, "Establishing homogeneity of the universe in the shadow of dark energy." *Comptes Rendus Physique* **13** (2012) 682–718, [arXiv:1204.5505].

[95] S. February, C. Clarkson, and R. Maartens, "Galaxy correlations and the BAO in a void universe: structure formation as a test of the Copernican Principle." *JCAP* **1303** (2013) 023, [arXiv:1206.1602].

[96] W. Valkenburg, V. Marra, and C. Clarkson, "Testing the Copernican principle by constraining spatial homogeneity." *Mon. Not. Roy. Astron. Soc.* **438** (2014) L6–L10, [arXiv:1209.4078].

[97] B. Hoyle, R. Tojeiro, R. Jimenez, A. Heavens, C. Clarkson, and R. Maartens, "Testing Homogeneity with the Galaxy Fossil Record." *Astrophys. J.* **762** (2012) L9, [arXiv:1209.6181].

[98] P. Peter and J.-P. Uzan, *Primordial cosmology.* Oxford University Press, 2013.

[99] E. Poisson, *An advanced course in general relativity.* 2002.

[100] K. A. Malik and D. Wands, "Cosmological perturbations." *Phys. Rept.* **475** (2009) 1–51, [arXiv:0809.4944].

[101] M. Bruni, S. Matarrese, S. Mollerach, and S. Sonego, "Perturbations of space-time: Gauge transformations and gauge invariance at second order and beyond." *Class. Quant. Grav.* **14** (1997) 2585–2606, [gr-qc/9609040].

[102] K. Nakamura, "Second-order gauge invariant cosmological perturbation theory: Einstein equations in terms of gauge invariant variables." *Prog. Theor. Phys.* **117** (2007) 17–74, [gr-qc/0605108].

[103] J. M. Bardeen, "Gauge-invariant cosmological perturbations." *Phys. Rev.* **D22** (1980), no. 8 1882.

[104] V. F. Mukhanov, H. A. Feldman, and R. H. Brandenberger, "Theory of cosmological perturbations." *Physics Reports* **215** (1992), no. 5 203–333.

[105] H. Kodama and M. Sasaki, "Cosmological Perturbation Theory." *Prog. Theor. Phys. Suppl.* **78** (1984) 1–166.

[106] E. M. Lifshitz, "On the gravitational stability of the expanding universe." *Zhurnal Eksperimentalnoi i Teoreticheskoi Fiziki* **16** (1946) 587–602.

[107] U. Seljak and M. Zaldarriaga, "A Line of sight integration approach to cosmic microwave background anisotropies." *Astrophys. J.* **469** (1996) 437–444, [astro-ph/9603033].

[108] A. Lewis, A. Challinor, and A. Lasenby, "Efficient computation of CMB anisotropies in closed FRW models." *Astrophys. J.* **538** (2000) 473–476, [astro-ph/9911177].

[109] N. Deruelle and V. F. Mukhanov, "On matching conditions for cosmological perturbations." *Phys. Rev.* **D52** (1995) 5549–5555, [gr-qc/9503050].

[110] J. Martin and D. J. Schwarz, "The Influence of cosmological transitions on the evolution of density perturbations." *Phys. Rev.* **D57** (1998) 3302–3316, [gr-qc/9704049].

[111] T. H.-C. Lu, K. Ananda, C. Clarkson, and R. Maartens, "The cosmological background of vector modes." *JCAP* **0902** (2009) 023, [arXiv:0812.1349].

[112] D. J. Eisenstein and W. Hu, "Baryonic features in the matter transfer function." *Astrophys. J.* **496** (1998) 605, [astro-ph/9709112].

[113] WMAP Collaboration, E. Komatsu et al., "Five-Year Wilkinson Microwave Anisotropy Probe (WMAP) Observations: Cosmological Interpretation." *Astrophys. J. Suppl.* **180** (2009) 330–376, [arXiv:0803.0547].

[114] S. Matarrese, S. Mollerach, and M. Bruni, "Second order perturbations of the Einstein-de Sitter universe." *Phys. Rev.* **D58** (1998) 043504, [astro-ph/9707278].

[115] S. Matarrese, S. Mollerach, A. Notari, and A. Riotto, "Large-scale magnetic fields from density perturbations." *Phys. Rev.* **D71** (2005) 043502, [astro-ph/0410687].

[116] M. Bruni, D. B. Thomas, and D. Wands, "Computing General Relativistic effects from Newtonian N-body simulations: Frame dragging in the post-Friedmann approach." *Phys. Rev.* **D89** (2014), no. 4 044010, [arXiv:1306.1562].

[117] D. Sarkar, P. Serra, A. Cooray, K. Ichiki, and D. Baumann, "Cosmic shear from scalar-induced gravitational waves." *Phys. Rev.* **D77** (2008) 103515, [arXiv:0803.1490].

[118] D. Baumann, P. J. Steinhardt, K. Takahashi, and K. Ichiki, "Gravitational Wave Spectrum Induced by Primordial Scalar Perturbations." *Phys. Rev.* **D76** (2007) 084019, [hep-th/0703290].

[119] P. Schneider, J. Ehlers, and E. Falco, *Gravitational Lenses, XIV, 560 pp. 112 figs.* Springer-Verlag Berlin Heidelberg New York. Also Astronomy and Astrophysics Library, 1992.

[120] R. S. Ellis, "Gravitational lensing: a unique probe of dark matter and dark energy." *Philosophical Transactions of the Royal Society of London Series A* **368** (Feb., 2010) 967–987.

[121] S. Pires, J. L. Starck, and A. Refregier, "Light on Dark Matter with Weak Gravitational Lensing." *IEEE Sig. Proc. Mag.* **27** (2010) 76, [arXiv:0908.4157].

[122] N. Kaiser and G. Squires, "Mapping the dark matter with weak gravitational lensing." *Astrophys. J.* **404** (1993) 441–450.

[123] R. Narayan and M. Bartelmann, "Lectures on gravitational lensing." in *13th Jerusalem Winter School in Theoretical Physics: Formation of Structure in the Universe Jerusalem, Israel, 27 December 1995 - 5 January 1996*, 1996. astro-ph/9606001.

[124] M. Sasaki, "Cosmological gravitational lens equation: Its validity and limitation." *Prog. Theor. Phys.* **90** (1993) 753–781.

[125] M. Bartelmann and P. Schneider, "Weak gravitational lensing." *Phys. Rept.* **340** (2001) 291–472, [astro-ph/9912508].

[126] C. Pitrou, J.-P. Uzan, and T. S. Pereira, "Weak lensing B-modes on all scales as a probe of local isotropy." *Phys. Rev.* **D87** (2013), no. 4 043003, [arXiv:1203.6029].

[127] C. Clarkson, G. Ellis, J. Larena, and O. Umeh, "Does the growth of structure affect our dynamical models of the universe? The averaging, backreaction and fitting problems in cosmology." *Rept. Prog. Phys.* **74** (2011) 112901, [arXiv:1109.2314].

[128] T. Buchert, "On average properties of inhomogeneous fluids in general relativity. 1. Dust cosmologies." *Gen. Rel. Grav.* **32** (2000) 105–125, [gr-qc/9906015].

[129] T. Buchert, "On average properties of inhomogeneous fluids in general relativity: Perfect fluid cosmologies." *Gen. Rel. Grav.* **33** (2001) 1381–1405, [gr-qc/0102049].

[130] S. Rasanen, "Dark energy from backreaction." *JCAP* **0402** (2004) 003, [astro-ph/0311257].

[131] E. Barausse, S. Matarrese, and A. Riotto, "The Effect of inhomogeneities on the luminosity distance-redshift relation: Is dark energy necessary in a perturbed Universe?." *Phys. Rev.* **D71** (2005) 063537, [astro-ph/0501152].

[132] E. W. Kolb, S. Matarrese, and A. Riotto, "On cosmic acceleration without dark energy." *New J. Phys.* **8** (2006) 322, [astro-ph/0506534].

[133] S. Rasanen, "Accelerated expansion from structure formation." *JCAP* **0611** (2006) 003, [astro-ph/0607626].

[134] M. Kasai, "Apparent Acceleration through the Large-scale Inhomogeneities: Post-Friedmannian effects of inhomogeneities on the luminosity distance." *Prog. Theor. Phys.* **117** (2007) 1067–1075, [astro-ph/0703298].

[135] A. Ishibashi and R. M. Wald, "Can the acceleration of our universe be explained by the effects of inhomogeneities?." *Class. Quant. Grav.* **23** (2006) 235–250, [gr-qc/0509108].

[136] E. E. Flanagan, "Can superhorizon perturbations drive the acceleration of the universe?." *Phys. Rev.* **D71** (2005) 103521, [hep-th/0503202].

[137] C. M. Hirata and U. Seljak, "Can superhorizon cosmological perturbations explain the acceleration of the Universe?." *Phys. Rev.* **D72** (2005) 083501, [astro-ph/0503582].

[138] S. R. Green and R. M. Wald, "A new framework for analyzing the effects of small scale inhomogeneities in cosmology." *Phys. Rev.* **D83** (2011) 084020, [arXiv:1011.4920].

[139] E. W. Kolb, S. Matarrese, A. Notari, and A. Riotto, "The Effect of inhomogeneities on the expansion rate of the universe." *Phys. Rev.* **D71** (2005) 023524, [hep-ph/0409038].

[140] N. Li and D. J. Schwarz, "On the onset of cosmological backreaction." *Phys. Rev.* **D76** (2007) 083011, [gr-qc/0702043].

[141] N. Li and D. J. Schwarz, "Scale dependence of cosmological backreaction." *Phys. Rev.* **D78** (2008) 083531, [arXiv:0710.5073].

[142] C. Clarkson, K. Ananda, and J. Larena, "The influence of structure formation on the cosmic expansion." *Phys. Rev.* **D80** (2009) 083525, [arXiv:0907.3377].

[143] O. Umeh, J. Larena, and C. Clarkson, "The Hubble rate in averaged cosmology." *JCAP* **1103** (2011) 029, [arXiv:1011.3959].

[144] C. Clarkson and O. Umeh, "Is backreaction really small within concordance cosmology?." *Class. Quant. Grav.* **28** (2011) 164010, [arXiv:1105.1886].

[145] G. Marozzi and J.-P. Uzan, "Late time anisotropy as an imprint of cosmological backreaction." *Phys. Rev.* **D86** (2012) 063528, [arXiv:1206.4887].

[146] J. Adamek, D. Daverio, R. Durrer, and M. Kunz, "General Relativistic N-body simulations in the weak field limit." *Phys. Rev.* **D88** (2013), no. 10 103527, [arXiv:1308.6524].

[147] C. Pitrou, "The Radiative transfer at second order: A Full treatment of the Boltzmann equation with polarization." *Class. Quant. Grav.* **26** (2009) 065006, [arXiv:0809.3036].

[148] C. Pitrou, J.-P. Uzan, and F. Bernardeau, "Cosmic microwave background bispectrum on small angular scales." *Phys. Rev.* **D78** (2008) 063526, [arXiv:0807.0341].

[149] C. Pitrou, J.-P. Uzan, and F. Bernardeau, "The cosmic microwave background bispectrum from the non-linear evolution of the cosmological perturbations." *JCAP* **1007** (2010) 003, [arXiv:1003.0481].

[150] Z. Huang and F. Vernizzi, "Cosmic Microwave Background Bispectrum from Recombination." *Phys. Rev. Lett.* **110** (2013), no. 10 101303, [arXiv:1212.3573].

[151] Planck Collaboration, P. A. R. Ade et al., "Planck 2013 Results. XXIV. Constraints on primordial non-Gaussianity." *Astron. Astrophys.* **571** (2014) A24, [arXiv:1303.5084].

[152] S. Renaux-Petel, C. Fidler, C. Pitrou, and G. W. Pettinari, "Spectral distortions in the cosmic microwave background polarization." *JCAP* **1403** (2014) 033, [arXiv:1312.4448].

[153] C. Pitrou, F. Bernardeau, and J.-P. Uzan, "The y-sky: diffuse spectral distortions of the cosmic microwave background." *JCAP* **1007** (2010) 019, [arXiv:0912.3655].

[154] Y. Mellier, "Probing the universe with weak lensing." *Ann. Rev. Astron. Astrophys.* **37** (1999) 127–189, [astro-ph/9812172].

[155] J.-P. Uzan, "Tests of General Relativity on Astrophysical Scales." *Gen. Rel. Grav.* **42** (2010) 2219–2246, [arXiv:0908.2243].

[156] J.-P. Uzan and F. Bernardeau, "Lensing at cosmological scales: A Test of higher dimensional gravity." *Phys. Rev.* **D64** (2001) 083004, [hep-ph/0012011].

[157] C. Clarkson, G. F. R. Ellis, A. Faltenbacher, R. Maartens, O. Umeh, and J.-P. Uzan, "(Mis-)Interpreting supernovae observations in a lumpy universe." *Mon. Not. Roy. Astron. Soc.* **426** (2012) 1121–1136, [arXiv:1109.2484].

[158] I. Ben-Dayan, G. Marozzi, F. Nugier, and G. Veneziano, "The second-order luminosity-redshift relation in a generic inhomogeneous cosmology." *JCAP* **1211** (2012) 045, [arXiv:1209.4326].

[159] I. Ben-Dayan, M. Gasperini, G. Marozzi, F. Nugier, and G. Veneziano, "Do stochastic inhomogeneities affect dark-energy precision measurements?." *Phys. Rev. Lett.* **110** (2013), no. 2 021301, [arXiv:1207.1286].

[160] P. Fleury, H. Dupuy, and J.-P. Uzan, "Interpretation of the Hubble diagram in a nonhomogeneous universe." *Phys. Rev.* **D87** (2013), no. 12 123526, [arXiv:1302.5308].

[161] P. Fleury, H. Dupuy, and J.-P. Uzan, "Can all cosmological observations be accurately interpreted with a unique geometry?." *Phys. Rev. Lett.* **111** (2013) 091302, [arXiv:1304.7791].

[162] I. Ben-Dayan, M. Gasperini, G. Marozzi, F. Nugier, and G. Veneziano, "Average and dispersion of the luminosity-redshift relation in the concordance model." *JCAP* **1306** (2013) 002, [arXiv:1302.0740].

[163] F. Schmidt and D. Jeong, "Cosmic Rulers." *Phys. Rev.* **D86** (2012) 083527, [arXiv:1204.3625].

[164] D. Jeong and F. Schmidt, "Cosmic Clocks." *Phys. Rev.* **D89** (2014), no. 4 043519, [arXiv:1305.1299].

[165] D. J. Bacon, S. Andrianomena, C. Clarkson, K. Bolejko, and R. Maartens, "Cosmology with Doppler Lensing." *Mon. Not. Roy. Astron. Soc.* **443** (2014), no. 3 1900–1915, [arXiv:1401.3694].

[166] S. Seitz, P. Schneider, and J. Ehlers, "Light propagation in arbitrary space-times and the gravitational lens approximation." *Class. Quant. Grav.* **11** (1994) 2345–2374, [astro-ph/9403056].

[167] A. Cooray and W. Hu, "Second order corrections to weak lensing by large scale structure." *Astrophys. J.* **574** (2002) 19, [astro-ph/0202411].

[168] S. Dodelson, E. W. Kolb, S. Matarrese, A. Riotto, and P. Zhang, "Second order geodesic corrections to cosmic shear." *Phys. Rev.* **D72** (2005) 103004, [astro-ph/0503160].

[169] B. M. Schaefer and M. Bartelmann, "Weak lensing in the second post-Newtonian approximation: Gravitomagnetic potentials and the integrated Sachs-Wolfe effect." *Mon. Not. Roy. Astron. Soc.* **369** (2006) 425–440, [astro-ph/0502208].

[170] C. Shapiro and A. Cooray, "The born and lens-lens corrections to weak gravitational lensing angular power spectra." *JCAP* **0603** (2006) 007, [astro-ph/0601226].

[171] F. Bernardeau, C. Bonvin, and F. Vernizzi, "Full-sky lensing shear at second order." *Phys. Rev.* **D81** (2010) 083002, [arXiv:0911.2244].

[172] F. Bernardeau, C. Bonvin, N. Van de Rijt, and F. Vernizzi, "Cosmic shear bispectrum from second-order perturbations in General Relativity." *Phys. Rev.* **D86** (2012) 023001, [arXiv:1112.4430].

[173] VIRGO Consortium Collaboration, R. E. Smith, J. A. Peacock, A. Jenkins, S. D. M. White, C. S. Frenk, F. R. Pearce, P. A. Thomas, G. Efstathiou, and H. M. P. Couchmann, "Stable clustering, the halo model and nonlinear cosmological power spectra." *Mon. Not. Roy. Astron. Soc.* **341** (2003) 1311, [astro-ph/0207664].

[174] J.-P. Uzan and F. Bernardeau, "Cosmic strings lens phenomenology: General properties of distortion fields." *Phys. Rev.* **D63** (2001) 023004, [astro-ph/0004105].

[175] D. Yamauchi, T. Namikawa, and A. Taruya, "Full-sky formulae for weak lensing power spectra from total angular momentum method." *JCAP* **1308** (2013) 051, [arXiv:1305.3348].

[176] M. LoVerde and N. Afshordi, "Extended Limber Approximation." *Phys. Rev.* **D78** (2008) 123506, [arXiv:0809.5112].

[177] F. Bernardeau, C. Pitrou, and J.-P. Uzan, "CMB spectra and bispectra calculations: making the flat-sky approximation rigorous." *JCAP* **1102** (2011) 015, [arXiv:1012.2652].

[178] E. Beynon, D. J. Bacon, and K. Koyama, "Weak lensing predictions for modified gravities at non-linear scales." *Mon. Not. Roy. Astron. Soc.* **403** (2010) 353–362, [arXiv:0910.1480].

[179] Euclid Theory Working Group Collaboration, L. Amendola et al., "Cosmology and fundamental physics with the Euclid satellite." *Living Rev. Rel.* **16** (2013) 6, [arXiv:1206.1225].

[180] EUCLID Collaboration, R. Laureijs et al., "Euclid Definition Study Report." arXiv:1110.3193.

[181] R. J. Wilman et al., "A semi-empirical simulation of the extragalactic radio continuum sky for next generation radio telescopes." *Mon. Not. Roy. Astron. Soc.* **388** (2008) 1335–1348, [arXiv:0805.3413].

[182] A. Heavens, J. Alsing, and A. Jaffe, "Combining Size and Shape in Weak Lensing." *Mon. Not. Roy. Astron. Soc.* **433** (2013) 6, [arXiv:1302.1584].

[183] N. Kaiser, G. Squires, and T. J. Broadhurst, "A Method for weak lensing observations." *Astrophys. J.* **449** (1995) 460–475, [astro-ph/9411005].

[184] V. Springel et al., "Simulating the joint evolution of quasars, galaxies and their large-scale distribution." *Nature* **435** (2005) 629–636, [astro-ph/0504097].

[185] M. Boylan-Kolchin, V. Springel, S. D. M. White, A. Jenkins, and G. Lemson, "Resolving Cosmic Structure Formation with the Millennium-II Simulation." *Mon. Not. Roy. Astron. Soc.* **398** (2009) 1150, [arXiv:0903.3041].

[186] Q. Guo, S. White, C. Li, and M. Boylan-Kolchin, "How do galaxies populate Dark Matter halos?." *Mon. Not. Roy. Astron. Soc.* **404** (2010) 1111, [arXiv:0909.4305].

[187] P. E. Dewdney, P. J. Hall, R. T. Schilizzi, and T. J. L. Lazio, "The square kilometre array." *Proceedings of the IEEE* **97** (2009), no. 8 1482–1496.

[188] C. Howlett, A. Lewis, A. Hall, and A. Challinor, "CMB power spectrum parameter degeneracies in the era of precision cosmology." *JCAP* **1204** (2012) 027, [arXiv:1201.3654].

[189] W. Hu and B. Jain, "Joint galaxy - lensing observables and the dark energy." *Phys. Rev.* **D70** (2004) 043009, [astro-ph/0312395].

[190] B. Joachimi, E. Semboloni, S. Hilbert, P. E. Bett, J. Hartlap, H. Hoekstra, and P. Schneider, "Intrinsic galaxy shapes and alignments II: Modelling the intrinsic alignment contamination of weak lensing surveys." arXiv:1305.5791.

[191] M. Sasaki, "The Magnitude - Redshift relation in a perturbed Friedmann universe." *Mon. Not. Roy. Astron. Soc.* **228** (1987) 653–669.

[192] T. Futamase and M. Sasaki, "Light Propagation and the Distance Redshift Relation in a Realistic Inhomogeneous Universe." *Phys. Rev.* **D40** (1989) 2502.

[193] A. Challinor and A. Lewis, "The linear power spectrum of observed source number counts." *Phys. Rev.* **D84** (2011) 043516, [arXiv:1105.5292].

[194] J. Alsing, D. Kirk, A. Heavens, and A. Jaffe, "Weak Lensing with Sizes, Magnitudes and Shapes." *Mon. Not. Roy. Astron. Soc.* **452** (2015), no. 2 1202–1216, [arXiv:1410.7839].

[195] W. J. Percival et al., "The shape of the SDSS DR5 galaxy power spectrum." *Astrophys. J.* **657** (2007) 645–663, [astro-ph/0608636].

[196] BOSS Collaboration, L. Anderson et al., "The clustering of galaxies in the SDSS-III Baryon Oscillation Spectroscopic Survey: baryon acoustic oscillations in the Data Releases 10 and 11 Galaxy samples." *Mon. Not. Roy. Astron. Soc.* **441** (2014), no. 1 24–62, [arXiv:1312.4877].

[197] G. R. Dvali, G. Gabadadze, and M. Porrati, "Metastable gravitons and infinite volume extra dimensions." *Phys. Lett.* **B484** (2000) 112–118, [hep-th/0002190].

[198] K. Koyama and R. Maartens, "Structure formation in the dgp cosmological model." *JCAP* **0601** (2006) 016, [astro-ph/0511634].

[199] W. Hu and I. Sawicki, "Models of f(R) Cosmic Acceleration that Evade Solar-System Tests." *Phys. Rev.* **D76** (2007) 064004, [arXiv:0705.1158].

[200] K. Koyama, A. Taruya, and T. Hiramatsu, "Non-linear Evolution of Matter Power Spectrum in Modified Theory of Gravity." *Phys. Rev.* **D79** (2009) 123512, [arXiv:0902.0618].

[201] W. Hu and I. Sawicki, "A Parameterized Post-Friedmann Framework for Modified Gravity." *Phys. Rev.* **D76** (2007) 104043, [arXiv:0708.1190].

[202] L. Pogosian, A. Silvestri, K. Koyama, and G.-B. Zhao, "How to optimally parametrize deviations from General Relativity in the evolution of cosmological perturbations?." *Phys. Rev.* **D81** (2010) 104023, [arXiv:1002.2382].

[203] G.-B. Zhao, L. Pogosian, A. Silvestri, and J. Zylberberg, "Searching for modified growth patterns with tomographic surveys." *Phys. Rev.* **D79** (2009) 083513, [arXiv:0809.3791].

[204] T. Baker, P. G. Ferreira, C. D. Leonard, and M. Motta, "New Gravitational Scales in Cosmological Surveys." *Phys. Rev.* **D90** (2014), no. 12 124030, [arXiv:1409.8284].

[205] Planck Collaboration, P. A. R. Ade et al., "Planck 2015 results. XIV. Dark energy and modified gravity." arXiv:1502.01590.

[206] F. Bernardeau, S. Colombi, E. Gaztanaga, and R. Scoccimarro, "Large scale structure of the universe and cosmological perturbation theory." *Phys. Rept.* **367** (2002) 1–248, [astro-ph/0112551].

[207] B. Jain, U. Seljak, and S. D. M. White, "Ray tracing simulations of weak lensing by large scale structure." *Astrophys. J.* **530** (2000) 547, [astro-ph/9901191].

[208] R. D. Blandford, A. B. Saust, T. G. Brainerd, and J. V. Villumsen, "The distortion of distant galaxy images by large-scale structure." *Mon. Not. Roy. Astron. Soc.* **251** (1991) 600–627.

[209] J. Wambsganss, R. Cen, and J. P. Ostriker, "Testing cosmological models by gravitational lensing: 1. Method and first applications." *Submitted to: Astrophys. J.* (1996) [astro-ph/9610096].

[210] A. Loeb and S. Wyithe, "Precise Measurement of the Cosmological Power Spectrum With a Dedicated 21cm Survey After Reionization." *Phys. Rev. Lett.* **100** (2008) 161301, [arXiv:0801.1677].

[211] T.-C. Chang, U.-L. Pen, J. B. Peterson, and P. McDonald, "Baryon Acoustic Oscillation Intensity Mapping as a Test of Dark Energy." *Phys. Rev. Lett.* **100** (2008) 091303, [arXiv:0709.3672].

[212] S. Wyithe and A. Loeb, "The 21cm Power Spectrum After Reionization." *Mon. Not. Roy. Astron. Soc.* **397** (2009) 1926, [arXiv:0808.2323].

[213] A. Pourtsidou and R. B. Metcalf, "Gravitational lensing of cosmological 21 cm emission." *Mon. Not. Roy. Astron. Soc.* **448** (2015) 2368–2383, [arXiv:1410.2533].

[214] P. Bull, P. G. Ferreira, P. Patel, and M. G. Santos, "Late-time cosmology with 21cm intensity mapping experiments." *Astrophys. J.* **803** (2015), no. 1 21, [arXiv:1405.1452].